THE CALIBRATION AND UNIFORMITY MAPPING OF THE ALEPH ELECTROMAGNETIC CALORIMETER

John L. Hearns

Department of Physics and Astronomy
The University of Glasgow
Glasgow. Scotland

Thesis submitted for the degree of
Doctor of Philosophy

October 1992

ProQuest LLC.
789 East Eisenhower Parkway
P.O. Box 1346
Ann Arbor, MI 48106 – 1346

Acknowledgements

I have enjoyed very much the time I have been at Glasgow University, both as an undergraduate and as a postgraduate. I have made very many friends and acquaintances amongst the students and staff here over the years: in my undergraduate class, in the canoe club and in the Research Club (especially Ron who kept me well supplied with toasties). I have made too many friends to list individually amongst the research students in the Department, but the High Energy brothers and the Laser boys know who they all are. All of these people have made my years as a student worthwhile. My only regret is that I didn't make time to meet more people. The same goes also for the many people I met whilst living in Geneva!

Thanks are due to Prof. Smith (aka. Ken) my very patient supervisor. Thanks also to Dave Martin, Alan Flavell and Big Stan for their friendship and help with piffling problems even when they were overwhelmed with more pressing matters; to Ian Hughes with whom I enjoyed working during an all too short summer at CERN and to Ian Skillicorn for his dry wit and invaluable help. I must of course mention Catherine MacIntyre, as without her I would have faced financial ruin and stranding in foreign airports on many an occasion. Her cheery nature and gentle encouragement have brightened up the lives of a generation of research students.

This thesis was written using the TEX program written by Donald Knuth of Stanford University in conjunction with the TEXSIS package of E. Myers and F.E. Paige. Most of the figures were prepared with the help of John Bradley's XV imaging and display package. My thanks are also due to the manufacturers of Blue Dragon 3-minute noodle lunch boxes.

Of course, none of this would have been possible without the financial and moral support of my parents Sadie and John during the long years of my studies. I will never be able to pay them back adequately. I hope they are as proud of me as I am of them.

Abstract

The first chapter of this thesis is an introduction to the field of high energy physics, concentrating on the physics of electron–positron colliders. The historical development of electron beam colliders is discussed, culminating in the LEP and SLC accelerators. The principles behind the various techniques used in high energy particle detectors are discussed. A survey of the physics results so far obtained by the ALEPH collaboration is presented.

The next chapter is an overview of the principles of operation of calorimeter devices. The practical implementation of many varieties of calorimeter at accelerator facilities is discussed.

In the third chapter, the LEP accelerator complex at CERN and the four detectors in operation at LEP are briefly described. All parts of the ALEPH apparatus are described in detail.

The fourth chapter concerns the software implemented by the ALEPH collaboration for on–line data collection, reconstruction of events and Monte Carlo simulation. Emphasis is made on the aspects relevant to the electromagnetic calorimeter.

The next chapter is concerned with the design, construction, calibration and operation of the ALEPH electromagnetic calorimeter, concentrating on the end–cap segments. The various methods used to test and calibrate the device prior to its installation at the ALEPH experimental site and during data taking are discussed. The methods used to measure the uniformity of response of the end–cap segments are described. The thesis presents the analysis of the results of several different techniques which aimed to measure and map the uniformity of response of the calorimeter modules and to calibrate their response prior to LEP data taking. The calorimeter has an energy resolution of $17\%/\sqrt{E}$, and the uniformity is measured to be at the level of $\sim 2\%$. The original design concept of the calorimeter is shown to be sound. The device is demonstrated to be an admirable instrument, capable of taking data at the current LEP accelerator and at higher energy and higher luminosity in the future.

The final chapter of the thesis presents an analysis of the reconstruction of π^0 mesons using the electromagnetic calorimeter. The inclusive π^0 momentum spectrum is measured and is compared with the Lund fragmentation model and the results from the competing L3 experiment.

Preface

This thesis concerns work undertaken whilst the author was a member of the ALEPH collaboration, a large international team of scientists based at CERN in Geneva. The UK institutes within ALEPH were responsible for the construction of the electromagnetic calorimeter end–cap modules.

The author participated in the construction of the cosmic ray testing apparatus for the calorimeter modules at the Rutherford Appleton Laboratory, and in the subsequent cosmic ray data taking. He also participated in test beam data taking when end–cap and barrel modules of the calorimeter were measured at CERN in 1987 and 1988, and in taking radioactive gas spectra during the test beam running in 1988, and prior to the first LEP running in 1989. Prior to the LEP startup he also contributed to the installation and commissioning of the end–cap modules in the ALEPH detector in 1989.

The results presented here depend on the work of many people within the collaboration, as they must, given the wide range of techniques presented. However, the analysis and presentation of the data is entirely the work of the author. No portion of the work referred to in this thesis has been submitted in support of an application for another degree or qualification in this, or any other, institute of learning.

Contents

Chapter 1.
The Development of Particle Physics

Maybe I didn't love you quite as often as I could have
Little things I should have said and done
I just never took the time - *The King*

1.1. The Standard Model

There are known to be four fundamental forces in nature: gravitational, electromagnetic, weak and strong. Gravity is the force which acts between all bodies in the universe. The gravitational force is unimportant on the nuclear scale. The electromagnetic forces bind together electrons and nuclei into atoms and molecules: these are the forces which control the processes of everyday life. Weak forces mediate certain nuclear processes such as beta decay: the weak force underlies the nuclear reactions which cause the stars to shine. The strong forces are responsible for the inter-nucleon forces holding the atomic nucleus together and the forces binding quarks into nucleons.

According to quantum field theory, all forces are mediated by fields, or equivalently, by the exchange of particles which are the quanta of these fields. Table 1.1.1 shows the four fundamental forces and the properties of their exchange quanta. The gravitational force is thought to be due to the exchange of as yet undiscovered *gravitons*. The electromagnetic force is transmitted between charged particles by the exchange of (virtual) photons. Electromagnetism at the quantum level is explained by the theory of Quantum Electrodynamics (QED), formulated in the first half of this cerntury. QED is one of the most precise and rigorously checked theories so far invented. The weak nuclear force is carried by the *intermediate vector bosons*, which are spin-1 particles, analogous to photons in electromagnetism. The strong nuclear force is carried by the massless *gluon* particles, which have the property of themselves feeling the strong force. The theory of the strong interaction is called Quantum Chromodynamics (QCD). QCD is not a well-understood or exactly tested theory. The quanta of exchange in each case are bosonic particles, and as the theories are *gauge* theories, the particles are known as *gauge bosons*.

force	boson name	charge	spin	mass (GeV)
strong	gluon g	0	1	0
electromagnetic	photon γ	0	1	0
weak	W-boson $W^{\pm}$	± 1	1	80
	Z-boson	0	1	91.2
gravity	graviton	0	2	0

Table 1.1.1: Forces and Gauge Bosons

In the last 20 years it has been shown that the weak and electromagnetic forces, although very different in character, can be described as one unified force. The Glashow–Salam–Weinberg theory of electroweak interactions [1], introduced in 1968, shows that electromagnetism and the weak force, although appearing very different at normal energies have an underlying unity. The effects of the Z^0 boson were first seen in weak neutral current events at the Gargamelle bubble chamber [2]. The existence of the $W^{\pm}$ and Z^0 bosons was first demonstrated experimentally in 1983 at the CERN SPS $p\bar{p}$ collider by the UA1 and UA2 experiments [3–4].

The theories described in this section form the framework of the minimal Standard Model, which is the best and most widely accepted explanation of all the phenomena seen in particle physics to date. In this picture, matter itself is made of fermions, for example at everyday energy levels quarks (which bond together to form protons and neutrons) and electrons make up atoms. The interaction forces between these matter particles are mediated by bosons. The Standard Model consists of six quarks and six leptons organised into three generations, as illustrated in Eq. (1.1.1), plus force–carrying bosons. The leptons in the first generation are the familiar electron and its associated electron neutrino. The second and third generation leptons are the muon and the tau, which seem to be heavier replicas of the electron. The reason why the fundamental particles seem to be organised into three generations remains a mystery.

$$\begin{pmatrix} up \\ down \end{pmatrix} \quad \begin{pmatrix} charm \\ strange \end{pmatrix} \quad \begin{pmatrix} top \\ bottom \end{pmatrix}$$
$$\begin{pmatrix} electron \\ \nu_e \end{pmatrix} \quad \begin{pmatrix} muon \\ \nu_\mu \end{pmatrix} \quad \begin{pmatrix} tau \\ \nu_\tau \end{pmatrix} \tag{1.1.1}$$

In high energy interactions, a plethora of seemingly fundamental hadrons has been found. These hadrons (including the familiar proton and neutron) are made up from combinations of the quarks. The different types of quarks are known as *flavours*. Quarks may

be grouped in pairs in each generation, depending on their isospin. Quarks also possess the quantum number of *colour*. Hadrons are colourless combinations of the quarks. The top quark in the third generation has not yet been experimentally observed, but there are strong theoretical reasons to believe that it exists. Each of the fundamental leptons in the three generations, and the bosons, has an associated anti–particle. All of these particles, plus the Higgs boson mentioned later, form the basis of the Standard Model.

The great power of the Standard Model is that it can explain all of the phenomena so far seen in physics – from the physics of the sub–atomic scale, through everyday chemistry and biochemistry to the high–energy interactions of the cosmos. To date, no experimental evidence has been found which contradicts the Standard Model. Current particle physics experiments aim to test the Standard Model to its limits, and perhaps to find phenomena which cannot be explained by it, for example further particle generations or unexpected, exotic particles.

1.1.1 Quantum Chromodynamics

Quarks and gluons are the particles which experience the strong force. They have the property of *colour*, in analogy with electric charge. A quark may have any of the three colours red, blue or green. Anti–quarks have anti–colour: anti–red, anti–blue or anti–green. Gluons carry two colour charges: a colour and an anti–colour. Colour is conserved at each vertex in the Feynman diagram of the interactions. As the gluons are coloured and themselves 'feel' the force, the strong force has quite different properties as compared to the electromagnetic force transmitted by neutral photons. Gluons may couple directly to other gluons (the three gluon vertex). The strong force also results in the *confinement* of quarks, i.e. only colourless states are seen. The inter–quark potential rises linearly with separation so the effect of adding energy to a hadron is not to separate the quarks, but to create new quark–antiquark pairs from the vacuum as the quarks are pulled apart. The properties of the colour forces are described by the mathematics of Quantum Chromodynamics (QCD).

1.1.2 Gauge Theories

Quantum electrodynamics has the property of *renormalizability*, i.e. the infinite quantities arising from the theory may be cancelled by substituting in physical, observable quantities. This property is due to the gauge nature of the theory. QED is known as a local gauge theory since the Lagrangian which describes it is unchanged if the electron field and the photon field are altered by an arbitrary, local phase factor. The phase factors here belong to

the symmetry group U(1), that of unitary transformations in one dimension. Similarly, the other forces may have gauge invariance and other symmetry groups associated with them. Gauge invariance also requires the existence of gauge bosons (photons in this case).

The known fundamental particles may be grouped in doublets, for example $\begin{pmatrix} e \\ \nu_e \end{pmatrix}$. these are both light fermions, which carry the quantum number of 'electron–ness'. Similarly, other leptons and quarks can be grouped as: $\begin{pmatrix} \mu \\ \nu_\mu \end{pmatrix}$, $\begin{pmatrix} \tau \\ \nu_\tau \end{pmatrix}$, $\begin{pmatrix} u \\ d \end{pmatrix}$, $\begin{pmatrix} c \\ s \end{pmatrix}$, $\begin{pmatrix} t \\ b \end{pmatrix}$. These doublets can be described by two–component fields, and have gauge transformations which are 2×2 matrices operating on these fields. The elements of these matrices can change one member of a doublet into the other. The matrices belong to the group SU(2) of unitary transformations in two dimensions. Local gauge invariance then requires the presence of three gauge bosons: W^+, W^- and W^0. If these interactions are combined with the U(1) group of QED we get the SU(2) × U(1) electroweak theory of Glashow, Salam and Weinberg. The gauge bosons are predicted to be all massless, which is not seen experimentally. So the symmetry is not exact, and there is said to be *spontaneous symmetry breaking* at low energy. This results in a massless gauge boson, the photon, plus three massive gauge bosons: W^+, W^- and Z^0.

In the strong interaction, each quark carries one of three colours and may be described by a three–component field which is a superposition of the colours. The gauge transformation consists of 3×3 matrices belonging to the symmetry group SU(3). Mathematically, this group is non–Abelian (the matrices do not commute), which results in the unusual properties of the strong force described above. Local gauge invariance then requires there to be eight massless gauge bosons – the gluons.

The combination of this SU(3) group of QCD with the electroweak GSW theory results in the *Standard Model* of strong and electroweak forces. For the Standard Model to be renormalizable it also requires the presence of a scalar boson known as the *Higgs*, which arises from the mechanism of spontaneous symmetry breaking which gives masses to the weak gauge bosons, the leptons and the quarks. The Standard Model has been very successful, and no experimental evidence has been found so far to contradict it. However, the only predictions tested are those of the gauge interactions. No mechanism for the electroweak symmetry breaking, or explanation for the origin of quark and lepton masses and mixings has been found. Measurements of the quark and lepton masses, and their mixing matrix parameters, section 1.7, are the basis of the exploration of these mechanisms of the Standard Model.

1.2. A Historical Overview

At the beginning of the 20th Century, it was found that there was a flux of highly energetic and penetrating particles entering the earth's atmosphere from space. For the first half of the 20th Century, the only source of high–energy particles was this cosmic radiation. The cosmic rays were first studied by very elegantly constructed electrometers, carried aloft in balloon flights and across the oceans by liner. The *cloud chamber* – the first tracking detector – was invented by C.T.R. Wilson: in this device ionising particles leave trails in super–saturated vapour. Special thick layers of photographic nuclear emulsion were developed for cosmic ray work. These were carried to high altitude on mountains, or flown in balloons or aircraft to be exposed. Such emulsions are still in use at fixed–target experiments, for example to study charmed particle lifetime. Arrays of Geiger–Muller tubes in conjunction with the first coincidence circuits and scaler counters were developed to count and track cosmic rays. Many of the fundamental particles were first found by these methods.

The positron was first observed in a cloud chamber event in 1932 by Anderson [5]. This is the positive anti–particle partner of the electron, already predicted to exist by Dirac in 1928. The muon was first seen in cloud chamber photographs by Street and Stevenson in 1937 [6]. The muon was initially identified with the heavy meson predicted by Yukawa's theory of the strong nuclear force. However, experiments which showed that positive and negative muons decay at a similar rate in matter disproved this. The muon is, as already mentioned, a heavy lepton, and was the first particle of the second 'generation' discovered. Observation of the decay chain $\pi \rightarrow \mu + \nu$ in nuclear emulsion by Lattes et.al. [7], plus observation of nuclear disintegration initiated by pion capture, established the pi–meson as the particle predicted by Yukawa's theory as the carrier of the strong force. Neutral pions, decaying as $\pi^0 \rightarrow 2\gamma$ were discovered in cosmic ray experiments by Carlson et.al. in 1950 [8] and at the 184 inch synchrocyclotron in Berkeley [9]. The neutral pion was shown to be produced with a similar cross–section to the charged pions, and to have a similar mass.

The kaons, intermediate in mass between the muon and proton, were found in cloud chamber experiments [10] and nuclear emulsions in 1947. These particles are produced with a large cross–section, i.e. via the strong interaction, but, puzzlingly, have a long lifetime (on the scale of strong interactions), so they decay weakly. This was explained by the existence of a new quantum number strangeness.

1.2.1 Non–Accelerator Experiments

Although high energy physics is normally associated with experiments at large international laboratories involving high energy beams of particles, important fundamental measurements are being made with non–accelerator experiments. Such experiments include :

- searches for the magnetic monopole using superconducting flux loops or sophisticated 'Millikan oil drop' type experiments
- measurement of the proton lifetime. These experiments, conducted far underground for shielding against the cosmic ray background, take a large block of matter and instrument it with detectors sensitive enough to pick out the characteristic signal of a proton decay, which certain theories predict may occur very rarely in the detector.
- searches for non–luminous dark matter
- sensitive measurements of the neutrino mass from the end–point of the tritium decay spectrum
- measurement of the solar neutrino flux – e.g. the underground experiment at the Homestake gold mine
- ultra high energy cosmic rays – e.g. Fly's Eye in Arizona which looks at the Cherenkov light of large air showers.

This type of experiment will not be discussed further.

1.2.2 The First Accelerators

Naturally occurring radioactive isotopes, and the low energy electrons and X–rays from discharge tubes were the first laboratory sources of 'high energy' particles. For research into rare phenomena with sophisticated apparatus in a laboratory means of generating higher energy, more intense and controllable beams were obviously desirable. An early example is the Cockcroft–Walton apparatus, which used a diode–capacitor voltage doubling ladder and a vacuum chamber made of petrol pumps sealed with plasticine to generate high voltages for acceleration. This type of technology has culminated in enormous high–current Van der Graaf type generators used today for nuclear structure physics. However, very high voltages, of the order of a million or more volts, are very difficult to generate and to contain, which sets limits on the energies to which single–stage high–voltage acceleration can be pushed.

To circumvent this restriction, Lawrence and Stanley at the University of Berkeley in California conceived the idea of providing a particle with many small accelerating pulses. The first *cyclotron* was a device only a couple of inches across, with a vacuum maintained

by sealing wax. In the cyclotron, protons or deuterons move in a circular path in a large vacuum chamber which has a magnetic field normal to the plane of particle movement. The particles alternately pass through two D–shaped accelerating cavities. An alternating potential difference is applied between the cavities, in step with the orbit of the protons. The particles move in an orbit of radius:

$$R = \frac{pc}{Be} \tag{1.2.1}$$

The frequency of the applied voltage is equal to the angular frequency of the orbit which is the *cyclotron frequency*:

$$\omega = \frac{Be}{mc} \tag{1.2.2}$$

The cyclotron is no longer used in particle physics, but small cyclotrons and synchrotrons are still used as high–current sources, for example to produce medical isotopes or as synchrotron radiation sources for semiconductor manufacture.

During the Second World War, enormous cyclotrons were used for separating uranium isotopes in the Manhattan project [11]. Other early accelerators were also used at Los Alamos. Most US nuclear physicists, and some British were drafted into the Manhattan project. This not only produced the first nuclear chain reactions, but also provided the driving force for the development of the first digital computers and the first large–scale Monte Carlo calculations.

Using the high power RF devices invented for radar during the war, the development of particle accelerators proceeded rapidly following 1945. In the early 1950's experiments at the new accelerators had produced several types of unstable particles heavier than the nucleons, which are known as hyperons.

The advancement of knowledge in particle physics has depended on the achievement of higher and higher accelerator energies and on the development of the sensitive experimental techniques for studying the products of high energy events.

1.2.3 Particle Accelerators

There are two reasons for wanting the highest possible energy in the collisions which particle physicists study. Firstly, the resolution which can be achieved in a scattering experiment is of the order of the quantum wavelength of the incident particles: probing small distances requires high energy. Secondly, production of new heavy particles needs enough energy in the centre of mass frame to provide the rest mass energy of the new

particle. For instance, the Berkely Bevatron was built in the 1950's with a beam energy sufficient to create anti-protons, which were subsequently discovered there [12].

Particle accelerators provide the high-energy particles which are under study in today's particle physics experiments. Charged particles travel in a beam pipe evacuated to a very high degree and are accelerated in radio-frequency cavities. To achieve the gains in energy needed to accelerate particles to relativistic velocities the particles must pass through many cavities, as the accelerating voltage gradients available with today's technology are limited. In a *linear accelerator*, such as the two-mile long device at SLAC in California, the particles pass once along a straight vacuum chamber. The particles are accelerated using a series of accelerating regions with power supplied by a bank of klystrons. The voltages supplied to the accelerating cavities are phased in such a fashion that a travelling wave is created down the structure with velocity equal to that of the particles. Linear accelerators are also used as low-energy injectors for many circular accelerators. An ingenious scheme called the SLAC Linear Collider (SLC) has been implemented whereby beams of electrons and positrons are stored and accelerated in quick succession then brought into collision at an intersection between two arcs at the end of the accelerator. Collisions have been successfully achieved at energies of over 45 GeV per beam.

Most machines are circular *synchrotrons* where the beam passes many times through a set of accelerating cavities. In these machines, the accelerating frequency is phased in synchronism with the increasing velocity of the particles. The particles are constrained in a circular orbit by a series of dipole bending magnets. Quadrupole magnets serve to keep the beam focussed. The complex design of the particle beam optics for the stable, high—current operation of accelerators is a separate subject in its own right. Acceleration takes place in several stages, with the particles being injected at a low energy from a linac. For *fixed target* experiments where the collision is between high-energy particles and nuclei in a stationary target, often liquid hydrogen, the beam particles are extracted from the accelerator by a kicker and directed down long vacuum tunnels to the experimental areas. By suitable arrangements of targets, magnets and collimators intense beams of secondary particles may be created. Beams of neutrinos, photons, electrons, muons, pions, kaons and hyperons are available. The first accelerators were electron or proton cyclotrons where the beams were extracted and allowed to collide with a target. Perhaps the ultimate in this is the fixed-target program at the Fermilab Tevatron where proton beams are accelerated to over 1000 GeV. Once the particles in a circular accelerator have been boosted to the highest

running energy, the machine may be operated in storage ring mode where the bunches of particles are kept coasting in the machine, perhaps for many hours. In order to be used in storage rings, the particles must be stable and charged: electrons, positrons, muons, protons, anti-protons and ions ranging from helium to lead have been used.

Over the last 25 years colliding beam accelerators have become the most important machines in high energy physics. A collider consists of one or two particle storage rings in which counter-rotating beams of particles are brought together. In a conventional fixed-target experiment, when a particle of energy E_{beam} collides with a particle of the same mass at rest, only a fraction :

$$E_{cm}^2 = s = 2mc^2 E_{beam} \tag{1.2.3}$$

is available in the centre-of-mass frame of the collision. So, at high energy the energy available for the creation of new particles increases only as the square root of the beam energy. In order to make very heavy particles (such as the Z^0) the beam energy would be very great, and impractical with the technology available today. If a colliding beam configuration is considered, with two particles of equal mass and opposite momentum colliding, the full energy $2E_{beam}$ is available in the centre of mass system. There are also large cost savings per unit energy. However, one pays by having much reduced luminosity which is also a very important parameter when rare particles are under study or high statistics measurements are needed. The particles used may be two beams of identical particles, in which case two separate, interlinked storage rings are needed, or counter rotating beams of particles and anti-particles in which case only one vacuum vessel is needed. The first colliding beam machine constructed at CERN was the Intersecting Storage Rings. At the ISR two beams of protons from the CERN PS were kept in two beam pipes which intersected at four points. Another notable collider scheme is the CERN SPS, which was adapted in the early 1980's to operate in a mode which collided protons with anti-protons. This made possible the discovery of the Z^0 and $W^{\pm}$ bosons by the UA1 and UA2 experiments. The acceleration schemes used around the world to date have been electron/electron, electron/positron, proton/proton, proton/antiproton: and at the HERA machine, electron/proton.

1.2.4 History of Electron Accelerators

Electron positron collider rings were first proposed in 1957 [13]. The first colliding beam machines were electron machines as injection and stacking of stable electron beams is much easier than with protons. The first machine, ADA, was built in Frascati, Italy (which in fact

consisted of two intersecting electron storage rings)– this was on a pilot scale which proved the soundness of the concept. Over the last 35 years electron storage rings have grown from small room–sized devices to huge machines many kilometres in circumference – a summary of the electron colliders so far constructed is given in Table 1.2.1. Electron storage rings have also found application outside particle physics, for example as synchrotron radiation sources.

Name	Location	Beam Energy(GeV)
ADONE	Frascati	1.5
DCI	Orsay	1.7
BEPC	Beijing	2.8
SPEAR	Stanford	3.9
VEPP 4	Novosibirsk	5
DORIS	Hamburg	7
CESR	Cornell	8
PEP	Stanford	15
PETRA	Hamburg	23
TRISTAN	Japan	30
SLC	Stanford	50
LEP	CERN	50

Table 1.2.1: Electron Colliders

The motivation for the first electron colliders was the study of QED in an environment free of strong interactions: the first result was a measurement of the cross–section for Möller scattering ($e^-e^- \rightarrow e^-e^-$) in 1966 by a Princeton/Stanford collaboration [14]. However, hadron production via production and decay of a virtual photon soon became the object of interest. Unlike the situation in hadron–hadron collisions, when electrons and positrons annihilate to form a virtual photon the intermediate state has the well–defined quantum numbers of the photon. The e^+e^- system gives a very clean and simple final state. The reaction proceeds in what can be thought of as three steps. The electron and positron annihilate to produce a virtual photon. This intermediate state has an enormous energy density and simple quantum numbers. This 'spark' of energy then re–materializes into any collection of particles, if it is energetically possible and the spin of the entire system is one. There is very little background, and the angular distribution of products has no sharp forward and backward peaks, unlike the situation in proton collisions.

The first interesting high energy physics results came from the next two machines constructed: VEPP II at Novosibirsk and AC'O at Orsay. It was found that the cross

section up to 1GeV is dominated by production of the light vector mesons ρ, ω and ϕ. In the late 1960's, cross section measurements were extended to higher energies at the Adone facility in Frascati. It was found that, contrary to expectations, the R–ratio (the ratio of the hadronic production cross–section to the muon pair cross–section) above the ρ peak is three times greater than the naïve value expected from the Rutherford scattering formula, which is evidence for the existence of quarks with three colour charges.

In 1972 the SPEAR storage ring was constructed at SLAC. This facility had the Mark I detector, the prototypical 4π detector for e^+e^- physics: it consisted of a solenoidal magnet surrounding a spark chamber tracker, shower counters and muon identifiers. The charm quark was found simultaneously by two groups in November 1974. The Mark I group led by Richter at the SLAC e^+e^- collider SPEAR found a large, very narrow resonance in the process e^+e^- — hadrons at 3.1 GeV [15]. At the Brookhaven AGS a proton fixed target experiment led by Ting found a rise in the number of electron–positron pairs produced in proton–nucleus collisions [16]. The long lifetime of this resonance, subsequently named the J/Ψ, indicated that its decay to lighter particles via strong decay was inhibited. This was explained by the J/Ψ being a bound pair of quarks of a new flavour: charm.

The first member of the third family of leptons, the tau lepton, was discovered in 1975 at the SPEAR storage ring by a team led by Perl [17]. A new doublet of quarks was therefore needed to restore lepton–quark symmetry. The fifth quark, known as bottom or beauty, was discovered in 1977 by a group led by Lederman at Fermilab [18]. The group studied muon–antimuon pairs produced in proton–beryllium interactions. The Υ resonances show up as a peak in the mass distribution of the parent particles of the muon pairs. After this discovery, searches for the fifth quark were begun at e^+e^- machines. In 1978 the storage ring DORIS at DESY reached the energy threshold for producing the lowest lying Υ^{1s} and Υ^{2s} states. It could be said that the discovery of the J/Ψ followed by the discovery of τ lepton and the Υ marked the transition of high energy physics from a concern with the study and cataloguing of hadronic states to the study of quarks and leptons.

QCD predicts that isolated quarks are not seen, and that the initial quarks from an e^+e^- interaction 'fragment' into a collection of lower energy hadrons which are seen in the detector. These final state particles are produced at limited transverse momentum with respect to the parent quarks, so there should be observed collimated 'jets' of particles. The jet behaviour of fragmenting partons was first observed at SPEAR [19]. Jets are directly visible in interactions at the higher PETRA energies. The PETRA e^+e^- storage ring at

DESY operated from 1978 to 1986, mainly at energies of around 35 GeV, with a maximum at 46.8GeV. The PEP machine at Stanford started in 1980, and has run mostly at an energy of 29 GeV. The many experiments which have run at PEP and PETRA have accumulated a very large amount of data on e^+e^- interactions between 14 and 46.8 GeV. Some of the first results from these machines confirmed the existence of the gluon, in observations of three–jet events by TASSO and Mark J at DESY [20–21].

In Japan, the TRISTAN accelerator started operation at the KEK laboratory in 1986. The TRISTAN experiments have taken data in the energy range 50 to 64 GeV. As already mentioned, the Stanford Linear Collider (SLC) started operation at the Z^0 energy in 1989. This has been a very important and interesting project from a technical point of view, and was the first place where Z^0 bosons were produced in e^+e^- collisions. The LEP accelerator at CERN, see section 3.1, has been in operation since 1989 at energies around the Z^0 peak. As discussed in the next section, and in Chapter 3, four experiments have collected a large sample of events, and have made many precise measurements of Z^0 physics there.

In the future, as discussed in section 1.7, high–luminosity electron–positron colliders are proposed as 'factories' for producing bottom quark events at the Υ^{4s} resonance, or as 'tau/charm' factories. Proposals have also been made for building a large linear e^+e^- collider in the TeV energy range.

1.3. LEP Physics

1.3.1 Motivation for building LEP

The LEP accelerator (see section 3.1) was designed to run initially at the Z^0 peak, in effect being a Z^0 'factory' producing thousands of events per day. At electron–positron colliders, the cross–section for reactions proceeding via photon exchange is small, and falls as $1/s$. Specifically, the cross section for $e^+ + e^- \rightarrow \mu^+\mu^-$ is:

$$\sigma = \frac{4\pi\alpha^2}{3s} = \frac{21.7\,nb}{[E_{beam}\,(\mathrm{GeV})]^2} \qquad (1.3.1)$$

The cross–section for $q\bar{q}$ pair production is related to this by the R–ratio. However, near the Z^0 mass there is a resonance, where Z^0 exchange is also possible. This gives an increase in cross–section by a factor of 1000, and an expected reaction rate of around 2000 hadronic events per hour at the design luminosity of $1.7 \times 10^{31} cm^{-2}/sec$.

At the Z^0 much interesting physics was foreseen :

- measurement of the mass and width of the Z^0
- widths for Z^0 decay into different species
- measurement of the number of neutrino species
- the neutral current couplings of the different quarks and leptons
- measurement of the forward–backward asymmetry in $e^+e^- \rightarrow$ *leptons* events
- charge asymmetry measurements in $q\bar{q}$ events
- QCD physics with hadronic events, e.g. measurement of α_s, jet ratios, fragmentation functions etc.
- two–photon physics
- heavy flavour physics (i.e. properties of charm and bottom quarks, and the τ) The Standard Model can be tested by measuring heavy flavour cross–sections, asymmetries, branching ratios, lifetimes and mixing. QCD fragmentation models can also be compared with experiment, if it is possible to tag a particular jet as being from a heavy quark.
- measurements of the Kobayashi-Maskawa matrix parameters
- search for the top quark, which if it is in the energy range of LEP should give a very clear signal
- search for the Higgs particle. The mass of the neutral Higgs is not known, and each time a new energy range is opened a Higgs search is made. The detectors at LEP 1 should be able to discover the Higgs if its mass is $\leq$ 50GeV.
- search for exotica like magnetic monopoles and free quarks.
- search for other new particles. Theories which go beyond the Standard Model all predict new particles : e.g. supersymmetric counterparts of the known ones; new heavy vector bosons; heavy leptons, further generations of quarks etc.

Precise measurements at LEP of the quantities of the electroweak model, such as $sin^2\theta_W$ and the Z^0 mass are important as they then enable predictions of other parameters. For example measurements which are sensitive to higher order radiative terms give information about the masses of particles which are too massive to be produced directly at LEP, including possible particles outside the Standard Model. A review of the early physics results from LEP may be found in [22].

The next stage foreseen for LEP is an energy upgrade to around 200 GeV, where pair production of W^+W^- particles occurs. This again should provide rich physics with the study of the couplings and decay modes of the W.

1.3.2 e^+e^- cross–sections

Below the Z^0 resonance the production of hadrons from e^+e^- annihilation is given in lowest order by the quark–parton model in which the process is the formation of a virtual photon which decays into a $q\bar{q}$ pair. From QED the total hadronic cross–section in this model is

$$\sigma_{tot}^{hadronic} = \left[\sum_{colours}\sum_{flavours} Q_f^2\right]\sigma_{pt} \tag{1.3.2}$$

where Q_f is the charge of the fermion produced. and σ_{pt} is the point cross section already mentioned for $e^+e^- \rightarrow \mu\bar{\mu}$ in the Born approximation:

$$\sigma_{pt} = \frac{4\pi\alpha^2}{3s} = \frac{87\ nb}{s} \qquad \left(s \gg m_\mu^2\right) \tag{1.3.3}$$

where $s = E^2 = (2E_{beam})^2$. At energies below the Z^0 it is normal to measure the R–ratio which is defined as :

$$R \equiv \sigma_{tot}^{hadronic}/\sigma_{pt} = 3\left[(1/3)^2 + (2/3)^2 + (1/3)^2 + (2/3)^2 + (1/3)^2\right] = \frac{11}{3} \tag{1.3.4}$$

The terms are the contributions from the five quark flavours u,d,s,c,b. When real measurements are made. corrections for radiative and higher order terms must be taken into account. Applied to the R–ratio these give

$$R = \left[3\sum_f Q_f^2\right]\left[1 + \frac{\alpha_s}{\pi} + c_2\left(\frac{\alpha_s}{\pi}\right)^2 + \ldots\right] \tag{1.3.5}$$

where α_s is the strong coupling constant:

$$\alpha_s(s) = \frac{12\pi}{(33 - 2n_f)\ln(s/\Lambda^2)} \tag{1.3.6}$$

The process of Z^0 exchange is calculated in a similar way to photon exchange, replacing the QED vertex factor by:

$$\frac{-ie}{\sin\theta_W\cos\theta_W}\gamma^\mu\left[\frac{1}{2}(1-\gamma^5)\,T_3^f - \sin^2\theta_W Q_f\right] \tag{1.3.7}$$

and the photon propagator $1/s$ by:

$$\frac{1}{s - M_Z^2 + is\Gamma/M_Z} \tag{1.3.8}$$

where Γ is the width of the Z^0 resonance and θ_W is the weak mixing angle.

Near the Z^0 the cross section for production of a given fermion is given by a relativistic Breit–Wigner form:

$$\sigma_f(E) = \frac{12\pi}{M_Z^2}\frac{s\Gamma_e\Gamma_f}{(s-M_Z^2)^2+s^2\Gamma^2/M_Z^2}(1+\delta(E)) \tag{1.3.9}$$

where Γ_f is the partial width for flavour f, and $\delta(E)$ contains the radiative corrections. At the tree level in the Standard Model the partial widths are given by:

$$\Gamma_f = \frac{M_Z^3}{6\pi}\frac{G}{\sqrt{2}}\left[\left(g_V^f\right)^2+\left(g_A^f\right)^2\right] \tag{1.3.10}$$

with the vector and axial–vector couplings:

$$\begin{aligned} g_V^f &= T_3^f - 2\sin^2\theta_W Q_f \\ g_A^f &= T_3^f \end{aligned} \tag{1.3.11}$$

For the charged leptons, $g_V = -\frac{1}{2} + 2\sin^2\theta_W$ and $g_A = -\frac{1}{2}$. The neutrino couplings are solely V–A. Each quark or lepton makes a contribution to the overall width of the Z^0 peak, including the otherwise undetectable neutrinos. As the contribution from all charged species can be well measured by the LEP experiments, and no new charged particle types have been produced then a measurement of the total Z^0 width can be used to measure the number of light neutrinos, see section 1.4.4. Of course the radiative corrections, which are substantial at the Z^0 peak, must be taken into account. Careful corrections must be made for these effects when analysing the data. Radiative corrections can be divided into two categories:

- Photon corrections: higher order QED diagrams, including initial and final state radiation, photon loops and vertex terms. These corrections are of the order of 100%.
- QCD processes : gluon radiation, with gluon brehmsstrahlung and loops similar to the photon corrections.

Experimentally the cross–section is given by a sum of terms of flavours f given by:

$$\sigma_f(E) = \frac{N_f/\epsilon_f}{\int \mathcal{L}dt} \tag{1.3.12}$$

where N is the number of events; ϵ is the efficiency for detection and $\int \mathcal{L}dt$ is the integrated luminosity. The events used for measuring the Z^0 production and decay are hadronic events, muon pair events and tau pairs. Electron pairs require different treatment because there is also a contribution to their production from t–channel photon exchange. Background events in Z^0 physics include beam–gas interactions, cosmic rays and two photon events. In

two photon events much of the energy is lost down the beam pipe and these can be rejected on the basis of deficiencies in the visible energy and the energy balance along the beam pipe. Other background events are cleanly rejected by cuts on visible energy, multiplicity, event timing relative to the bunch crossing and position of the event vertex. The high multiplicity of hadronic events makes it easy to trigger on and select these events at LEP. There is also the possibility of contamination of the hadronic sample with misidentified τs. In general the systematic errors on N/ϵ are small. The value for ϵ is determined by using Monte Carlo simulation. The dependence of ϵ on the model used in the Monte Carlo is checked by comparison of event distributions (multiplicity, thrust, sphericity etc.) with the data. The measurement of integrated luminosity requires more care, as discussed in the next section.

1.3.3 Luminosity Measurement and Energy Calibration

At an accelerator it is very difficult to measure accurately all the beam properties which enter into a calculation of the luminosity, so this is usually obtained from measurements of a process with a well known cross-section. The integrated luminosity is then:

$$\int \mathcal{L} = \frac{N_n}{\epsilon_n} \frac{1}{\sigma_n} \tag{1.3.13}$$

The SLC and LEP experiments monitor the rate of small angle Bhabha scattering, where the cross-section is dominated by the QED t-channel process. This rate is then compared with the QED prediction. Dedicated low-angle calorimeters and tracking chambers are used for this task. However, as the Bhabha cross-section changes strongly with angle the systematic errors are dependent on the alignment and edge inefficiency of these devices. The devices used by ALEPH to measure luminosity are described in section 3.12. With the high statistics available at LEP the systematic error in the luminosity, currently of the order of 0.6% at ALEPH [116] is the dominant error in Z^0 lineshape measurements.

For a measurement of the lineshape a precise measurement of the beam energy is also needed. At the SLC this is done using spectrometers downstream of the interaction point. For the 1989 and 1990 running at LEP, the absolute calibration was performed by measuring the velocities of protons and positrons circulating with a momentum of 20 GeV. This gives a calibration of the magnetic field at 20 GeV, which is scaled up to 45 GeV using flux-loop measurements. The uncertainty in the energy scale was of the order of 20 MeV at the Z^0 peak. The dominant contribution to the error was the uncertainty in the thickness of the nickel layer which was deposited on the beam pipe, discussed in 3.1. In 1991, the absolute

energy was measured by using a resonant depolarization technique. The absolute energy has an error of ±8 MeV, and the reproducibility of the energy setting is 6 MeV. The relative energy setting error is 10 MeV.

1.4. Electroweak Physics at ALEPH

During the 1989, 1990 and 1991 running periods at LEP, energy scans across the Z peak were performed at energy intervals of 1 GeV. The cross sections for $Z^0 \rightarrow$ hadrons, $Z^0 \rightarrow e^+e^-$, $Z^0 \rightarrow \mu^+\mu^-$ and $Z^0 \rightarrow \tau^+\tau^-$ were measured as a function of the centre-of-mass energy. The large increase in statistics of the 1991 data sample allowed a more precise determination of the parameters of the Z^0. Fig. 1.4.1 shows the hadronic cross-section as measured by ALEPH.

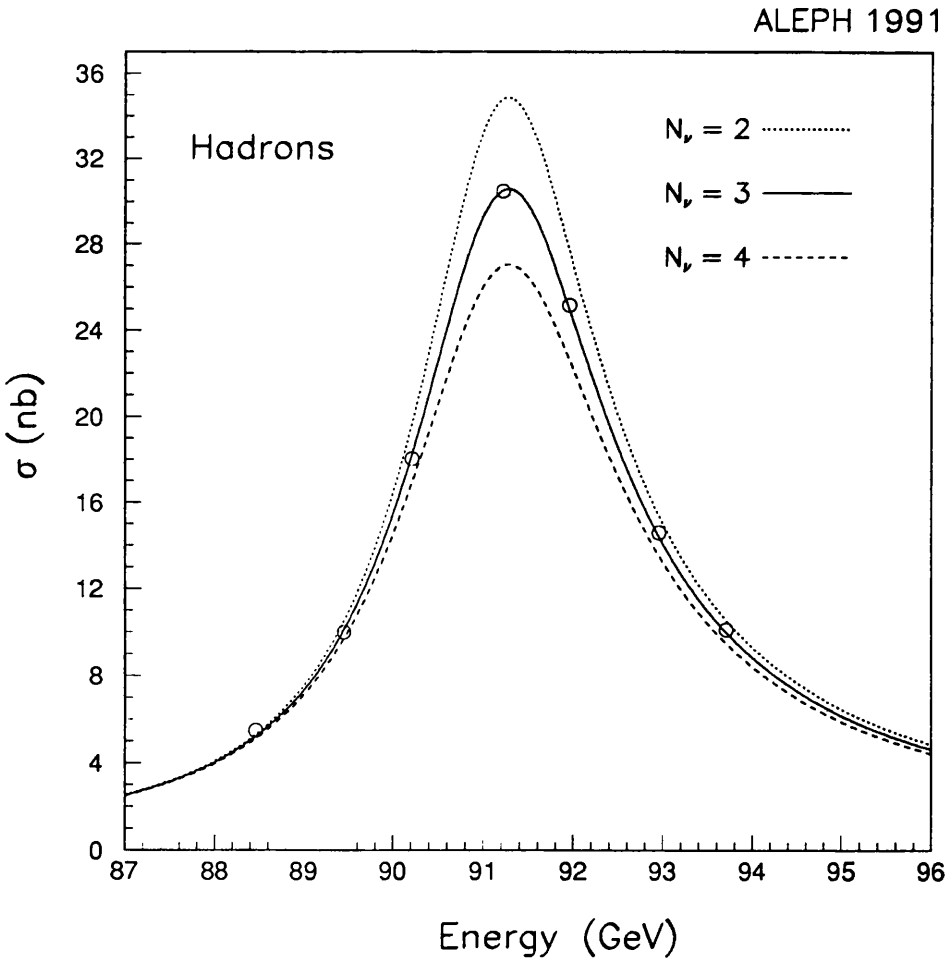

Fig. 1.4.1: Hadronic cross-section at the Z^0. ALEPH data.

The raw experimental data are corrected for the apparatus acceptance and resolution, using comparison with Monte Carlo. The theoretical Born level cross–sections have radiative corrections applied to them, which lead to the physical cross–sections which the experiment measures. Assuming a Breit–Wigner form for the line shape, plus the validity of the QED corrections, by fitting the hadronic and three leptonic cross–sections six parameters may be determined: the Z mass, the total Z width, the peak hadronic cross–section σ^0_{had} and the three lepton partial widths (in units of the hadronic width).

1.4.1 Z–Mass

In the fit to the line shape, the Z mass is not dependent on the other parameters. The latest value of the Z^0 mass, from a fit to the whole ALEPH data sample, is 91.187 ± 0.009 GeV [23]. The error is dominated by the uncertainty of the absolute energy calibration of LEP, discussed above, which gives a systematic uncertainty of 6.3 MeV in the Z^0 mass [24].

1.4.2 Total Z^0 Width and Hadronic Cross–section

A fit to the line shape as measured with all Z — hadrons and $Z \rightarrow$ leptons events gives the total width of the Z^0. The current ALEPH value for the total width is $\Gamma_Z = 2501 \pm 12$ MeV. This is in agreement with the minimal Standard Model prediction of $2488 \pm 2 \pm 6$ MeV, where the first uncertainty arises from M_Z and Δr and the second from m_t and m_H [25]. The hadronic peak cross–section (in the Born approximation, before radiative corrections) is found to be $\sigma^0_{had} = 41.60 \pm 0.27 nb$.

1.4.3 Partial Widths of the Z^0

The current values for the leptonic widths of the Z^0 are:

$\Gamma_e = 84.43 \pm 0.60$ MeV

$\Gamma_\mu = 83.66 \pm 0.95$ MeV

$\Gamma_\tau = 84.09 \pm 1.10$ MeV

These are in agreement with the Standard Model prediction of $\Gamma_{ll} = 83.7 \pm 0.1 \pm 0.2$ MeV [25]. As the branching ratios for the Z^0 decays to the three lepton generations agree within experimental errors, this confirms the concept of lepton universality.

1.4.4 Number of Neutrino Families

By measuring the 'invisible' width of the Z^0, i.e. $\Gamma_{inv} = \Gamma_Z - \Gamma_{had} - 3\Gamma_{ll}$, the number of neutrinos with $m_\nu < m_Z/2$ can be counted, and hence the number of particle generations.

To first order, each neutrino species contributes a partial width of 167 MeV. From the measured value of $\Gamma_{inv}/\Gamma_{ll} = 5.91 \pm 0.11$, and assuming $\Gamma_{inv} = N_\nu \Gamma_\nu$, the current fit to the ALEPH data gives $N_\nu = 2.97 \pm 0.05$. Referring again to Fig. 1.4.1, it may be seen that the possibility of four generations is clearly ruled out. Each of the four LEP experiments has found that the number of generations with light neutrinos $N_\nu = 3$.

1.4.5 Forward–backward asymmetry in $e^+e^- \rightarrow$ leptons

The leptonic vector and axial vector coupling constants may be determined from the Z leptonic widths and the leptonic forward–backward asymmetries. At the Z^0 peak, the lepton forward–backward asymmetry is given by:

$$A_l^{FB} = \frac{3}{4} A_e A_l \tag{1.4.1}$$

where:

$$A_l = 2\frac{g_{Vl} g_{Al}}{g_{Vl}^2 + g_{Al}^2}$$

By measuring the forward–backward asymmetry in $e^+e^- \rightarrow$ leptons events as a function of $\sqrt{s}$ and using the leptonic widths, the lepton coupling constants g_{Vl} and g_{Al} can be determined. The forward–backward asymmetry at the peak is $A_{FB} = 0.0164 \pm 0.0047$ [23]. The ratio of the effective coupling constants is

$$\frac{g_{Vl}^2(M_Z^2)}{g_{Al}^2(M_Z^2)} = 0.0052 \pm 0.0016 \tag{1.4.2}$$

and the effective coupling constants are $g_{Vl}^2(M_Z^2) = 0.0013 \pm 0.0002$ and $g_{Al}^2(M_Z^2) = 0.2521 \pm 0.0008$. The measurements for each species are in agreement with each other, and agree with the Standard Model predictions of $g_V^2(M_Z^2) = 0.0011 \pm 0 \pm 0.0001$ and $g_A^2(M_Z^2) = 0.2513 \pm 0.0002 \pm 0.0004$ [25].

1.4.6 Charge Asymmetry Measurement

A forward–backward asymmetry near the Z^0 arises from the difference in the right handed and left handed couplings to the Z^0, both for the initial state e^+e^- and the final state quarks. The ALEPH collaboration has studied the forward–backward asymmetry in hadronic events [26]. The quark direction is given by the thrust axis, and a momentum weighting procedure is used which gives the jet (and hence original quark) charge on a statistical basis. The forward–backward asymmetry found in hadronic events is $A_{FB} = -0.0084 \pm 0.0015 \pm 0.0004$.

If the quark coupling constants measured by neutrino–nucleon scattering are used, the charge asymmetry may be used to determine the ratio of the vector and axial vector coupling constants of the electron.

$$\frac{g_{Ve}}{g_{Ae}} = +0.073 \pm 0.024 \qquad (1.4.3)$$

The asymmetry in heavy flavour events has also been studied by ALEPH and the jet charge method has also been applied by ALEPH to the measurement of $b\bar{b}$ mixing.

1.4.7 $\sin^2\theta_W$

The Standard Model formulae for the Z lineshape and asymmetries can be written in terms of the electroweak mixing angle $\sin^2\theta_W$. Defined in this way, fits to the values of the couplings obtained from lepton asymmetry give $\sin^2\theta_W\,(M_Z^2) = 0.2320 \pm 0.0028$. The charge asymmetry measurement above can also be used to give a value for $\sin^2\theta_W\,(M_Z^2)$, as can the forward–backward asymmetry in $b\bar{b}$ and $c\bar{c}$ events. A value has also been obtained from studies of the τ polarization. Combining all of these measurements results in a value of $\sin^2\theta_W\,(M_Z^2) = 0.2328 \pm 0.0016$.

1.4.8 Hadronic Z Decay Widths

The identification of jets as originating from a particular quark type is know as *flavour tagging*. There has been success with identifying charm and bottom events. There are four main methods of improving the purity of charm and bottom samples:

- selecting on high–p_T leptons
- using event shape parameters (boosted sphericity)
- separated vertices or large impact parameter tracks
- reconstruction of exclusive final states, such as D^* or Ψ

The features of bottom hadron events which have been used to tag them are all consequences of the large b–quark mass : the presence of prompt leptons, hard fragmentation and high p_T particles. ALEPH uses a lepton cut of $p_T = 2$GeV to get an enriched sample of b–meson events. From these data ALEPH finds $\Gamma_b/\Gamma_{had} = 0.220 \pm 0.01 \pm 0.024$ [27] compared to the standard model value of 0.217. Samples of $b\bar{b}$ enriched events tagged with leptons have also been used to measure the fragmentation function, charge asymmetry, B^0 mixing and the b lifetime.

Parameter	
M_Z (GeV)	91.187 ± 0.009
Γ_Z (GeV)	2.501 ± 0.012
σ^0_{had} (nb)	41.60 ± 0.27
R_e	20.69 ± 0.21
R_μ	20.88 ± 0.20
R_τ	20.77 ± 0.23
Γ_e (MeV)	84.43 ± 0.60
Γ_μ (MeV)	83.66 ± 0.95
Γ_τ (MeV)	84.09 ± 1.10
$Br(Z \to e^+e^-)\%$	3.375 ± 0.019
$Br(Z \to \mu^+\mu^-)\%$	3.345 ± 0.036
$Br(Z \to \tau^+\tau^-)\%$	3.362 ± 0.041
σ^0_e (nb)	2.011 ± 0.023
σ^0_μ(nb)	1.993 ± 0.021
σ^0_τ (nb)	2.003 ± 0.025

Table 1.4.1: Results of the fits to the cross-section for the whole ALEPH data sample

1.4.9 Electroweak Summary

Table 1.4.1 is a summary of the cross-sections and branching ratios at the Z^0 peak, taken from fits to the combined ALEPH 1989–1991 data sample.

Reference [28] contains a compilation of the results on the Z^0 parameters from the four LEP experiments from the 1989/1990 data sample. This paper also presents a combination of the results. All of the results so far found by the ALEPH collaboration, and all the other LEP experiments, are in agreement with the predictions of the Standard Model.

1.5. QCD at ALEPH

Quantum chromodynamics is the theory currently used to describe the interactions between quarks and gluons (collectively known as partons). As has already been discussed, the colour force confines the quarks, i.e. they are only seen as members of colour neutral

mesons ($q\bar{q}$) or baryons(qqq). To describe hadronic events as they appear in a real detector, the model used to generate the initial partons must have in addition a description of the process of conversion of partons into hadrons, i.e. the *fragmentation.* A quark or hard gluon is seen in a high–energy experiment as a 'jet' of particles, roughly following the original parton direction. With respect to the jet axis, the scale of transverse momentum is 150–200 MeV. The scale of the longitudinal momentum is the parton momentum, around $\sqrt{s}/2$. With increasing energy narrowing jet structures are seen, with a fixed transverse, but growing longitudinal extent in momentum space.

1.5.1 Fragmentation

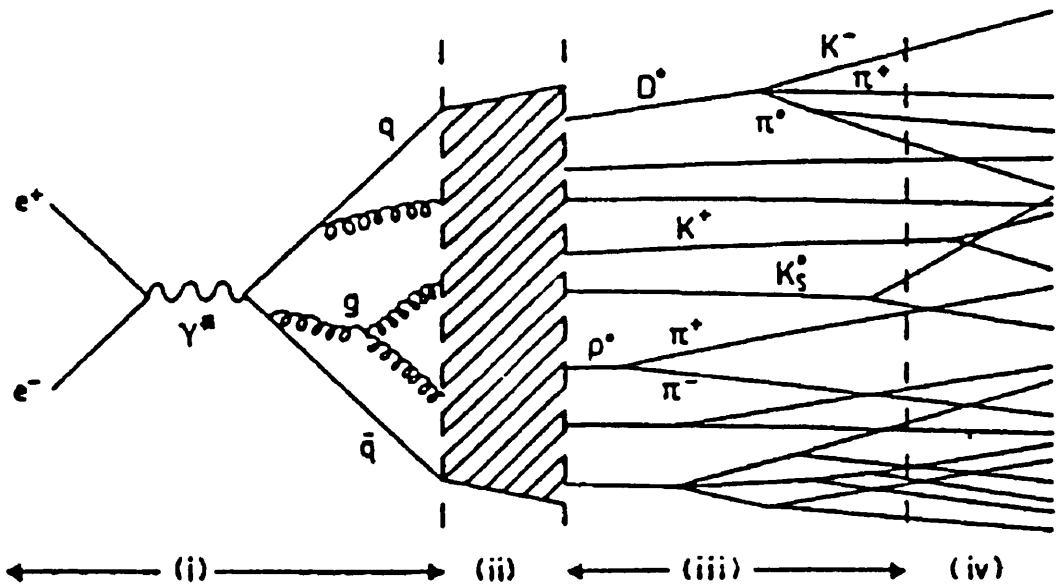

Fig. 1.5.1: The Fragmentation Process

The process of $Z^0 \rightarrow q\bar{q}$ and the subsequent hadronisation of the quarks into the particles seen in the detector is illustrated in Fig. 1.5.1. The first stage, the creation of a $q\bar{q}$ pair, is well described by the electroweak theory discussed above. The second stage of gluon radiation and gluon splitting is considered to be well modelled by perturbative QCD theory. Two approaches are taken in practical Monte Carlo codes for this stage:

- the Matrix Element (ME) approach – this uses exact second order calculations to give the relative proportions of two, three and four parton states. The

momentum distributions of the partons are tuned to fit the data. As this is an order (α^2) calculation, it is limited to four partons in the final state.

- the leading logarithm approach (LLA) or Parton Shower. In this method the primary cross section is calculated to lowest order. The quarks then lose energy by gluon bremsstrahlung. The quarks and gluons undergo splittings: $q \rightarrow qg$, $g \rightarrow gg$ and $g \rightarrow \bar{q}q$. The probabilities for these splittings are given by an approximation to each higher order term of the QCD perturbation series, which is based on the leading logarithm of this term. The process proceeds until some cut–off scale is reached.

The early LEP data were used to see which of the ME or LLA approaches is the best description of the data. In the ALEPH study [29], the event shape parameters such as sphericity, aplanarity and thrust were examined, as were the inclusive variables x_p, $p_\perp^{in}$, $p_\perp^{out}$ and y for the charged particles. The data were seen to agree better with models based on LLA, and are less well described by an ME model. The ME approach is seen to underestimate the amount of gluon radiation required to agree at high energy. Higher order processes become more important at higher energy, and as has been said the ME approach is to order (α^2).

At the third stage the *hadronisation* of the partons takes place on a momentum scale of the order of 1GeV. Hadronisation is due to soft non–perturbative processes which cannot be calculated from first principles. There are several semi–empirical approaches to modelling this process:

- independent hadronisation
- string hadronisation
- string hadronisation with colour coherence
- cluster hadronisation

These will be described in the following sections. The very last stage in the process is the decay of unstable particles into 'stable' (detectable) mesons/baryons.

1.5.2 Independent Hadronisation Model

This model was originally due to Field and Feynman [30]. Extensions to the model to account for gluon production, baryon production and the harder fragmentation of heavy quarks have been made. The model takes into account the experimental observations that the hadrons have a limited transverse momentum w.r.t. the jet axis and that 'scaling' is seen

by plotting the distribution of hadrons with the Feynman variable $x = 2p/\sqrt{s}$. The primary partons and their development into jets are assumed to have negligible effects on each other. The hadrons in the jet are formed by the repetition of a single basic process: alongside the initial quark a new $q\bar{q}$ pair is materialized in the colour field; the antiquark is paired with the original quark to form a meson; this leaves a new unpaired quark which goes on to form the next step in the chain. The process is repeated until the momentum of the remaining quark falls below a cut–off value. The momentum distribution of the mesons at each stage is chosen according to a 'fragmentation function'. Independent hadronisation models are known not to describe the data adequately unless some *ad hoc* fixes are made for such things as Lorentz invariance, energy/momentum conservation and baryon production. These models require arbitrary parameters which need to be tuned to the data. Independent fragmentation models have become less popular in e^+e^- physics, due to the lack of a theoretical basis for the mechanism.

1.5.3 String Models

As the net colour of hadrons is neutral, the colour of a scattered quark is balanced by the recoiling system. They can be considered to be joined by colour flux lines. The colour flux lines gather into a tube or string since the gluons which transmit the force have a self–attraction. If the string has a constant energy density per unit length then the potential energy in the string rises linearly as the charges separate. Once the potential energy is sufficient to create a quark–antiquark pair the string breaks, leaving two quark–antiquark pairs. If the invariant mass of these new strings is large enough, they may in turn break, a process which continues until ordinary hadrons remain. Gluons are seen as 'kinks' in the string. Therefore, the gluon fragmentation is included naturally as the string splits into two pieces, stretched from quark to gluon and gluon to antiquark. String fragmentation is implemented in the commonly used JETSET Monte Carlo [127], which has become the standard code used in e^+e^- physics.

1.5.4 Cluster Models

These models use LLA calculations to generate the initial quarks and gluons. At the cut–off point the final partons are mostly gluons. The gluons in the final state are split into $q\bar{q}$ pairs on the mass shell. Adjacent quarks and anti–quarks are combined to form clusters. The clusters form hadrons which are then allowed to decay with their known branching ratios and lifetimes. This mechanism is attractive from a theoretical view point as it follows

naturally from QCD theory and has few free parameters. The most popular cluster model is incorporated in the HERWIG Monte Carlo code [31].

1.5.5 Fragmentation Functions

The description of fragmentation of quarks far above threshold is given by the *fragmentation function* $D_q^h(z)$ which is a parameterization of the fraction z of the original quark momentum which is carried by a hadron type h. For light particles, $D_q^h(z)$ is peaked at low x–values, since many light particles equally share the quark's momentum.

The fragmentation function for heavy quarks has a different form than that for u, d and s. Conservation of flavour means that the original quark will survive the fragmentation process bound in one of the hadrons, called the leading hadron. A c or b quark (Q) is most likely to combine with one u, d or perhaps s quark to form a D or B meson. In the fragmentation a light meson $q\bar{q}$ is created from the vacuum. The heavy meson $Q\bar{q}$ is connected by colour force lines to the other quark q. Through this interaction the unpaired quark drags the heavy meson and reduces its momentum. This will be a small effect if q is much lighter than Q. Thus the heavy hadrons are expected to have more momentum on average than the light ones – i.e. there is a harder distribution. This is the rationale for the parameterization of Peterson [32]:

$$D_Q^H(z) = \frac{N}{z(1 - 1/z - \epsilon_Q/(1-z))^2} \tag{1.5.1}$$

where ϵ_Q is a factor which is fitted to the data.

1.5.6 ALEPH results

Most of the information on the fragmentation process has come from studies of the overall properties of events, such as multiplicity and event shape parameters, which do not depend on identifying individual particle species. In [33] ALEPH presents a study of the event shapes, jet production rates and inclusive charged particle momentum distributions from 53000 hadronic events taken in 1989 and 1990 near the Z^0 peak. These are compared with various Monte Carlo models: JETSET, Ariadne [34] and HERWIG. The JETSET and Ariadne parton shower models with string fragmentation are in good agreement with the data. The HERWIG model with cluster fragmentation fits the data less well. The JETSET parton shower model is found to be in better agreement than the JETSET model with matrix element calculations. This study is an extension of the work in [29] mentioned above.

1.5.7 Inclusive Particle Production

Inclusive particle production means measurement of the process $e^+e^- \rightarrow hX$, where h is the particle of interest and X is all other types. The measurement of the production rates of individual particle species enables more detailed examination of the fragmentation process. For example, the ratio of the production rates of kaons to pions measures the rate of strange quark production during fragmentation. Measurements of baryon production rates enable the different baryon production mechanisms in the Monte Carlo models to be evaluated.

Many different particle species have been measured in e^+e^- interactions, both at the Z^0 and at lower energies. The Lund and Herwig models both reproduce well the majority of particle multiplicities and distributions. The inclusive particle x distribution is of particular relevance to the work presented later in this thesis. The scaled particle momentum $x_p = 2p/E_{cm}$ is closely related to the fragmentation variable $z = (E + p_\parallel) / (E + p_\parallel)_{quark}$. In the absence of other complicating effects, such as hard gluon radiation and particle decays, measurement of $d\sigma/dx_p$ would allow the quark fragmentation function to be unfolded.

Typical x distributions show the same general features: the multiplicity is dominated by soft particles with $x < 0.1$, and there is a steep fall from $x = 0$ to $x \sim 0.7$, above which there are fewer measurements. As the inclusive distributions contain particles coming from decays, as well as those from the primary fragmentation (in the case of pions, these are mostly from decays), it is not possible to unfold directly the fragmentation function. The approach taken is to compare the distribution with a Monte Carlo prediction which uses a particular fragmentation function which is then varied until it agrees with the data.

Chapter 6 of this thesis deals with the neutral particle content of the shower, specifically the π^0 content. The x_p distribution of π^0s is compared with the Lund parton shower model.

1.6. Searches for New Particles

The LEP collaborations have devoted a great deal of effort to studies which search for particles predicted to exist by the Standard Model and which have not yet been observed, and to searches for new exotic types beyond the Standard Model. A comprehensive discussion of the new particle searches made by ALEPH with the 1989/1990 data sample may be found in [35].

1.6.1 Top Quark

The decay $Z^0 \rightarrow t\bar{t}$ should lead to an easily recognizable spherical event shape. From the early LEP data, ALEPH was able to rule out the existence of the top quark up to the kinematical limit, i.e. $m_t > 45.8\text{GeV}/c^2$ [36]. The CDF collaboration at the Fermilab Tevatron $p\bar{p}$ collider have since set a limit of $m_t > 89\text{GeV}/c^2$ [37]. An upper limit of around 200 GeV/c^2 on the top mass may be obtained from the ratio of neutral current to charged current interaction in ν– nucleon scattering.

The top quark mass may be indirectly measured, by using the constraints the already known parameters place on the Standard Model. A high top–quark mass is predicted from the large size of the observed $B\bar{B}$ mixing, as the top quark enters into the box diagram for the mixing process. The top quark mass is one of the parameters input to the Standard Model. If all the other parameters were precisely known, then a fit to these parameters would give the top mass. Using the electroweak parameters of the Z^0 found by ALEPH in a fit with α, G_F and the value for M_W from $p\bar{p}$ experiments sets limits of $m_t = 162^{+25+16}_{-29-19}$ GeV where the central value assumes a Higgs mass of 300 GeV. The second set of limits results from varying the Higgs mass from 50 to 1000 GeV. The current limits on the top mass, obtained from several different measurements including the electroweak results at LEP, $B\bar{B}$ mixing and $p\bar{p}$, are $m_t = 144^{+23+19}_{-26-21}$ GeV [38]. The upper and lower bounds given depend on the Higgs mass used in the calculation. The top quark has not been found at LEP I, and very probably LEP II will not have enough energy for top pair production. Perhaps the most likely place to find top will be in proton collisions at the Tevatron, where searches are under way.

1.6.2 Higgs Boson Searches

In the Standard Model the Higgs mechanism of spontaneous symmetry breaking gives masses to the bosons and fermions. In the 'minimal standard model' a doublet of Higgs fields is introduced, which requires there to be a single, neutral, spin–0 Higgs boson H^0. The mass of this boson is not given by the theory. A Higgs boson will preferentially decay to the highest mass state available. The most direct way to find a Higgs boson is through the decay $Z \rightarrow H^0 Z^*$, searching for the decay products of the Higgs and the decay of the virtual Z to lepton pairs. (The much more numerous $Z^* \rightarrow$ *hadrons* mode will suffer from the large backgrounds from conventional events). Searches for several different final state configurations from this decay have been conducted by ALEPH [35], and by the other LEP experiments. The methods for Higgs searches have been chosen with two main aims:

reaching the highest efficiency for large Higgs masses and pushing the lower mass limits for light Higgs to zero.

For a very low Higgs mass, $m_{H^0} < 2m_\mu$, the only decay channels open to the Higgs are to electron or gamma pairs. The coupling of Higgs to *ee* pairs is very weak, and therefore such a Higgs will have a long lifetime, and can have the possibility of leaving the detector before decaying. The signal for such an 'invisible' light Higgs is the lepton pair (e^+e^- or $\mu^+\mu^-$) from the Z^* with a missing energy–momentum signal.

For a Higgs in the intermediate mass range $2m_\mu < m_{H^0} < 15$GeV the main decay mode is into two charged particles. If the Z^* decays into a neutrino pair, then searches may be made for acoplanar charged particle pairs with missing energy. At lower energies, the H^0 decay will be to $\tau\bar{\tau}$ pairs, but at higher energies the decay to hadrons will give a 'monojet' event. For a large Higgs mass, above the $b\bar{b}$ threshold, the dominant decay mode of the Higgs will be to hadrons. In the case of $Z^* \rightarrow \nu\bar{\nu}$, searches in this mass range are made for pairs of acoplanar, acollinear jets with missing energy. In the case of $Z^* \rightarrow e^+e^-$ or $\mu^+\mu^-$, a search is made for a pair of energetic, isolated leptons in hadronic events.

A neutral Higgs in the mass range from 0 to 48 GeV/c^2 has been ruled out at the 95% confidence limit.

1.6.3 Supersymmetric Particles

Supersymmetric extensions to the Standard Model have many attractions from a theoretical point of view. In these models, a supersymmetric partner differing in spin by a unit of 1/2 is required for each of the particles in the theory, e.g. the Z boson will have a fermion partner, the 'zino' etc. Searches for many types of supersymmetric and other exotic particles have been made by the ALEPH collaboration [35], including : scalar leptons; neutralinos; charginos; squarks.

In the minimal supersymmetric extension to the Standard Model additional doublets of Higgs fields are introduced which lead to further Higgs particles. The theory predicts two neutral Higgs particles, h and A, plus charged Higgs bosons. ALEPH has ruled out the existence of the charged Higgs below 41.7 GeV/c^2. Lower mass limits of 41 GeV/c^2 and 20 GeV/c^2 have been obtained for the h and A neutral Higgs bosons. Searches for non–minimal Higgs are again described in [35].

ALEPH has also made searches for forbidden decays of the Z^0, e.g. $Z^0 \rightarrow$ a pseudoscalar plus a vector boson or $Z^0 \rightarrow e\mu$, $e\tau$, $\mu\tau$ which are forbidden in the Standard Model. No such decay has been found.

1.7. Heavy Flavour Physics

Heavy flavour physics is the physics of partons whose mass cannot be neglected when compared with the energy of the collision. This means the study of tau leptons and the charm, bottom and top quarks. The discoveries of the charm quark, the bottom quark and the tau have already been discussed in section 1.2.4. The search for the top quark has been discussed in section 1.6.1.

Some of the most interesting heavy flavour physics is shown by the bottom quark. As will be discussed, b–quarks readily undergo mixing to their anti–particle states. It may well be possible to study CP violation in the b–quark system, in the same way as has already been done with s–quarks using K^0s. Searches are also made for 'rare' B–decays, which are forbidden by the Standard Model. If the Kobayashi–Maskawa matrix elements involving the c–quark and t–quark are examined, it may be realised that these particles decay very quickly: the heavy flavour physics of the c– and t–quarks may well be limited to measuring their masses and cross–sections.

1.7.1 B–Quark Experiments

Most of the data on heavy flavours has come from e^+e^- experiments. For the τ, there is no other source of data, and for c and b quarks the largest and cleanest data samples are from e^+e^-. This is due to the basic characteristics of e^+e^- collisions:

- possibility of tuning the centre–of–mass energy to sit directly on a resonance
- the simplicity of the final state, which has none of the initial beam particles
- roughly equal production rates for all flavours of quark and lepton

Due to the large mass of the b, and its relatively small cross section in fixed–target experiments, where there are also complicated final states with spectator particles and the exact energy of the interacting quarks is uncertain, most of the studies of b–quark properties have been made with e^+e^- experiments. Prior to LEP, most of the data on b–quark physics has been gathered at electron colliders running at the Υ resonances. The Υ^{4s} only has sufficient energy to produce B_d mesons: the energy threshold for the production of B_s^0 mesons (the particle consisting of an anti–b–quark and a strange quark) is at the Υ^{5s}. This fact is exploited by the workers at CESR. There, the energy is finely tuned to the Υ^{4s} where a pure sample of B_d particles is produced. The team concentrated for several years on measuring the parameters and understanding the systematics of the B_d, in preparation for moving

onto the Υ^{5s} and measuring the properties of the B_s with a greater understanding of the B_d processes.

Studies of bottom–quark physics are possible using the following types of apparatus :

- e^+e^- colliders running at the Υ resonances. Υ experiments have the best statistics and cleanest samples.
- e^+e^- colliders in the 'continuum' , e.g. PEP/PETRA and KEK. The major drawback here is the low event rates. KEK may be the worst place to do heavy flavour physics as the cross section is lowest here.
- e^+e^- colliders at the Z^0 resonance – LEP and SLC. These are better than PEP/PETRA as there is a larger fraction of b and c events. The LEP/SLC detectors also have better lepton ID than the PEP/PETRA generation.
- fixed target experiments. These have the advantage of a prolific event rate (one Fermilab experiment has over one million events on tape), but have severe triggering and background problems to contend with.
- $p\bar{p}$ colliders of the present generation : e.g. UA1 (where $b\bar{b}$ mixing was discovered) , CDF and D0
- pp colliders in the TeV energy range : LHC and SSC. Some of the more easily done and most useful physics at the SSC may well be heavy flavour studies.

There have been many proposals recently for the construction of dedicated B 'factories', devoted to high luminosity running near the Υ. This would facilitate studies of CP violation and the searches for rare B decays. Such schemes have been proposed at TRIUMF, SLAC, and Spain.

1.7.2 Heavy Flavours with ALEPH

At the Z^0 resonance, there is a significant branching fraction to heavy quarks. Several years of LEP running should provide a sample of hundreds of thousands and perhaps several million heavy flavour events. This will mean that high–statistics measurements of the forward–backward asymmetry, cross-sections and decay modes of the heavy quarks will be possible. These measurements will be an important part of the LEP experimental programme, and help to test the Standard Model rigorously.

The heavy flavour physics possible with ALEPH covers :

- measurement of the branching ratios of $Z^0 \rightarrow b\bar{b}$; $c\bar{c}$; $\tau\bar{\tau}$
- measuring the fragmentation parameters of heavy quark jets

- physics of charm decays. (Tag using $D^{*\pm}$)
- lifetime measurements of the various B–particles
- search for the B_s^0 meson (using for example $B_s^0 \rightarrow l l \Phi$)
- search for beauty–flavoured baryons
- forward– backward asymmetry
- the mixing of B^0 mesons.
- measurements of elements of the CKM matrix
- with a sufficiently large data sample, measuring CP violation in the b system.

The last topic, the measurement of CP violation in b–quark events at LEP may require a sample of as much as $10^6 Z^0$ events. This is one of the reasons for the proposals mentioned for building a dedicated b–meson factory.

1.8. Modern Particle Detectors

The modern particle physicist has a large armoury of devices available to measure the momentum, mass, energy, charge, position, time of flight and type of the many particles which result from interactions at an accelerator. In a typical particle physics experiment, a combination of several types of detector is used, in conjunction with a trigger system to recognize valid events, a data readout system, on–line computers to write the data to magnetic tape and off–line computers for event reconstruction and analysis. Complete detector systems are very briefly discussed in section 1.8.6. The configuration of detector(s) chosen by an experimental collaboration depends on the type of accelerator facility, the physics goals of the experiment, the currently available technology and of course finance.

1.8.1 Interaction of Particles with Matter

In order to detect the passage of a particle, it must be caused to interact with some matter in its path. Neutral particles are detected indirectly via the charged particles their interactions produce. Photons interact via the photoelectric effect, the Compton effect or by pair production. Neutrons are detected by the fragments from their collisions with nuclei, and neutrinos (with extremely low efficiency) by their weak interactions with matter. Charged particles are detected via their interaction with the atomic electrons of the detector. The energy loss of charged particles is given by the Bethe–Bloch formula, discussed in section 2.2.1.

1.8.2 Position Measurement

Tracking detectors measure the following properties of (charged) particles: position (usually in 3 dimensions, perhaps by taking two or more projections); time of passage and the track angles. Some of the devices used in high energy physics for tracking are:

- bubble chambers
- flash, spark and streamer chambers
- proportional chambers
- multi–wire proportional chambers
- drift chambers of various configurations
- time projection chambers (described in section 3.7)
- solid state detectors - silicon microstrip and CCD devices

Bubble chambers, invented by Glaser in 1952 [39], consist of a large volume of liquid, for example liquid hydrogen or freon, near to the boiling point. An expansion mechanism triggered at the time of the beam pulse causes a transition to the superheated state. The passage of charged particles causes ionisation of the liquid: these ions then act as nucleation centres for the formation of bubbles along the track. The trails are photographed by flash illumination before the bubbles grow too large. The images are recorded on film in stereo pairs, which are subsequently analysed by hand on scanning machines which digitise the tracks into computer readable form. The chamber is normally located in a strong magnetic field, which permits momentum measurement from track curvature. Bubble chambers feature very high spatial resolution and fully three–dimensional readout. However, they suffer from several disadvantages: they cannot be triggered, have a large dead time after expansion, can accept only one event per accelerator pulse, and require a large effort in the manual scanning of many films. They are also not suited to operation at colliding beam accelerators, where there is essentially a continuous interaction rate.

A flash chamber is a simple, cheap device consisting of a large number of tubes filled with a mixture of neon and helium. The tubes are placed between two planar metal electrodes to which a high voltage pulse is applied when the device is triggered. The glow discharge in the tubes is recorded photographically or electronically. Due to the extremely low cost, such devices are used for the construction of large volume calorimeter–like detectors. A spark chamber consists of a set of electrodes in a volume of noble gas. The plates are alternately connected to ground or a triggered high voltage source. When an event occurs, a trigger causes a large high voltage pulse to be applied to the electrodes. Passage of charged particles

leaves a trail of ionisation, and sparks occur parallel to the electric field in the gaps at the places where particles have traversed the chamber. In common with bubble chambers, these two types of chambers suffer problems of low rate capability.

A streamer chamber consists of a volume of gas in which an electric field of perhaps 50 kV/cm is applied perpendicular to the track direction, which creates avalanches with high gas amplification and light emission along the ionisation trails of charged particles. If a very short ($\approx 10ns$) high voltage pulse is applied then short streamers develop. A track image similar to that in a bubble chamber is obtained. Streamer chambers have a good multi-track capability, and can have excellent spatial resolution, perhaps of the order of 10's of microns. They can also be triggered, and have a fast response.

Most modern tracking devices use some form of *wire chamber*. Proportional wire counters have been used for a long time in nuclear and high-energy physics. A single wire proportional counter consists of a volume of gas held in a cylindrical tube (radius r_a). A thin central wire (radius r_b) is held at a high positive potential with respect to the outer tube. The electric field is then:

$$E(r) = \frac{V}{(r \ln(r_a/r_b))} \tag{1.8.1}$$

which reaches very high values near the surface of the wire. Charged particles traversing the volume leave a trail of ionised atoms and electrons. Under the influence of the electric field, the electrons drift to the central wire and the positive ions to the walls of the container. When the electrons reach the high field regions near the central wire they accelerate and start an avalanche, which gives a detectable signal. In moving the distance r_1 to r_2 the electron gains kinetic energy ΔT :

$$\Delta T = e \int_{r_1}^{r_2} E(r)\, dr \tag{1.8.2}$$

and if ΔT exceeds the ionisation potential of the gas a secondary ionisation can occur. A series of such ionisations leads to an avalanche of electrons and ions. The number of secondary electrons for one primary electron, i.e. the gas amplification factor, reaches 10^3 to 10^5 in the proportional region, where the amplification factor is independent of the number of primary electrons. The amplification process described means that the proportional counter gives a signal proportional to the incident particle energy, and which is independent of the position of the particle's trajectory across the chamber. The chamber is in proportional mode when it is set at such a voltage that gas amplification takes place and the output

signal is proportional to the number of primary ion pairs. At a higher applied voltage, this proportionality is lost and the device is in the limited streamer or Geiger modes.

The multi–wire proportional chamber was invented by Charpak and colleagues at CERN in 1968. It consists of a planar array of anode wires with cathode planes on either side, Fig. 1.8.1. The cathode planes can be arrays of wires or, more usually, flat conducting planes or strips. As the multiwire chamber only gives positional information in one direction, arrays of chambers with crossed orientations are used to define particle trajectories. Spatial resolution as good as several tens of microns can be achieved by MWPCs by using the signals induced on cathode strips and taking the centre of gravity of several strips. However multiwire chambers for large scale experiments are costly to construct and need many individual channels of electronics, which takes up space. This is why drift chambers and time projection chambers were invented.

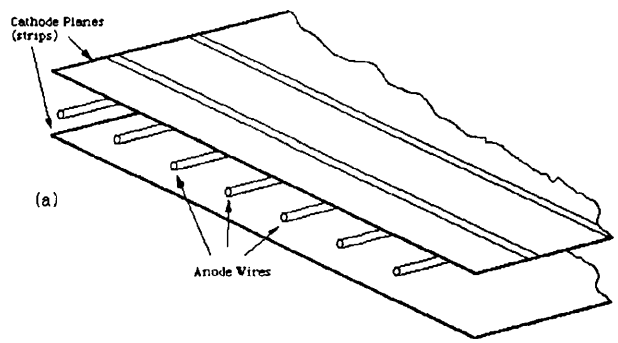

Fig. 1.8.1: Schematic of Multiwire Proportional Chamber

Drift chambers make use of the fact that the time between the passage of a charged particle through a wire chamber and the pulse on the anode wire is proportional to the distance of the particle trajectory to the anode wire. A great reduction in cost of chamber construction can be made by drifting the electrons from the primary ionisation over a distance of the order of perhaps 10cm in a low–field region before reaching the anode wires. Spatial resolutions of the order of 0.1mm are obtained. Cylindrical drift chambers, known as jet chambers, have been constructed for use at collider detectors. The cylindrical geometry is matched to the solenoidal magnetic fields in such detectors. Jet chambers are used as

central detectors for the measurement of the curvature and initial directions of tracks from the interaction point. The time projection chamber (TPC) is a major extension to the concept of the drift chamber. Section 3.7 contains a brief description of the principle of operation of TPCs.

Detectors based on semiconductors (principally silicon) are used for high–precision tracking [40]. The active area of such devices is the depletion region in a p–n semiconductor junction: ionising radiation liberates charges in this region, which are drifted across the junction and produce a detectable signal. The advantage of semiconductor detectors is that the energy needed to create an electron–hole pair (e.g. 3.6 eV in silicon) is much less than that needed to create an electron–ion pair in a gaseous detector (e.g. 26 eV in Argon)– thus giving much better statistics. Semiconductor detectors are also much more dense than traditional gas detectors. Silicon strip detectors (consisting of many parallel junctions constructed a few μm apart) are used in the ALEPH microvertex detector, section 3.5. Semiconductor detectors are also used for the readout of sampling calorimeters, see section 2.7.4. Concern about the radiation hardness of silicon detectors (the primary area of application for semiconductor detectors is as vertex detectors near to the interaction point) has led to interest in the use of other semiconductors, principally gallium arsenide.

1.8.3 Time Measurement

The time of passage of charged particles is usually measured by a combination of scintillator and photomultiplier tubes. Time resolutions of the order of nanoseconds are easily achieved. The time–of–flight of a particle from the interaction gives its velocity, which when combined with momentum measurement is used in particle identification. Scintillation detectors have always been widely used in nuclear and particle physics, for example in triggers; beam halo vetoes; time of flight counters and in scintillating fibre calorimeters. There are many types of scintillator used for different purposes, and it is not appropriate here to have a detailed discussion of such an extensive subject.

1.8.4 Momentum and Energy Measurement

The momentum of charged particles is measured using magnetic spectrometers – the particles pass through a large, uniform magnetic field and the trajectory is measured using an array of multi–wire proportional chambers. Charged and neutral particle energy is measured by *calorimetry*: a destructive technique where the particle is absorbed in a mass of dense material with embedded detectors, see Chapter 2.

1.8.5 Particle Identification Techniques

It is of obvious importance to be able to identify the type of particles in an interaction. The charge sign is determined by the direction of bend in a magnetic field. Methods used for particle identification are :

- dE/dx – the energy loss along a particle track, measured by e.g. counting the bubble density in a bubble chamber picture
- time of flight (combined with momentum measurement)
- Cherenkov counters
- transition radiation detectors

Cherenkov radiation is the electromagnetic radiation emitted by charged particles traversing matter faster than the speed of light in that medium, i.e. with velocity $v > c/n$, where n is the refractive index. The radiation is emitted in a cone with angle $\cos\theta = 1/\beta n$. This means that the Cherenkov effect may be used to measure particle velocity. A threshold Cherenkov counter is used to discriminate between two types of particles with the same momentum. It consists of a volume of gas: the pressure (and hence refractive index) of the chosen gas is adjusted till one of the particle types is below threshold. In a differential Cherenkov counter, the cone of Cherenkov light is focussed by a lens or spherical mirror. An adjustable diaphragm stop at the focus transmits light to a photomultiplier tube: varying the diaphragm diameter permits the selection of different particle velocities. A further development is the ring imaging Cherenkov (RICH), which enables measurements of off–axis particles. In a RICH the Cherenkov photons are focussed by mirrors to give a ring image which is read out by a photosensitive wire chamber system.

When a charged particle traverses a medium with varying dielectric constant, for example a series of foils and air gaps, radiation is emitted from the interfaces between the materials. This 'transition radiation' depends on the γ value of the particle, and so is useful in identifying particles of very high energy where other methods are not applicable.

1.8.6 Complete Detectors

Since the 1950's there has been a steady increase in the size, speed and complexity of particle physics experiments. Size – as higher energies demand larger detectors to contain the particles; collider detectors are also built to cover the whole 4π region around the interaction point. Speed – devices based on, for example, bubble or spark chambers, which need long recovery times were well suited to operation with cyclic accelerators; devices based on

proportional and drift chambers can cope with hundreds of events per second. Complexity – experiments now use exclusively electronic readout techniques, and this coupled with computers means that tens (if not hundreds) of thousands of readout channels are routinely used. Computers also enable the processing and storage of much larger event samples, with over a million events taken being quite common.

A typical high energy physics experiment will involve the detection, measurement and identification of many particles, charged and neutral, from each event. Modern particle detectors are huge devices, with dimensions of the order of 10s of metres, and weigh thousands of tons. They are highly complex, using several different types of detector in concert, with typically $10^5 - 10^6$ channels of information. It is the job of the experimental physicist to design and construct these machines: to install them in position with a very high accuracy; to ensure their stable operation over long periods of time and to analyse the data produced.

There are many different configurations used for fixed target experiments, as these depend very much on the incident particle, target used, energy, and physics reaction under study. Fixed target experiments are often devices specialized to one particular channel. Fixed target experiments continue to be useful, as they have the highest luminosity and can have triggers concentrating on certain types of events.

The trend for detectors at collider facilities is towards combined multi–purpose detectors. These normally have a high magnetic field, and surround (as much as possible) the interaction point with large volume tracking and electromagnetic and hadronic calorimetry. Such experiments may have triggers which look for important event configurations, but normally also take data with a minimum bias trigger, which is designed simply to remove background events. This is possible due to the lower event rates at colliders. To cope with the large volumes of data generated by such a detector, and also to ensure the fastest possible analysis in a competitive environment, all of the readout of such detectors is performed electronically with computers. Each experiment obviously has its particular areas of strength and reasons for choosing a particular configuration. The design and operation of the four detectors constructed for use at the LEP e^+e^- collider will be discussed in section 3.2.

Chapter 2.
Calorimetry

'Ever fallen in love with someone you shouldn't've fallen in love with?'

2.1. Introduction

This chapter describes particle energy measurement by the technique of *calorimetry*, concentrating on the electromagnetic calorimeters used in high energy accelerator experiments. Calorimeters form a part of nearly all current large experiments at accelerators, both fixed target and colliders and are used in nucleon decay experiments, magnetic monopole searches, neutrino physics and cosmic ray physics. A calorimeter consists of a large block of material, in which the particle interacts and loses its energy via electromagnetic or strong interactions. Most of the energy of the secondary particles is eventually given out as heat (hence calorimeter) but a fraction can be seen as an ionisation or scintillation signal. Although it may be stating the obvious, it is important that the readout signal quantity is proportional to the incident particle energy.

Traditionally, high energy experiments used large magnetic spectrometers to measure charged particle momentum (and hence energy). Calorimeters are used more frequently now as they have the following advantages over the older techniques of energy/momentum measurement:

- calorimeters measure both charged and neutral particles
- they are better suited to colliding beam experiments where they can provide almost 4π coverage around the interaction point.
- due to the statistical nature of the shower process, calorimeter accuracy improves with energy (unlike techniques based on measuring track trajectory, which become less accurate at high energy). So for high energy (10-100 GeV) a precision comparable to that from magnetic spectrometers can be obtained. Also, magnetic spectrometers measure the momentum of charged particles, whereas calorimeters measure the energy: in conjunction with other information this can be used to measure particle mass.
- as the depth of material needed to contain a shower increases only as the logarithm of the energy, calorimeters can be (relatively) compact and cheap

devices. Magnetic spectrometry at very high energy requires large devices with a long lever arm (magnetic spectrometer size scales as $(\text{momentum})^{1/2}$ for a given resolution). Given a dense enough material the calorimeter can be made small enough to fit inside the magnet solenoid of a collider detector. Over 20 radiation lengths of material are needed to completely absorb a typical shower, therefore a typical device using lead ($X_0 = 0.56cm$) as an absorber will be of the order of 10s of centimetres thick.

- they can be highly segmented, which gives a measurement of the direction of the incoming particle
- calorimeters do not depend on a magnetic field for operation
- the readout time can be very fast, important at a high rate collider
- they can also give a fast ($\approx$ 100ns) 'total energy' signal for use by a trigger system
- particle identification based on the characteristic energy deposition shape in the shower may be possible

Over the last few years, the trend in large particle physics experiments has been away from devices which seek to measure the 4-vectors of each and every track in an event, towards multi-purpose detectors which are good at measuring the global properties of an event, measuring jets of particles and the energy balance of events. Substantial effort is already committed to designing calorimeters for the high rate/high radiation environment of the SSC and LHC. As their size and complexity grows, simpler readout methods and cheaper construction techniques may have to be found. Several excellent reviews of the field can be found in references [41–45]

2.1.1 Types of Calorimeter

Several different types of calorimeter devices have been used for different roles:

- **Electromagnetic calorimeters** : which measure electrons, positrons, gammas and neutral pions
- **Hadron calorimeters** : to measure hadronic particles (pions, protons, neutrons etc.) by their nuclear interactions
- **Neutrino detectors** : large masses of cheap material like iron and marble are instrumented to study neutrino interactions, for example the CHARM detector at CERN [46]. In this field calorimeters have taken over from the very large

bubble chambers because of their electronic readout, smaller cost per unit mass and their ability to be triggered.

- **Proton decay detectors** : one class of proton decay detector (e.g. Frejus [47], Soudan [48]) consists of a large mass of iron instrumented with wire chambers which are used to search for the decay products of the large number of protons in the device. The other type consists of a large tank of ultra–pure water deep underground (e.g. Kamiokande [49], IMB [50]). Photomultiplier tubes detect the Cherenkov radiation from proton decay products. None of these devices has found evidence for proton decay, however they are being used to measure the solar neutrino flux and the neutrinos from supernovae.
- **Cosmic ray detectors** : Calorimeters were originally invented for use in cosmic ray physics [51]. The first consisted of layers of lead interspersed with layers of ionisation chambers. Today, large arrays of detectors at ground level are used to study high energy cosmic ray showers in the atmosphere, for example the 'Fly's Eye' detector [52] in Arizona uses photomultiplier tubes to detect the Cherenkov light from extensive air showers. This technique can be likened to a form of calorimetry, with the earth's atmosphere as the absorbing medium.
- **Miscellaneous types** : Low temperature germanium and silicon detectors are being used to search for Weakly Interacting Massive Particles (WIMPs) [53]. Other detectors based on low temperature phenomena are proposed, for example the Superconducting Supercooled Colloid (S.S.C.) calorimeter [54] which aims to detect neutrinos using a collection of superconducting grains. Deposition of heat energy causes some grains to flip to normal conductivity, causing a jump in magnetic flux which can be sensed by using a SQUID.

Reference [55] is a recent review of calorimetry techniques in non–accelerator experiments.

2.1.2 Parameters of interest

The following are the main parameters used to characterize calorimeters:

- Energy resolution
- Position resolution
- Timing parameters
- Uniformity within a segment and between segments

- Linearity
- Cost
- Size
- Hermeticity (the proportion of the solid angle covered by sensitive material)
- Useful energy range
- Resistance to radiation damage
- Long term stability
- Performance in a magnetic field

The perfect device would of course have infinite position resolution, perfect energy measurement, 4 π steradian coverage, cost very little and require no calibration. Real devices are compromises among these various goals, and the solutions chosen are determined by the physics goals of the detector in question.

The rest of this chapter will concentrate on the calorimeters used at accelerator experiments. The basic physical processes of electromagnetic and hadronic showers will be described, the various readout technologies used will be presented and the implementation of real devices will be examined.

2.2. The Electromagnetic Cascade

When a high energy electron hits a block of material it emits bremsstrahlung photons, which undergo pair production to produce more electrons and positrons, which produce more photons... resulting in a cascade or shower of secondary particles. The same process occurs for high energy gamma rays. Electromagnetic calorimeters use these phenomena to measure the energy of electrons, positrons, photons and neutral pions (by $\pi^0 \rightarrow 2\gamma$).

If a charged particle has sufficient energy, it will ionise atoms in the medium it is traversing. The ionisation process also forms the basis of many forms of particle detector, as the ionisation charge may be collected in an electric field and amplified. It is also possible to excite materials to produce scintillation light or, depending on the particle velocity, Cherenkov light. At higher energies, charged particles lose energy by producing bremsstrahlung photons and knock-on δ-rays. The relative contributions of the various energy loss mechanisms for electrons in lead is shown in Fig. 2.2.1. Photons lose energy by the photoelectric effect, where all the photon energy is absorbed by an atom, the Compton effect and at energies above 1.2 GeV by pair production. The energy loss of photons in lead is shown in Fig. 2.2.2.

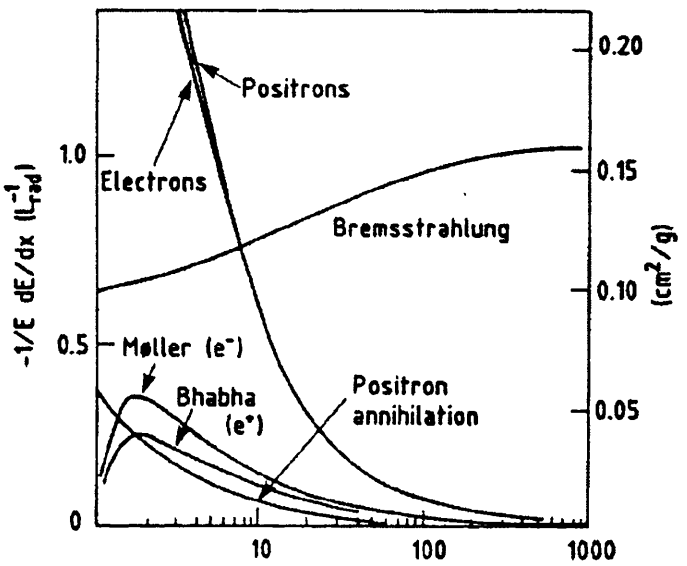

Fig. 2.2.1: Energy Loss in Lead as a Function of Electron Energy

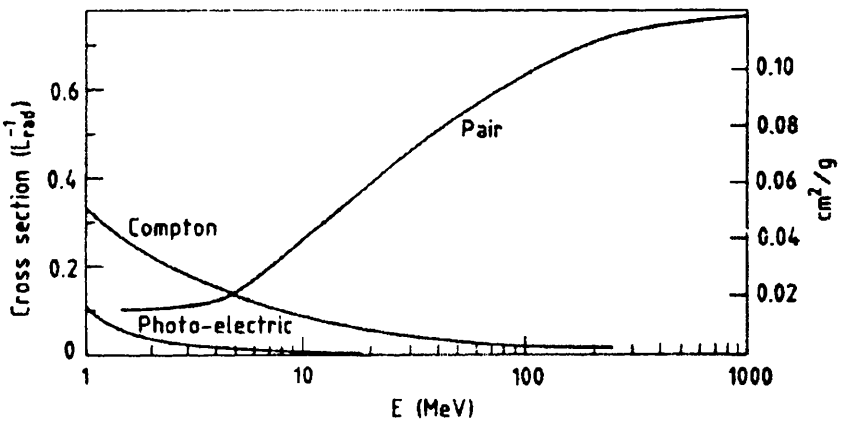

Fig. 2.2.2: Energy Loss in Lead as a Function of Photon Energy

The process of electromagnetically interacting particles showering in matter is well understood. Rossi [56] first gave a rigorous treatment of shower development in connection with cosmic rays.

2.2.1 Bethe–Bloch Formula

The energy loss of charged particles passing through matter is described by the Bethe–Bloch equation, Eq. (2.2.1) [57] which gives the mean rate of energy loss by ionisation for a charged particle:

$$\frac{dE}{dx} = \frac{4\pi N_0 z^2 e^4}{mv^2}\frac{Z}{A}\left[ln\left(\frac{2mv^2}{I(1-\beta^2)}\right) - \beta^2\right] \qquad (2.2.1)$$

where:

x : thickness of material traversed

N_0 : Avogadro's number
Z and A : atomic and mass numbers
ze : the charge of the particle
$v = \beta c$: the particle velocity
m : mass
I : an effective atomic ionisation potential ranging from 13.5 eV in hydrogen to 1 keV in lead

Thus dE/dx varies as $1/\beta^2$ at low velocity, passes through a minimum at $E \approx 3Mc^2$ where $dE/dx \simeq 2\text{MeV}\,(gcm)^{-1}$ and then rises logarithmically – the 'relativistic rise' region. Those particles which when traversing matter lose energy at the characteristic rate close to the minimum of the curve are known as 'minimum ionising particles' or mips.

2.2.2 Radiation Length, Critical Energy and Rossi's Approximation B

At high energies, following Eq. (2.2.1) the energy loss by ionisation of electrons is given by :

$$-\left(\frac{dE}{dx}\right)_{ion} = 4\pi N_0 \frac{Z}{A} r_e^2 mc^2 [ln\,(2mv^2\gamma^2/I) - 1] \tag{2.2.2}$$

where:

$r_e \simeq 2.8fm$ is the classical radius of the electron

The Bremsstrahlung energy loss takes the form :

$$-\left(\frac{dE}{dx}\right)_{brem} = 4\alpha \frac{N_0}{A} Z^2 r_e^2 E ln\frac{183}{Z^{\frac{1}{3}}} = \frac{E}{X_0} \tag{2.2.3}$$

which defines the *radiation length* X_0. An incident high-energy electron of energy E_0 loses energy via bremsstrahlung at an average rate of $dE/dx = -E/X_0$. The radiation length X_0 is then the distance over which a high energy electron (above approx. 1GeV) loses all but $1/e$ (on average) of its incident energy. The numerical value of X_0 is approximately given by :

$$X_0\,(g/cm^2) \simeq 180A/Z^2 \tag{2.2.4}$$

The interaction of photons is characterized by the *conversion length* λ, which is the average distance which a high energy photon travels before converting to an e^+e^- pair. More precisely, it is the distance at which all but $1/e$ of a set of photons will be lost due to pair production. The interaction cross-section of photons at high energy is given by :

$$\sigma_{pair} = 4\alpha Z^2 r_e^2 \left[\frac{7}{9} ln\left(183/Z^{\frac{1}{3}}\right) - \frac{1}{54}\right] \tag{2.2.5}$$

This gives the probability P for pair creation to occur within one radiation length as :

$$P = \sigma_{pair} \frac{N\rho}{A} \frac{X_0}{\rho} = \frac{7}{9} \tag{2.2.6}$$

Therefore the conversion length is related to the radiation length by:

$$\lambda = (9/7)\, X_0 \tag{2.2.7}$$

In the paper by Bathow [58] shower sizes were studied in various materials. Fig. 2.2.3 shows the longitudinal deposition of energy of showers in lead and copper, and demonstrates that the shower does scale longitudinally with radiation length in different materials.

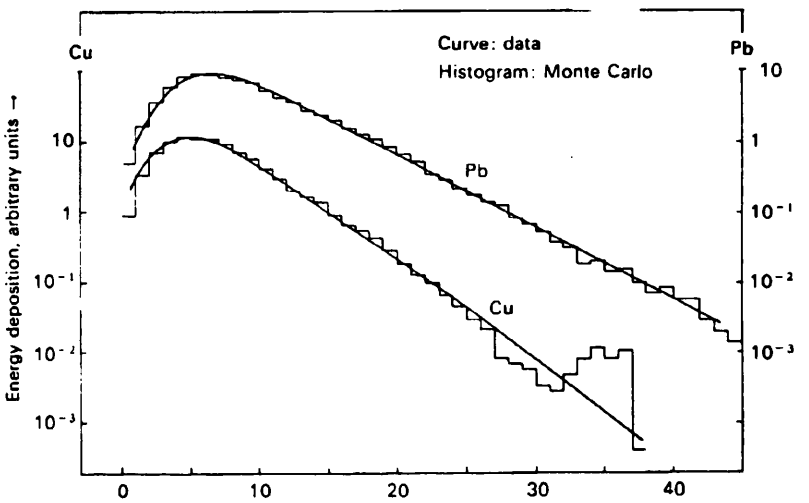

Fig. 2.2.3: Energy Deposition vs. Radiation Length. From [58].

To contain on average 95% of the energy, an electromagnetic calorimeter has to be of depth (in radiation lengths):

$$d(E) = 2.5\,(ln\,(E/\epsilon) + a)\, X_0 \tag{2.2.8}$$

where a=0.4 for electrons and 1.2 for γ. A typical device will have a depth of around 20 radiation lengths in order to absorb completely a typical shower.

At the low energy end of the cascade, the mechanism is dominated by the *critical energy* ϵ. This is the crossover energy where the ionisation energy loss starts to dominate the bremsstrahlung energy loss. The cascade then stops growing at the point where the mean particle energy approaches the critical energy. From Eq. (2.2.2) and Eq. (2.2.3), the ratio of ionisation to bremsstrahlung energy loss is $R \simeq ZE/550$, with E in MeV. A good approximation for ϵ, valid for high Z materials, is then $\epsilon(\mathrm{MeV}) = 550/Z$.

An analytical description of the longitudinal development of showers was first made by Rossi [56]. Rossi's Approximation B makes certain assumptions :

1. the cross–section for ionisation is energy independent i.e. $dE/dx = \epsilon/X_0$
2. After one radiation length, an electron of energy E_0 emits a bremsstrahlung photon of energy $E_0/2$, so that $E_e = E_0/2 = E_\gamma$
3. After one radiation length, a gamma undergoes pair production to an equal energy electron and positron.
4. Compton scattering and collision loss are neglected for electrons greater than the critical energy ϵ.
5. The cascade dies out when the electron energy reaches the critical energy.

After t radiation lengths there are 2^t particles, comprised of equal numbers of gammas, electrons and positrons. The average particle energy is then $E_0/2^t$. Shower development continues to a maximum at $E = \epsilon$ when there are $N_{max} = E_0/\epsilon$ particles. Maximum depth is at $t_{max} = ln(E_0/\epsilon)/ln2$.

In an electromagnetic cascade energy is deposited by many individual electrons and positrons. The sum of all the charged particle track segments can be considered as combining to form an *equivalent track length* T. In a naïve picture, this signal should be equivalent to that produced by minimum ionising particles traversing the detector and whose combined track length equals that of the track segments of the shower. From the arguments of Rossi's Approximation B, the total track length is then $T(X_0) = E_0/\epsilon$.

2.2.3 Shower Lateral Spread

An electromagnetic shower spreads out laterally due to the multiple scattering of electrons away from the shower axis, and in the later stages of the shower, due to bremsstrahlung photons travelling far away from the shower axis before being absorbed.

The lateral spread of the shower is characterized by the *Moliére radius* R_M, which describes the average lateral deflection, due to multiple Coulomb scattering, of electrons of energy ϵ after traversing one radiation length. R_M is defined using the ratio of radiation length and critical energy: $R_M = 21X_0/\epsilon \approx 7A/Z\,(g/cm^2)$. Expressed in the quantities of X_0 and R_M the development of electromagnetic showers is approximately material independent: Fig. 2.2.4 shows the lateral profile in lead and copper. The shower size can be seen to scale with the Moliére radius.

An electromagnetic shower consists of a dense core surrounded by a halo. In the early part of the shower before the maximum, over 90% of the shower is contained within a cylinder one radiation length in diameter. In the later stages of the shower, after the

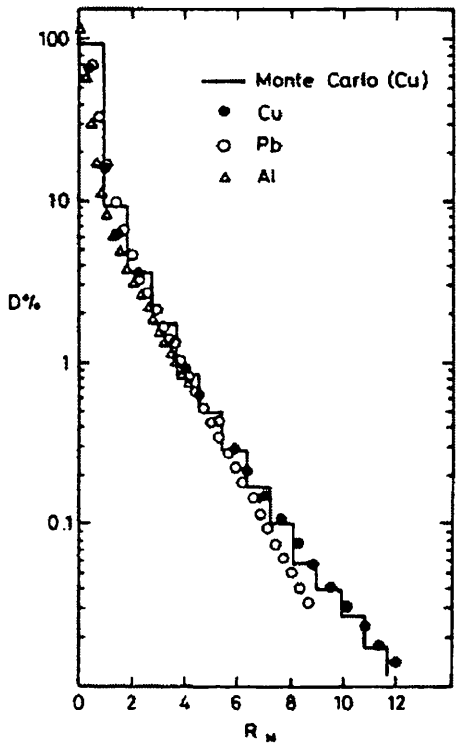

Fig. 2.2.4: Lateral Profile of Showers in Different Materials. From [58].

maximum, the core disappears and the halo broadens, such that 95% of the energy is contained in a cylinder of radius $\approx 2R_M$, see Fig. 2.2.5.

In order to distinguish two showers and measure their energy separately they have to be more than one Moliére radius apart. The Moliére radius is therefore a measure of the intrinsic lateral position resolution possible in a calorimeter with highly segmented readout. The spatial resolution of calorimeters will be more fully discussed in 2.7.6.

2.3. Energy Resolution of Electromagnetic Calorimeters

The ultimate resolution of a calorimeter is dictated by the statistics of the detected number of particles, and depends on the energy threshold η (at least for $\eta > \epsilon$). The threshold energy η is the lowest particle energy which produces a signal in the detector.

As discussed in 2.2.2 the track length is:

$$T = X_0 \frac{E_0}{\epsilon} \tag{2.3.1}$$

The track length traversed by the charged particles is proportional to the incident energy E_0 only if the particles can be detected until they have zero energy. In practical detectors, there is a cutoff energy η below which a device is not sensitive to the track segments. The

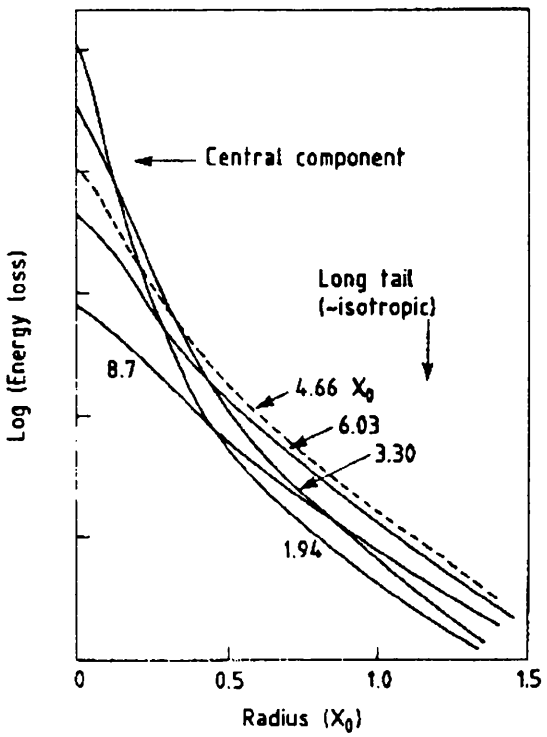

Fig. 2.2.5: Radial shower profile of 1GeV electrons in aluminium. From [59].

total track length as seen by the detector is shortened. The *detectable track length* T_d is then the equivalent track length corresponding to the measured signal:

$$T_d = F(\xi) \times X_0 \frac{E_0}{\epsilon} \tag{2.3.2}$$

where F, the fraction of the total track length, may be calculated using Rossi's Approximation B to be:

$$F(\xi) = \left[1 + \xi ln\left(\frac{\xi}{1.526}\right)\right] exp(\xi) \tag{2.3.3}$$

and ξ is related to the threshold energy and the critical energy by:

$$\xi = \frac{4.58 Z \eta}{A\epsilon} \tag{2.3.4}$$

Numerical calculations of this fractional reduction are shown in Fig. 2.3.1.

It has now been demonstrated that the detectable track length T_d is proportional to the incident particle energy, and hence calorimetry is possible. The response of an ideal calorimeter is proportional to the incident energy and the intrinsic energy resolution will be determined by the fluctuations in T_d. Using the familiar Poisson statistics of counting such quantities, the size of fluctuations may be estimated using the following argument: the maximum number of track segments is $N_{max} = E_0/\eta$, so $\sigma(E)/E \propto \sigma(N_{max})/N_{max} \propto$

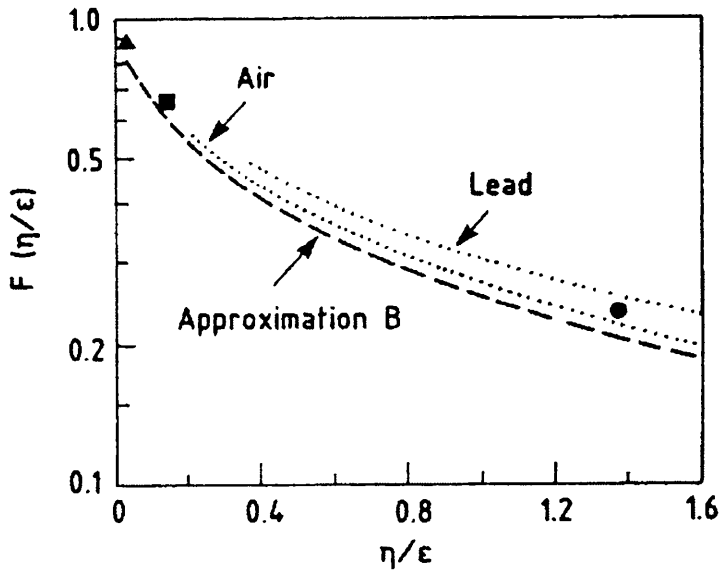

Fig. 2.3.1: Fractional reduction in track length. From [89].

$1/\sqrt{N} \propto 1/\sqrt{E}$. For instance, the intrinsic resolution of lead–glass counters has been calculated to be [60]:

$$\frac{\sigma(E)}{E} = \frac{\sigma(T)}{T} = \frac{0.7\%}{\sqrt{E(\mathrm{GeV})}} \tag{2.3.5}$$

In real devices, other effects contribute to the energy resolution. Instrumental effects such as noise, non–uniformity etc. will worsen resolution. Incomplete containment of the shower – 'energy leakage' will also worsen resolution. The longitudinal energy leakage (energy lost 'out of the back') is usually greater than the lateral leakage. The contribution of longitudinal energy leakage to the resolution, again for a lead–glass calorimeter, can be parameterized (for $E < 100\mathrm{GeV}$) as:

$$\frac{\sigma(E)}{E} = \left(\frac{\sigma(E)}{E}\right)_{f=0} \times (1 + 2f\sqrt{E(\mathrm{GeV})}) \tag{2.3.6}$$

where f is the fractional leakage loss. As f increases with energy, this introduces a non–linear energy dependence in the energy resolution. Such additional terms which worsen the energy resolution and do not improve as $1/\sqrt{E}$ are typical of instrumental effects, which may dominate at high energies. This is why homogeneous devices with a high intrinsic resolution at a few GeV cannot perform as well at high energy. As discussed in 2.7.5, sampling calorimeters have a much worse energy resolution than homogeneous types, due to sampling statistics, Landau fluctuations and path length fluctuations. At high energies however, the intrinsic resolution becomes less important as this improves with $1/\sqrt{E}$, and instrumental effects often dominate the resolution.

2.4. Energy Loss by Muons in Calorimeters

When traversing matter, muons also lose energy by the same electromagnetic processes as electrons. However, the cross-sections for the higher order QED processes, such as bremsstrahlung or pair production are suppressed by a factor of $(m_\mu/m_e)^2 \approx 40000$ compared to those for electrons. For example, the critical energy for muons is of the order of 200 GeV. The dominant mechanism of energy loss at most normally encountered energies is therefore ionisation processes. The mean energy loss per unit length by ionisation is again given by the Bethe-Bloch formula. For relativistic muons, the dE/dx is at a minimum for β around 0.96 (i.e. they are minimum-ionising particles) and rises slowly with increasing β to level off at $2-3\mathrm{MeV}/gcm^{-2}$ for most materials. The ALEPH electromagnetic calorimeter has layers of lead 2mm thick, so the mean energy loss per layer will be around 6 MeV. The range of energy loss values will be quite large because of the small number of collisions which occur and the large fluctuations on energy transfer which can occur in these collisions. The energy loss spectrum follows a *Landau* distribution.

It is normal practice to calibrate the absolute energy scale of a given calorimeter using muons. In sampling calorimeters, it may be noted that the absorption of electrons gives an observable signal which is reduced relative to the energy scale give by muons, i.e. the e/μ ratio is less than one. This is due to what are known as 'transition effects', i.e. the different responses of the absorber and sampling layers to the low energy electrons and photons in the later stages of the shower.

2.5. Hadron Calorimeters

Hadron calorimeters are intended to measure the energy of strongly interacting particles: pions, protons, neutrons etc. Hadron calorimeters consist of absorbing layers of dense metal (e.g. iron, tungsten, lead, uranium) interleaved with active sampling layers. Hadron calorimeters were first developed in the 1970's for use in fixed target experiments at the SPS and Fermilab, and are an important part of most current multi-purpose collider detectors. Nearly all current collider detectors have a calorimeter system divided into two sections: a dedicated electromagnetic part and a hadronic calorimeter behind this. In fact, many hadrons start to shower in the electromagnetic calorimeter, so for hadronic energy measurement the combination of both parts must be considered. In the future, hadron calorimeters will certainly find a place at the multi-TeV energies of the LHC and SSC, however the distinction between a purely electromagnetic and a hadronic section to the calorimetry may

become blurred and both functions may be fulfilled by one device. There follows a short discussion of the mechanisms of hadron showering, and the factors affecting the resolution of hadronic energy measurement. The remainder of this chapter will concentrate mainly on electromagnetic calorimeters, but there will be some discussion of hadron calorimeters where appropriate. A good general review of current hadron calorimetry may be found in [61].

2.5.1 The Hadronic Shower

The absorption of high energy hadrons in a block of matter proceeds in a similar fashion to the electromagnetic shower, although the mechanisms involved are much more complicated and not as well understood.

A hadron penetrating a block of matter will collide with one of the atomic nuclei. This collision produces some mesons (pions and kaons). Some energy is transferred to the nucleus, which releases this energy by emitting nucleons and low energy gammas, the nucleus also recoils from the collision and loses energy by ionisation. The nucleus may split into many particles with a large transverse momentum (spallation) and heavy nuclei may also undergo fission. The secondary particles from the collision may go on to hit other nuclei, thus causing a shower to develop. The transverse momentum of the secondaries dictates the shower size rather than multiple scattering.

There are two components to a hadronic shower: a hadronic part and an electromagnetic part. The interactions in the hadronic shower produce mainly neutrons, protons, charged pions and neutral pions. The π^0s (and other secondaries such as η, $e^{\pm}$ and γ) form a prompt electromagnetic shower. The size of the π^0 part is largely determined by the primary interaction, so fluctuations in this rate are very important. The fraction of the initial hadron energy converted into this electromagnetic fraction will vary strongly on an event to event basis, depending on the detailed processes at the start of the shower process, where production of these particles is energetically possible. The hadrons produce a longer range shower whose energy is absorbed slower.

The dimensions of hadronic showers are related to the *nuclear interaction length* λ_{int}. This is related to the cross-section, and thus strictly speaking depends on the type and energy of the incoming particles. To first order, the cross section varies as the nuclear radius, and a good approximation is $\lambda_{int} = 35A^{1/3} g/cm^2$. Experimental data indicate that the longitudinal and lateral profiles of hadronic showers show scaling in units of λ_{int}.

Parameterizations of the development of hadronic showers are obviously more difficult than for purely electromagnetic showers. A lot of the knowledge on hadronic showers has been obtained from Monte–Carlo simulation in conjunction with experimental measurements. The depth of the shower maximum may be parameterized as :

$$t_{max}(\lambda_{int}) = 0.2lnE(\mathrm{GeV}) + 0.7 \tag{2.5.1}$$

The longitudinal depth for 95% containment is

$$L_{95\%} = t_{max} + 2.5\lambda_{att} \tag{2.5.2}$$

where $\lambda_{att} = \lambda_{int} \times E(\mathrm{GeV})^{0.13}$ describes the exponential decay of the shower beyond t_{max}. As the fluctuations in hadronic showers are very large, and the shower may not start till a point well within the calorimeter, practical devices need to be thicker than the value for 95% containment would suggest. In order to contain 95% of the shower energy 95% of the time, around $3\lambda_{int}$ more of material is needed. Having said this, studies of calorimetry at the LHC and SSC have found that the energy leakage for a thinner device will not seriously affect the physics signals and it may be the case that devices with a coarse readout resolution in the latter planes may be built for the LHC/SSC.

The transverse profile of hadronic showers also roughly scales with λ_{int}. The shower consists of a central core surrounded by a halo extending to around $2\lambda_{int}$, and the transverse radius for 95% containment is approximately λ_{int}.

2.5.2 Fluctuations in Hadronic Showers

One reason for the large fluctuations in hadronic showers is the *invisible energy.* A major difference between hadronic and electromagnetic showers is that in hadronic showers part of the energy is dissipated in an undetectable form. Up to perhaps 25% of incident energy goes into breaking up and exciting nuclei (to cause nuclear breakup binding energy has to be supplied): only a tiny part of this will appear in the detectable signal. Energy is also lost by muons, neutrons and neutrinos which escape the detector. The fraction of invisible energy can be up to around 40%. So each incident hadron of the same energy may give rise to a very different shower composition.

Another important difference between hadron and electromagnetic calorimetry is that in the hadronic shower a considerable fraction of the energy is carried by soft neutrons from nuclear breakup. Since low-energy neutrons lose energy only by collisions with atomic

nuclei, their contribution to the signal from the calorimeter depends on the properties of materials used for the absorber and detector layers.

As has already been mentioned, there is a substantial electromagnetic component in the hadronic shower arising from $\pi^0 \rightarrow 2\gamma$. The fluctuations in the size of this component are a major contribution to the resolution. The average number of π^0s produced is:

$$n_{\pi^0} \approx 5lnE\,(\mathrm{GeV}) - 4.6 \tag{2.5.3}$$

and is small, therefore the fluctuations in this number are relatively large. Experimental evidence (for materials over a range from aluminium to lead) indicates that the intrinsic resolution is around :

$$\frac{\sigma(E)}{E} \approx \frac{0.45}{\sqrt{E\,(\mathrm{GeV})}} \tag{2.5.4}$$

Table 2.5.1 shows a comparison of the performance of several hadron calorimeters.

Detector	Type	$\Delta E/E$
MAC	Iron/PWC	$0.75/\sqrt{E}$
UA1	Iron/scintillator	$0.80/\sqrt{E}$
UA2	Iron/scintillator	$0.30/E^{\frac{1}{4}}$
CHARM	Marble/scintillator	$0.53/\sqrt{E}$
AFS	Cu/Uranium/scintillator	$0.36/\sqrt{E}$

Table 2.5.1: Examples of Hadron Calorimeters

2.5.3 Compensation

If a (hadron) calorimeter is sensitive only to the ionising part of the signal, i.e. the electrons, positrons and charged hadrons, then it will only be sampling a fraction of the deposited energy. The resolution will be dominated by the intrinsic shower fluctuations, of at least the 45% figure quoted in Eq. (2.5.4), and there will be deviations from linearity since the invisible energy fraction is itself energy-dependent.

In a given calorimeter, hadron showers have a worse energy resolution than electromagnetic ones: this is due to the fluctuations in the energy carried by ionising particles, as discussed above. The distribution in energy signal for pions is wider, and normally has a smaller mean value, than that for electrons of the same energy. That is to say the e/π ratio

is greater than 1. The level of nuclear effects, and the difference in response to the electromagnetic and hadronic parts of the shower is *experimentally* measured in a test beam by the e/π ratio, i.e. the ratio of calorimeter response to electrons and pions of the same energy. The inequality of response to the hadronic vs. the electromagnetic parts of the shower is measured by the electron:hadron response ratio e/h. The e/π ratio is energy dependent, but may be related to e/h. If we take the detector efficiency for the electromagnetic part of the shower as ϵ_e and the efficiency for detecting the hadronic part as ϵ_h, then $e/h = \epsilon_e/\epsilon_h$. Every material (or combination of materials) has its own characteristic e/h value. Due to the effects described above, for most calorimeters $\epsilon_h < \epsilon_e$ and $e/h > 1$: a typical value for e/h is around 1.4.

The fraction of the shower energy which goes into π^0 production has large, non–Gaussian fluctuations and from Eq. (2.5.3) it can be seen that this fraction increases logarithmically with energy: so in a calorimeter with $e/h \neq 1$ the following effects may be seen:

- the signal distribution for mono–energetic particles is non–Gaussian
- the fluctuations in the size of the electromagnetic fraction of the shower worsen the energy resolution
- the energy resolution does not improve as $1/\sqrt{E}$
- nonlinearity of response is observed
- the e/π ratio is energy dependent

It is therefore desirable to design a *compensating* device where e/h is as close as possible to unity.

Compensation can be achieved either by reducing the response to the electromagnetic shower components or by boosting the response to the non–electromagnetic components (in particular neutrons) or by a combination of both. The original idea was to use uranium as the absorber which would contribute an additional compensating signal from nuclear fission. Fission compensation was first investigated by Fabjan et.al. in 1977 for a sampling liquid argon calorimeter [62]. The first successful device to make use of fission compensation was the AFS uranium/scintillator calorimeter at the CERN ISR in the early 1980s [63]. Uranium calorimeters were constructed which had e/π close to one over a wide energy range and showed an improved energy resolution for hadron showers.

However, compensation is not simply explained as arising from fission alone. The mechanisms of compensation are now well understood, as explained by Wigmans in [61]

and [64]. The low–energy neutrons in the shower, and their conversion and absorption by the active material play a leading part. Neutrons may be detected by the ionisation losses from the protons in neutron–proton collisions, so a calorimeter with hydrogenous material in its sampling layers will have a larger fraction of the neutron energy measured in these layers.

Another important part of bringing e/h closer to unity is decreasing the response to the electromagnetic part of the shower. The e/h ratio can be altered by changing the ratio of high–Z absorber to low–Z sampling materials, due to the Z–dependence of the absorption mechanisms in the shower. The cross–section for ionisation is proportional to Z, that for pair production to Z^2 and for the photoelectric effect to Z^5. Therefore, most of the low energy electrons in the shower are produced in the high–Z absorber and deposit their energy there. They will only produce a signal when they escape into the absorber layers, which only happens at the boundaries hence the importance of the thickness ratio of these layers.

Another method of compensation, which does not aim at having $e/h = 1$ as an intrinsic property of the detector, is to make off–line corrections to the measured data, for example [65]. This approach requires a finely segmented device giving information on the longitudinal shower development. An attempt is made to determine the π^0 content for each shower, and a weighting scheme is applied to correct for the different calorimeter responses to the π^0 and hadronic parts of the shower. A weighting scheme is also used for hadronic energy measurement in the combined ALEPH calorimeters [148,149].

As indicated in 2.1, the current and next generations of collider experiments are concerned with the measurement of jets, which consist of a mix of neutral and charged leptons and hadrons. In an uncompensated device (where this is the purely electromagnetic section of the calorimeter,the hadronic section or a combination of both) the calorimeter response to jets will be dependent on the jet composition, which may have effects on the physics being studied. In [66] Wigmans discusses the consequences of having a calorimeter which is non–compensating, using the combined ALEPH calorimeters as an example. He goes on to discuss the compensated calorimeters being installed, or planned for the next generation of experiments, with special reference to the scintillating fibre 'spaghetti' calorimeter.

If the performance of the compensated calorimeters constructed to date is examined, it is found that the intrinsic resolution is around $0.22/\sqrt{E}$. Eventually, even for a compensated calorimeter, instrumental effects such as light collection uniformity, leakage or calibration

issues will be the limiting factor to the energy resolution at very high energies, since they do not improve as $1/\sqrt{E}$.

2.6. Homogeneous Calorimeters

In an *homogeneous* or total absorption calorimeter the incoming particle collides with a block of material and deposits all or most of its energy in it; a readout signal is obtained from the bulk of the material. There are two categories of homogeneous calorimeter: those which use scintillator materials and those which measure the Cherenkov radiation produced by relativistic e^+e^- tracks. The materials used are high-Z, transparent and have short radiation length.

Homogeneous shower counters offer the best possible energy resolution. Homogeneous devices are also compact (as there are no sampling gaps). Compensation is much harder to achieve in a homogeneous device, where it is not possible to adjust the thicknesses and types of absorber and detector layers. It could be possible to perform offline corrections, but only if the detector is highly segmented and it is possible to determine the electromagnetic and hadronic fractions in the shower. Homogeneous calorimeters have therefore traditionally been employed as electromagnetic calorimeters. Hadronic calorimeters, given the large intrinsic fluctuations in hadron showers, are normally of the sampling type. In large experiments, homogeneous calorimeters may prove too costly: and thus many electromagnetic calorimeters at collider detectors use sampling readout, as discussed in 2.7

2.6.1 Readout

The readout is usually performed by photomultiplier tubes either directly joined to the scintillator blocks or coupled via optical fibres. If the number of photoelectrons detected is small, then the counting statistics of this quantity will have a contribution to the resolution:

$$\frac{\sigma(E)}{E} = \sqrt{\frac{1 - g^{-1}}{\langle n_{pe} \rangle}} \tag{2.6.1}$$

For instance, in lead glass this contribution is around $3\%/\sqrt{E}$.

The term g^{-1} in equation Eq. (2.6.1) describes the contribution due to the finite gain of the photosensitive device, and represents fluctuations at the dynode or collecting surface. It is unimportant in photomultiplier tubes (which have gains of $\approx 10^5$), but is significant with photodiodes/triodes which have gains of order 1–10. With low gain detectors the electronic noise of the readout circuit must also be taken into account, and will have an impact at

low energies. Readout via photodiodes and phototriodes has become more common in high energy applications, in spite of their low gain, because there are difficulties in operating conventional photomultiplier tubes in magnetic fields. Photodiodes/triodes are insensitive to magnetic fields: for instance the OPAL and DELPHI calorimeters at LEP use vacuum photo–triodes in fields of 0.7 and 1.2 Tesla.

2.6.2 Total Absorption Cherenkov Counters

In these detectors the incident particles are totally absorbed in the detector medium, and produce Cherenkov light by two processes :

- the electrons and positrons in the shower produce Cherenkov light
- a secondary of the interaction e.g. a recoil proton, produces Cherenkov light

For use as calorimeters, Cherenkov detectors are made of liquid or solid materials, as these have the required density and have a high refractive index which reduces the threshold energy as much as possible. As Cherenkov detectors only detect the relativistic particles in the shower, they have a high threshold energy and a low light yield.

The most common type of these devices is an array of lead–glass blocks with photomultipliers. The lead decreases radiation length without affecting light transmission. For lead-glass the resolution is around $3\%/\eta^{1/2}E^{1/2}$ (the Cherenkov radiation process yields many fewer photons than scintillation, so we have the extra photon statistics term η to add to the resolution). Typical resolutions achieved are of the order of $5 - 10\%/\sqrt{E}$(GeV), see Table 2.6.1. The Cherenkov light is produced in the picoseconds when the electrons are slowing down, so these detectors have excellent timing resolution. The main disadvantages of such devices are the expense and space occupied by the readout photomultipliers; lead glass also suffers from darkening when exposed to intense radiation flux, and there is great interest in using other materials such as lead fluoride.

2.6.3 Scintillator–Based Homogeneous Calorimeters

Scintillators fall into three categories: organic, inorganic and liquid noble gases. They are characterized by efficiency of light output: light output spectrum (and its matching to the PM tube response); speed and linearity. Calorimeters based on arrays of inorganic scintillator crystals read out by photomultipliers have been used for many years in nuclear physics and astrophysics applications. The most common material used is sodium iodide NaI(Tl), which has a high light yield and a spectral output well suited to standard photomultipliers. A good example is Crystal Ball, which is a spherical array of NaI crystals [67].

Other scintillator materials are used, and new materials are under investigation. More recent devices, for instance the CLEO II calorimeter [68], have used CsI(Tl) which has the advantages of being less hygroscopic; mechanically easy to work with; having a spectrum better suited to silicon photodiodes and a shorter radiation length. The L3 detector [69] uses Bismuth Germanium Oxide. (which has the shortest radiation length amongst the presently known optically transparent materials). BGO is capable of a resolution of $1\%/\sqrt{E}$ [70]. Other materials such as BaF_2, GSO and CeF_3 are being investigated. The interest here is in exploiting a fast component of light output for high rate applications, and in finding materials with a high radiation resistance. Table 2.6.1 shows a comparison of the properties of several typical homogeneous electromagnetic calorimeters.

Detector	Type	$\Delta E/E$
OPAL	Pb Glass Cherenkov read out by VPT	$5\%/\sqrt{E}$
DELPHI (forward)	Pb Glass Cherenkov read out by VPT	$5\%/\sqrt{E} + 0.35\%$
TOPAZ	Pb Glass Cherenkov PM tubes	$5\%/\sqrt{E}$
Crystal Ball	sphere of 672 NaI crystals	$2.7\%/E^{\frac{1}{4}}$
CLEO II	CsI blocks photodiode readout	1.6% at 5GeV
L3	BGO scintillator	1% for > 5GeV

where: VPT – vacuum photo-triode, PM - photomultiplier
Table 2.6.1: Examples of Homogeneous Calorimeters

2.7. Sampling Calorimeters

The other main class of calorimeters are *sampling* devices. These are the most popular and diverse class of devices. A sampling calorimeter consists of sheets of absorber (usually a high-Z material) interspersed with active sampling layers: the shower multiplies in the absorbing layers and sweeps through the sampling layers where it is measured.

As only a small fraction of the shower is detected in sampling devices fluctuations are larger, as discussed in 2.7.5. These 'sampling' fluctuations are not the dominant factor in hadron calorimetry, which has large intrinsic fluctuations. Compensation may also be achieved very much more easily in a sampling device, where the different compositions and thicknesses of the layers may be tuned. Thus hadron calorimeters are normally sampling devices. They are also appropriate for medium resolution electromagnetic calorimeters. Sampling calorimeters are cheaper, using materials like lead and iron for the absorber and mass-produced elements for the readout planes. Sampling calorimeters have very flexible designs, and can be built to suit the space constraints in a detector. The readout geometry of sampling calorimeters can be very finely segmented without too great a cost of material or readout electronics. This gives good position resolution and the possibility of particle identification by inspecting the longitudinal and lateral shower development.

The sensitive layers may use scintillators, liquid noble gases or warm liquids read out by ionisation chambers, gaseous wire chambers (multi-wire chambers, limited streamer tube chambers etc.) or silicon detectors. The most common metal absorber is lead : other high-density metals such as tungsten and uranium are also used. Fig. 2.7.1 shows a schematic representation of the readout configurations for various types of sampling calorimeter.

Table 2.7.1 shows a comparison of the performance of several sampling calorimeters.

Electromagnetic calorimeters are used to measure not only the energy of incoming electrons or photons, but also their spatial position and direction. Particle identification may be aided by using the pattern of energy deposition; thus electrons and photons may be distinguished from hadrons or muons.

Sampling calorimeters can be further divided into two classes: 'digital calorimeters' where only the number of tracks traversing the sampling planes are counted; and 'proportional calorimeters' where the energy of the electrons and positrons traversing the gaps is measured. This distinction will have a consequence when the calculations of energy resolution in sampling calorimeters is discussed.

2.7.1 Scintillator Readout of Sampling Calorimeters

Scintillator readout is very often used with sampling calorimeters. The 'classical' form of sampling calorimeter consists of lead sheets separated by plastic or liquid scintillator. In scintillator-based calorimeters charged particles in the shower produce flashes of scintillation light in the scintillator planes. The signal is large, which makes the contributions of photon statistics to the energy resolution very small, and fast, and so is suitable for use in a high

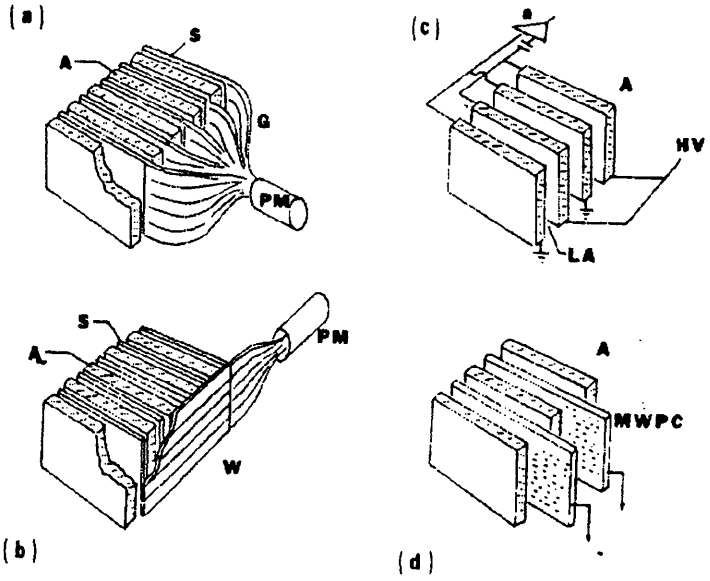

a – scintillator plates individually coupled to a photomultiplier
b – scintillator plates read out by wavelength shifter
c – liquid argon. Charge is collected by electrodes which are absorber plates
d – proportional wire chamber readout

Fig. 2.7.1: Schematics of common calorimeter readout techniques. From [41].

rate environment. Compensation is possible by selecting the correct scintillator material and adjusting the thickness ratio.

However, it is not possible to operate photomultiplier tubes in a magnetic field – which requires a complex light guide system, or an alternative readout device. Also, it is difficult to make highly segmented scintillator calorimeters. For large scintillator sheets position measurement is possible however by comparing the differences in light signal from both ends of wavelength-shifting bars on the edges of the sheets. Optical readouts in general are affected by non-uniformities in light collection over the sheets and gain variations between the photomultipliers. Aging and radiation damage will also decrease the light output over time. The calorimeter is calibrated by its response to minimum ionising particles and test-beams. Stability of output is monitored by LED flasher systems or laser systems, as discussed in 2.9.

Many variations exist on the theme of scintillator calorimeters, For example, the WA70 electromagnetic calorimeter [71] is a typical device for fixed target experimentation. It is a device 4m x 4m x 0.5m, consisting of 4mm lead sheets interspersed with tubes of liquid scintillator and read out by photomultiplier tubes. This achieves an energy resolution of

Detector	Absorber thickness (mm)	Sensitive material	Total Depth(X_0)	σ/E ($\%/\sqrt{E}$)
ARGUS	1 Pb	5mm Sc	12.5	8
CELLO	1.2 Pb	3.6mm LAr	20	13
MARK II	2 Pb	3mm LAr	15	13
MARK III	2.8 Pb	12.7mm PWC	12	18
Taggedγ	1.6 Pb	12.7mm LSc	19	12
PLUTO	Pb	Sc	8.6	35
TASSO	2 Pb	5mm LAr	14	11
MAC	Pb	PWC	18	17
TPC	3mm Pb/Al/fibreglass	Geiger cells	10	16
AFS	1.6 U	2x2.5mm Sc	19.5	16
UA1	3 Pb	2mm Sc	26	15
UA2	3.5 Pb	4mm Sc	17	14
ALEPH	2/4 Pb	4mm PWC	22	17
DELPHI	3.5 Pb	8mm PWC	28	17
UA6	4 Pb	5mm PWC	24	28

where : Sc – plastic scintillator; LSc – liquid scintillator; LAr – liquid argon; PWC – proportional wire chamber

Table 2.7.1: Examples of EM Calorimeters

$3.5\% + 2.25\%/\sqrt{E}$. Other readout methods use optical fibres to couple directly to photomultipliers or wavelength shifting bars on the edge of the scintillator sheets. This saves space and enables the PMs to be located outside of magnetic fields. Another technique is the use of wavelength shifting fibres stretched across the scintillator sheets to collect the light [72]. A new concept in scintillator calorimeters is the 'spaghetti calorimeter' which consists of scintillating fibres embedded in a heavy metal matrix and read out by multi–anode photomultipliers [73].

2.7.2 Charge Collection Readout of Sampling Calorimeters

In this type of calorimeter the absorber again consists of sheets of metal. The gaps contain liquid–filled ionisation chambers, where the charge produced by ionising particles

as they pass through a dense liquid is collected by electrodes. The most usual liquid is liquid argon: several large sampling calorimeters based on liquid–argon filled ionisation chambers with iron or uranium absorbing plates have been built [74]. Liquid argon calorimetry has been used for example by the CELLO experiment, and is being used by the H1 detector at HERA.

A liquid argon calorimeter has a series of metal plates, typically a few mm apart, immersed in a cryostat of liquid argon. The plates are at a positive high voltage, so ionisation electrons drift towards the plates. The liquid argon is dense and an adequate amount of charge can be measured using a simple ion chamber. As there is no charge multiplication process, these devices are not subject to the problems of gain control and stability of wire chamber readout devices. The disadvantages are the necessity for a bulky cryogenic system, purification systems for the liquids (especially for room temperature liquids and xenon) and the slow readout times (which are a function of the high electrode capacitance as well as the slow drift times in the liquid). Liquid argon calorimeters also have a rapid deterioration of the energy resolution at low energies: as the signal levels are very low, electronic noise is a major problem and dominates the resolution at low energies. Advantages are long–term stability, immunity to magnetic fields, high uniformity and accurate calibration.

More modern devices are proposed using liquid xenon [75] which would seem to be the ideal approach. With liquid xenon it would be possible to build more compact devices with a higher energy resolution – the prototype device mentioned achieves an energy resolution of $3.4\%/\sqrt{E}$. Also being investigated are room temperature liquids like tetra-methyl-pentane (TMP), which was proposed for the UA1 detector upgrade [76]. However, this suffered from problems with extreme sensitivity to any impurities in the liquid, and was not put into practice.

2.7.3 Gaseous Readout of Sampling Calorimeters

The alternative to liquid filled ionisation chambers is 'gaseous readout', which involves the use of Geiger tubes, multi–wire proportional chambers or streamer chambers as active layers and can give a very fine spatial resolution.

As the applied voltage in a wire chamber is increased the mode of operation changes from the ionisation chamber mode, where there is no amplification of the signal, through the proportional mode with gas amplification, to the Geiger-Muller region where the output signal is independent of the deposited energy. There are two broad classes of wire–chamber based calorimeters, depending on the mode of operation.

The first are *digital* devices where only the number of gap crossings is counted (which is proportional to the energy). A disadvantage of digital calorimeters is that they saturate at energies above a few GeV due to the higher track density near the shower axis. Digital calorimeters are used in the applications where a massive device with low cost per channel is needed, but where the ultimate in energy resolution is not necessary, e.g. in neutrino detectors and in proton decay experiments. Digital calorimeters have been used with flash tube readout, and more modern devices use Iarocci streamer tubes.

The second broad class of gas readout calorimeters are *proportional* calorimeters. The energy of electrons and positrons in each gap is measured and summed to give the total signal. The mechanism of operation of proportional counters has already been introduced in section 1.8.2. As has been said, the gas amplification factors reach values of 10^3 to 10^5. This greatly improves the signal-to-noise ratio, and means that less external amplification of the signal is needed. However, the response is very sensitive to factors which affect the uniformity and stability of the gas gain. Mechanical variations and distortions of the chambers can distort the electric field. Impurities and changes in the gas pressure and temperature can change the gas amplification. These issues are discussed in detail in section 2.9.1.

Gaseous readout has the advantage of being affected little by magnetic fields, so these calorimeters can sit inside a detector solenoid. Gaseous readout devices also have the advantages of built in amplification, high radiation resistance and relative cheapness. They can be read out with a high spatial segmentation. A two-dimensional readout with small cell sizes is good for resolving multi-shower events. Disadvantages include low energy resolution and slow response. Another disadvantage is that the absorber planes have a low density, and need to be relatively thick to be efficient. This leads to a less compact device. Another undesirable feature of readouts employing gas gain mode is the comparatively small amount of active material; this usually introduces additional sampling fluctuations which may be quite noticeable in electromagnetic calorimeters, as discussed in 2.7.5, but are thought to be less important for hadron calorimeters.

Wire chamber calorimeters may also suffer from non-linearities due to saturation at high energy. If a large number of slowly drifting positive ions are formed in a cell by a large deposit of energy they will distort the electric field within the cell. This is a problem for detectors which are required to operate efficiently over a large dynamic range, for example from minimum ionising particles to 100 GeV as at LEP.

Early gas sampling calorimeters used the signal from the central anode wires, or from the cathode wall. If only the cathode itself is used to pick up the induced signal, the requirements for an electrode to be both cathode and detection element may create problems and limitations in the design. The pattern of the readout geometry is limited by the construction geometry of the chamber and the cathodes must be designed carefully so that the electrostatic field for the sense wires is not disturbed by their pattern. A big advance was the development of resistive cathodes, first investigated by Battistoni et.al. [77]. One side of the proportional chamber cell, or perhaps the whole cathode in the case of plastic tube chambers, is formed by a layer of conductive material with a high resisitivity. This resistive layer does not shield fast transient signals, so the induced signal can be read out by exterior cathode pads or strips independent of the geometry of the proportional tubes. This means that two functions of the cathode are split, separating the field shaping cathode of the chamber from the signal pick-up electrode, and allowing a complicated readout geometry. In this way any problems of interference between the high-voltage system and the read-out system are avoided. This also results in cost savings, as the tubes can be mass-produced and complicated cathode geometries which fit a projective readout can be overlaid on them. Configurations using conductive plastic tubes, or a resistive layer forming one side of an aluminium extrusion, as in the ALEPH electromagnetic calorimeter, are used. In many devices the anode signals are not used and read-out is only via cathode pick up. In order to have a reasonable transparency for typical geometries of the order of centimetres, resistivities of the order of $2 \times 10^5 \Omega/cm^2$ are needed. If a smaller readout pattern is wanted, then a higher resistivity is needed to avoid a broadening of the amplitude distributions on adjacent channels.

At LEP, the Aleph electromagnetic calorimeter [78-79], [109] uses MWPC planes with signal readout both on the anode wires and via highly segmented cathode pads. This gives a very detailed picture of the shower. The DELPHI detector [80] employs what is known as a 'High Density Projection' (HPC') device [81] which is based on work with medical gamma imaging cameras and large volume drift chambers. Here the ionisation is drifted along tubes in the device. This technique gives very detailed images of the interactions in the detector.

Many large calorimeters utilizing proportional gas gain readout are in use- Table 2.7.2 and Table 2.7.3 give some examples of past and current calorimeters employing wire chamber

Detector	Physics Regime	Construction	Readout	$\sigma(E)/E$
CLEO	e^+e^-	1.7mm Pb Al prop. tubes	anode wires	$17\%/\sqrt{E}$
UA6	pp	4mm Pb+1mm steel	anode wires	$28\%/\sqrt{E}+0.6\%$
TPC	e^+e^-	1.4mm Pb + 0.25mm Al + 1.6mm fibreglass	cathode strips and anode wires	$16\%/\sqrt{E}$
AMY	e^+e^-	3.5mm / 7mm Pb plastic tubes	cathode strips and anode wires	$29\%/\sqrt{E}+1.0\%$
CDF endplug	pp	2.7mm Pb plastic tubes	cathode pads and anode wires	$28\%/\sqrt{E}$
ALEPH	e^+e^-	2mm / 4mm Pb	cathode pads and anode wires	$17\%/\sqrt{E}+1.7\%$
DELPHI	e^+e^-	3.5mm Pb	cathode pads	$23\%/\sqrt{E}+1.1\%$
L3 hadcal	e^+e^-	5mm C	proportional chamber planes	$55\%/\sqrt{E}+5\%$
CPLEAR	low energy $\bar{p}$	1.5mm Pb	cathode strips	$15\%/\sqrt{E}$

Table 2.7.2: Performance of Gas Calorimeters with Proportional Readout

readout. For more detailed reviews of wire-chamber based calorimeters see for example [43] and [82–86].

2.7.4 Silicon Instrumented Detectors

Devices using semiconductors as the active elements are in the early stages of development, and have only very recently been installed in some detectors. Silicon detectors are being used at the moment in smaller calorimeters which fill in the space between the main calorimeter and the beam pipe: such devices are used for low-angle tracking and luminosity measurement, for example the SLD luminosity monitor and the H1-PLUG calorimeter. The ZEUS collaboration intend to have large arrays of silicon detectors embedded at depths of 3 and 6 X_0 in their uranium/scintillator calorimeter. This precise imaging of the shower development will help in the discrimination between electrons and hadrons. This year, ALEPH has installed the SICAL device – a small silicon based calorimeter. There are proposals for silicon instrumented hadron calorimeters for the SSC detectors.

Detector	Physics Regime	Construction	Readout	$\sigma(E)/E$
FNAL E594	ν	sand + steel shot flash chambers	cathode strips magnetostrictive wires	$\approx 8\%$
ALEPH hadcal	e^+e^-	5cm Fe streamer tubes	cathode pads cathode strips	$84\%/\sqrt{E}$
DELPHI hadcal	e^+e^-	5cm Fe streamer tubes	cathode pads	$1.2/\sqrt{E}$
SLD hadcal	e^+e^-	5cm Fe streamer tubes	cathode strips cathode pads	$80\%/\sqrt{E}$
OPAL hadcal	e^+e^-	8cm Fe multiwire chamber	cathode pads	$1.05/\sqrt{E}\%$

Table 2.7.3: Performance of Gas Calorimeters with Digital Readout

Silicon detectors are expected to display several advantages over other detectors. The number of electron–hole pairs collected is much larger than, for example, the number of ionisations in a typical gas. This will lead to much lower statistical fluctuations. Silicon detectors do not suffer from saturation, and compensation is possible. They are solid, and therefore dense, and will enable more compact devices to be built. The main disadvantage is the sensitivity of silicon detectors to radiation damage and the high cost.

2.7.5 Energy Resolution of Sampling Calorimeters

This section deals with the processes determining the resolution of electromagnetic sampling calorimeters. The results apply to all such devices, but special attention will be paid to calorimeters with gaseous wire chamber readout. In practical sampling calorimeters, the intrinsic fluctuations due to finite cut-off energy are insignificant when compared to fluctuations due to other processes. The sampling fluctuations are particularly important for very thin active layers e.g. gaseous readouts.

Only a fraction of the shower energy is measured in sampling devices. The 'intrinsic sampling' fluctuation is the fluctuation in the number of e^+e^- pairs crossing active layers. For an active layer thickness t, the total track length T (assuming a cut-off energy η of zero) is cut into N track crossings as seen in the sampling gaps:

$$N = \frac{T}{t} = \frac{E}{\epsilon t} = \frac{E}{\Delta E} \tag{2.7.1}$$

where ΔE is the energy loss of a minimum ionising particle crossing an active layer. This then gives a contribution to the energy resolution of:

$$\left(\frac{\sigma(E)}{E}\right)_{samp} = \left(\frac{\sigma(N)}{N}\right) = \sqrt{\frac{\epsilon\, l}{E}} = 3.2\%\sqrt{\frac{\epsilon(\mathrm{MeV})\, t}{E(\mathrm{GeV})}} \qquad (2.7.2)$$

These fluctuations in track counting are called *sampling fluctuations.* For a typical hadron calorimeter, the sampling fluctuations add a contribution of around 9% to the resolution.

From Eq. (2.7.2) it can be seen that in order to have a good energy resolution a material with a low critical energy should be chosen. Values for the radiation length and critical energies of common absorber materials used in calorimeters are given in Table 2.7.4. This explains the choice of lead as an absorber in many calorimeters. Uranium will give no great improvement in the sampling fluctuations. It is interesting to note tungsten, which due to its density has the shortest radiation length of any metal, and hence would make a very compact calorimeter. The high cost prevents its use in all except small specialist devices, for example the ALEPH BCAL described in 3.13. It can be seen that if iron is used (as in many hadron calorimeters), the resolution will be much worse.

Material	Al	Ar	Fe	Cu	W	Pb	U
$X_0\,(gcm^{-2})$	24.0	19.6	13.9	12.0	6.89	6.52	6.13
ϵ(MeV)	39.3	29.8	20.5	18.7	7.9	7.2	6.6

Table 2.7.4: Critical Energy of Various Materials

When applied to real devices, the rough estimate of Eq. (2.7.2) represents a lower bound to the sampling fluctuations and must be refined as there are other effects, principally:

- there is a finite cut-off energy η which reduces the number of tracks by the factor $F(\xi)$ as described in 2.3
- multiple scattering, especially in high-Z materials, spreads out the shower, thus effectively thickening the absorber layers and increasing the track length

The sampling fluctuations are then described by:

$$\left(\frac{\sigma(E)}{E}\right)_{samp} \geq 3.2\%\sqrt{\frac{\Delta E(\mathrm{MeV})}{[F(\xi)\langle\cos\theta\rangle E(\mathrm{GeV})]}} \qquad (2.7.3)$$

where ΔE is the energy lost by a minimum ionising particle crossing an active layer. A Monte-Carlo calculation by Fischer [87] of the mean angle for all cascading particles

gives $\langle \cos\theta \rangle = 0.57$. Then, to a first approximation, the energy resolution of a lead based sampling calorimeter with $\epsilon = 1$MeV is:

$$\left(\frac{\sigma(E)}{E}\right)_{samp} = 13.7\%\sqrt{t/E(\text{GeV})} \tag{2.7.4}$$

With digital sampling calorimeters, only the sampling fluctuations as already described are important. In analogue sampling devices, the deposited energy in each gap is also measured. This then introduces new sources of fluctuations :

- Landau fluctuations – from the long tail in the energy deposition in thin layers, due to δ ray emission
- path length fluctuations – due to low energy electrons which scatter at large angles and travel long distances in the sampling gap.

The electrons and positrons in a shower which deposit energy in the active layers can be considered to be minimum–ionising particles. The energy losses of minimum–ionising particles follow the *Landau* distribution: peaked at the most probable energy loss, and having a long high-energy tail. This then gives a contribution to the resolution of:

$$\left(\frac{\sigma(E)}{E}\right)_{Landau} = \frac{3}{\sqrt{N}\ln(1.3 \times 10^4 \delta E)} \tag{2.7.5}$$

where δE(MeV) is the energy loss per active plane.
The Landau fluctuations are small for δE in the range of a few MeV, e.g. planes of scintillator, but become comparable to the sampling fluctuations for very thin detectors, i.e. gaseous detectors where δE is a few keV.

With gaseous detectors path length fluctuations are also significant. Path length fluctuations are much larger in a gas than in a solid detector as:

1. the cut–off energy in gaseous chambers is lower than in other media, so the contribution of low energy electrons which deposit energy when travelling along the sensitive layers is greater
2. in the gaseous layers, multiple scattering is much less. Electrons have a long mean free path and can travel along the detector planes. In solid detectors they are quickly scattered back into an absorbing layer.

Monte Carlo calculations have been used to study these fluctuations, and to investigate schemes for reducing them to acceptable levels, several of which have been put into practice. Path length and Landau fluctuations dominate in gas–filled detectors, as demonstrated

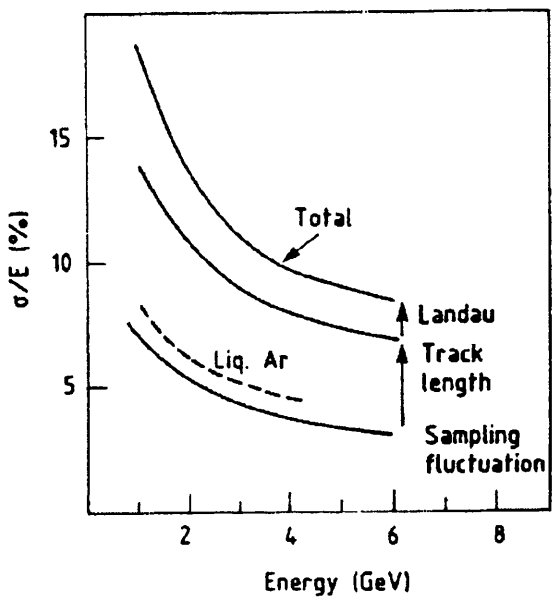

Fig. 2.7.2: Contributions of sampling, path length and Landau fluctuations to the energy resolution of a lead/MWPC sampling calorimeter. From [87].

in the paper by Fischer [87] in which an early version of EGS [90] is used to study the contributions to the resolution in lead/wire chamber calorimeters, see Fig. 2.7.2.

One remedy for reducing path length fluctuations is to stop those tracks which travel too far from the shower axis. If an array of proportional tubes is used, instead of a planar multiwire proportional chamber, the majority of the δ-rays are stopped by the tube walls, and electrons can escape away from the shower axis in one direction only. This approach was taken by Ludlam et.al. in an early device [88]. They include a Monte Carlo simulation which compares the contributions to the resolution in calorimeters with an array of tubes or planar chambers. This shows that the path length fluctuations are reduced in the former case. This is one reason why many gaseous readout calorimeters use arrays of proportional tubes. The use of high-Z gases such as Xenon (as used in the ALEPH calorimeter) will absorb δ-rays along the tube direction. The Landau fluctuations may be reduced by operating the proportional chambers at a higher voltage, in the region of partially saturated gain. Here, there is a shielding of the central wire by the high ionisation density, which reduces the large signals in the Landau tail. This has the disadvantage of causing non-linearity however. The gain chosen for the device will be a compromise between good energy resolution and non-linearity at high energy.

To summarize, Landau and path-length fluctuations dominate the energy resolution of sampling calorimeters with proportional counter readout and add in quadrature with the sampling fluctuations. See reference [89] for further discussion of these fluctuations.

2.7.6 Spatial Resolution

The spatial resolution of a calorimeter is limited by the lateral spread of the shower, which is mainly due to the multiple scattering of electrons. An electromagnetic shower consists of a dense core surrounded by a halo. The core disappears after the shower maximum. As discussed in 2.2.3, the scaling variable for the lateral distribution is the Moliére radius R_M. For two showers to be distinguishable, they have to be at least one Moliére radius apart. Approximately 90% of the total shower energy is contained within a cylinder of radius R_M, and 95% within $2R_M$. High-Z materials, such as lead, have larger R_M due to their lower critical energy, and therefore showers have a larger transverse width than in low–Z materials. In a solid block of lead, the Moliére radius is 1.5cm. This becomes wider when sampling gaps are introduced. The calorimeter must be as compact as possible to keep the Moliére radius small and avoid the overlap of adjacent showers. Accuracies of the order of millimetres on electromagnetic shower position are possible, even if the readout has a coarse granularity, e.g. lead–glass blocks. Higher spatial resolution can be achieved by using a MWPC or silicon strip detector embedded within the calorimeter at the depth of a few radiation lengths.

In a real device, the *granularity* of the readout cells is the factor determining the spatial resolution, (a device with a high granularity has many small readout cells). It is in this area of fine readout that wire chamber based calorimeters have a great advantage, as a large number of small cells may be read out without great complication. The position of electromagnetic and hadronic showers is obtained from the centre of gravity of the transverse energy depositions. If the granularity is adequate, the resolution is dominated by the signal/noise ratio, and therefore improves with increasing energy.

Hadronic showers similarly have a narrow core, surrounded by a halo several times the core diameter. Measurements of the spatial resolution of the impact point of hadronic showers, for example [63], may be parameterized as: $\sigma_{vertex}(cm) \simeq \langle\lambda\rangle / \left(4\sqrt{E\mathrm{GeV}}\right)$. Spatial resolutions of a few centimetres at 1 GeV are possible, reaching a few millimetres at 100 GeV.

2.8. Computer Simulations

It is the normal practice to simulate calorimeter performance by Monte Carlo computer models before prototyping or construction. Exact analytical solutions for any radiation transport problem involve sets of coupled differential equations which may well be very difficult or impossible to solve except under very simple approximations. The mathematics are complicated, and the results only apply in the longitudinal direction. Three dimensional shower theory is even more complicated.

Monte Carlo simulation is obviously a much better way of investigating shower behaviour, as all of the fundamental processes are included, complex geometries may be used and other minor processes of interest may be added. Another fundamental reason for using Monte Carlo is the intrinsically random nature of showers. Since showers develop by quantum processes, each shower is different. For applications where only summations over many showers are of interest an analytical solution is sufficient. However, for most situations in high energy physics, e.g. calorimetric measurements of single high–energy particles, the shower by shower fluctuations are important. Analytic solutions for such situations would need not only the computation of the mean values, but quantities such as the probability that a certain amount of energy is deposited in a given volume of material. Such calculations are obviously next to impossible, so the Monte Carlo method must be used. Computer simulation also allows the experimenter to 'try out' different techniques and materials to see if they achieve the design and cost goals, without going to the time consuming and expensive process of building a complete device.

The standard code for electromagnetic calorimeter simulation is the EGS4 code system [90]. EGS is a system of computer codes for the simulation of electromagnetic showers produced by electrons and photons in an arbitrary geometry. EGS4 can track photons down to 10 keV and electrons to rest. It has been well tested, and gives very accurate results (at least for the present energy ranges). The EGS code system is used with the GEANT detector simulation package at CERN [91]. Of course, the results from simulation must be checked against real data. In [92] Del Peso and Ros investigate the energy resolution of EM sampling calorimeters using EGS4. They study how the energy resolution depends on the shower energy, absorber thickness, sampling layer thickness and on materials used in construction. A comparison of Monte Carlo results with data shows that the intrinsic resolution of most calorimeters is well reproduced by Monte Carlo, but that very often instrumental effects (e.g. noise) worsen the resolution, and these cannot be predicted.

The simulation of hadron calorimeters is more difficult, as it involves simulation of complex, low-energy nuclear phenomena. Several programs have been developed to simulate the particle production in the hadronic cascade. These require careful tuning to ensure agreement with the data. The proceedings of the LEP workshop on shower simulation [93] contain extensive discussions of the use of the codes TATINA, GHEISHA, CASCADE84, EGS, FLUKA, HETC and the CERN detector simulation package GEANT. This workshop is mainly concerned with shower simulation for the four LEP detectors, but there is also discussion of the UA1 experiment, and applications in radiation shielding and dosimetry. For a description of the simulation methods used for the ALEPH electromagnetic calorimeter see 4.3.1.

2.9. Monitoring and Calibration

The present generation of calorimeters are large, complex devices with many tens of thousands of readout channels. At the high energies now being investigated i.e. of tens to hundreds of GeV, the intrinsic shower fluctuations are of the order of only a few percent. The excellent intrinsic resolution can only be utilized effectively if care is taken with the absolute calibration of the device, and the relative calibration of each channel. The difficulties of calibrating and maintaining the stable operation of a large detector over long periods of time become very important. Monitoring of all the components with an accuracy at the 1% level is needed. The success of a calorimeter installation can depend on the strategy and devices chosen for the monitoring of performance. Calibration and monitoring of a calorimeter follows several stages.

The first stage is a primary calibration in a test beam. A number of the calorimeter modules are exposed to beams of muons, electrons, pions and protons of known energy. This gives the absolute energy scale, the e/π ratio, the energy resolution and the linearity. A scan of the test beam over the face of a module measures the channel-to-channel variations. Ideally, all calorimeter cells would undergo this primary calibration. However, this is not always possible, and a combination of test beam calibrations of selected modules plus cosmic ray muon runs (or some other technique) on all modules is often used to transfer the calibration to all modules.

When the experiment is running, a monitoring system is used to give a reference signal to transfer the energy scale from test beam measurements to the running experiment and to track the stability of calibration over the months or years during which the experiment is

running. Types of monitoring system depend on the type of calorimeter, which splits into two broad classes: photon–collection or charge–collection types.

Calorimeters having optical readout methods are troubled by two main complications: light collection is inherently non–uniform requiring elaborate correction methods; photon detectors with internal multiplication (photomultipliers as opposed to vacuum phototriodes) require cumbersome calibration procedures. The light output of scintillator based calorimeters decreases with age and radiation exposure; the latter is likely to have a non–uniform effect. In such calorimeters a stable light source is often used for stability measurement. Radioactive sources coupled to a scintillator or a standard calibrated light source may be used. Many calorimeters use a system consisting of a photodiode or laser light source coupled to each photomultiplier by fibre optics. Another technique is to scan intense radioactive sources across the face of the calorimeter.

A recently devised technique is to use periodically a small radio–frequency quadrupole based accelerator within the detector to give a low energy calibration beam. In the system developed by CalTech for the L3 experiment [9-4] there is a small RFQ accelerator mounted within the detector. A proton beam from the accelerator is directed onto either a lithium or CaF_2 target, producing a photon beam which is used as a calibration source. This can give an absolute calibration of the L3 BGO calorimeter to an accuracy of 0.7% within a few hours, or a relative calibration to 0.4% within minutes. Of course, this technique is useful only for scintillator based calorimeters. In the future, neutron emitting targets may be used for the calibration of large hadron calorimeters.

The deposition of energy by cosmic rays may be used for a monitoring signal. At e^+e^- colliders, large–angle Bhabha scatter events give a signal with a well–known energy.

Uranium based calorimeters may use the background radiation from the uranium as a standard reference. For instance, the L3 hadron calorimeter uses the uranium noise spectrum to obtain a gain per channel to within an accuracy of 2%.

In those detectors using ion chamber readout, i.e. liquid argon or room temperature liquids, excellent uniformity of response is obtained by close mechanical tolerances in construction and long term stability depends on the purity of the liquid. A precision pulse generator may be used to inject known charges into these devices and so monitor stability. A precision of 0.5% in calibration is typically achieved with these devices.

In fixed–target experiments, a beam of known energy may be swept across the face of the calorimeter to give a relative cell–to–cell comparison.

Finally, it may be possible periodically to re-calibrate a module in the test beam, although this does take time and effort and may be done at intervals of years if at all.

It has proved possible in many devices to maintain the calibration to the 1–2% level. References [95–97] give descriptions of the problems encountered in the calibration and monitoring of typical calorimeters, viz. a neutrino experiment and two lead-scintillator calorimeters.

2.9.1 Uniformity and Stability in Wire Chamber Based Calorimeters

Calorimeters having gas gain type readouts must be exceedingly carefully constructed to control the numerous effects which contribute to the non-uniformities and gain variations. The mechanical effects which cause variations in gain are wire diameter variation, wire displacement, transverse gap variations and variations in the distance between proportional tubes and resistive pads. Using a rectangular geometry for the wire chamber tubes minimizes the dependence on cell dimensions, and this is the type chosen by most collaborations

Calorimeters using wire chamber readouts also have to cope with long term global gain variations due to changes in the gas gain caused by impurities in the gas, fluctuations in the gas composition, pressure, temperature and high voltage. In carefully constructed devices gain variations of $\sigma \approx 5\% - 10\%$ are reported. Averaging of the gain non-uniformity over the dimensions of a shower will reduce these variations to a level which should not in most cases affect the performance of these devices. High voltage, gas flow and gas composition have to be controlled to the necessary precision of several parts in a thousand. Calibration is done with test beams and elastic scattering events. Penetrating muons may also be used. The global gain variations due to the gas conditions may be monitored by a set of monitor chambers containing radioactive sources, which sit in the gas volume [98–99]. The CDF endplug and forward calorimeters use Fe^{55} sources in monitoring tubes to track the gain changes to within 2%. Using an Fe^{55} source installed on each pad the gain of the DELPHI HPC is controlled to within 1.5% [100]. The ALEPH electromagnetic calorimeter also uses Fe^{55} monitoring sources, as described in 5.4. An intercalibration among modules is also made using radioactive ^{83m}Kr gas.

At the Fermilab workshop in 1982, Mishina [84] gave typical values for the various contributions to the gain variations, as shown in Table 2.9.1. It may be concluded that there is, in principle, no fundamental barrier to the high-precision performance of gaseous readout devices. The careful construction methods used by the ALEPH collaboration for

the electromagnetic calorimeter, discussed in 5.2, were designed to result in a device with a uniform response. The various factors influencing the uniformity and stability of this calorimeter are discussed in detail in 5.4.

Parameter	Measured Tolerance	Measured gain change	Standard Regulation	Corrective Procedure
tube cell size	1.4%	4–5%	device dependent	scan across
wire diameter	1%	5–7%	0.5% tolerance	surface with
wire displacement	3%	1%	device dependent	showers
high voltage	±1 volt	0.9%	within 0.1 volt	monitor using
gas temp.	$\pm 1°C$	2.5%	within $0.1°C$	mips or
gas pressure	1 %	8%	device dependent	radioactive
gas composition	device dependent	device dependent	within 0.5%	sources

Table 2.9.1: Effects of Mechanical Tolerances and Operating Parameters

Careful attention must also be paid to mapping and dealing with non–functioning read-out channels. In a calorimeter, dead channels have a much more serious impact than in a tracking chamber: in a tracking device, a dead channel will slightly affect the accuracy of measurements on an otherwise well constrained track; in a calorimeter, missing channels lead to systematically wrong measurements of showers near to that point.

Chapter 3.
LEP and the ALEPH Detector

'Depression is for the middle classes. The rest of us have an early start in the morning.' – Riff Raff

3.1. The LEP Accelerator

The Large Electron Positron Collider (LEP) [101–102] is situated at the CERN laboratory near Geneva in Switzerland. The LEP project was first conceived at CERN in 1976 when two study groups were formed to investigate the feasibility of a large electron–positron storage ring [103–104]. After undergoing several re–designs [105–106] the accelerator was finally approved for construction in 1981. The construction of LEP began in September 1983 and was finished in July 1989. The first positron beam circulated successfully in LEP on the 14th of July 1989 and the first collisions producing Z^0 were achieved during a pilot run in August 1989. A good review of the design, construction and operation of LEP over the first year's running may be found in [107].

The LEP complex, shown in Fig. 3.1.1, is situated below the plain between Geneva airport and the Jura mountains. LEP is a very large facility consisting of the main storage ring, eight underground experimental caverns, purpose built injector stages, the CERN Proton Synchrotron (PS) and Super Proton Synchrotron (SPS), plus beam transport lines, and a large infrastructure of power supplies, cooling water, gas supplies, cryogenics etc.

3.1.1 Injectors and Pre–injectors

Electrons for LEP are generated by an electron gun, and positrons from the collision of the electron beam with a tungsten convertor foil. The particles go through several acceleration stages before stable colliding beams are available in the experimental areas.

The first stage of acceleration occurs in the LEP Injector Linacs (LIL) which are two linacs in tandem, producing electrons at 400 MeV and positrons at 600 MeV. The electron and positron bunches are stacked in the Electron Positron Accumulator ring (EPA). The EPA ring acts as a buffer between the fast cycling LIL and slower PS.

The next stage of acceleration uses the CERN Proton Synchrotron (PS) as a 3.5 GeV e^+e^- accelerator. The PS was one of the first machines built at CERN in the 1950s, and is still in use in its original role as a 28 GeV proton accelerator, an injector for the LEAR

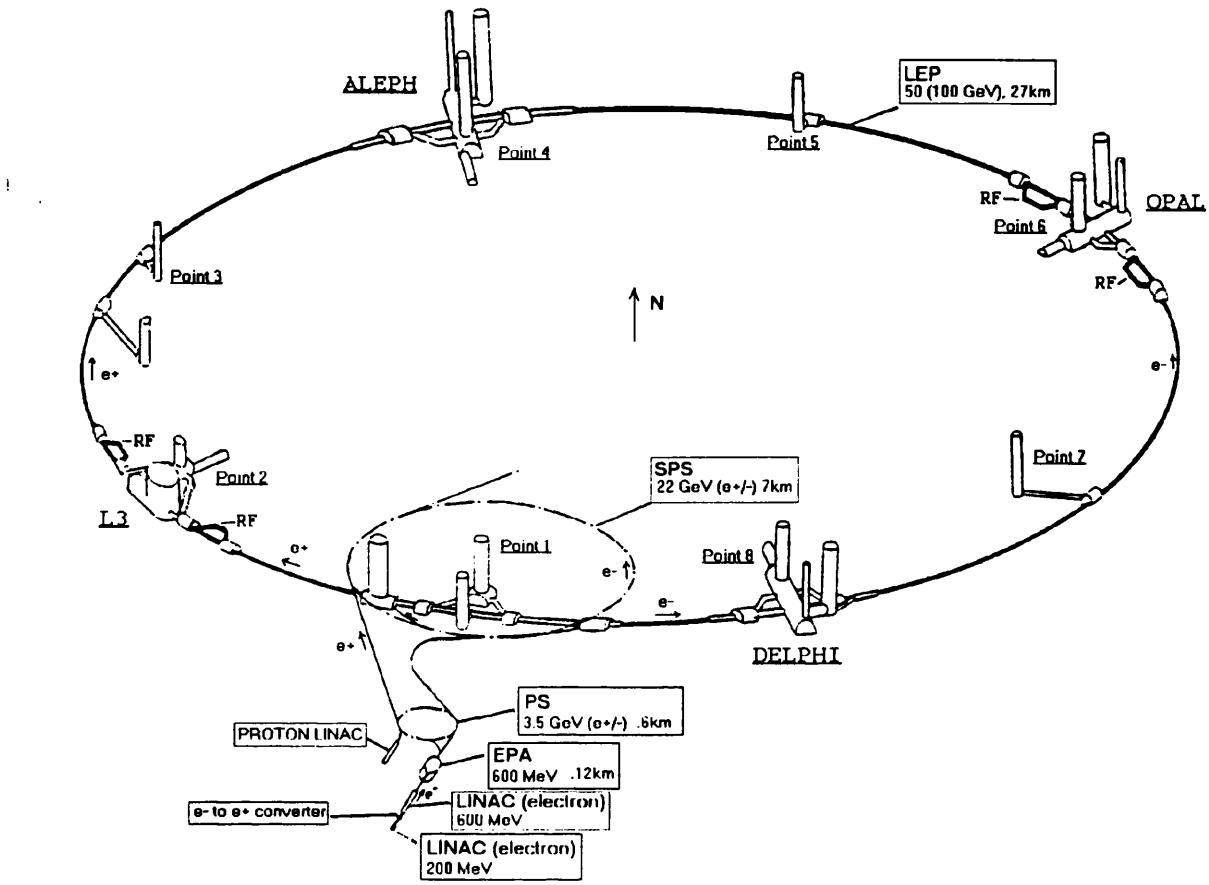

Fig. 3.1.1: The LEP Complex.

anti-proton ring, an injector for the SPS and as part of LEP (a role for which it was not originally designed). The next accelerator in the chain is the SPS which acts as a 20 GeV injector for LEP. The SPS was originally commissioned in 1976 as a 450 GeV proton accelerator. In addition to its original use in fixed target physics, the SPS has been used as a proton/anti-proton collider, a heavy ion accelerator and as an e^+e^- accelerator for LEP. For LEP running, the PS and SPS operate in a multicycle mode: an accelerator cycle has been developed which allows four e^+e^- cycles followed by a proton cycle. So LEP running has little impact on the normal SPS fixed-target operations, which can run in parallel. The decision to make use of two large accelerators already in place at CERN saved the LEP project a large amount of money and time.

After accumulation of the beams in LEP, the energy is ramped up to the collision energy of around 45 GeV per beam. The superconducting quadrupoles at the experimental points are adjusted to squeeze the beams, the energy is held constant and the experiments take data over a period of several hours. Barring a catastrophic loss of the beam, the intensity decays away slowly, due to losses by collisions and instabilities of the beam. At a certain point, a decision is then taken to dump the beam and refill.

3.1.2 The LEP Ring

The LEP ring is in the shape of an octagon with rounded corners, having eight straight sections where the experiments and RF power installations are located. The LEP tunnel is 3.8 metres wide, varies in depth from 50 to 150 metres and is 27 kilometres in circumference.

This enormous size is required in order to reduce the synchrotron radiation losses from the circulating electron beams. Synchrotron radiation is the radiation emitted by charged particles travelling on a curved trajectory. The energy lost per turn as synchrotron radiation by a charged particle in a circular accelerator is:

$$\Delta E = \frac{4\pi}{3} e^2 \beta^3 \frac{E^4}{r} \tag{3.1.1}$$

where :
- e : electron charge;
- β : velocity;
- E : total energy;
- r : radius of accelerator.

Synchrotron radiation losses dominate the power requirements for electron machines, as the particle mass is small. There is a compromise between the costs of accelerator components and the civil engineering works on the one hand, and the expense of extra RF components and electricity costs to counter the synchrotron losses on the other. The large radius chosen is the result of this compromise.

The accelerator has counter–rotating beams of electrons and positrons in the same vacuum vessel. The vacuum vessel is lead–coated to absorb the intense synchrotron radiation. The magnetic field guide and beam focusing system of LEP is comprised of several different types of conventional magnets. The machine lattice has 3368 dipole bending magnets, 816 quadrupoles, 248 focusing sextupoles and 256 defocusing sextupoles. Each of the eight arcs of the machine is comprised of 31 'standard cells' of magnets grouped in the following order: a defocusing quadrupole, a vertical orbit corrector, six bending dipoles, a focusing

sextupole, a focusing quadrupole, a horizontal orbit corrector, six bending dipoles and a defocusing sextupole. The dipole magnets are of a unique design with a core of steel laminations interspersed with concrete. This produced a cost saving of around 40% compared with conventional solid steel cores. The maximum dipole magnetic field at LEP I is 0.059 Tesla.

The design beam current is 3mA, with the beams concentrated in 4 bunches, each a few centimetres long and a few millimetres high and wide. However, the collision points in LEP are arranged as so–called low–β points, where the beams are squeezed by super–conducting focusing magnets to a size of fractions of a millimetre, hence increasing the *luminosity*. The number of interactions occurring per second is given by the product of the cross–section for that particular reaction, multiplied by the luminosity, i.e. $N = L\sigma$. The luminosity at a collider depends on the number of 'bunches' of particles in each beam, the number of particles per bunch, the revolution frequency (i.e. the time between bunch crossings– which is $22\mu s$ at LEP), and the size of the beam spot at the collision point. The luminosity in LEP is given by the expression :

$$L = \frac{n_e n_p k f}{4\pi\sigma_x\sigma_y} \qquad (3.1.2)$$

where:

n_e,n_p are the number of particles in each bunch of electrons and positrons;
k is the number of bunches in each beam;
f is the revolution frequency;
σ_x and σ_y are the horizontal and vertical r.m.s beam radii at the collision point

Using data from the 1991 LEP running, a study was made by ALEPH [108] which used the mini–vertex detector to measure the primary Z^0 decay point for selected $Z^0 \rightarrow \mu^+\mu^-$ and $Z^0 \rightarrow e^+e^-$ events. The size of the beamspot in the horizontal plane was found to be $142 \pm 2\mu$m and less than 8μm in the vertical.

3.1.3 Radio–Frequency System

The bending radius is the most critical parameter in the minimization of RF power. The LEP accelerator was designed such that the W pair production energy of around 90 GeV per beam could be reached by using only conventional room–temperature RF cavities. The constraints of the number of cavities needed for this, the maximum power of cavities then available, and the length of straight section needed to house them gave the LEP circumference of 27km. At LEP I, with a beam energy of around 50 GeV, there are 128

conventional RF cavities. The RF power, at a frequency of 352 MHz, is provided by 16 klystrons each of 1 MW.

A large amount of effort has since gone into the development of superconducting RF cavities, where there is essentially no energy loss in the RF cavities. These are currently in use in the SPS, and will be used at LEP II. The present option for upgrading to LEP II involves installing 192 superconducting cavities, with an increase of only 12 MW in the RF power.

3.1.4 Future Plans for LEP

At the moment, the LEP accelerator has an energy of up to 50 GeV per beam, and is known as 'LEP I'. As discussed in section 1.3.1, the experiments at this energy concentrate on the properties of the Z^0 boson.

However, LEP is currently incapable of reaching its design luminosity. The maximum current per bunch is limited to 0.5mA, due to couplings between the synchrotron and betatron oscillations of particles within a bunch. The couplings are caused by a thin ($\sim \mu$m) layer of nickel deposited on the beam pipe at manufacture, which has become magnetized. The nickel layer was used by the manufacturer to bond on the lead coating already mentioned. The luminosity at LEP would be substantially increased if there were more bunches per beam than the current four. However, this would result in collisions at the odd–numbered interaction regions, which is undesirable due to beam–beam interactions. To avoid this, the beams are separated at these points by electrostatic separators, in what is known as a 'pretzel' scheme. It is planned to increase the number of bunches to eight per beam during the 1992 running. Increasing the number of bunches will also necessitate changes in the triggering and readout sequences of the detectors.

It would also be possible to arrange for the beams at LEP to have longitudinal polarization, which would enable very precise measurements of the weak couplings of the Z^0. However, with the very good results already achieved by the LEP experiments, the physics needs for polarized beams are far from clear and there are no plans to install the necessary equipment in LEP.

In the late 1990's, LEP is due to be upgraded in energy to the 'LEP II' configuration, with up to 100 GeV per beam and a design luminosity of $2.9 \times 10^{31} cm^{-2}/sec$. At LEP II there will be sufficient energy to create W^+W^- pairs, and the physics of these particles will be under intense study.

3.2. The LEP Detectors

LEP was constructed with eight experimental areas where the beams may be made to collide. Four of these house experiments : ALEPH (A detector for LEP pHysics), DELPHI (Detector with Lepton, Photon and Hadron Identification), L3 (Letter of Intent number 3) and OPAL (Omni Purpose Apparatus for LEP). The detectors are general–purpose devices, but each experiment has a different emphasis, which is reflected in the detector elements used. The DELPHI experiment is the most technologically sophisticated, and is the only one to use Ring Imaging Cherenkov (RICH) detectors for particle identification. It also should have excellent calorimetry with its High density Projection Chamber (HPC) device. The OPAL detector is the most conventional of the LEP detectors: it has a warm iron solenoid, and uses lead-glass detectors for calorimetry. The L3 device is the largest, and concentrates on precision measurements of photons, electrons and muons with a resolution of 1%. The ALEPH apparatus will be discussed in detail in section 3.3 and subsequent sections of this chapter.

The usual form chosen for a detector at a colliding beam machine is that of a cylindrical barrel section, closed by two end–caps. The tracking devices which measure the trajectory of particles are the first layer surrounding the beam pipe. These devices aim to measure the initial trajectories of the charged particles from the interaction point. As the particles will scatter from any material in their path, this implies that vacuum beam pipe and all the inner detectors ought to have as low a density of material as possible. Next come destructive detectors where the particles collide with the detector and the signals from this are detected.

All four LEP experiments have a large axial magnetic field to bend the particle tracks for momentum measurement and to separate the particles in a jet on entrance to the calorimeters. The OPAL experiment has a normal warm coil, as this was proven technology. Their 0.4 Tesla coil is within the calorimeters. The L3 experiment, with its emphasis on high–precision muon tracking built a very large 12 metre diameter warm coil, with a field of 0.4 Tesla. The ALEPH and DELPHI experiments use superconducting coils of 1.5 and 1.2 Tesla respectively, which are outside the calorimeter layer. Both of these experiments use time projection chambers, which depend on a uniform axial magnetic field.

Measurements of the trajectories of charged particles are obviously important, not only for momentum determination, but also for jet studies and for searching for neutral vertices. Small and very precise tracking devices called vertex detectors are placed close to the beam

pipe. In OPAL, this device is a wire chamber with a position resolution of 50μm. ALEPH and DELPHI use silicon micro–strip based devices with a position resolution of around 5μm. The vertex detectors will be used to study the secondary decay vertices of short lived particles. The next layer is the tracking chambers proper, which need to be a metre or more in diameter, in order to measure the bend in the trajectories of particles up to 100 GeV. ALEPH uses a combination of an inner drift chamber (ITC) plus a large time projection chamber. DELPHI also uses a time projection chamber, OPAL has a more conventional wire jet chamber and L3 has a device known as a Time Expansion Chamber, similar to a TPC.

The next layer is a calorimeter to measure charged and neutral energy. The electromagnetic calorimeter chosen for the OPAL detector uses an array of 10 x 10cm lead glass blocks where the Cherenkov light from showering particles is measured by vacuum photo–triodes. The L3 calorimeter uses a similar technique, using 2×2 cm Bismuth Germanium Oxide (BGO) crystals. The superior properties of BGO make this the most precise and compact of the four calorimeters, but also the most expensive. ALEPH has a sampling calorimeter made of lead sheets interspersed with proportional wire chambers. The DELPHI device is the ambitious High–density Projection Chamber. Lead sheets are used as an absorber, and the ionisation signal is drifted along the sampling gaps to an end plate detector, rather in the fashion of a drift chamber. This device gives highly detailed information on the shower development. Table 3.2.1 gives the performance figures for the calorimeters from test–beam results.

	Energy Resolution $\sigma E/E$ (%)	Position Resolution (mm)
ALEPH	17	2.5
DELPHI	23	3–10
L3	3	3
OPAL	5	3.7

Table 3.2.1: Performance data on the LEP EM Calorimeters

The energy and position of photons is measured by the showers in the electromagnetic calorimeter. Calorimeters are usually segmented laterally to improve spatial resolution. Adjacent segments with deposited energy above some threshold are grouped together offline

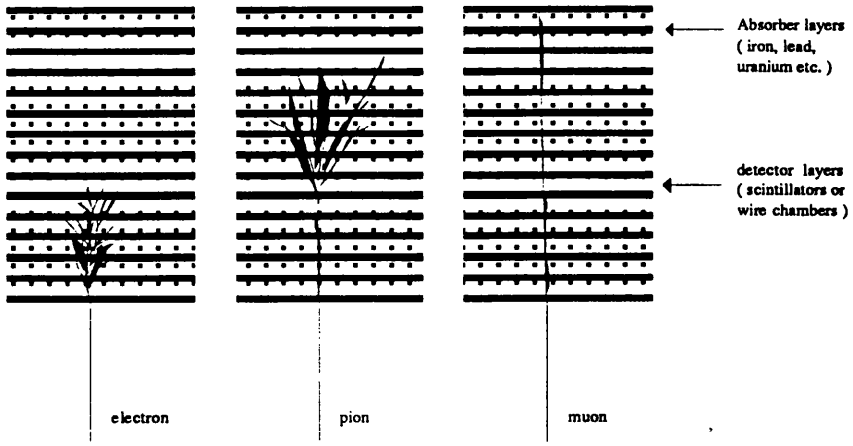

Fig. 3.2.1: Idealized Particle Interactions with a Calorimeter

to form clusters: photons are defined as energy clusters which have no charged tracks pointing at them. If the detector is longitudinally segmented then the depth development of the shower can be used to identify and reject showers from neutral hadrons, e.g. neutrons and K^0, which have much longer showers than photons and tend to start further into the calorimeter. Once the photons have been isolated then the invariant mass of photon pairs can be computed to search for $\pi^0 \to \gamma\gamma$ and $\eta \to \gamma\gamma$. As there are typically 6 π^0 per event, there are $\sim$ 60 wrong combinations in the background. The number of π^0 or η is obtained by fitting the invariant mass spectrum with a Gaussian plus background. The width of the Gaussian depends on the detector resolution. Additional cuts may be necessary to obtain a reasonable signal to background ratio. Most photons come from π^0 decay and their x distribution peaks at low values. There is a tail of high-x photons from initial state photon radiation: the distribution of these photons can be used to check the radiative photon generators used by the Monte Carlo programs.

After traversing the coil and the ECAL layers most hadronic particles have not started to shower. More interaction lengths of material are needed to stop and measure these. In the ALEPH, DELPHI and OPAL experiments the iron structure of the flux return from the magnet has been instrumented as the hadron calorimeter. The L3 experiment uses a uranium-scintillator calorimeter around the BGO electromagnetic calorimeter.

Muons are identified as those particles which penetrate all the detector layers. A fit connecting these external tracks with the central tracking chambers is required: this is done in the cases of ALEPH, DELPHI and OPAL by using tracking chambers covering the outer surface of the detector. In the L3 detector the muons are tracked within the very large

magnet using three layers of very precisely positioned wire chambers which have a position resolution of 40μm.

The identification of particle types is important as, for instance, leptons can be the signature of super–symmetric decays or are used to identify heavy quark decays and the separation of kaons from pions is useful in reconstructing resonances. The ability to distinguish leptons within a jet of particles is highly useful and leads to a requirement for devices with high granularity. The separation of muons, hadrons, electrons and photons is achieved by their distinctive patterns of energy deposition in the calorimeters. The identification of the other charged particles: pions, protons and kaons, may be done on the basis of their rate of energy loss (dE/dx) in the tracking chambers.

The DELPHI experiment uses a Ring Imaging Cherenkov detector, introduced in section 1.8, to supplement dE/dx information.

The following types of 'particles' are seen in a typical detector at an e^+e^- collider:

electron	electrons and positrons are seen as charged tracks in the central track chambers (the track curvature giving the momentum and the sign of the charge). They are also recognized by the pattern of energy deposition in the calorimeter. Fine–grained calorimetry is important for disentangling the signals of electrons close to jets.
muon	a muon is recognized as a charged track in the central trackers which matches with signals in the outer muon chambers
photon	gammas appear as an electromagnetic calorimeter cluster with no charged track pointing to it
tau	a tau decay is recognized by its low–multiplicity topology.
high energy jet	which is seen as a set of associated tracks or as a large cluster of energy in the calorimeters, which is interpreted as coming from a quark or gluon (or possibly several collinear partons) which has fragmented into the visible particles. The vector sum of the tracks and calorimeter cell hits gives the energy and direction of the original particle.
missing p_T	It is important to have a hermetic coverage over the solid angle. If the components of momentum transverse to the beam are measured for all visible particles, any imbalance

can be attributed to penetrating neutral particles which do not interact. These are normally neutrinos, but for example could be a signature for supersymmetric particles.

Accurate measurement of the luminosity is important for measurement of cross-sections and widths. At e^+e^- machines, luminosity is measured by counting the numbers of Bhabha events. The angular distribution for these is strongly forward peaked and so very forward detectors are needed here, and the experiments have opted for a configuration involving some sort of tracking device backed by an electromagnetic calorimeter.

As soon as possible after the bunch crossing the trigger system makes a decision to read out all the channels in a detector and write the data to tape. A typical detector will have up to a million readout channels. The signals are collected, amplified and multiplexed as close to the detector as possible, then sent along cables to the electronics barracks. Here, the data acquisition system, based on the CAMAC, VME or FASTBUS standards digitises and processes the signals, from where they are sent to the on-line computers to be assembled into complete events and written to tape.

In the offline analysis, an attempt is made to reconstruct the four-vectors of the original particles producing the signals seen in the detector. Selection cuts are applied to search for and count specific types of events. The LEP detectors are expected to record several million interactions over their working lifetimes. A similar volume of Monte Carlo events will also be needed. This implies a need for large computing resources to store and analyse these events, both at CERN and in the home laboratories. CERN has installed a CRAY XMP-48 supercomputer, partially for LEP data analysis. There is also a six-processor IBM mainframe with a very large amount of disk space and tape drives. The experiments themselves are running private computer analysis facilities, with L3 having a private IBM mainframe, and ALEPH opting for a large cluster of VAX workstations.

3.3. The ALEPH Detector

The ALEPH experiment is at LEP interaction point number 4, which is 143 metres below ground level near the village of Echenevex. The ALEPH detector was designed as a general purpose detector to measure events at up to 200 GeV centre of mass energy. These events are complex, with typically 40 particles being produced over the entire sphere around the interaction point. An ideal detector, which measures the momentum and charge of each particle in an event perfectly, identifies it unambiguously, and hermetically covers the whole

region around the interaction point is impossible to construct. The ALEPH detector was designed to satisfy the following goals, with compromises being reached on each one in order to have the best overall detector:

- 4π acceptance
- detector size optimized for the operating energy
- good spatial separation of particles in jets
- a high magnetic field for accurate momentum measurement of charged particles
- fine grained calorimetry for energy measurement of neutrals
- identification of electrons and muons
- identification of hadrons
- good measurement of very short-lived particles

The design of the detector has been influenced by the expected physics processes of interest at LEP and LEP 200, for example :

electroweak physics	precise measurements of the weak couplings of the individual quarks and leptons are needed to test the standard model to its limits. To achieve these measurements for the heavy quarks good electron and muon identification and a π/e rejection efficiency of $\sim 10^{-3}$ are needed. For short-lived heavy hadron reconstruction, e.g. $D^0 \rightarrow K^-\pi^+$, good mass measurement and kaon /pion identification is needed.
new particle searches	for example Higgs production via the processes $Z^0 \rightarrow H^0e^+e^-$ and $Z^0 \rightarrow H^0\mu^+\mu^-$. The detector is designed to identify both the leptons and the jets from such events, and to separate the leptons within jets so that H^0 decays can be fully reconstructed, up to a limit of around 40 GeV on the H^0 mass.
W physics at LEP 200	ALEPH has been designed to study e^+e^- events up to the highest LEP energies: it has good momentum measurement at high energy for asymmetry measurements, and hadron calorimetry for measuring jet–jet invariant masses.

Calorimetry which has coverage over nearly all of the solid angle around the interaction is important as gaps could fake genuine missing energy signals. An importance has been placed on good lepton identification ('good' meaning both high efficiency and low background) as electrons and muons have often been the signature of new physics in the past.

The letter of intent setting out the design for the detector was submitted in January 1982. The original concept of ALEPH also contained the proviso that no sub–detector was to use scintillator readout, with its problems of photomultiplier drift, radiation aging of scintillators and the problems of operating photomultipliers in a magnetic field. All of the major sub–detectors opted for gaseous wire chamber read–out. The exceptions are the silicon–based mini–vertex detector and the low–angle BCAL which uses scintillators.

The remainder of this chapter describes the overall layout of the detector, its relationship to the LEP accelerator and has detailed descriptions of each of the sub–detectors. The ALEPH technical reports and the ALEPH Handbook [109–111] contain more detailed information on the detector.

The detector, Fig. 3.3.1, is built as a series of concentric cylinders, with two 'end–caps' covering the end regions. The whole detector is mounted on a system of rollers which enable it to move on rails along the floor of the experimental hall from the 'garage' position to the data taking position on the LEP beam. The end–caps can also be moved outwards to permit access to the inner detectors. Electronics and services barracks are on either side of the detector. Once in place, each of the sub–components of the detector is surveyed with a high accuracy to determine its position relative to the overall ALEPH reference frame. These coordinates are then used in the reconstruction software to improve the accuracy of tracking. The coordinate system for the ALEPH detector is defined as follows :

the origin is at the nominal interaction point;
the z–axis is along the LEP tunnel e^- direction (which is anticlockwise from above);
the x–axis points towards the centre of LEP;
the y–axis is upwards;
the spherical coordinate angles are θ (rotation around the x–axis), and ϕ (rotation around the z–axis)

This coordinate frame is in fact tilted slightly with respect to the vertical, as the LEP tunnel dips.

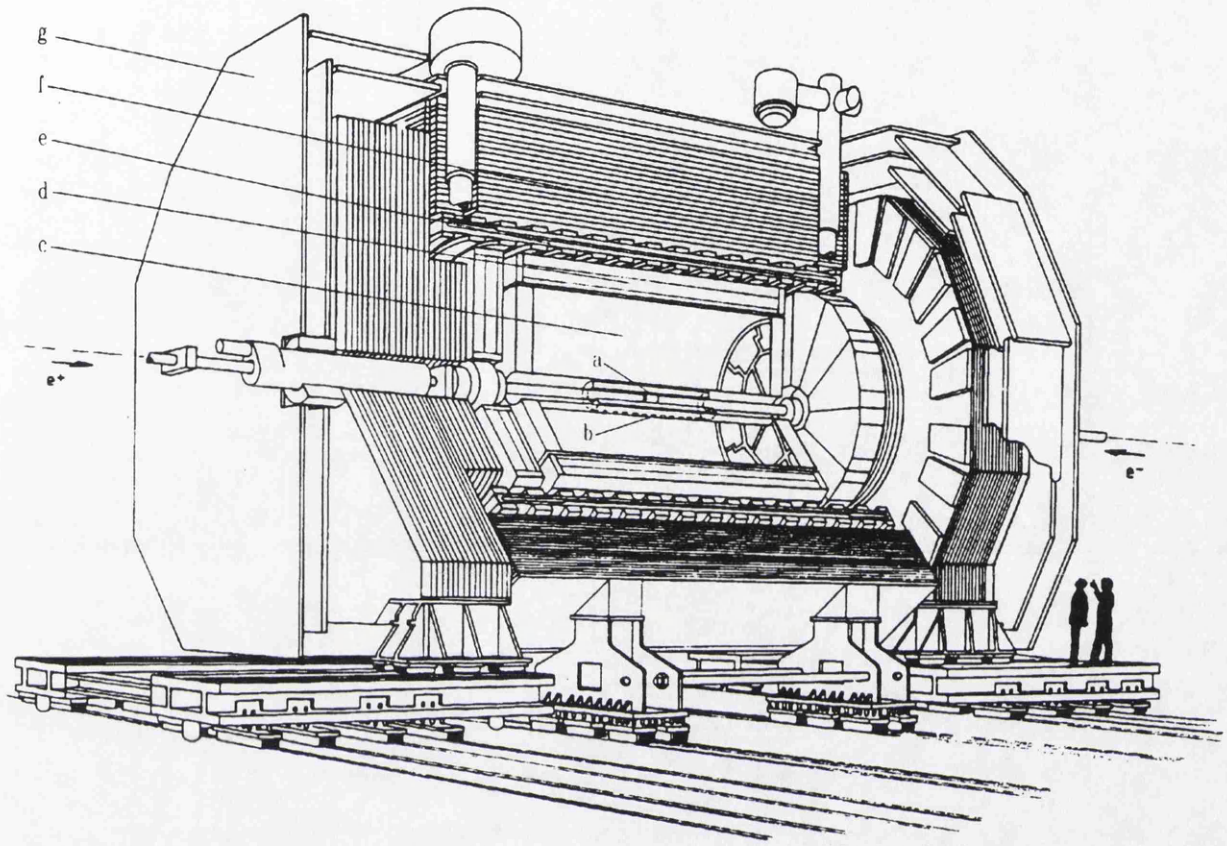

a – vertex detector
b – inner tracking chamber
c – time projection chamber
d – electromagnetic calorimeter
e – superconducting coil
f – hadron calorimeter
g – muon chambers

Fig. 3.3.1: The ALEPH Detector

3.4. Beam Pipe

Going radially outward from the interaction region, the first component is not an active part of the detector, but the beam pipe. The beam pipe section through the ALEPH detector is 5.5 metres long and 16cm in diameter. The diameter of the beam pipe is chosen to be as small as is practicable without increasing backgrounds from the beams striking

the walls. The beam pipe has 0.5 mm walls and is made of an aluminium alloy in order to present the least possible density of material before the first active layers of the detector. This material must be kept to a minimum because of conversion of γ's to e^+e^- pairs and energy loss or multiple scattering of charged particles. A carbon fibre support structure for the mini vertex detector is also placed on the beam pipe around the interaction region. For the 1991 running, a smaller 11cm diameter beryllium beam pipe was installed.

The beam pipe extends between the two quadrupole magnets on either side of ALEPH. As already discussed in 3.1.2, these superconducting low-β magnets serve to focus the beams on the interaction point.

3.5. Mini Vertex Detector

The mini vertex detector [112] consists of an array of silicon strip detectors placed around the beam pipe as shown in Fig. 3.5.1. The vertex detector is intended to help in the studies of production and decay properties of short-lived particles by improving the accuracy of impact parameter measurements and resolving secondary vertices close to the interaction point. During the 1989 running this detector had only one set of wafers installed for test purposes and the data were not read out. For the 1990 running the original version of the detector was installed and the data read out for many runs, but problems were encountered. When the smaller diameter beam pipe was installed for the 1991 running, a new version of the detector was built.

The apparatus consists of two cylindrical barrel layers of double sided detectors: the inner one has 9 faces of detector chips at 6.3 cm from the interaction point, and the outer 15 faces at 10.7 cm. Both layers are 20 cm long. The faces are arranged to overlap to allow full ϕ coverage. The device covers an angular range in θ of $\pm 58°$ for the inner layer and $\pm 44°$ for the outer. Both layers together cover 74% of the solid angle.

Each silicon wafer has readout strips on a 100 μm pitch, parallel to the beam on one side, and at right angles on the other side enabling a position measurement from the charge centroid. This two-sided readout scheme reduces both the number of modules needed and the amount of scattering material near the beam pipe. Readout is by a specially developed 64-channel CMOS VLSI analogue amplifier chip, CAMEX64A. This gives a high gain, low noise operation with low power consumption and fast switching, which is vital for a device mounted in a small space in the centre of ALEPH. The mini vertex detector has a total thickness of about 4% of a radiation length at $\theta = 90°$. The device has been very carefully

constructed with respect to the spatial accuracy and positioning of the strips. Once in place in the centre of ALEPH, the final positions of all the detector wafers were determined by using extrapolations of tracks measured in the ITC and TPC.

The device has a position resolution for single muon hits of $\sigma_{r\phi} = 12\mu$m and $\sigma_z = 13\mu$m. A preliminary measurement of the impact parameter resolution gives $\sigma = 26\mu$m in $r\phi$ and $\sigma = 34\mu$m in z. The capabilities of the device for precision vertex finding, and for finding the beam centroid, will be fully exploited in studies of τ, beauty and charm physics.

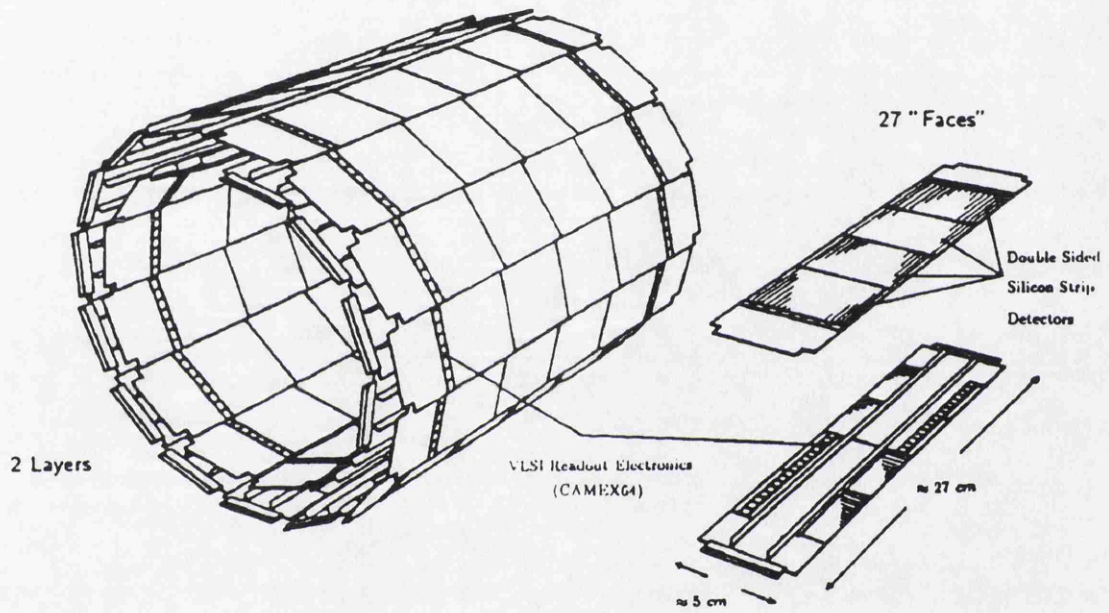

Fig. 3.5.1: The ALEPH Minivertex Detector

3.6. Inner Tracking Chamber

The Inner Tracking Chamber (ITC) is a cylindrical multiwire drift chamber with three dimensional coordinate readout. The ITC serves two purposes in ALEPH: to act as the Level 1 charged track trigger, and to give several highly accurate points in 3D to complement the TPC tracking at low angles and near to the vertex. The ITC gives up to eight $r - \phi$ points between 160 and 260mm from the interaction point. All tracks with ϕ between $-166°$ and $+166°$ will traverse all the layers of the ITC.

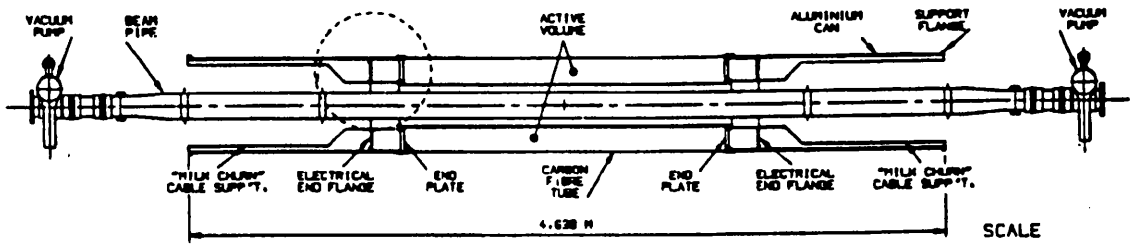

Fig. 3.6.1: The ALEPH Inner Tracking Chamber

The overall device, see Fig. 3.6.1, is 4.64 metres long, with an active length of 2 metres. The inner wall is made of polystyrene and aluminium foil and is 0.002 radiation lengths thick. The outer load-bearing wall is of carbon fibre and presents 0.01 radiation lengths. These walls are as thin as possible to minimize conversion of photons and multiple scattering. There are eight concentric layers of sense wires running parallel to the Z-axis. The inner four layers have 96 wires, and there are 144 wires in the outer four. Each sense wire has four field wires grouped round it, forming a hexagonal drift cell, of which there are 960 altogether. The device is run at a positive voltage of between 2.2 and 2.4 kV.

For the Level 1 trigger, the ITC readout has an $r-\phi$ processor which finds tracks in two dimensions: the coordinate is given simply by the number of the hit wire, and gives a signal in 500 nsec, In the future, an $r-\phi-z$ processor may be used. This works in three dimensions, and information is available in less than $3\mu sec$.

The sense wires are attached to preamplifiers mounted on the ends of the device. These are read out by CAMAC and FASTBUS time-to-digital converters. The $r-\phi$ coordinates are obtained by measuring the drift time, and are accurate to 100 μm . The z-coordinate is obtained from the time difference of the arrival of the signal at the ends of the wire, and is accurate to around 3cm. A more detailed discussion of the ITC construction and performance may be found in [113].

3.7. The Time Projection Chamber

The Time Projection Chamber (TPC) is the main tracking device in ALEPH. A device of this type was chosen as the best method to measure with good momentum and angular resolution the 20 or so charged tracks arising from a typical e^+e^- event. A TPC was chosen because of its high z-coordinate resolution, good two-track separation and the ability to measure the ionisation energy loss for particle identification. The ALEPH TPC measures

21 three dimensional points for fully-contained tracks, and also gives up to $330\,dE/dx$ measurements per track, which can be used for particle identification. A similar device could have been constructed using a conventional drift-chamber setup, but only at the cost of a much larger amount of read-out electronics and cables and probably lower reliability.

The Time Projection Chamber concept was first proposed by Nygren [114]. TPC devices have been built and successfully operated by other collaborations, but the ALEPH device is the largest yet built. A TPC is a tracking device consisting of a large cylindrical volume of gas with parallel, axial magnetic and electric fields. Charged particles leave a trail of ionised gas molecules and electrons on their passage through the gas volume. The electrons are drifted along the z-axis by the large electric field and the charges are recorded by a system of proportional wire chambers at each end. As the electric and magnetic fields are parallel, there are no $E \times B$ forces to broaden the tracks. The strong magnetic field reduces diffusion broadening of the tracks. The combination of electric and magnetic fields means that the trajectory of a charged particle in the TPC is a helix thus by measuring the sagitta of the arc of the circle which this track makes at the end-plates, the transverse momentum of the track is measured. The resolution in the transverse momentum, p_T, is related to the error in sagitta measurement by :

$$\frac{\Delta p_T}{p_T} = 0.027 p_T \frac{\Delta s}{l^2 B} \tag{3.7.1}$$

where:

Δs (mm) is the error in curvature measurement;
B (Tesla) is the magnetic field;
l(m) is the length of the projected track

The ALEPH TPC was designed to have a resolution of 10% for the highest momenta particles foreseen (muon or electron pairs at the LEP 200 energy of 100 GeV per beam), which means an error in the sagitta measurement less than 100 μm. Given a magnetic field of 1.5 Tesla, it was necessary to construct a device with the largest possible radial size, hence the radius of the sensitive area is l = 1.4 metres.

The principles of operation of the TPC and the electronics designs were first studied on a smaller prototype, known as TPC 90.

3.7.1 Construction

The ALEPH TPC, Fig. 3.7.1, consists of a cylindrical drift volume with a central membrane electrode and planar wire chambers at either end. It has an outer diameter of

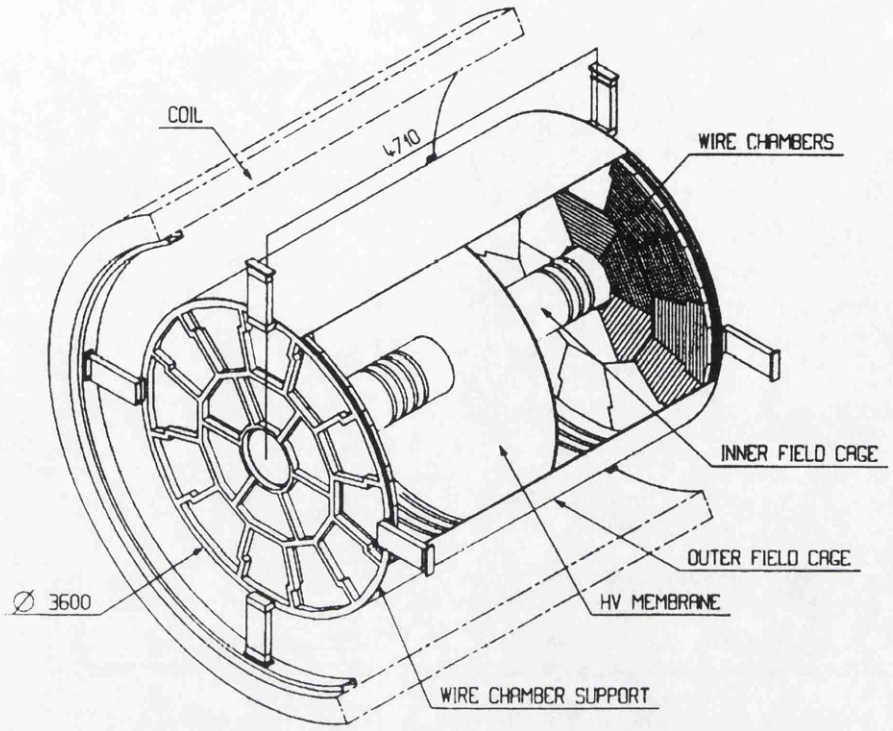

Fig. 3.7.1: The ALEPH TPC

3.6m, and is 4.4m long. The gas used is a 91% argon / 9% methane mixture at atmospheric pressure. The central mylar electrode divides the chamber into two parts. A drift field of 11 kV/metre is applied between the centre and the ends. Electrons from the ionisation tracks drift to the end-plates in this field. The end-plates have a system of proportional wire-chambers; there are 18 sectors of wire-chambers on each end-plate. These sectors are arranged in two concentric circles, the inner with 6 and the outer with 12 sectors. The geometry has been chosen such that a straight track lying along a sector edge will still give a sufficient number of hits for reconstruction. The sectors have concentric rings of cathode pads which give the $r\phi$ position. The z-coordinate is obtained from the drift time. There are 41004 pad readout channels and 6336 wire channels. Up to 21 points from each track may be measured. Between the pad rows there are rows of long trigger pads, which are used in the second level trigger. There are 32 trigger pads per sector. The trigger pad signals require fast processing, and are read out by specialized electronics.

3.7.2 Gating

If the TPC were to be operated in a continually sensitive mode problems would arise due to the build up of space charge from background electrons on the sense wires at the end-plates. A grid of gating wires is placed in front of the sense wires. When this is 'closed',

at a low positive voltage, ionisation electrons cannot drift beyond it to the sense wires. At the appropriate time in the machine cycle after a bunch crossing, when the TPC is ready to be read out, the gating grid is grounded to open it and electrons may pass through. The grid is held open for the full 45 μs drift time only if there is a first level trigger. The electrons then drift into the high-field region between the cathode grid and the sense wires where they avalanche: this gives a signal on the sense wire, and an induced signal on the cathode pads.

3.7.3 Electronics and Readout

FASTBUS modules known as Time Projection Digitisers (TPDs) are used to read out the TPC. These use eight-bit flash ADC's to measure the amplitude and time profile of each hit with a sampling frequency of 12.5 MHz. During the 45 μs drift time up to 510 samples may be taken. Read out of the TPDs is controlled by the Time Projection Processor modules (TPPs), based on the Motorola 68020 microprocessor. The TPPs read out the data from the TPDs, format it, perform compaction of wire data, calibration, and monitor selected events. Each TPC sector has one TPP for pads and one for wire readout. Data from the TPPs is assembled into a complete event by the Event Builder (EB). There are three Event Builders for the TPC, which perform the tasks of readout and data formatting, data monitoring, analysis of any abnormal conditions during the run and passing of complete events to the VAX cluster.

3.7.4 TPC Performance

The straightness of the tracks in the TPC is measured by taking cosmic ray tracks and by using a laser calibration system built partly by Glasgow University. A system of two UV lasers creates tracks by a process of resonant two-photon ionisation of residual impurities in the gas. A system of mirrors and prisms creates thirty straight tracks in the TPC emanating from near the interaction point. Information from this system, and information from the detailed magnetic field map is used to correct the TPC tracks in the reconstruction program. Tracks from the leptonic Z^0 decays recorded in 1989 and 1990 have been used to measure the performance of the TPC [115]. After corrections the resolution for a single point coordinate of 173 μm in the azimuthal direction, and 740 μm in the z-direction is achieved. This gives a momentum resolution of $\Delta p/p^2 = 1.2 \times 10^{-3}(\mathrm{GeV}/c)^{-1}$, satisfying the design requirements. Using information from the ITC also, the detector as a whole then achieves a momentum resolution of $\Delta p/p^2 = 0.8 \times 10^{-3}(\mathrm{GeV}/c)^{-1}$. The two

track resolution is such that for energies over 5GeV, tracks separated by larger than 2° are separated. For particle identification measurements the TPC achieves a resolution of 4.4% in dE/dx.

3.8. The Electromagnetic Calorimeter

The ALEPH electromagnetic calorimeter (ECAL) measures the energy of electromagnetically interacting particles (electrons and photons) and in conjunction with the hadron calorimeter, pions, protons etc. The device consists of alternating layers of lead converter sheets and proportional wire chambers. The particles shower in the lead, and as they traverse the gaps the signals are measured by the wire chambers. The electromagnetic calorimeter has a barrel section made up from twelve identical modules, together with two end-cap sections each with twelve 'petal' modules. Insensitive cracks between the detector modules account for 6% of the end-cap and 2% of the barrel coverage. The total angular coverage is 3.9π sr with coverage in the polar angle extending down to 13° of the beam axis. The ECAL is read out in 72 000 projective towers, each divided into three depth sections. This longitudinal depth separation is for use in particle identification as different particles deposit energy in the calorimeter with a different shower shape. The ECAL was designed to have an energy resolution of $15\%/\sqrt{E(\mathrm{GeV})}$. Chapter 5 describes the end-cap calorimeter modules in detail.

3.9. The Magnetic Coil

The axial magnetic field for the ALEPH detector is created by a superconducting solenoid. The magnet normally runs at a field of 1.5 Tesla, this high field being needed to bend energetic particles sufficiently for precise tracking. A superconducting coil was chosen for reasons of power consumption. The superconducting coil encloses the ECAL, TPC, ITC and beampipe. It is 7 metres long, with an outer diameter of 5.84 metres. The coil was designed to present as little density of material as possible to particles coming from the interaction region, and consists of a single layer of superconducting NbTi cable reinforced by high purity aluminium. The coil is supported by a shell of aluminium alloy which withstands the magnetic forces of several thousand tons. The total structure has a thickness of 1.6 radiation lengths, or 0.4 absorption lengths. There are 1532 turns in the main coil, and a current of 5000 amps in the coil results in a field of 1.5 Tesla. The magnetic energy stored by the coil is 136 MegaJoules. At the ends of the main coil there are two compensation

coils each of ninety turns which are fed with current in parallel with the main solenoid, and are intended for correction tuning of the field. The solenoid and magnet yoke were carefully designed to provide a uniform field over the TPC volume since momentum measurement depends on the field strength and uniformity. The design criterion was for a distortion of less than 0.2 mm in the sagitta of the TPC tracks. Careful maps of the magnetic field within the coil/yoke were taken with an automated Hall and NMR probe assembly in 1987 when these parts were assembled in the BEBC hall at CERN. The aim was to measure the field components to an accuracy of $\approx 10^{-4}$. For the z–component, $\Delta B/B < 0.2\%$. The radial and azimuthal components also show variations, which are due to differences in the magnetic reluctance of the return yoke end–cap modules. Given a field map, corrections can be applied to the measured TPC momenta. The uniformity of field achieved is of the order of 0.2%, and the variations in the transverse field components result in sagitta distortions in the TPC which are less than 0.2mm.

3.10. The Hadron Calorimeter

The flux return path of the magnet coil is a massive iron structure, which is instrumented to form the hadron calorimeter (HCAL). The HCAL acts an an absorber for the hadronic particles from the interaction (charged pions, protons, neutrons etc.) and acts as a 'fourth layer' to the ECAL, as any leakage from the ECAL is measured in the HCAL. The HCAL also serves as a muon filter, as muons are the only particles likely to traverse this thickness of material. The muons are then detected by a system of wire chambers on the outer surface.

The HCAL is made up of 24 barrel modules, each covering a 15° angle in azimuth and weighing 70 tons, plus 2 × 6 end–cap modules of 75 tons each, the total weight being 2580 tons. The magnetic force on the end–caps at full field strength is of the order of 2000 tons. The end–caps give coverage down to an angle of 6°. The HCAL modules are offset with respect to the ECAL modules by 15° to eliminate the overlap of dead zones. The iron in both the barrel and end–caps is subdivided into 23 slabs; the outer one is 10cm thick while all the others are 5cm, giving a total thickness of 120cm of iron. This represents in total 7.6 interaction lengths at 90° in the barrel. A 5mm thick inner layer of iron sheet is added to support the first layer of tubes in the barrel. The end–caps are designed such that there is maximum symmetry in the φ angle, thus making least disturbance on the uniformity of the magnetic field.

The active part of the detector is 23 layers of Iarocci streamer tubes inserted into the 2.2cm gaps between these iron slabs. The tubes used are wire counters made of a graphite coated plastic operated in limited streamer mode, at a high voltage of around 4000 volts. The gas mixture used is Ar /CO_2 /isobutane. The streamer tubes have a 9 x 9mm^2 active cell size, a separation wall thickness of 1mm and a 100μm anode wire. Three of the cell walls are formed by plastic extrusions coated with graphite. The signals are picked up by 4mm wide aluminium strips which run parallel to the wires, plus copper cathode pads. Due to the presence of strengthening rods between layers, there is a complicated geometry of streamer tubes, leaving some dead regions, which amount to around 6% of the total solid angle.

Each tube layer is equipped with pad readout for integrated energy measurement. The pads in each layer are connected into towers pointing to the vertex, which subtend on average 3.7° x 3.7°. The pad dimensions increase projectively from approximately 20 x 20cm at the first plane up to 33 x 33cm. There are 4788 HCAL towers in all, with a geometry which is chosen to match that of the ECAL: on average there are 14 ECAL towers covered by one HCAL tower. A typical energy resolution is $84\%/\sqrt{E(\mathrm{GeV})}$. The tubes are also equipped with strip readout, parallel to each tube and on the opposite side to the pads: this is known as the digital readout, as there is only a single level indicating if the tube has fired or not. A spatial accuracy of 0.35 cm perpendicular to the strip direction is possible with the digital readout. These strips provide a detailed, two-dimensional view of the hadronic shower development and are invaluable for muon tracking and identification, which is decided upon the number of planes fired.

For the trigger, signals from the HCAL wire planes are used. The HCAL is grouped into 24 'supermodules', and an OR signal of all pairs of wire planes is taken from each supermodule which gives a value corresponding to the number of planes fired. The triggers implemented in the 1989 running were a cosmics trigger and a single muon trigger, which uses ITC information also. After initial low efficiency due to changing gas mixtures and electronics problems, the muon pair triggering efficiency rose to $99.6 \pm 0.1\%$ at the end of the running. Other HCAL triggers foreseen for the future are charged and neutral hadronic energy triggers.

3.11. The Muon Chambers

The ALEPH detector is surrounded by two double layers of streamer tubes – the muon chambers. These are constructed as a barrel, two end–cap and two middle–angle sections, there being 94 chambers in all. The inner layer of muon chambers covers 92% of the solid angle, and the outer layer 85%. The muon chambers are separated by a distance of 40cm or 50cm so that the position and angle of a track may be measured. The streamer tubes are of the same type as the HCAL tubes. Each layer has two planes of readout strips parallel and perpendicular to the wires. No cathode pad readout is necessary with these devices. There are in total 23378 x–strip and 31432 y–strip readout channels. The muon exit angles are measured to an accuracy of 10 mrad. The HCAL digital tube readout also serves to track muons, and as the muon trigger. The muon chambers are basically an extension of the muon tracking in the HCAL.

3.12. The Luminosity Monitors

The luminosity detector is a very important component of ALEPH. The luminosity is determined by counting the number of small–angle Bhabha scatter events. In this region, there is no interference between γ and Z^0, and the cross–section is well predicted by QED to be :

$$\frac{d\sigma}{d\Omega} = \frac{4\alpha^2}{E^2}\frac{(\hbar c)^2}{\theta^4} \tag{3.12.1}$$

at small angles θ, and to first order in α. The luminosity measurement is crucial for determining the Z^0 peak cross–section and line shape. The ALEPH experiment measures luminosity with an uncertainty below 1%, so that the error in the Z^0 cross–section is not dominated by uncertainty in the luminosity. This confidence in luminosity measurements enabled ALEPH to claim the most accurate results in the 1989 and 1990 LEP running.

Luminosity events are counted by triggering on a single electron and positron in coincidence on either side of the detector. In order to trigger on good luminosity events and to reject background an accurate energy measurement of the electrons is necessary. Good angular measurement of the tracks is also needed as the Bhabha cross–section is strongly dependent on angle. The ALEPH luminosity monitors, Fig. 3.12.1, consist of small–angle tracking chambers (SATR) on either end–cap close to the beam–pipe. These are backed by luminosity calorimeters (LCAL).

The small–angle tracking chambers use individual drift cells made from square brass tubing. This configuration was chosen due to the high background from synchrotron radiation expected at low angles. The SATR are in four half–cylindrical modules, covering

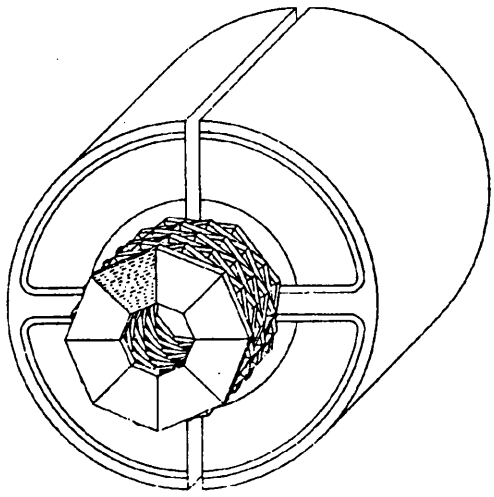

Fig. 3.12.1: One Half of the Luminosity Monitor, with SATR and LCAL

the region from 92mm to 300mm radially from the beam. Each module has nine layers of drift tubes. The chambers are at 245.5 cm from the interaction point, and are 170mm long. The SATR covers the angular range from 40 to 90 milliradians. The SATR has a track position resolution of 800μm in the radial direction and 3.8mm in the azimuthal direction. The SATR position is surveyed along with the LCAL modules, to which it is mounted.

The luminosity calorimeter again consists of four modules around the beam–pipe. It is a lead–wire chamber sandwich sampling calorimeter, of a construction very similar to that of the ECAL. Each module has 38 layers, read out in 3 stacks, and is 24.6 radiation lengths deep. The LCAL is situated 262.5 cm from the interaction point and extends from 10cm to 52 cm from the beam, covering the angular range from 45 to 155 milliradians. Together, the luminosity monitors cover the polar angular range of 55 to 90 mrad, and have an acceptance of 300 degrees in the azimuthal direction. A knowledge of the exact positions of the sensitive regions is critical for determining the errors in luminosity measurement. The modules have been constructed to high mechanical tolerances. Once mounted on ALEPH optical surveys have measured the positions of the modules with an error of 0.32mm in the radial direction and 0.85mm in z. Combined with mechanical tolerances, this gives an average error of 0.134mm in the position of a tower, which should keep the error in acceptance to below 0.6%.

The expected trigger rate for the luminosity monitors is 0.3 Hz at a luminosity of $10^{31} cm^{-2}$. The luminosity calorimeter readout is by small cathode pads, in a similar fashion

to the ECAL. The pads are arranged into projective towers, there being 384 towers in each module. Readout from each of the 38 layers of anode wire planes is also possible. The readout electronics used are essentially the same as that for the ECAL, although an ALEPH Event Builder is used instead of a Read Out Controller. The LCAL modules are calibrated in a fashion similar to the ECAL: modules were tested in a beam line, Fe^{55} sources are used, and an electronics calibration is performed between each LEP fill. The LCAL has a resolution of $20\%/\sqrt{E}$. After careful corrections to the LCAL acceptance and alignment (based also on on Monte Carlo data), an error of 0.6% (experimental) and 0.3% (theoretical) has been achieved in the measurement of luminosity [116].

3.13. The BCAL

The BCAL is a luminosity monitor for very small angle Bhabha events, from 5 to 10 mrad. It is intended to give an immediate measure of the luminosity to the people on shift, and as it can operate independently of ALEPH, measures the luminosity when ALEPH is not accepting events and so helps in measuring the ALEPH efficiency and dead-time.

The BCAL is composed of four modules wrapped around the beam pipe, on the far sides of the superconducting quadrupoles. Each pair is 7.7 metres from the interaction point and extends to within 6.5cm of the beam, as they are inset into elliptical sections of the beam pipe. Each of the modules is a sampling calorimeter made of tungsten sheets interspersed with layers of plastic scintillator. Tungsten is chosen as this has the shortest radiation length (3.8 mm) of any material, making for the most compact design. Each module is rectangular in shape. There are ten layers: the first layer is 4 radiation lengths thick and the nine others 2 radiation lengths thick. The sampling planes are 3mm thick plastic scintillators read out by small photo-multiplier tubes. A plane of vertically oriented silicon strip detectors is located after the first eight radiation lengths. There are 40 silicon strip channels on a 0.5 mm pitch. These provide very accurate angular tracking. Finally, there is a 6 radiation length thickness of tungsten to protect the sampling layers from synchrotron radiation entering from the rear.

3.14. The Trigger

The purpose of the trigger system is to decide quickly which signals are genuine events and to provide a signal to initiate the full read out of the detector as soon as possible after a valid event has occurred. The trigger system is intended to reduce the dead time of the

apparatus, and to reduce the flow of events to the cartridge drives and reconstruction farm to a manageable level. The trigger must be good at rejecting background events, yet must also not be so narrowly set that any new physics events are overlooked. The interaction rate at LEP is low enough that it is not necessary to have a trigger decision to select specific types of events and to reject the more common ones. Five sub–detectors play the major roles in the trigger: the hadron calorimeter, electromagnetic calorimeter, luminosity calorimeter, ITC and TPC. The ECAL and HCAL give trigger information from both wires and pads, and the LCAL provides pad signals only. The ITC and TPC give a bit pattern which indicates through which segments of these detectors a charged track has passed. The basic philosophy is to look for either a charged track or a deposit of energy anywhere in the detector, or a combination of both, above certain thresholds. Triggers based on single 'objects' in the detector are the best for accepting any new types of events, but triggers based on the simultaneous detection of signals in two parts of the detector are also used. The trigger scheme implemented is a three–level configuration.

The Level–1 trigger uses essentially digital information based on tracks from the ITC and special fast trigger sum signals from the pads and wires of the ECAL and HCAL. The LCAL is also used to trigger on forward Bhabha events. Level–1 needs to deliver a decision within $\approx 5\mu s$ (there are $22\mu s$ between beam crossings): this means there is no dead time introduced by this trigger. The detectors are split into 60 trigger segments (plus 24 for the LCAL) which closely follow the physical construction. The trigger electronics sums the signals arriving from the calorimeters to get values for each segment, which are compared to four preset threshold levels, giving four YES–NO signals per sector. The resulting 60–bit arrays are given to the modules which make physics trigger decisions. The total energy in each of the 36 individual ECAL modules and 24 HCAL modules is also given to the trigger system. For the ECAL modules the total wires energy signal is an AND of the signals from the even and odd planes. This reduces any accidental triggers due to noise or sparks in just one plane. A total energy sum is computed for the barrel and each end–cap. A particular physics trigger is defined by setting the threshold level in each segment of each sub–detector in the trigger, then ORing the results. The overall Level 1 trigger is the OR of all the individual triggers. Information on which triggers have fired is written out to tape with each event.

It is possible to define up to 32 different triggers. Possible trigger types are :

- single muon

- double muon
- neutral electromagnetic cluster
- charged electromagnetic cluster (with ITC track)
- neutral hadronic cluster
- charged hadronic cluster (with ITC track)
- isolated photon
- various Bhabha event triggers
- total energy in calorimeters
- n– track event
- cosmic event in ECAL
- cosmic event in HCAL
- random

The Level–1 trigger rate is a few hundred hertz. Once a Level–1 trigger has been satisfied a full readout of the detector is initiated with data conversions by ADCs and TDCs started.

At the end of the TPC drift time the Level–2 trigger is applied. The Level–2 trigger bases its decision on the Level–1 information plus TPC tracks and a requirement for the tracks to come from the vertex. The signals for the second level trigger are taken by rows of special trigger pads in the TPC. Hard-wired processors look at tracks from the TPC in the r–z plane. Straight tracks found in r–z then set bits in the 60–bit array, and the second level decision is made by replacing ITC information with the TPC. The Level–2 decision takes $45\mu s$. A Level–2 NO will stop and clear the data acquisition for that event. If the second–level rejects an event, the subsequent drift time in the TPC and the time needed to refresh the ECAL amounts to $61\mu s$. The experiment is then ready to take data again after the fourth bunch crossing following that event. The Level–2 reduces the trigger rate to around 10 Hz.

The Level–3 trigger is a more sophisticated software–based system which is run on the VAX cluster. The Level–3 trigger tries to identify genuine e^+e^- interactions from the background of events caused by cosmic rays, two–photon events, beam gas interactions, and beam–related particles travelling along the tunnel. At the design luminosity, the Level–3 trigger should reduce the trigger rate to ≈ 1 Hz, which is the maximum rate for writing to magnetic tapes. The level 3 trigger is run on complete events at the time they are being processed by the reconstruction farm (FALCON) after the event has been read out – this

degree of parallelism is necessary in order to keep up with the event rate. The algorithm has been optimized for high efficiency of pattern recognition and low CPU time, and does not depend upon calibration of the analogue signals having been performed. Reconstruction is applied only to those detector segments showing activity at Level 1 or Level 2.

3.14.1 Trigger Conditions in 1989

During the 1989 running with ALEPH, two main types of triggers were used to identify Z^0 events. The first used the ECAL wires signals and the ITC. (The ECAL pads were not used in the trigger in 1989). The following thresholds were used :

- total energy > 6.5 GeV in ECAL Barrel
- total energy > 3.8 GeV in either of ECAL end-caps
- total energy > 1.6 GeV in both end-caps
- a single ECAL Module > 1.3 GeV (Single neutral EM trigger)
- a single ECAL Module > 1.3 GeV plus at least one ITC track in the same azimuthal region (single charged EM trigger)

It should also be noted, as mentioned above, that the sums of the odd and even wire planes are also required to exceed half of these values. This, along with the low values of electronic noise, means that triggers are feasible on energy deposits as low as a few hundred MeV. The thresholds were chosen such that at least 50% efficiency was achieved.

The second trigger type used the HCAL and ITC information to trigger on penetrating particles. The requirement was for a track candidate in the ITC and a digital pattern readout of 4 double planes out of 12 in the HCAL, in the same azimuthal region.

Luminosity events were triggered using the LCAL, with the following requirements :

- a coincidence of > 20 GeV of energy on one side with > 16 GeV on the other
- a single-arm trigger of > 31 GeV on one side

The conditions achieved by the LEP machine in its first months of operation were such that Level 1 trigger rates of around 0.5 Hz at at luminosities of $10^{30} cm^{-2} s^{-1}$ were achieved. As most events satisfy more than one trigger, the trigger efficiency could be measured easily, and was found to be 100% for hadronic Z^0 decays and $99.7 \pm 0.2\%$ for Bhabha events. The triggering scheme used was very successful, as the event sample has a large physics content. There were 538472 triggers taken, of which 28592 were identified as hadronic Z^0 decays and 52669 as Bhabha events. The rest of the events are from beam-related muons (which come from the beams scraping the collimators upstream of ALEPH), beam-gas interactions

(during 1989 the vacuum pumping station at ALEPH was inoperative, therefore there was not such a good vacuum as in the rest of LEP), off–momentum electrons, cosmic rays and triggers due to electronic noise problems in ECAL.

3.15. Data Acquisition System

The modular nature of the data acquisition computer system reflects the way the ALEPH detector is configured as a set of sub–detectors. It was required in the design that each sub–detector can be run independently, during the hardware development phase, when bringing the complete detector into operation prior to data taking and during times when parallel activities, e.g. calibration runs, are taking place.

The system is implemented using modern hardware and software standards. The hardware used is almost all FASTBUS which is the most modern standard for high-density electronics for use in nuclear experiments. FASTBUS offers more channels of readout per crate (up to 96 single-width modules), a data transfer rate 10 times faster than CAMAC and a 32 bit data bus. There are in addition a few CAMAC and VME units. NIM hardware is used for fast timing and trigger related electronics. A database system is used to keep track of the detector configuration. FASTBUS crates and their interconnects, and is used to initialize the system. The embedded processors in the FASTBUS system are all from the Motorola 68000 family (with the exception of the bit–slice processors in the ECAL ROCs). These use the OS–9 operating system. The OS–9 based micros are connected by an Ethernet network, which also has links to the VAX cluster. The FASTBUS system handles all of the zero–suppression, formatting and on–line calibration of the data, thus taking a considerable load of the processing.

All of the data from the individual sub–detectors is collected and written to tape by the on–line computer system. The data acquisition computer system is a VAX cluster, with one large VAX as the main machine plus three smaller VAXes dedicated to the large subdetectors: TPC, ECAL and HCAL. The VAXes are located in the surface control room and are connected to the FASTBUS in the barracks by a fibre optic link. The ALEPH online system is based on the CDF collaboration's buffer manager scheme [117]. This has many simultaneous processes which create or consume data. A program called the *switcher* is run at each terminal, this allows the operator to switch control from one to another process. The switcher is controlled by the UPI menu package. There exists one *scheduler* process

per VAX which is responsible for the creation and deletion of processes, and inter-process communication.

There are also several VAX graphics workstations in the cluster. The work-stations are used for control, monitoring and on-line event display purposes. Programs run on the ECAL computers to check constantly the functioning of the ECAL, recording pedestal stability, high voltage and low voltage, gas conditions and the energy deposits in each module. Histograms of the time evolution of all the relevant quantities may be viewed on the workstations. The excellent ALEPH on-line event display can display the ECAL in great detail, and is very useful for spotting non-functioning modules, or modules where pedestal drifts have occurred, which results in many towers above threshold. These monitoring activities are intended to find problems quickly and allow experts to fix them as soon as possible, also the relevant information is available for possible off-line corrections.

3.15.1 FALCON

On the main VAX, raw events are written to cartridge tape and also to a dual-ported disk. When the run ends, this disk is turned over to the FALCON 1 cluster. This is a farm of VAX workstations which perform event reconstruction. The cluster consists of 12 diskless VAX stations, one microVAX server and 3.6 Gigabytes of disk. These disks are 'dual-ported' devices, such that when the on-line VAXes have written all the data from a run to these disks, the FALCON cluster can then take control and process the same files.

The microVAX server does a preliminary scan of the data to produce an event directory (EDIR) with the location of each event, and also any global reconstruction variables, such as those ECAL towers which are flagged as being noisy in many events. Sets of events are then allocated to the workstations which run in parallel and have random access to the raw event data. Each workstation runs the full JULIA reconstruction code. The files of reconstructed events are written to separate disk files which are joined together by the server node. Reconstructed events are immediately written via a fast link to disks on the CERN IBM and the ALEPH workstation cluster at the Meyrin site. Reconstruction of events by our own computers takes a great load from the central computers at CERN, and also means that data are available for off-line analysis within a matter of hours of the events being taken. The availability of fully reconstructed data within a short time of the events occurring was extremely useful in debugging and monitoring the performance of the detector

The FALCON cluster has also proved its worth during times of no LEP beam as the ALEPH data sample has had to be reprocessed several times to use the most up–to–date calibration constants and reconstruction techniques. This takes a prodigious effort, and the CPU power for this may not have been available on the main CERN machines, but the FALCON cluster is well suited to this sort of task.

Chapter 4.
ALEPH Software

'Don't know what I want, but I know how to get it' – the Pistols

This chapter describes the ALEPH software used for Monte Carlo generation of events, event reconstruction of real and Monte Carlo events, physics analysis and graphics.

It is common practice in high energy physics to generate many simulated *Monte Carlo* events, and to analyse them in a similar fashion to the real data sample. The physics processes and parameters input to the Monte Carlo sample are well known. Comparison of the simulated with the real data enables the effects of detector resolution and acceptance to be calculated and gives estimates of background events which mimic processes under study. The cross sections measured by an experiment are corrected for detector acceptance and initial state radiation using factors obtained from Monte Carlo samples, giving values which can then be compared with other experiments.

Once the raw data from events have been written to tape or disk by the online computers, the events undergo a process of offline *reconstruction.* The reconstruction package does tasks such as track fitting, calorimeter clustering etc. The events are then available for use by *analysis* packages and graphics programs for event scanning. Within ALEPH, the reconstructed events are available in several different formats, and are distributed worldwide to the various collaborating institutes.

4.1. Software Engineering, ADAMO and the ALEPH Database

In the first stages of the writing of the ALEPH computer programs, it was decided to use software engineering techniques to overcome the software problems which have affected large HEP experiments in the past. The ALEPH experiment uses software engineering methods such as SASD (Structured Analysis, Structured Design) [118]. SASD involves using data flow diagrams, which identify sub-parts of the software which can be developed independently and updated without affecting the overall operation, as the data-flows are the only couplings between modules. All ALEPH data structures are rigorously described by an entity-relationship database model, known as ADAMO [119–120]. ADAMO is a data management system for defining and manipulating data with FORTRAN programs.

The data structures are mapped into tables which are compatible with a relational data base management system. The ADAMO system has been applied to the online system, the detector database and the offline analysis packages. In actual fact, the ALEPH analysis programs do not use the ADAMO code for accessing the data directly. The Table Access Package (TAP) of ADAMO was not used due to possible extra CPU demands and overheads in software development. The BOS memory management package was used for reasons of speed and economy. However, all the data banks and their relationships are strictly defined using the Data Definition Language of ADAMO. If the data are rigorously defined in such a fashion, the software has a uniform way of accessing all data, the attributes of all data banks are known and software upgrades can be easily applied.

A database [121] was constructed for the ALEPH detector, based on the ADAMO model. It contains such quantities as:

- physical parameters, e.g. geometrical and alignment information
- FASTBUS configuration data and readout addresses
- trigger setup information
- experiment book-keeping
- LEP machine information -- exact energy and luminosity of runs
- detector slow control parameters, e.g. HT and pressure settings
- calibration constants for each subdetector, e.g. ECAL 'platine' data, TPC drift time
- a detailed description of the geometry of each of the towers in ECAL
- lists of dead ECAL storeys and 'glowing' towers

The subdetectors of ALEPH were designed such that the individual data acquisition system for each subdetector readout performs zero-suppression and applies calibration factors to the individual channels of the raw data. The data read out onto tape are already corrected to the level of individual modules, so only a small number of calibration constants is needed in the off-line database.

The HISTORIAN package [122] is used for software code management: this allows teams of programmers in separate locations to work on developing the code independently. HISTORIAN also enables the writing of code which can be run on several different operating systems. Modifications and new code are periodically gathered together and released as official versions. All new code is tested before release on IBM/VMS, VAX/VMS and UNICOS. The ALEPH offline software uses the BOS memory management package to store

data. BOS [123] is a 'memory management' package where collections of data are held in structures known as 'banks'. The movement of these banks into and out of computer memory, and their mapping into a FORTRAN COMMON block are the function of the BOS package. Each data entity described by the ADAMO data definition language is organised into a BOS–bank.

4.2. KINGAL

KINGAL (KINetics for GALeph) is a library of Monte Carlo event generators interfaced to the ALEPH software. The Kingal generators are computer programs which use models of physics processes to generate events of a required type. After generation each event is held in a standard form with lists of particles and their four–vectors ready for input to the next step of the chain. The following types of generators are available :

- zero mass final states e.g. $Z^0 \rightarrow \gamma\nu\bar{\nu}$
- Bhabha scattering (with radiative corrections)
- muon pair production
- tau pair production
- quark pair production (and other QCD processes)
- two–gamma physics
- other physics e.g. supersymmetry, Higgs production
- background processes : cosmics and beam–gas interactions

4.2.1 The HVFL02 Generator

The KINGAL generator which is of most relevance to this thesis is known as HVFL02. The HVFL02 generator was developed by the ALEPH Heavy Flavours physics group and contains facilities to deal with heavy flavour decays and mixing [124–126]. It is the standard generator used for production of Monte Carlo $q\bar{q}$ events by the ALEPH collaboration. The generator may use different generators for the initial $q\bar{q}$ pairs: JETSET [127], BREM5 [128] or DYMU3 [129]. At this stage aspects specific to heavy flavours are added. Mixing and CP violation parameters for $b\bar{b}$ events may be changed by data cards. The most up–to–date branching fractions and decay modes are given in a standard set of data cards. The decays to bottom hadrons are included.

As has been discussed in 1.5, fragmentation is the process by which the initial quarks and gluons form into the colourless hadrons seen in the experiment. Fragmentation cannot

be calculated from first principles in QCD and is described by semi–empirical formulae, the *fragmentation functions*. The fragmentation function gives the probability for a quark to produce a certain hadron with a certain momentum. Within HVFL02, the Peterson fragmentation functions are used for charm and bottom quarks: as explained in section 1.5.5, heavy quarks have a harder fragmentation distribution, which is better modelled by the Peterson fragmentation functions.

4.3. GALEPH

For software testing purposes, optimization of reconstruction algorithms and physics event generation the GALEPH (Geant for ALEPH) detector simulation program provides simulated raw data which is similar to the real data from the detector. This gave the collaboration opportunities for very detailed testing and debugging of the full reconstruction and analysis chain before real data were taken. GALEPH uses the GEANT detector simulation package [91], which was developed at CERN. The GALEPH program takes as an input the particles produced by KINGAL and simulates their decays and interactions with the detector, both the active components and the passive material such as cables and the magnet feet etc. The output from GALEPH is a set of BOS banks identical in format to that of raw data, containing ADC readings and hits as in real data. Any analysis programs can then be used in exactly the same fashion with simulated data as with real data.

4.3.1 ECAL Simulation in GALEPH

Within GALEPH, no highly detailed ECAL geometry at the plane–by–plane level has been implemented. Rather, an 'average' medium is used, which consists of a mixture of lead, aluminium, fibreglass etc. with their atomic weights and atomic numbers considered. Regions covering each stack and areas like the electronics boxes, signal cables and outer case are used. Signals corresponding to each stack of active material are given by the simulation. A highly complex geometry would consume lots of computer time, and would give no more useful physics results.

Energy deposits in the ECAL are simulated by parameterizations of the showers, since detailed simulation with, for instance, EGS4 would consume too much computer time for routine use [130]. In a calorimeter the deposited energy has fluctuations from event to event, as explained in Chapter 2. The mean deposited energy signal s is made to fluctuate with a Poisson distribution such that $\Delta s/\sqrt{s} \simeq 0.17\mathrm{GeV}^{1/2}$. The parameterizations

for the longitudinal shape, transverse shape and fluctuations were chosen by comparison with results from the calorimeter prototype and Monte Carlo simulation using the EGS4 program [131–132]. The prototype data were electron showers between 5 and 50 GeV, and pion showers of 5 and 10 GeV. The EGS4 data ranged from 25 MeV to 25 GeV. The parameterization used for the mean shower is :

$$\frac{dE}{ds} = Ns^{A-1}e^{-Bs} + Ce^{-Bs} \qquad (4.3.1)$$

where:

s is the path length measured from the entrance face in radiation lengths;
N is the normalization = $(EB - C)\,B^{A-1}/\Gamma(A)$;
A and B are functions of the particle energy E:
$\Gamma(A)$ is the gamma function:
C describes the energy loss of an incident electron before the first bremsstrahlung:
(C = 0.016GeV and is the measured mean energy loss of a minimum–ionising particle per radiation length, obtained from measurements of non–interacting pions).

If C is neglected, this parameterization reduces to a standard shower formula, and is independent of the incidence angle of the electron. The testing of ECAL petal and barrel modules in a test beam of known energy is described later in section 5.8. The test beam data were used to determine the best parameters for these GALEPH simulations. According to [110] and [133] the test beam data agree well with an EGS simulation if the following parameter values are used for $E > 0.1$GeV:

$$A/B = 5.26 + 1.04 log E \qquad (4.3.2a)$$

$$1/B = 1.86 + 0.04 log E \qquad (4.3.2b)$$

and if $E < 0.1$GeV:

$$A/B = 6.36 + 1.53 log E \qquad (4.3.3a)$$

$$1/B = 4.31 + 1.07 log E \qquad (4.3.3b)$$

A good simulation will not only give a good value for the mean shower behaviour, but will also include the fluctuations of individual events. Two mechanisms are responsible for these, called the shape and sampling fluctuations. The sampling error was estimated from the width of the total detected signal, and is found to be unimportant above 1 GeV, and comparable to the shape fluctuations at around 500 MeV. The shape fluctuations are intrinsic to the cascading process occurring in the passive layers and they affect the energy profile. The method used to simulate these is to consider fluctuations of the A and B

parameters. In fact $1/A$ and B/A are the parameters chosen as these are uncorrelated and display a Gaussian fluctuation. A Gaussian smearing is applied to these two parameters in the Monte Carlo.

The transverse shape of the shower is given by :

$$\frac{\delta^2 N}{\delta x \delta y} = \frac{A}{(r+a)^n} \tag{4.3.4}$$

in a coordinate frame where x and y are the transverse dimensions and z is depth in the calorimeter. The ECAL simulation includes the addition of noise, and the trigger signal from a module is simulated.

4.4. JULIA

JULIA (Job to Understand Lep Interaction in Aleph) is the ALEPH reconstruction program. It takes the digitisations read out by the detector, and attempts to assemble these into objects of interest to physicists, which are accurate representations of the particles participating in an event. JULIA performs the following main tasks :

- track fitting in TPC and ITC (i.e. hits are associated into helical tracks, and the momenta and directions of these tracks are computed)
- association of TPC and ITC tracks
- vertex detector coordinate finding
- kink finding and (neutral) vertex finding
- calorimeter calibration
- calorimeter corrections for missing pads/wires and for the effects of dead zones
- calorimeter clustering. This involves searching for all those pads which are 'connected' and summing their energies to form a single object. The impact point in the ECAL based on the centre-of-gravity of the hit pads is computed.
- association of charged tracks, ECAL objects and HCAL objects. This helps in separating neutrals, hadrons and electrons.
- energy flow
- finding of muon tracks by examining the pattern of strips fired in the HCAL and muon chambers
- particle identification, from dE/dx in the TPC, shower transverse and longitudinal shapes in the ECAL and HCAL, and penetration of the HCAL and muon chambers

4.5. ECAL Reconstruction in JULIA

The parts of the JULIA program which deal with the electromagnetic and hadronic calorimeters process the raw data from the online system and construct 'Ecal Objects' (PECO) and 'Calorimeter Particles' (PCPA). The philosophy is first to locate as many single particles as possible. Then individual particle types (electrons, gammas, neutral hadrons) are reconstructed and identified. The reconstruction of energy deposits in the calorimeters and the identification of particles in the calorimeter takes place via the following steps :

1. unpacking the raw data and application of calibration factors
2. find topological clusters of fired calorimeter storeys*
3. associate, if possible, tracks from the ITC and TPC to these clusters (or report no matches in the case of neutral particles)
4. associate clusters in the ECAL with clusters in the HCAL, using the charged track trajectory
5. evaluate particle identification probabilities for the clusters

4.5.1 Cluster Finding in ECAL

The raw energy read out from the ADCs has a calibration factor (i.e. MeV per count) applied to it on-line by the ROCs. These calibration factors are loaded before the start of the data taking period and may be taken from radioactive gas measurements or from the data of previous runs [134]. The radioactive gas calibration of the end-cap petal modules is described later in section 5.9. The procedures used to obtain calibration constants are discussed in this section, and the calibration constants taken prior to the LEP startup in 1989 are given. At the JULIA reconstruction stage improvements are made to the energy calibration, principally based on Bhabha scattering data. There is one calibration factor calculated for the pads of each module, and one for the wires. These calibration factors are kept in the ECHE bank of the POT (Production Output Tape).

In the JULIA routine EPREDA, the raw ECAL data are read from the bank ETDI (Ecal Towers DIgitisations). Any 'glowing' towers (i.e. towers which are consistently firing)

* As explained in section 5.2, the calorimeter modules are divided in depth into three *stacks*. The readout pads are grouped into projective *towers* which point at the intersection point. Each tower is subdivided into three *storeys*, which correspond in depth to the stacks.

are suppressed. The glowing towers are identified by an algorithm running on the FALCON cluster and a list is kept with the run data. A calibration factor is applied to the data from each whole module, as described in the previous paragraph. The bank ESDA (Ecal Storeys DAta) is created which contains the energy, module number, θ, ϕ and depth of each fired storey. If platine based corrections are available for that run, these are applied at this stage. As described in 5.4, the platine devices take data from Fe^{55} sources which track the changes in gas gain for each module with time. Gain changes at the 0.4% level can be measured. These time dependent factors are applied to each module by JULIA and are kept in the ECMC (ECAL Module Correction) bank.

The EDST (Ecal Dead STorey) bank is built from a combination of the list of permanently dead storeys from the database (EDDB - Ecal dead storeys) *; glowing storeys identified at the FALCON stage (EGLO); and the storeys killed in the ROCs (EKLS). Before the clustering algorithm is run, a check is made to see whether any of the storeys in the ESDA bank of fired towers is also in EDST, which are then flagged. A correction is made for missing pads based on interpolation of its expected value depending on its depth in the shower profile.

The JULIA routine ECCLUS handles the association of ECAL storeys into clusters and sums up their energies. A topological cluster is a group of spatially connected storeys. This is defined to mean that connected storeys share at least one corner. The conditions for connectivity are applied equally in all regions of the calorimeter - therefore clusters can include storeys from different modules and can span the barrel/end-cap overlap region.

The raw data input to the clustering algorithm is the bank ESDA. The clustering algorithm uses two thresholds: t_{low} which is currently set to 30 MeV and t_{high}, currently 90 MeV. A storey must have at least one storey above t_{high}. Only storeys which are above t_{low} are considered for inclusion in clusters. The cluster thresholds are held in the ECNS bank in the detector database. The thresholds may be altered if the data are later reprocessed. The algorithm scans the storey data bank, and starts a cluster around the first storey it finds exceeding t_{high}. A recursive algorithm then scans all the neighbours, adding them to the cluster if their energy exceeds t_{low}. The access method is optimized to run quickly [135]. The process is repeated until all clusters have been found. The output is a BOS bank called ECLU which contains the position and energy in the three stacks of each cluster. For each cluster there is also a pointer to the first storey in the ESDA bank which

* dead storeys may be found using the wire pulsing technique described in section 5.6

was used to start the cluster. In the ESDA bank, each storey is tagged with the index of the cluster to which it belongs, and a chain of pointers is kept between all the storeys in a cluster.

The possibility of dead storeys occurring within a cluster must be dealt with. As each event is being passed through the clustering routine, this bank EDST (Ecal Dead STorey) is accessed. If one of the neighbours to a cluster is a dead storey it is added to the cluster with an energy of 0.1 MeV. No attempt is made to correct further for the energy contained in a missing storey.

The routine ECFOBJ transforms ECAL clusters into calorimeter objects – ECOBs. The following quantities are computed for every cluster : region (end–caps, barrel, overlap); positions in theta and phi; particle identification variables; raw and corrected energy. To compute the corrected energy, corrections are applied for :

- **geometrical losses**: a particle entering a crack between two modules does not deposit its energy evenly. The energy in the HCAL directly behind may be used to compensate for losses in the crack. Also, a particle entering the overlap region between barrel and end–cap deposits energy in an insensitive region, and may also leak energy at the back as there is less depth of material here. An algorithm exists for energy compensation in this region.
- **clustering losses**: during clustering, storeys below threshold are not included, but their energy should then be accounted for and added to the cluster. A correction based on the region in the ECAL and the raw energy of the cluster is applied. The procedure used is based on test beam data.
- **saturation**: If the cluster has been identified as an electron or a photon, a correction is also applied for saturation in the calorimeter. The correction factor used is $1+7.8\times10^{-4}E$ *. This reflects the fact that the device does not measure all of the energy in the core of the highest energy electron showers. In the overlap region no saturation correction is applied as no electron identification probability is computed in this region.
- **leakage**: which takes into account leakage of energy from the back of the ECAL. Leakage can occur at any point in the calorimeter, due to the statistical fluctuations in shower size. This loss is parameterized as a function of energy

* based on the testbeam results of section 5.8

and incident angle. Energy losses in material before the calorimeter are not considered.

- **overlap correction**: in the barrel–endcap overlap region the energy observed is reduced. A correction based on test beam work is applied.
- **dead channel** corrections are not applied
- **an e/π ratio** correction is applied to the non–electromagnetic showers

The output of the clustering algorithm is the BOS bank ECOB (ECal OBject) which contains a list of clusters, their θ and ϕ coordinates, the energy in each stack, the region of the cluster, the number of dead storeys included in the cluster, and pointers to associated TPC tracks.

4.5.2 Charged Track Matching

The next step is to associate charged tracks with ECAL clusters. The information from the charged track banks (FRFT) is extrapolated to the entrance point into the ECAL. The track information (position, direction cosines, momentum and charge) at the entry point to the ECAL is put in the bank ETP1. Certain low momentum spiralling tracks are not considered safe to be extrapolated and are flagged as such i.e.–

- those tracks which spiral more than five turns
- tracks with a momentum less than 500 MeV (this threshold is in ECNS)
- tracks which end at a secondary vertex

A stepwise helix extrapolation is performed for each track. At each step the storeys intersecting the track are found. The clustering algorithm routines are used to see if this track or its neighbours are a member of a cluster. A track and a cluster are associated if one point of the track is in one storey of the cluster or if the track has one point in a storey which is neighbouring with one storey of the cluster. Therefore, the size of the 'road' searched for associating a track with a cluster is of the order of 3cm. The extrapolation is then continued until the track exits the ECAL. At this stage more than one cluster may be associated with a track. It is possible for many tracks to point to a cluster, but many clusters arising from one track would be difficult to interpret and so this is not allowed. Next, EcalObjects are constructed from the tracks and clusters. (It would be possible to split clusters to create composite entities, e.g. gamma plus extra energy, but this is not done.) Each ECAL cluster becomes an EcalObject. However, a given track may only be part of one EcalObject. This cluster is the one with which the track intersects first. The many–to–many relationship

between clusters and tracks is thus resolved. The EcalObjects bank ECOB also contains information on the particle identification hypotheses.

4.5.3 Association of HCAL Clusters

Next, the association of TPC tracks and ECAL objects with HCAL objects is performed. The data input to this stage consists of TPC tracks, EcalObjects and HCAL clusters. The tracks are split into two classes: those which are minimum ionising particles (i.e. those TPC tracks associated with no ECAL object or an ECAL object with an energy consistent with the particle being a mip) and others. For mip tracks the track is extrapolated through the HCAL (using the muon tracking routines). At each plane in the HCAL the distance to the neighbouring fired HCAL storeys is computed. If the neighbouring storeys in HCAL are within a distance consistent with multiple scattering then that HCAL object is associated with the track.

For other charged tracks which interact in the ECAL the association between the HCAL cluster and the EcalObject is made on the basis of the p_T w.r.t. the track. The smallest angle between the entering track and any storey in the HCAL cluster under consideration is computed. This together with the HCAL cluster energy gives the p_T. The decision to make an association is based on the angle, the p_T and the HCAL cluster energy. Neutral EcalObjects are assumed to have a straight track from the origin pointing to the barycentre of the cluster. These are then associated to HCAL objects in a similar fashion, based on the p_T with respect to the track (unless they are deemed to be isolated gammas – see below).

The last part of this stage is the formation of Calorimeter Objects – CalObjects, stored in the PECO bank. Each CalObject is a set of connected EcalObjects and HCAL clusters. A CalObject includes all the ECAL and HCAL storeys in which one or more primary particles have deposited energy. A primary particle should deposit all of its energy in one CalObject.

4.5.4 Neutral Particles

Neutral particles are isolated gammas and neutral hadronic particles which result from a comparison between the energy of a CalObject and the total momentum of all associated charged tracks. For each CalObject the program examines the particle identification hypothesis for each contributing EcalObject. The most likely candidate type is used and each particle is added to the bank PCPA. If the EcalObject is flagged as a mip, the energy is multiplied by the μ/ϵ ratio, otherwise the remaining energy is assumed hadronic and is

multiplied by the π/e ratio. Then all associated HCAL clusters are scanned, with the assumption that the HCAL is only hit by pions. Finally, the neutral energy particle associated with the CalObject is found. Its momentum is the difference between the sum of residual energies and the sum of track momenta. In order to obtain the best energy resolution with ALEPH, the TPC momentum is used for charged particles and the combined calorimeters are used for neutrals.

4.5.5 Energy Flow

The energy flow algorithm attempts to improve the uniformity of response and minimize the resolution of the calorimeter. It uses information from the three stacks of the calorimeter, plus the HCAL energy in a weighted fit which is dependent on the angular position of the shower in the calorimeter. The objectives of the energy flow analysis group was to devise methods in the JULIA reconstruction program to optimize the performance of the calorimeter. Their goals were to:

- achieve an unbiased estimate of the energy entering the calorimeters, unaffected by angular effects or dead zones
- achieve the best energy resolution possible
- give a precise value for the energy vector in the event

This is done to get the best possible physics : good measurement of jet energy and angles is needed for searches for non-interacting particles: missing energy and momentum imbalances are needed in the search for new particles.

The inputs to such an algorithm are from three sources. Firstly, the calibration information, which is discussed extensively elsewhere in this thesis. The calibration work ensures that the data input to JULIA is correctly calibrated with respect to absolute calibration, electronics (ADC and amplifier gains) and uniformity corrections. Corrections for missing pads will be handled by the on-line system. More complicated faults are handled off-line. Slow control corrections for pressure, temperature and voltage drift are computed in JULIA or at the analysis stage with code in ALPHA. Secondly, corrections are made for losses in the apparatus which are due to :

- dead zones : there are dead zones at the edges of all modules and also in HCAL there are spacer bars between the iron sheets.
- dead channels
- energy loss in the magnet coil and other non-sensitive material

- losses at small angles, which could be corrected using luminosity calorimeter information
- losses of low energy charged particles, which spiral in the magnetic field and do not enter the calorimeter and of low energy photons which are below ECAL threshold

Thirdly, corrections are included which depend on the physics processes in a particular event :

- the e/π ratio. ECAL calibrations are applied assuming the particle is an electron or photon : however the e/π ratio of the device is about 1.3 - 1.4. This is the factor which must then be applied if the deposited energy in ECAL is identified as belonging to a hadronic cluster.
- non-interacting charged hadrons in ECAL
- high energy muons. Muon energy is not well measured by the calorimeters; the TPC momentum should be used.

4.5.6 Electron Identification

The identification of electrons relies on information from the ITC, TPC and ECAL. This consists of momentum, dE/dx measurements, extrapolation into the ECAL and the energy deposit in each storey of the ECAL. Identification is only done for charged tracks in ITC and/or TPC which are associated with an ECAL cluster. Also, the following discussion is only valid for those clusters not near a crack. Seven 'estimators' are calculated for each candidate. The estimators are dimensionless quantities, which are the deviations of specified parameters from the expected values for a true electron. The estimators are based on test-beam data and Monte Carlo simulation. Four of the estimators describe some feature of a shower: its compactness, the longitudinal shape, the fraction of track energy deposited within the calorimeter. The others are the dE/dx and a comparison of the impact point on the ECAL with the shower centre. The energy deposited in the ECAL is more useful at high energy and the dE/dx at low energy.

Momentum-energy balance: The first estimator R_1 measures the difference in the TPC measured momentum and the energy measured by the ECAL :

$$R_1 = \frac{(E-p)}{\sigma(E,p)} \tag{4.5.1}$$

where: E is ECAL measured energy; p is track momentum; $\sigma(E,p)$ is the quadratic sum of the resolutions of the TPC and ECAL.

Transverse compactness: From ECAL test beam data, it was found that $\approx 83\%$ of the shower energy for an electron is deposited in the four central towers, independent of energy. The second estimator then measures the transverse compactness of the shower:

$$\begin{aligned} r &= \frac{\sum_{i=1}^{3} E_i^{(4)}}{p} \\ R_2 &= \frac{(r - r_0)}{\sigma(E)} \end{aligned} \tag{4.5.2}$$

where $E_i^{(4)}$ is the energy in the four closest storeys to the charged track extrapolation and r_0 is the value expected for an electron shower.

Longitudinal shape: The third and fourth estimators are concerned with the longitudinal development of the showers. As explained in 4.3.1, the showers are parameterized as:

$$dE/ds = s^{A-1}e^{-Bs} \tag{4.5.3}$$

The quantities chosen for the estimator are $a = 1/A$ and $b = B/A$ as A and B are strongly correlated. a and b are related to the energy deposition pattern in the four central towers:

$$a = \frac{E_0}{\sum_{i=1}^{3} E_i S_i} \tag{4.5.4}$$

where S_i is the barycentre in depth of stack i which is deduced by optimizing the parameterization of the energy deposition with respect to E. The estimators used are then:

$$\begin{aligned} R_3 &= \frac{(a - a_0)}{\sigma(a)} \\ R_4 &= \frac{(b - b_0)}{\sigma(b)} \end{aligned} \tag{4.5.5}$$

Energy loss in TPC: The fifth estimator uses the dE/dx information from the TPC to give a probability for a track to be an electron.

$$R_5 = \frac{(I - I_0)}{\sigma(I)} \tag{4.5.6}$$

Shower Barycentre: The final two estimators are based on a comparison of the shower barycentre calculated from the four central towers and the track extrapolation into the ECAL. In fact, these estimators are not used in JULIA.

The estimators are held in the bank EIDT (Electron IDenTification). This bank also has the overall electron identification hypothesis, which is computed from the estimators. The electron efficiency has been measured at 98%, and the pion rejection at 99%, (for single

particles above 2 GeV). In simulated hadronic events the electron efficiency above 5 GeV is 87%, with a hadron contamination of 0.7%. For lower momentum tracks, down to around 2 GeV, the dE/dx cut maintains hadron contamination at around 1%.

4.5.7 Photon Identification

In the case of photons, a given neutral ECAL cluster may either come from a photon, a $\pi^0 \rightarrow 2\gamma$, several photons, a neutral hadron or a mixture of these. Probabilities for each of these hypotheses are computed, using the longitudinal and transverse profiles of the shower. A search for photon energy contained within charged clusters is also made. The results of the identification of neutral clusters. i.e. candidate π^0s, gammas and neutral hadrons are stored in the bank PCPA (Pot Calorimeter PArticles). Neutral clusters in the ECAL are classified into the following types. depending on their proximity to discontinuities in the structure:

- cluster contained wholly in one module
- cluster close to a crack between modules
- cluster near the barrel–endcap overlap region
- clusters at low angle end of end–caps

For each of these categories, a different algorithm is used to extract information on the nature of the particle(s) responsible.

Clusters wholly within a module Similar techniques to the electron identification are applied to classify the cluster into one of three types: purely EM, hadronic or ambiguous. A second operation based on the transverse spread is then done to separate the electromagnetic clusters into single photons, double photons from π_0 decay and multi photons.

Clusters close to a crack The algorithm uses the ratios of the energies on either side of the crack to get the energy and location of a presumed photon. For particles near a crack, a correction is made. If the location of impact is directly in a crack, where most of the energy will be lost, a nominal energy is computed. HCAL information is not used at the moment. Monte Carlo studies have been made to tune this algorithm.

Barrel–endcap overlap region At present, these clusters are treated in the same way as wholly contained clusters, but are all classified of type ambiguous.

Low angles No correction is made at the moment for photons in this region.

4.6. ALPHA

ALPHA (Aleph PHysics Analysis) is the program used for physics analysis of ALEPH data. It is intended for use by the ordinary physicist in the collaboration, who is not an expert in the analysis software described above. ALPHA can process all types of ALEPH data: Monte Carlo tracks, raw data and reconstructed data in the full POT, DST and condensed mini-DST formats. All event input-output and BOS bank unpacking etc. is handled by ALPHA using the ALREAD package; the user only needs to supply a set of steering cards. ALPHA has many mnemonic names for physical variables, e.g. momentum or energy, meaning that the user does not need a detailed knowledge of the ALEPH data structures in order to do physics. Utility routines for event analysis, e.g. jet finders, sphericity products etc. are also part of the ALPHA package. Additional ALPHA routines which have been written by collaboration members, but which are not a part of the official ALPHA package may be placed on the UPHY (User PHYsics) disk. In this area, there are routines for the calorimeters energy flow algorithm, searching for π^0 in the ECAL, photon identification, tau tau selection, alternative fitting algorithms, ECAL calibration, selection of events good for physics etc. The ALPHA analysis program was used extensively for the data analysis presented in Chapter 6. Output from the ALPHA package is usually in the form of histograms or n-tuples, which can be displayed and manipulated by the PAW (Physics Analysis Workstation) program [136]. It gives one facilities for plotting, making cuts on and fitting HBOOK data and producing presentation quality graphs.

4.7. Event Directories

A new concept developed for the ALEPH experiment is that of the *event directory* or EDIR. An EDIR (electronic directory) is a file containing the physical location of each event (disk or tape file) and an entry for each event, which allocates it to one or more classes. These event types are based on the trigger fired, e.g. a luminosity trigger or an ECAL trigger, and on an event selection criterion, e.g. hadronic Z^0 decay. An EDIR file is created for each ALEPH run. One can use the EDIR as a preselection mechanism to ignore events not of interest in the particular analysis, e.g. beam-gas events, luminosity events and cosmic triggers, or to select only certain types of events, for instance all hadronic decays, in the data sample.

4.8. Graphics Displays

DALI (Display of ALeph Interactions) [137] is a two–dimensional event display program which runs on VAX graphics workstations. Its basic philosophy is to display events in several different projections : x–y, y–z. r–z, theta–phi etc. This enables one to see the characteristics of an event, i.e. match tracks and calorimeter clusters without needing a 3–dimensional view. Cuts can be made on track momenta, and also on the theta and phi angles. Fig. 4.8.1 shows a DALI plot of the first event taken by ALEPH, on the 14th of August 1989. This is a $Z^0 \rightarrow q\bar{q}g$ three–jet event.

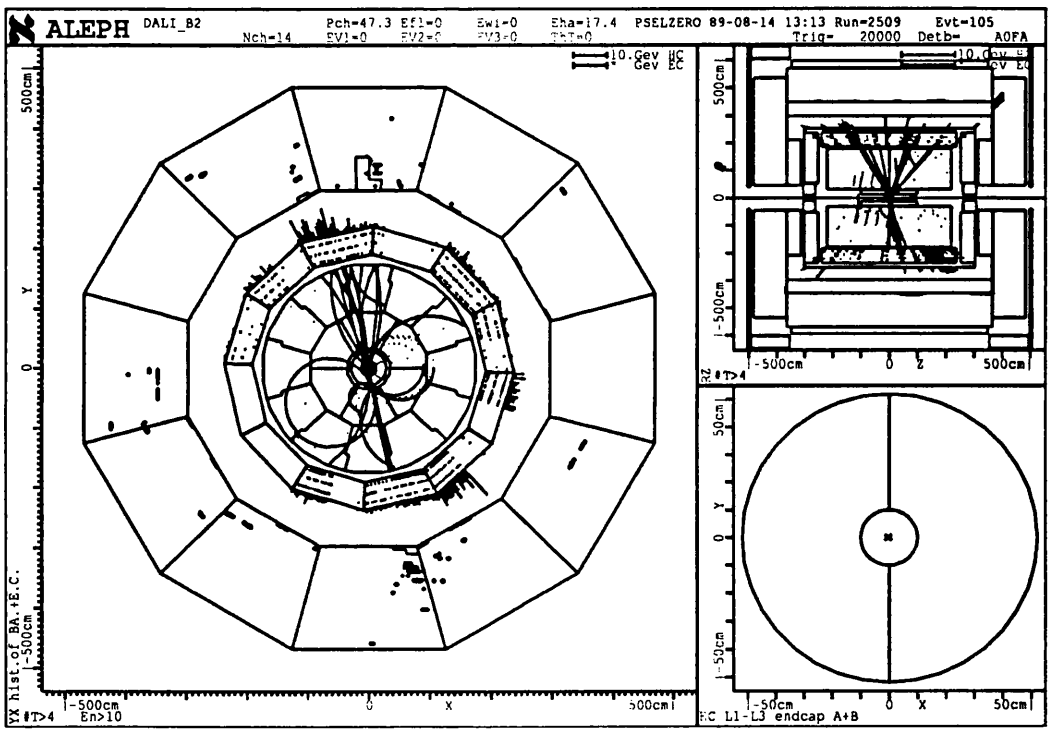

Fig. 4.8.1: DALI plot of the first ALEPH event

PIGAL (Prolog Interactive Graphics for ALeph) [138] is a 3–dimensional graphics and physics analysis program for ALEPH data. It is partially written in the Prolog artificial intelligence language. Using PIGAL, one can either draw or list any ALEPH data bank, and draw any part of the ALEPH detector in 3–dimensions. Rotations, zooming and the picking of tracks of interest are all possible.

4.9. Conclusion

The test beam measurements on which the parameterizations used in the GALEPH simulations are based is described in 5.8. The calibration constants used in the JULIA

reconstruction are based on this test beam work, plus radioactive gas calibration and wide-angle Bhabha scatter events, as discussed in 5.9 and 5.10. The validity of the Monte Carlo event simulation of hadronic events by ALEPH and the GALEPH simulation of gamma ray energy deposits in the electromagnetic calorimeter will be examined in part in Chapter 6.

Chapter 5.
The ALEPH Electromagnetic Calorimeter

'If work is so good, how come the rich haven't taken it all for themselves?'

5.1. Introduction

The ALEPH electro–magnetic calorimeter is intended to detect electrons, photons and neutral pions with a good energy resolution, high spatial precision and also to help in particle identification. At high energy, the electron energy measurement will improve on the accuracy of the momentum measurement possible in the TPC. The detector was designed to measure particles over as much of the 4π region around the interaction point as possible. The design goals were [139]:

- an energy resolution of $15\%/\sqrt{E}$
- measurements of particles from 50 MeV to 100 GeV
- a uniformity of response of 1% across the face of a module
- a granularity similar to the size of a typical EM shower
- position determination for showers to within $\approx$ 5mm

The above objectives had to be satisfied by a device capable of operating in a magnetic field of 1.5 Tesla, with high reliability, stable with time and able to absorb high rates of synchrotron radiation without aging. The device is placed within the magnet solenoid as studies indicated that if the calorimeter was to be placed behind 10cm of aluminium (equivalent to the magnet coil) the π/e rejection was significantly degraded; a high proportion of the particles would start to shower in the coil, worsening the position resolution and two–particle separation. In addition very low energy photons would be absorbed in the coil and could not be detected. The calorimeter was designed to have a high granularity to permit the separation of the many individual particles and specifically electrons in a jet and the isolation and measurement of photons. A conventional lead/scintillator design was rejected as the fine granularity would have been impossible to achieve with this technique. Large area scintillator based calorimeters also suffer from non–uniformity of response over the large scintillator sheets, problems of photomultiplier drift and radiation aging of scintillators which necessitates regular calibration with very stable light sources or radioactive

sources. The device chosen to satisfy all the criteria was a sampling calorimeter with gaseous wire–chamber readout. Monte Carlo studies indicated that this design should achieve an energy resolution of $15\%/\sqrt{E(\mathrm{GeV})}$. Due to the large number of readout channels the signals are highly multiplexed and read out by custom–built FASTBUS modules.

In order to achieve an overall consistent performance of the detector satisfying the design goals, the knowledge of the calibration and of the stability of operation must be at the 1% level. This chapter is concerned with the various methods used by the ALEPH collaboration to perform these tasks. The chapter begins by describing in detail the construction and layout of the end–cap modules. The tests performed on the modules at the time of building and the tolerances achieved in construction are presented. The readout electronics for the many thousands of channels in the calorimeter are discussed. The method of assessing the module performance by wire pulsing, where test signals are applied to the anode wire planes is described and the information gained by this technique is discussed. The cosmic ray test station which was constructed at the Rutherford Appleton Laboratory is described. All of the end–cap modules were tested using the cosmic ray muon flux, which gives a check on the correct functioning of all channels and may be used to give a uniformity map. Three of the modules were taken to CERN and placed in a test beam. This gives an absolute calibration with known electron, photon and pion energies. The modules were also tested in conjunction with barrel modules, to characterize the behaviour in the end–cap/barrel overlap region, and with a prototype HCAL module to investigate the response of the combined ALEPH calorimeter to pions. The next section concerns the technique of radioactive gas calibration. This gives a relative calibration among modules, and when compared with the test beam results gives an absolute energy scale. The radioactive gas results may also be used for uniformity mapping, although this was not the primary purpose for obtaining these data. Finally, a very short study has been made using Bhabha scatter events for energy calibration of the calorimeter.

5.2. ECAL Module Construction

The electromagnetic calorimeter, shown in Fig. 5.2.1, consists of twelve barrel modules together with two end–cap sections each with twelve 'petal' modules. Fig. 3.3.1 shows the ECAL in relation to the whole detector. Several of the French collaborating institutes are responsible for the barrel construction, the gas system and associated electronics. The UK institutes involved with the electromagnetic calorimeter are the Rutherford–Appleton

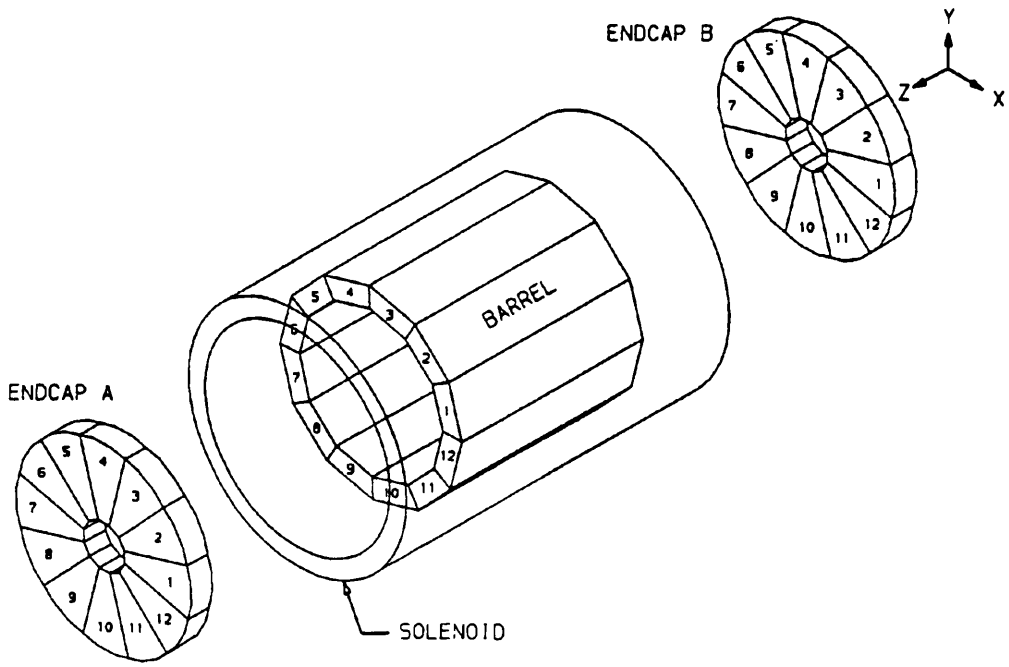

Fig. 5.2.1: The ALEPH Electromagnetic Calorimeter

Laboratory (RAL), Royal Holloway College and the Universities of Glasgow, Sheffield and Lancaster.

Each module (petal and barrel) consists of 45 layers of lead sheets interleaved with multiwire proportional chambers. The petal and barrel modules are constructed in a different fashion due to their different shapes and because the mechanical stresses on them are very different when they are in place on the detector: the barrel modules being oriented at all angles and the petal modules hanging vertically. The modules are constructed from non–magnetic materials in order to prevent any disturbance to the magnetic field. The petals weigh 2.6 tons each, the barrel modules 10.4 tons. The modules are divided up into three depth sections, making 22 radiation lengths in total. These are known as stacks 1, 2 and 3. Stack 1 consists of 10 layers of 2mm lead, making 3.46 radiation lengths. Stack 1 is separated from stack 2 by an aluminium plate. Stack 2 consists of 23 layers making 8.86 radiation lengths. Again, stack 2 is separated from stack 3 by an aluminium plate. Stack 3 has 12 layers of 4mm lead making 8.91 radiation lengths. The thicker layers in stack 3 reduce the number of readout channels and reduces the volume of each module. Early simulation studies [140] showed that there is no significant worsening of resolution with the coarser sampling in stack 3 as an electromagnetic shower is dying away in this region.

5.2.1 Wire Planes and Towers

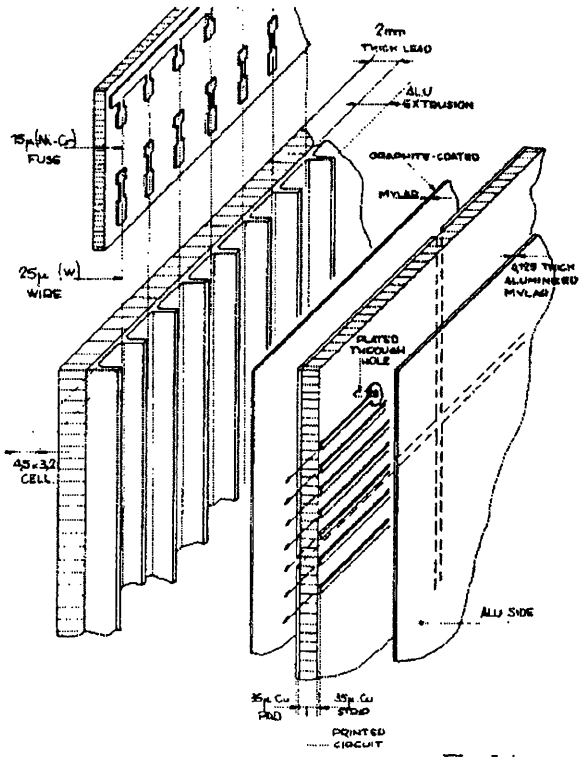

Fig. 5.2.2: Detail of Multiwire Chamber

Between each pair of lead sheets there is a multiwire proportional chamber, Fig. 5.2.2. The multiwire proportional chambers in the barrel section have wires running along the length of the module. In the end–caps the wires run parallel to the edge of a petal, rather in the fashion of a harp. Looking from the rear of a petal, the wires run parallel to the right hand edge. Each wire is contained in an aluminium extrusion of rectangular cross–section on three sides and on the other by a resistive layer of graphited mylar which permits signal pickup on a system of segmented cathode pads. The mylar has a resistivity of between 2 and 2.8 $G\Omega$/m. The extrusions were sorted into batches which have the same overall height to $\pm 50\mu$m and channel depth to $\pm 12.5\mu$m. Each layer is built of extrusions from the same batch. Overall, the extrusions have been measured to have have a height of 3.774 ± 0.038mm and a channel depth of 3.200 ± 0.022mm. As explained later, the uniformity is critically dependent on the constancy of these dimensions. The wires are 25 μm gold–plated tungsten on a 5.5mm pitch. There are 210 wires per plane. The high voltage supply to each plane is split into three sections, each with approximately equal area, using the circuit in Fig. 5.2.3. The wires are connected in pairs by fuses to the HT supply. This means that if there

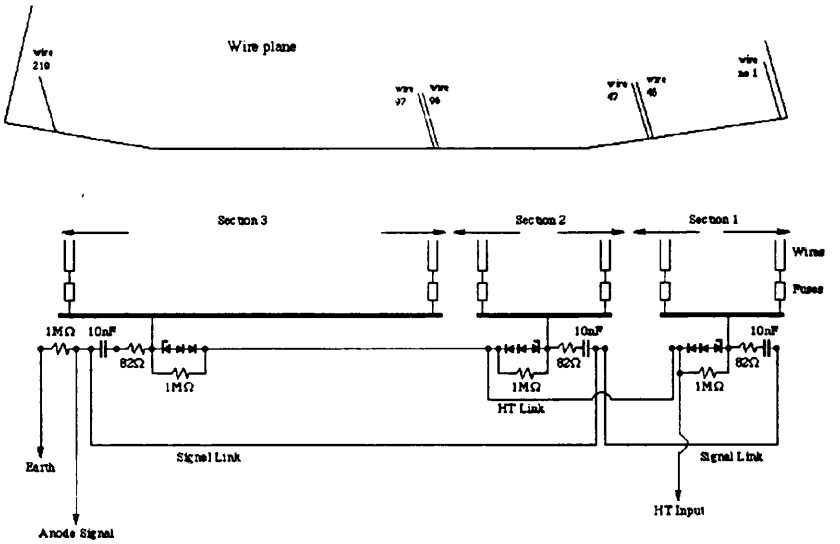

Fig. 5.2.3: Anode Wires HT Circuit

are broken or shorting wires, a pulse of current can be applied which blows the fuse and disconnects that pair of wires. This procedure has had to be carried out on most modules.

The wires are not positioned in the exact centre of the extrusion, as discussed in 5.4.2, but are 200 microns lower than centre. The wires are positioned to the correct height by nylon supports running at right angles: these wire supports are not necessary for electrical stability, but are intended to keep the wires from sagging, thus keeping the gain uniform to 1–2 % over a plane. The wire supports are staggered from plane to plane so that there are no 'dead' regions through the calorimeter. There is a signal read out from each complete wire plane, i.e. 45 channels per module, which is used in the level 1 trigger.

The main readout is from the cathode pads. The pads, of average size 3cm by 3cm, are grouped together to form 'towers' pointing at the interaction point, as shown schematically in Fig. 5.2.4. Each tower on average subtends 1.67×10^{-4} steradians, which is approximately the size of a typical electromagnetic shower. There are 25576 towers in the end–caps and 49152 in the barrel. The 45 pads in each tower are ganged together into the three depth sections mentioned above, and so there are three readouts per tower, which are known as storeys. One of the differences between petal and barrel is that in the barrel modules these cathode pads are on PVC sheets, whereas in the end–caps they are on fibreglass printed circuit (PC) boards. The printed circuit boards were manufactured in four sections per layer, and are carefully dowelled into place during construction. The pads are connected via through–plated holes to tracks on the reverse side which run to the edge of the module.

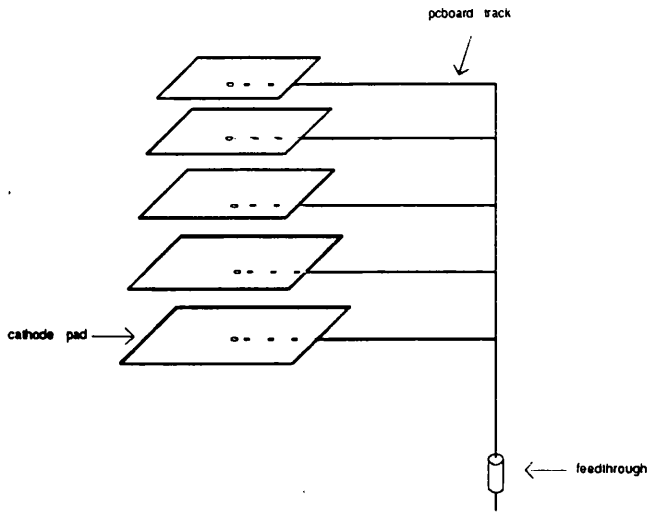

Fig. 5.2.4: Pad Tower

On the edges, the pads forming a tower are wired together and connected to the front-end electronics box by cables which pass through feed-throughs on the back face of the module. The pad boards in the petals have a complicated geometry. There are 50 rows of pads, laid out in two halves. When the petals are mounted one next to another on the end-caps these rows form concentric rings. The pad towers are planned such that there are no gaps in these concentric rings, however the modules must have casings and space for the readout cables down the sides. To leave space, one line of pads at the side is cut almost in half, resulting in 'half-pads'. In fact, some pads are completely missing even though they are logically in the readout order. The projective geometry also means that some pad rows are physically missing near the back of the petals - the towers simply project out of the module. The pads grow in size from the front of a tower to the back, and from the foot end of the module to the broad end. There are twenty different types of PC boards used to create this geometry. The pad geometry was planned using computer programs written by Steve Fisher of the Rutherford Lab. and outputs from these programs were used to instruct the computer-controlled routing and drilling machines used to manufacture the PC boards. The uniformity of the calorimeter is very dependent on the precision of manufacture and positioning of the pads. Fig. 5.2.5 shows the composition of one complete layer of the detector.

5.2.2 Slow Control Platines

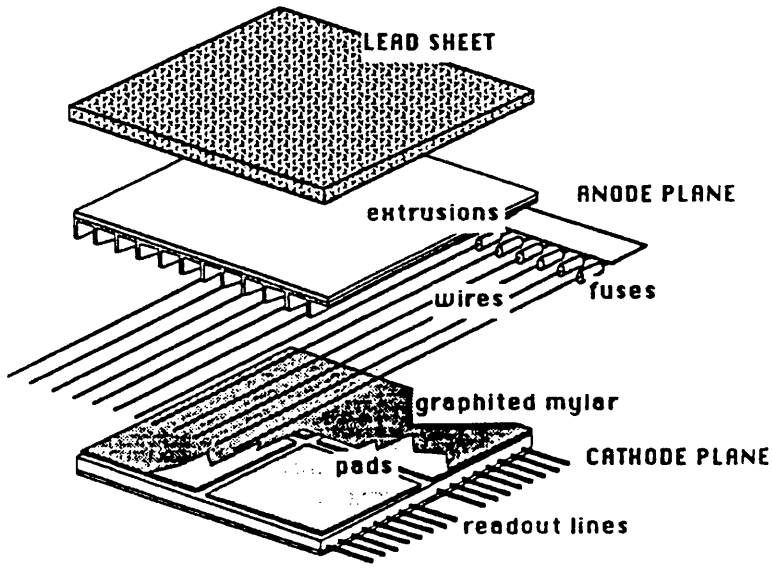

Fig. 5.2.5: Composition of one layer of the ALEPH ECAL

The gas conditions inside each petal are monitored by devices known as *platines.* A platine is bolted onto the back plate of a module, and is in contact with the gas volume. In ALEPH platines are mounted on each of the barrel modules, and one of each pair of end-cap modules. (The end-cap modules can share a platine as they are connected in pairs to the gas circulation system.) Each platine has a pressure sensor and a temperature sensor, plus a small ionisation chamber equipped with an Fe^{55} source which measures the mean charge collected from 6 keV X-rays absorbed in the gas, and so monitors the gas gain. The Fe^{55} chambers are inter-calibrated to 0.5% after manufacture. The response of gas gain to gas density changes is different for 6 keV X-rays than from ionising particles traversing the cells, so that for gain changes of more than 5% corrections must be applied for these effects. This is discussed in the section on electron calibration, 5.8.4.

The data from the platines, and such information as low voltage power supply settings and high voltage settings for each module is known as slow-control information. In ALEPH, such information is handled by a system based on the G64 bus. The slow control information is available to operators at the surface console, and is written periodically in the data stream as slow control records.

5.2.3 Tests During Assembly

Each component was tested before assembly into the final structure, and the completed module underwent several testing and calibration stages. Before assembling the module, all PC boards were checked and if necessary repaired to ensure good electrical contact from the interior of the petal to the outside. The aluminium extrusions which form the wire chambers were all selected to be within a small tolerance, as described above, since a very small change in dimension will affect the electric field and hence change the gain. The wire planes were assembled on a flat metal surface, and the anode wires for each plane were positioned, tensioned and soldered into place by a specially constructed wiring machine. Completed wire planes were 'flare tested' – where high tension is applied in air and the corona discharge from the wires is photographed. Such discharges indicate deformed regions on the plane and tracking at the HT rails. Any unconnected wires show up as dark lines. The planes at this stage were also visually inspected whilst high voltage is applied. Any area which sparks consistently indicates a fault, which was repaired. Next the PC boards, wire planes, mylar sheets and lead sheets were married in a partial stack. This stack was then 'tank tested' – high voltage is applied in an 90%Ar/10%CO_2 atmosphere and the currents drawn and spark rate per plane is monitored. Then all 45 planes were assembled and compressed for several days to make them as flat as possible. The individual pads were wired up into the projective towers, and the wiring checked. Completed towers were checked by measuring their capacitance. The assembly was then surrounded by a vacuum tight case. PVC bags were inserted between the layers and the top and sides of the case and araldite resin was pumped in under a pressure of 0.4 bar and allowed to cure. This procedure is intended to stop mechanical deformation of the planes when the modules are hung vertically on the end-caps of ALEPH. Detailed simulations of the mechanical loadings on the petals were performed using the NASTRAN finite-element package at the design stage. Also of concern is the possibility of creep in the lead planes since they are hung vertically. The lead alloy selected and the construction method chosen should minimize this. Fig. 5.2.6 shows the construction details of one complete petal.

5.2.4 Choice of Operating Conditions

The original choice for a gas mixture was 50% Argon / 50% Ethane. In the prototype tests, this mixture gave a resolution of $18\%/\sqrt{E}$ in the absence of a magnetic field. However, in a magnetic field of 1.37 Tesla parallel to the wires (as is the case for the barrel modules in ALEPH) the resolution worsened to $24\%/\sqrt{E}$. Simulations using EGS showed that this was due to low energy electrons spiraling along the wires. Tests were repeated using a

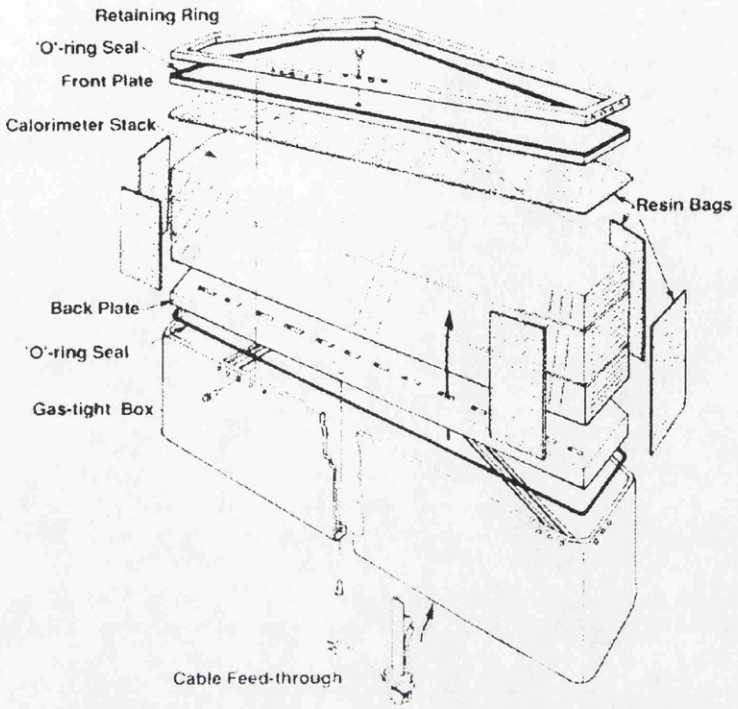

Fig. 5.2.6: An ECAL Petal

80% Xe / 20% CO_2 mixture and a resolution of $18.5\%/\sqrt{E}$ was measured. Xenon is a denser gas, which has a lower mean free path for the low energy electrons. This gas mixture should present no problems with chamber aging as no hydrocarbon–based additives are used*. The gas system constantly recirculates the mixture in the modules to ensure a uniform distribution of gas pressure and composition throughout the many small volumes of gas in each module, as the stability of the calorimeter depends critically on the gas gain. This will also help to avoid gas aging effects, although these are not a concern with this mixture. The gas system keeps the proportion of Xenon in the mixture to $80 \pm 1\%$. (It has been noted that a change of 1% in the proportion of Xenon changes the gain by 8% [110].) The gas system incorporates oxygen filters, as oxygen is an electronegative gas which stops the gas multiplication process. The petals operate at atmospheric pressure plus 60 mbar. Running at above atmospheric pressure means that if there are small leaks the gas mixture should escape, rather than atmospheric gases getting in. The gas temperature is required to be controlled to within 0.5°C. Samples of the gas in each module are taken periodically and analysed using a mass spectrometer. This was also done during the beam line tests.

* In multiwire proportional chambers using gas mixtures containing hydrocarbons, deposits of polymerized molecules can build up on the wires leading to changes in electric field and hence gain

The choice of high voltage setting for the running period is based on a calibration performed with radioactive gas, as described in section 5.9.

5.3. The Readout Electronics

Each tower of pads is wired together inside the petal and a connection is brought out through a feed–through to the front end electronics box which is situated within the detector. A typical tower has a capacitance of around 2 nanoFarads. Each tower is connected to an integrating amplifier, see Fig. 5.3.1. This shows the circuitry of one eight–channel front–end amplifier hybrid (the individual towers are connected to the points marked IP0 to IP7.) The front–end chips are manufactured to a custom design by the Neohm company using a thick–film hybrid process.

Due to the very large number of readout channels (216 000 in total) in the ECAL, it is impracticable due to reasons of cost, power consumption and space to attach a cable, an amplifier and an analogue to digital converter to each one. Therefore multiplexing of the readout must be carried out. The individual integrating amplifiers are grouped into sets of 32 which are read out by *summing amplifiers*, see Fig. 5.3.2.. The summing amplifier has two outputs: a low gain and a high gain which is 8 times the low gain. This is to enable the electronics to cover the full dynamic range required. The signals from the summing amplifiers go via twisted pairs to the FASTBUS analogue–to–digital converters (ADCs) in the barracks. The readout sequence is under the control of a FASTBUS module called the *sequencer* which uses digital control lines to operate the switches A, B, C and D. The sequencer is a programmable device, and the timings of the readout sequence can be changed between LEP fills.

Fig. 5.3.2 shows a diagram of the whole readout chain. For reasons of clarity, only one of the integrating amplifiers from Fig. 5.3.1 is shown.

5.3.1 The Readout Sequence

Looking at Fig. 5.3.2, the readout circuitry functions in the following manner. The charge from the front–end pads is integrated onto the feedback capacitors of the integrating amplifiers. Initially, the output from the summing amplifier is the sum of all 32 channels connected to it. When this has been read the summing amplifier is cleared, then each of the 32 channels are read out in turn.

The front–end electronics is normally cycling through a *refresh cycle* where signals are accumulated on the integrating amplifiers. If no event has occurred during the integration

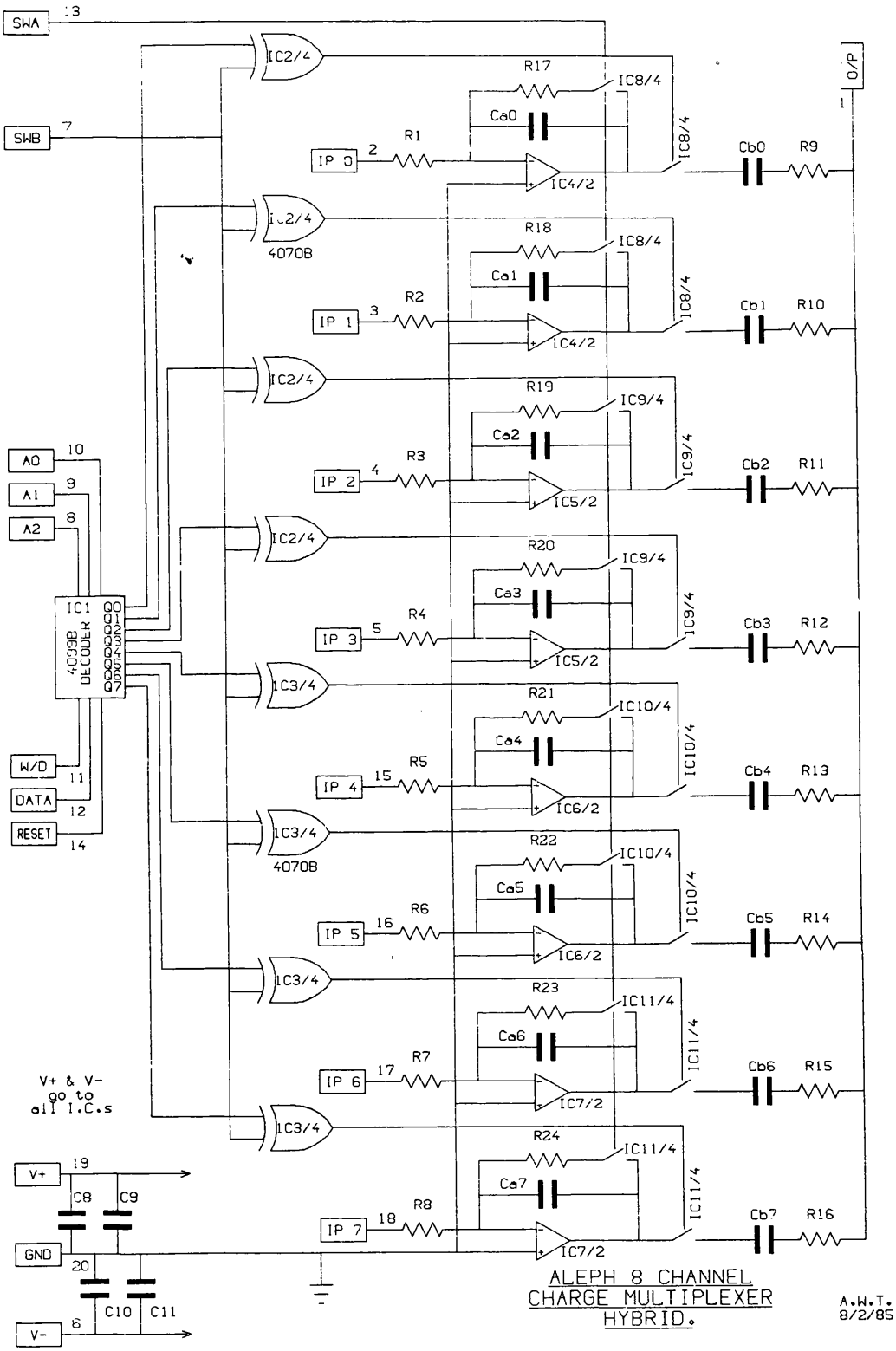

Fig. 5.3.1: Circuit Diagram of 8-Channel Hybrid

time, the accumulated charge on the capacitors of the integrating amplifiers is discharged. The refresh cycle is as follows :

- The switches are initially set to A open, B closed, C open and D open.

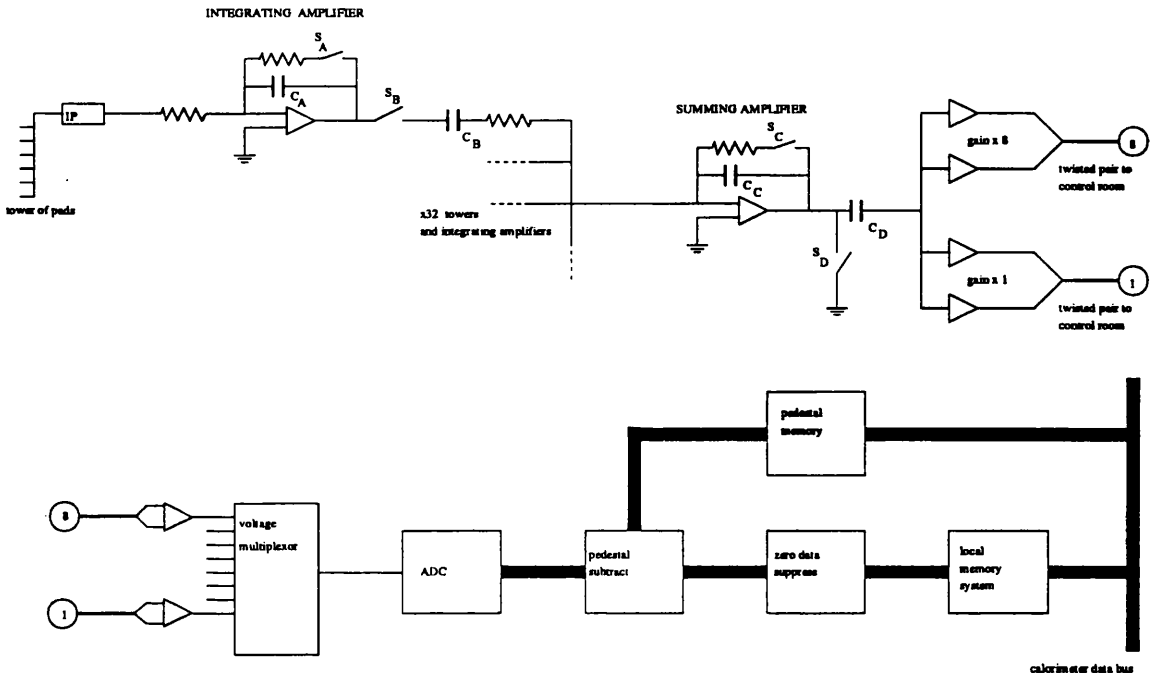

Fig. 5.3.2: Front-End Electronics

- After $1\mu s$ switch A is closed for $2\mu s$ to allow the capacitor C_A to discharge. Switch A is then re-opened. Simultaneously the C switch is also closed but C remains closed for $8\mu s$ to allow any transients produced by closing the A switches to die away.
- After $10\mu s$ the D switch is closed for $1\mu s$ to discharge capacitor C_D. The B switch remains closed.
- At $15\mu s$ the system has accumulated any signal on the front-end integrating amplifiers and is ready to receive a trigger signal to perform a readout.

If no trigger is received by $22.5\mu s$ a fresh sequence is started.
When the trigger signal is received, a readout sequence is started. Each of the integrating amplifiers transfers its charge to the storage capacitors C_B. These are then read out one-by-one by the summing amplifiers. The readout sequence is as follows:

- Initially, the switches are at A open, B closed, C open and D open. When a particle showers in the calorimeter, charge is collected from the tower pads on the capacitors C_A. (A 1 GeV particle deposits around 6 picoCoulombs of charge per storey.)

- Over the first $5\mu s$ switch A is open and the B switch remains closed. The operational amplifiers then act as integrating amplifiers. The time constant of the circuit is 720 ns, so waiting for $5\mu s$ means all the charge is collected on C_A.
- After $5\mu s$ the B–switches are opened, which isolates the capacitors C_B. After $6\mu s$ the A–switches are closed to discharge the capacitors C_A.
- The C–switches are closed at $5.1\mu s$ to prevent charges being accumulated on C_C due to transients. After a further $6\mu s$, when the circuit has settled, the C–switches are re–opened.
- Then each of the 32 integrating amplifiers is read out in turn, by the following steps in each case :
    1. the appropriate B switch is closed for $3\mu s$, thus transferring the charge on this channel to C_C.
    2. after a $7\mu s$ delay the C switch is closed for $2\mu s$, transferring the charge to C_D
    3. the voltage on C_D is then read by the FASTBUS ADC.
    4. the C switch is then closed

The whole readout sequence takes of the order of $400\mu s$.

5.3.2 The FASTBUS System

The components for the readout and control of the calorimeter are based on the FASTBUS standard. The ADC modules (F6845 ADC [141]) are single–width FASTBUS modules which process and zero suppress 3072 channels. This corresponds to the high and low gains for 512 towers, i.e. half a petal module or one fourth a barrel module. As has been said, the front–end electronics are multiplexed by a factor of 32, and at each of the 32 digitisation cycles the ADC digitises the data from 16 towers, using another level of internal multiplexing by 8. The ADC contains 3 digitising sections (one for each stack) and a zero–suppression section. A digitising section contains four AM6112 12–bit ADCs and three 512×12 bit memories, containing the high gain data, low gain data and zero– suppression thresholds. Zero suppression involves choosing either the high–gain or the low–gain signal (if the high–gain has saturated the ADC) and comparing this with a threshold before pedestal subtraction. The AM6112 chips have a conversion time of 7 μs and the total conversion time for the 3072 channels is 2.2 milliseconds. The readout cycle of the front end and the digitisation cycle of the ADCs are controlled by the sequencer module. Signals are sent from the sequencer

to the digital control cards in the front end boxes via the *fan-out* modules. The anode readout is controlled by the MUX45 module in its own special crate. To save space and power in the electronics racks, the wire signals are sent to spare channels in the normal pad ADCs, and the anode signals are then part of the normal pad read-out sequence and have to be separated out by the ROC. For each module an anode wire signal summed over all 45 planes is also taken. The PASTIS module takes a sampling every 512 ns during the rise time of these signals. This gives a measurement of the time of interaction of these particles in the ECAL with a resolution which varies from 50 ns at 500 MeV to 20 ns at 45 GeV. This timing information is used to reject out of time events, e.g. cosmic background events. A full readout of the calorimeter takes around 6 milliseconds (including 10 refresh cycles to get charge on the integrating amplifiers back to base level).

After digitisation and zero-suppression in the ADCs the data are read out by a Read-Out-Controller (ROC). The ROC is a device unique to the ECAL. It performs the tasks of:

- radioactive gas signal readout
- control of wire pulsing
- calibration of front-end electronics between fills
- downloading of zero-suppression thresholds at start of run
- readout of the ECAL data
- pedestal subtraction
- gain correction
- on-line corrections for e.g. missing pads
- formatting of the ECAL data into an order suitable for the offline programs

The ROC is a FASTBUS master module, based on a bit-slice processor. Each ROC reads out 17 barrel or 27 end-cap ADCs. A single Event Builder (EB) module reads out the data from all the ROCs and presents this to the main ALEPH EB, which is then read out by the online system computers. If a valid event has occurred then the ECAL data are read out from the front-end FASTBUS crates by the main ALEPH data acquisition system, described in 3.15. The online system uses a combination of FASTBUS hardware and VAX computers to interrogate each sub detector, read out the relevant data and format it into complete events.

5.3.3 Electronics Calibration

The calibration of the front–end electronics consists of injecting a known charge (of the order of pico–coulombs) into the input of the amplification chain. The response measured is the ADC counts for that channel. For the wire electronics, calibration is possible for each plane as there is a known injection capacitor for each channel. It is not possible to calibrate each individual front end pad channel since they are multiplexed. For the pads, test pulses are injected after the multiplexer. The gain of the first part of the chain, the integrating amplifier plus multiplexer, depends only on the ratio of two capacitors. This is trimmed to be 1.000 ± 0.005 at the production stage.

The purpose of the calibration is to check that the readout chain is working, to identify disconnected summing amplifiers and to measure the gain and linearity of each summing amplifier. Diagnostic histograms of these quantities are presented in the control room to help with fault diagnosis. The electronics is calibrated before each LEP fill and the results are loaded into the ROC for corrections, or in the case of dead channels are included in a bank in the event read–out.

5.4. Uniformity

The ALEPH ECAL uses multi–wire proportional chambers for readout, therefore the response is critically dependent on the gas gain. This in turn is dependent on both the physical parameters of the gas and the exact mechanical dimensions of a wire cell (which affects the electric field around the wires). An early study [142] showed that the gain was most sensitive to the vertical position of the wire in the extrusions, the height of the extrusions, the radius of the wires and the lead sheet thickness. During construction, as has been explained, great attention was paid to the quality control of these parameters and also great care was taken in compressing the stacks to achieve flatness of the layers. The figure aimed at was a flatness of 1mm per metre. The later sections of this chapter discuss the various methods used to measure the uniformity of response.

5.4.1 Pad Position

Tests on a small test chamber where a vertical force was applied on the cathode pad layer showed a variation of 7.5% to 10% for a change in position of 100 microns. As discussed above, the wire planes were built from aluminium extrusions which were sorted into batches with depths to $\pm 12.5 \mu$m. This should result in gain variations between wire layers of $\pm 1\%$.

5.4.2 Wire Position and Wire Diameter Variation

The gas gain at the wire depends on the electric field, which is at a minimum when the wire is exactly centred in the middle of the cell. The gas gain has a quadratic dependence on the vertical position of the wire in the cell as shown in Fig. 5.4.1. The same quadratic dependence on position also holds for the pads, however the minimum in gain for the pads is at a wire position of 300μm below the centre. This displacement is due to the pad–to–wire coupling. The least sensitivity of wire (pad) gain to small displacements is obviously achieved when the wire is at the minimum point. It was chosen to position the wires at 200 microns lower than centre where the gain dependence for the pads is $\frac{2}{3}$ that for the wires. The plastic wire supports keep the wires to within $\pm 30\mu$m of the nominal value. This should result in $\Delta g/g$ of $\pm 0.8\%$ for the pads and $\pm 1.2\%$ for the wires. No effect due to horizontal wire position was noted in [142].

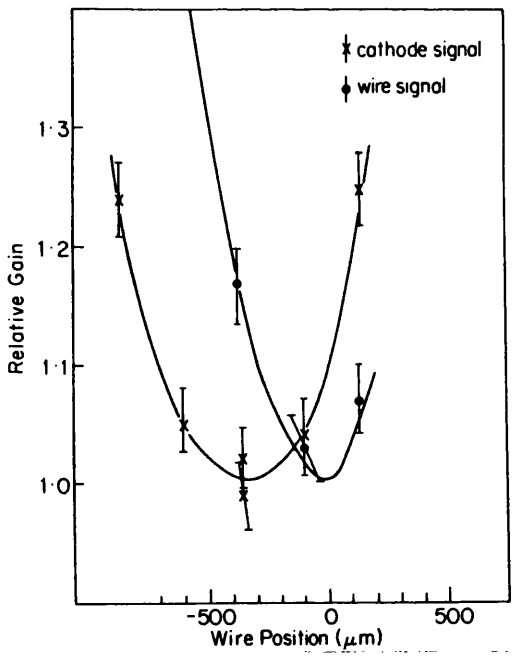

Fig. 5.4.1: Variation of wire and pad gain with vertical wire displacement

The anode wires have a tolerance of $\pm 0.25\mu$m on their 25μm thickness. The gain variation as a function of wire diameter has a dependence to the power 3.5 to 4, so a 1% change in wire diameter results in a 3.5% to 4% local variation in gain.

5.4.3 Layer Thickness

Variations in the thickness of stacks will affect the sampling ratio between active and passive layers. Variations in the thickness are due to the cathode pad boards, which in the petal have a tolerance of $\pm 70\mu$m, and the lead sheets which have a tolerance of $\pm 50\mu$m. Local thickness variations will also cause a change in the pad to wire coupling in the regions between wire supports. The wire supports in successive planes are staggered to average out these effects. Also, as a typical shower is sampled over 15 planes the differences should average out. A systematic 50μm increase in all lead planes would result in a 2% change in gain.

5.4.4 Voltage Variation

The changes in gain as a function of high voltage are discussed in the sections on beam line tests, section 5.8, and radioactive gas calibration, section 5.9. The slow control system aims to keep the voltage setting constant to within one volt.

5.4.5 Gas Density

Variations in the gas density through the module will cause changes in the gas gain. These are caused by absorption or outgassing and by temperature gradients in the modules. Daily variations in the gas gain have been measured with the platine temperature probes during the test beam running in the West Area. However, the ALEPH pit is, in principle, a constant temperature environment and these problems should not occur in normal running. Using test beam results, the gas gain was found to depend on the density to the fifth power, as discussed in section 5.8. As the pressure changes due to outgassing, leaks etc. there will be changes in gas gain. These are tracked by the Fe^{55} chambers in the platines and corrections may be applied. At constant density the gas gain has no measurable temperature dependence.

5.4.6 Electronics

The uniformity of response also depends on the response of the front–end electronics. Each group of 32 channels has been designed to have a tolerance in gain of 0.5% by matching of the capacitors to $\approx 2nf$. Measurements have shown that this requirement has been met. The summing amplifiers are calibrated by injecting known charges and, after calibration, are within similar tolerances.

5.5. Calibration

Calibration is the procedure involved in obtaining the formula for turning the raw data values from the calorimeter into accurate measurements of the deposited energy. This relationship is given by the formula [145]:

$$E = \left(\frac{1}{C_M}\right) \langle F \rangle \sum_{k=1}^{3} \sum_{j} f_{jk} \left(R_{jk} - P_{jk}\right) \tag{5.5.1}$$

where :

E : energy in GeV;
C_M : calibration constant of the module (in pC/GeV) ;
$\langle F \rangle$: mean electronic gain (in fC/GeV) for all channels;
f_{jk} : normalized fractional electronic gain of storey j of stack k. (These values were determined by injecting test charges into the summing amplifiers);
R_{jk} : ADC counts from this storey;
P_{jk} : ADC pedestal for this storey.

The relationship between the energy deposited and the charge collected on the pads can only be determined experimentally. The calibration procedure determines this relationship for each module, tracks its variation with time and corrects for malfunctioning channels. In the following sections, we are primarily concerned with the calibration for electro-magnetically interacting particles (electrons and photons). Muons and hadrons require different calibration procedures. The methods of calibration and monitoring are as follows :

- absolute calibration with electrons of known energy in a test beam. Unfortunately, only a small number of the modules can be tested in this fashion, and it may also not be possible to repeat this calibration at regular intervals
- relative calibration among modules and between the channels of a module (uniformity mapping) using the response to cosmic rays and to filling with radioactive gas
- use of events with well-known energy (Bhabha scatter events) during LEP running
- monitoring of the drift of gain versus time using the Fe^{55} test cells in the platines

The relative calibration among modules again depends on their mechanical construction, the gas gain and the gain of the electronics. A precision of 1–2% in the relative calibration is expected. The uniformity of the channels in each module has been measured to the 1–2% level, so the relative gain of each channel will not be dominated by systematic errors. The calibration methods are presented in the following sections.

5.6. Wire Pulsing

In the wire pulsing technique signals are applied to each of the anode wire planes and the induced signals are read out from each pad channel. This enables confirmation to be made of the successful operation of the module readout. The technique serves as a diagnostic for finding faults, either in the hardware of the petals themselves or in the readout electronics chain. The end-cap modules have had the wire pulsing technique applied to them on many occasions, principally following manufacture to diagnose any serious shortcomings, prior to installation at LEP in 1989 and between periods of LEP running. The results in this section are based on studies made with a complete set of wire pulsing data taken in July 1989.

It was also intended to use the wire pulsing data to measure the petal uniformity, as the signal induced on a pad is proportional to its capacitance, and any variations in capacitance due to differences in pad-to-wire coupling will have an effect on gas gain. This method is used for barrel modules to measure the distance between pad and wire – from which the wire position in the cell is deduced – and thus to determine the wire gain and the module gain maps for pads and wires. As will be explained, this procedure is not possible for the end-caps because of stray capacitances. The rest of this section discusses the method of data collection, analysis and display by graphical means of the wire pulsing data for the end-caps.

5.6.1 Data Collection

The electronics for applying the signals to the anode planes are contained in the MUX 45. The petal is first disconnected from the HT supply (this is not strictly necessary as the circuitry was designed to operate with the voltage on, but there is less possibility of noise if the petal is disconnected). For each plane in turn, the anode wires are pulsed with a signal of around 20 volts. This induces a signal on the cathode pads which is read out using a normal readout sequence. (Even though the pad planes are grouped into 3 storeys for readout, it can be seen that this technique gives signals for each individual pad plane when the readout is taken.) Each plane is pulsed 100 times and the results averaged.

5.6.2 Graphics Display of Wire Pulsing Data

In order to examine the approximately 45000 pieces of data from each of the petals, it was decided to develop a graphical display for the wire pulsing data. Standard histogram plots, such as those in the PAW system are useful for comparing the data from petals, for

taking means etc., but the special geometry of the petal pads means that a standard square histogram plot would not be useful to display the raw data. The data are read onto the disk of a VAX graphics workstation. The display software is based on the GKS graphics standard. In one version of the program, the data may be displayed on a plane–by–plane basis, and in another each stack of the petal is summed and the data displayed. The user is asked to choose the end–cap containing the petal, the number of the petal and the plane of interest. For each plane, those pads which are logically missing from the readout are flagged (e.g. those pads near the broad end of the petals nearing the rear face, since the towers project out of the module). For each plane requested, the program chooses the correct printed circuit board type (of which there are 20 in the end–caps). Before display, the data may be corrected in several different ways, as discussed below. A mean data value is taken for each plane, and the data are then plotted as a percentage of this, on a 'temperature scale' with increasing red hues indicating high values, and blue low. Pads within 2% of the mean are displayed in yellow. Each pad is displayed using its real geometrical shape. The positions of pad corners and pad areas were taken from a program written by Mehrzad Talebzadeh of the Rutherford Lab, which in turn was based on the programs used to drive the milling machines which made the pad boards. The wire supports and boundaries of the high voltage feed regions may also be drawn in. The display shows the correct geometrical relationship of pads, wire supports and the three high voltage regions on each plane. Facilities exist for the printout of values for a particular plane, and the creation of PAW n–tuples for planes or entire petals worth of data. Fig. 5.6.1 shows the wire pulsing results from a typical plane, viz. plane 4 of petal A1. The values in the key are percentages of the mean value. No corrections have been made to the values presented in this figure.

When the raw wire pulsing data are examined, it is clear that there is a large range of values for the pads. Fig. 5.6.2 shows the values of wire pulsing data from a typical wire plane, again the fourth wire plane of petal A1. The plot shows the wire pulsing values as a function of the row number 1–50 which increases from the narrow end of the petal near the beam line. There is a very complicated structure in the data. However, the values follow an obvious pattern – increasing along pad rows, getting larger towards the broad end and some very small values for the 'half–pads' at the edges. Detailed studies of the uniformity would need corrections to be applied for the effects which produce this complicated distribution.

5.6.3 Corrections to Wire Pulsing Data

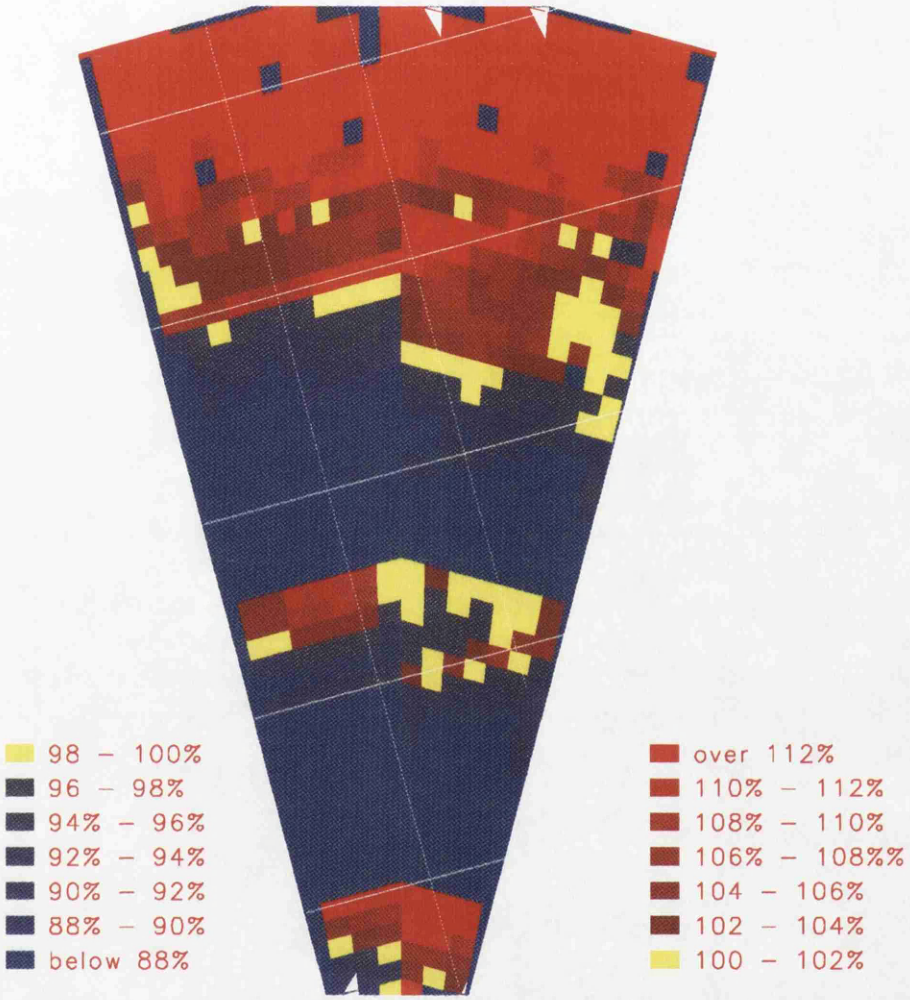

Fig. 5.6.1: Wire Pulsing Results for One Plane

The first approach tried for the uniformity correction was to make a correction for capacitance per unit area, ie. to normalize the pad signals to a certain area. This correction results in plots such as Fig. 5.6.3, which is again plane 4 of petal A1. The variations in pad response along rows are eliminated, but there remains a gross imbalance between the two sides (the left side being lower than the mean) and the region near the broad end shows very high values. The reason for the two–sided imbalance is that on the left hand side the pad rows run mostly at right angles to the wires, so wires cross pads in a regular fashion. On the other side there is a more complicated situation. The reason for the broad end having a very much higher response is less clear. After much discussion, it was realised that the tracks on the reverse side of the PCBs which connect the pads to the readout wiring at the

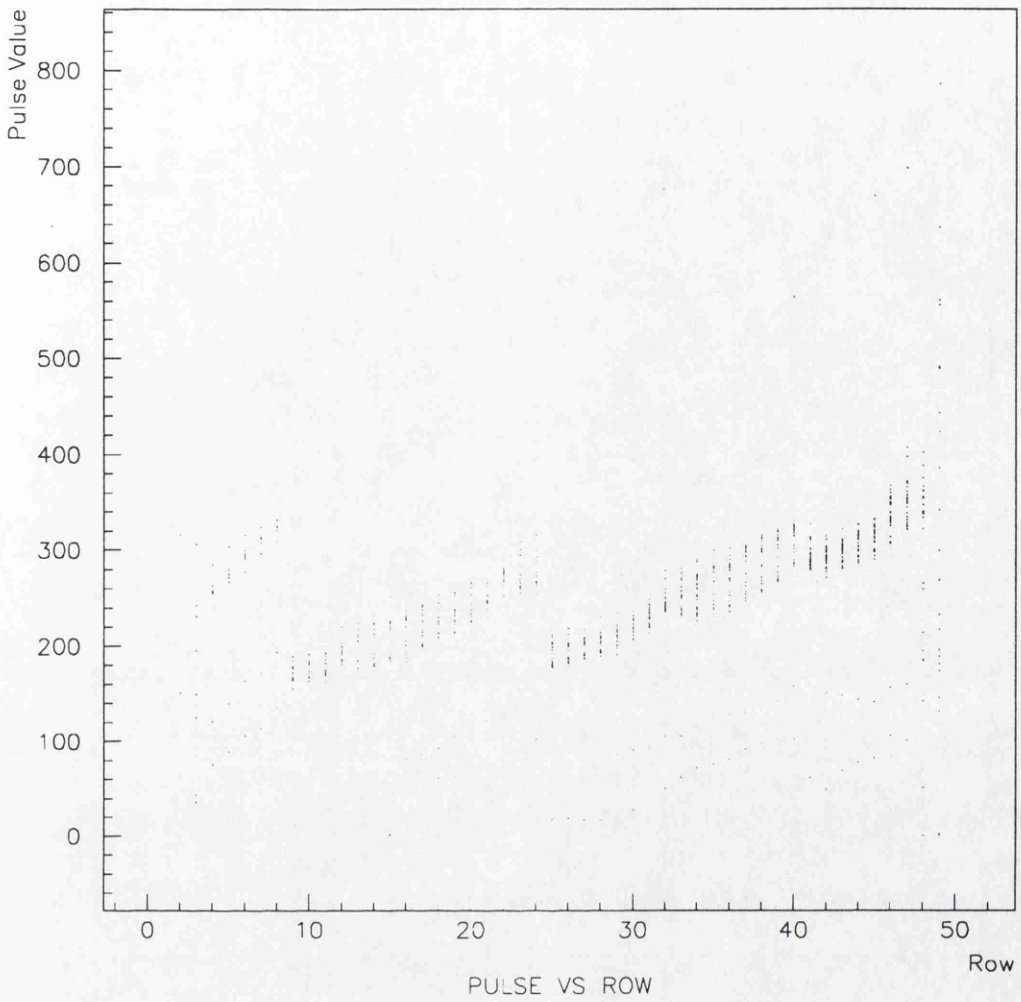

Fig. 5.6.2: Wire pulsing values along plane

side of the petal are also influencing the wire pulsing readout signals. At the narrower end of the petal, the tracks exit from the sides. At the broad end of the petal the tracks run towards the top end of the petal, rather than the sides in the same fashion as all the other pads. These readout tracks cross over the high voltage supply lines. It was also noted that the very topmost row of pads on each layer was giving very high signals. This is due to coupling between the high voltage rail running along the top of the module and this last pad row, which overlaps it. This problem is not present in the barrel modules which have a different design.

The next attempt at a uniformity correction was to correct each pad for the length of wire under each pad, rather than just the pad area. Fig. 5.6.4 shows plane 1 of petal A2. The data values in this plot have been corrected for the length of anode wire below each pad. The effect of the wire supports, which increase the capacitance and hence the signal of

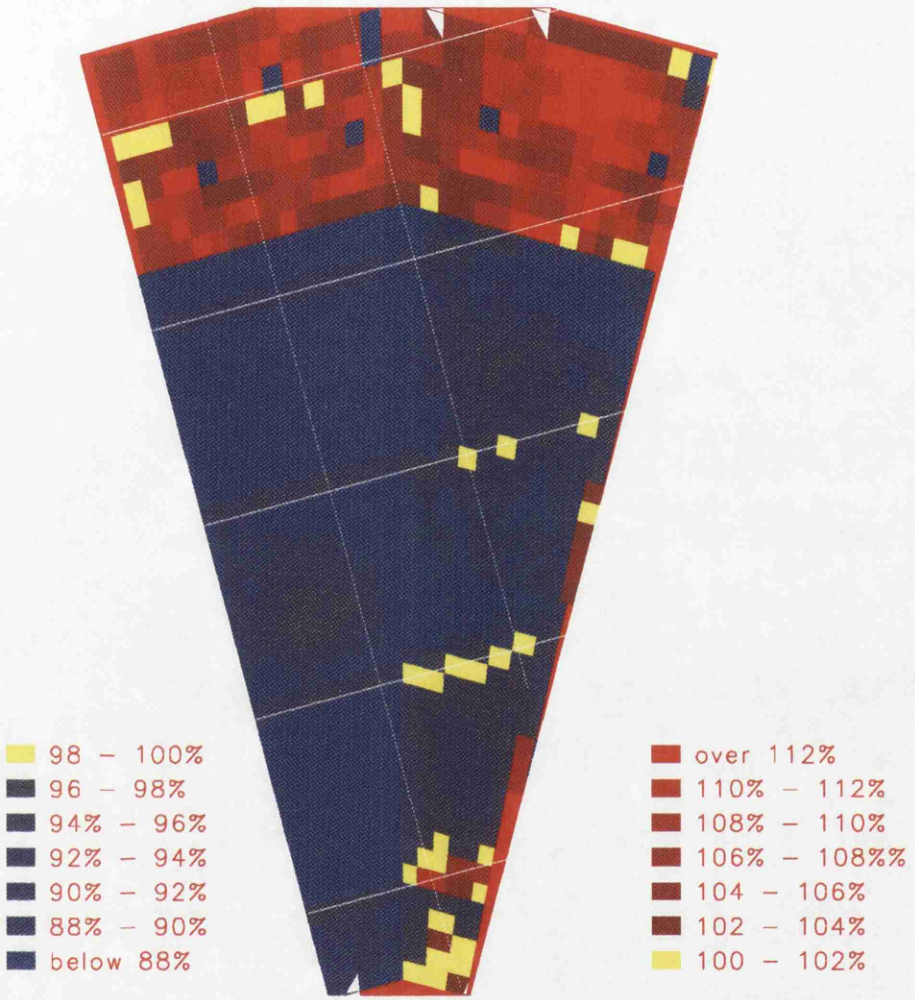

Fig. 5.6.3: Wire pulsing data – corrected for pad area

the pads which are above them by a few percent, can be seen. This plot clearly shows the left/right imbalance in the wire pulsing values and the very high values at the broad end of the petal. On the right hand side, there is some evidence for high and low areas between the wire supports. These high and low areas may well be related to measurements of the pad–to–wire coupling in these regions. If corrections could be found for the gross imbalances, then the wire pulsing technique could be used to look at the pad–to–wire coupling in the end–cap modules.

In order to try to correct for the gross imbalances described above and hence to approach a usable uniformity map, an approach which takes into account more factors which affect the pad response was tried. The PC board track length can have a significant contribution

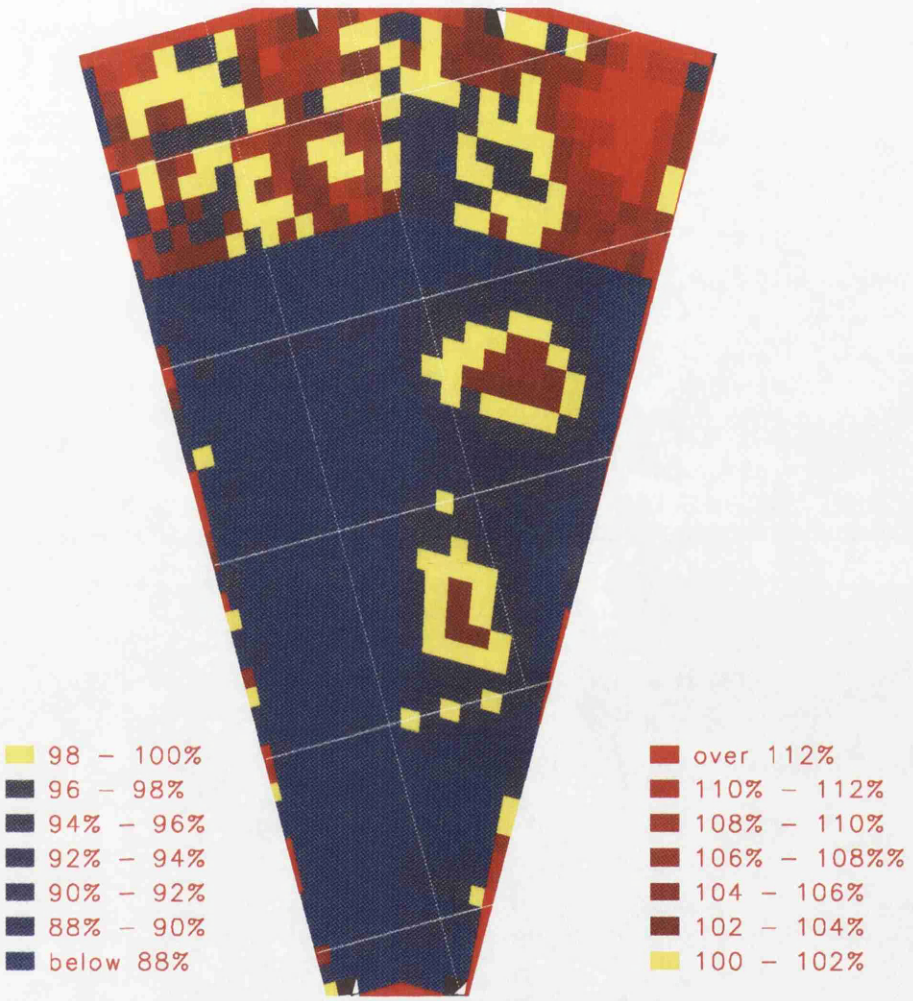

Fig. 5.6.4: Wire pulsing data – corrected for wire length

to the capacitance of channels in the end-caps. Files were obtained which give the PC board track length: both the 'screened' length under the lead layers and the 'unscreened' length at the sides for each of the 20 PC board types. Studies were made using PAW and the MINUIT package to assess the contribution of the PC board track length to the wire pulsing signal. The approach taken was to find a weighting function for the length of anode wire under a given pad, the screened track length and unscreened track length which minimizes the spread in values of pad response. Attempts to find such a function which would be valid for all petals were unsuccessful.

5.6.4 Search for Faults

The wire pulsing technique may however be used to diagnose any defects in the modules themselves, or in the readout electronics. Such defects give rise to characteristic patterns. For instance, a single storey of pads which has not been correctly connected to the side wiring shows up as a low in the plot of values for a stack. Faults in the front end electronics generally show up as groups of adjacent anomalous channels. The defects in the modules may include:

- single disconnected pads
- connected pads
- broken anode wires
- missing anode wire sections (HV disconnected and/or wire signal not available)
- disconnected planes
- disconnected storeys
- shorted storeys
- malfunctioning front-end amplifier channels
- faulty summing amplifiers

In the case of small corrections for defects which produce a perturbation in one layer of a shower, such as missing pads, connected pads, missing wires or missing wire layers the software in the online system is used to apply the corrections to the reconstructed storey and wire energies. The corrections are based on an average shower profile. In the case of a defect which affects the formation of a cluster, or the cluster energy by a significant amount, for example a dead storey which is part of a cluster, that storey is added to the cluster with an energy of 0.1 MeV.

Disconnected wires show up very well on the colour plots of wire pulsing values. As has been detailed in the section on petal construction, section 5.2, the anode wires on each plane are connected in pairs by a fuse to the high voltage supply. If the graphics display is used to examine each plane, certain planes show a characteristic stripe of low values, which indicates a 'dead' pair of wires where the fuse has been blown. Fig. 5.6.5 shows a plot of the wire pulsing values for plane 7, petal 2 of end-cap B. These data have not had any corrections applied to them. The solid white lines show the position of the wire supports for this plane and the dotted lines show the boundaries between the three high voltage regions. The missing wire pair may be seen as a blue line of low values running parallel to the rightmost dotted line. It is obviously important to be able to identify exactly

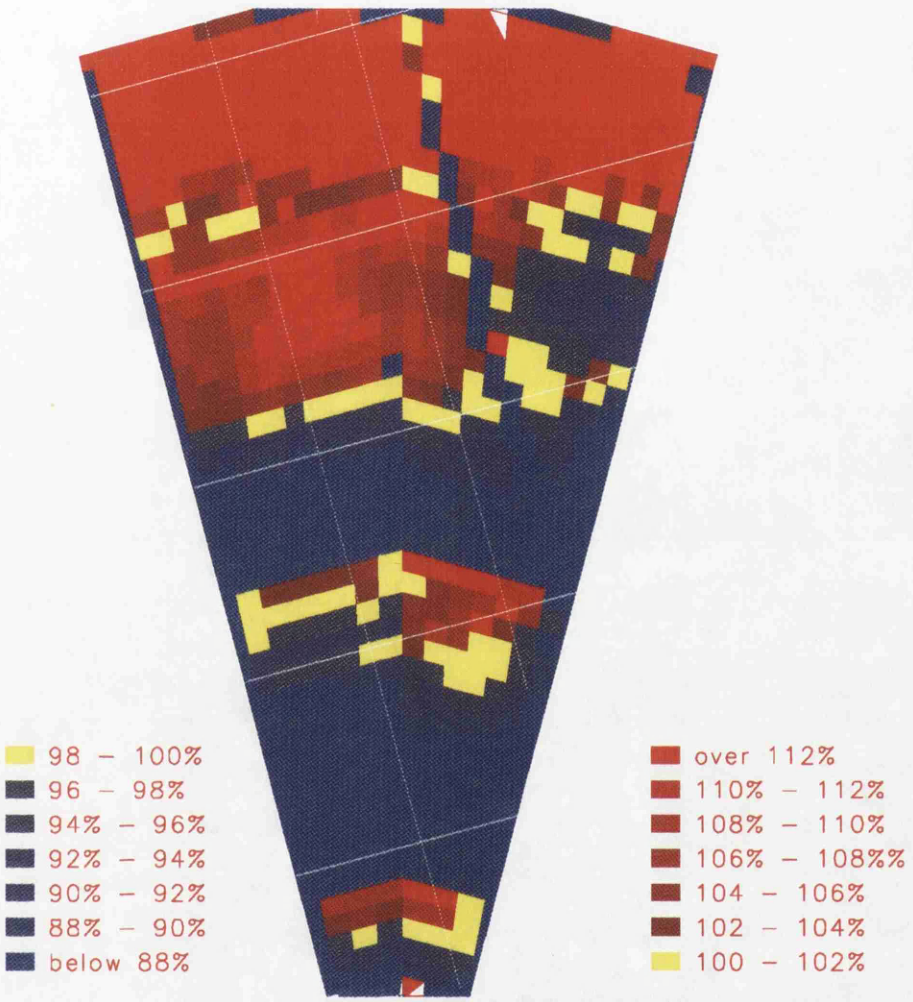

Fig. 5.6.5: A Plane with a Dead Wire Pair

which wires on which petal planes are disconnected. Such information could be used in any detailed offline correction of petal response.

A substantial effort was put into a study of methods to identify which wire pair(s) on a given plane were disconnected from the HT supply. The approach taken was to identify all pads below a given threshold and then to histogram all wires which couple to these pads. Such a histogram is shown in Fig. 5.6.6. In this case the threshold for 'low' pads is set at 75%. Further plots were made after varying this threshold, but no improvement in the identification of the wire pair was seen. It has proved not to be possible to isolate the missing wire or wire pair to within better than plus or minus one wire pair by such a

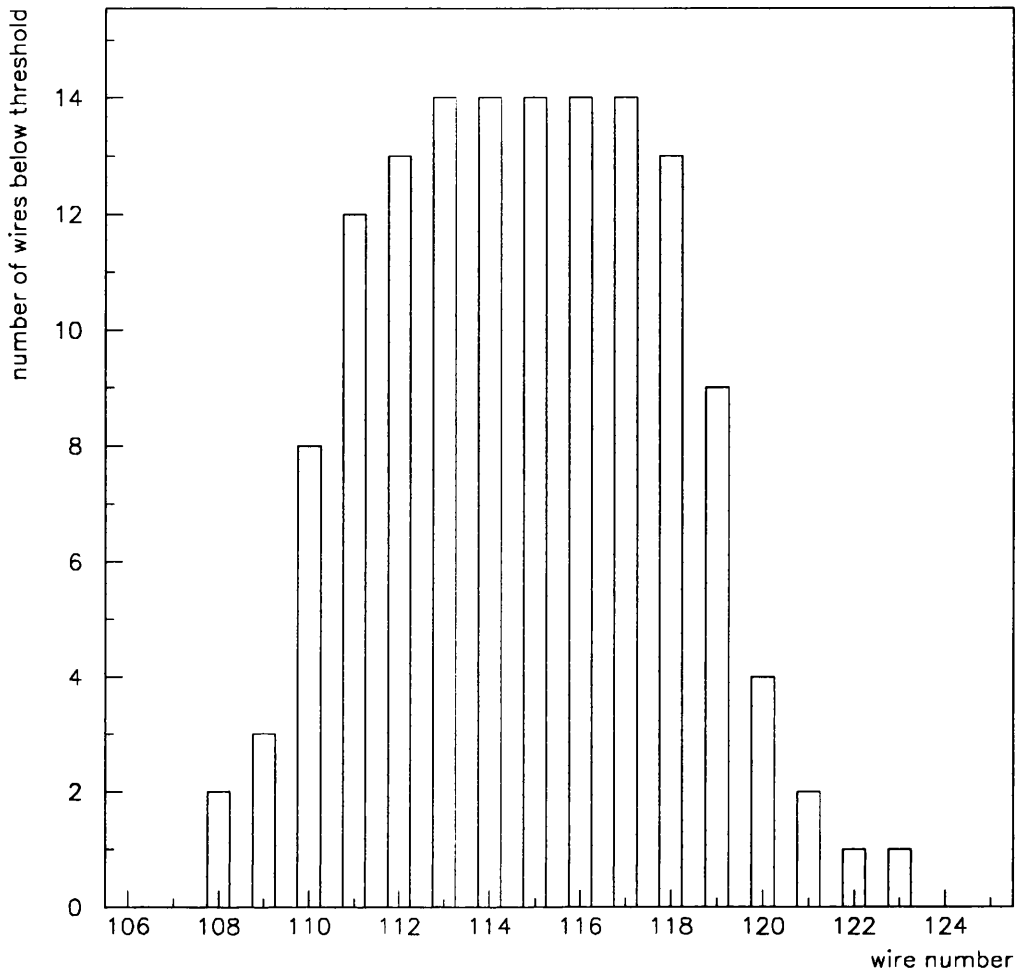

Fig. 5.6.6: Histogram for missing wire identification

method. This can be explained if it is realised that there are on average six wires below each pad.

Fig. 5.6.7 shows the wire pulsing results for plane 2 of petal 2, end–cap A. The data have been normalized for pad area. There is clearly shown a low area covering the middle third of the plane, where there is no response. This is a section of this plane which is disconnected from the HT supply. Such a fault shows up extremely readily in the wire pulsing data, but is fortunately very rare. It must also be pointed out that it is not absolutely clear if such sections are in fact not receiving high voltage but rather are just disconnected from the wire pulsing signal injection circuitry. If this is the case, then the pads coupling to these sections will contribute to the ionization signal in a shower. Information from real events which deposit energy on the pads of these layers is necessary to confirm this.

5.6.5 Conclusion

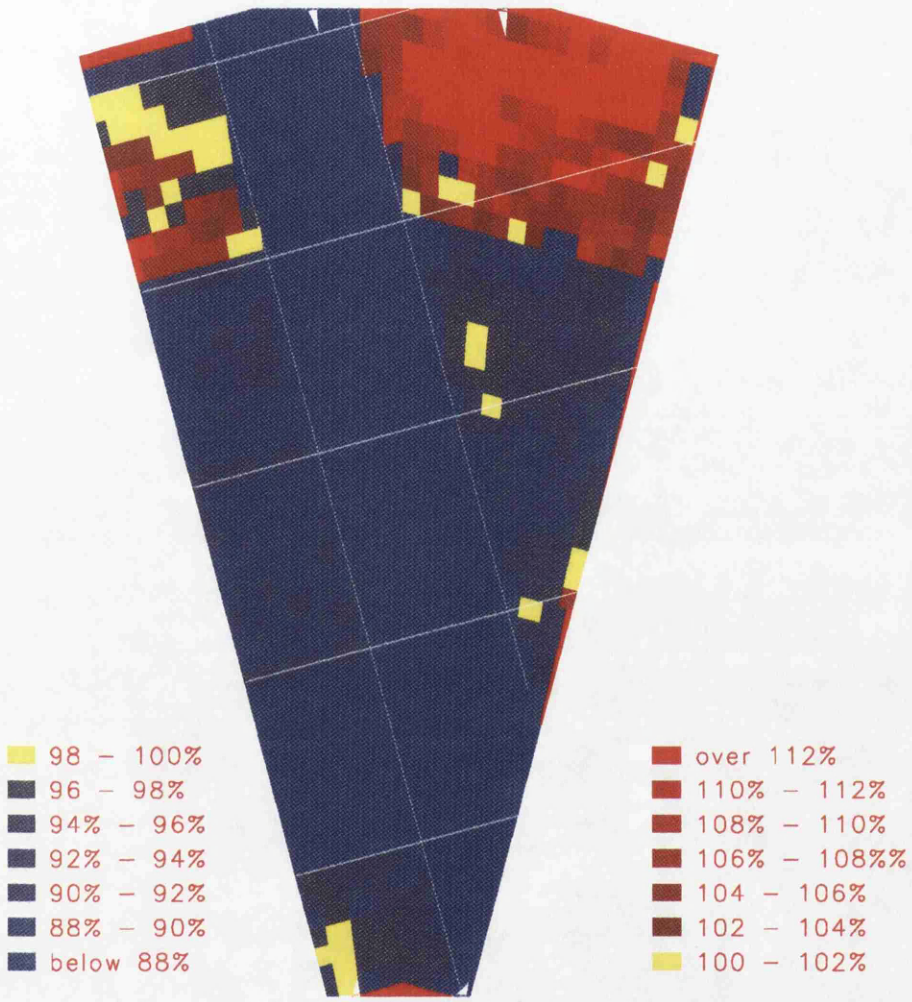

Fig. 5.6.7: Plane with disconnected HT section

In the case of the barrel modules, other workers have implemented a very sophisticated set of corrections, based on a numeric calculation of the electric field strength around an individual wire and its coupling to the pads. The wire pulsing technique has proved capable of measuring the uniformity of ECAL barrel modules, giving results similar to those obtained from cosmic rays and electron beam tests.

Unfortunately, the end–caps have a more complicated geometry and it has proved impossible to separate out purely geometrical effects, edge effects and pickup on the PC board tracks. There is pickup from the HT supply rail at the topmost end of the module. Each pad has a different length of PC board track connecting it to the outside, which will introduce additional capacitance. The end–cap modules are smaller than the barrel, and

there are therefore more edge effects contributing to the capacitance. The complicated non–rectangular shapes of the pads in the end–caps also prevent corrections being easily calculated for these effects. A large amount of time went into collecting and analysing the wire pulsing data from the end–caps. Due to the effects discussed above, the technique as applied to uniformity measurements of the end–caps must be unfortunately judged a failure. However, the wire pulsing technique has been applied to every petal for the purposes of fault finding, and the results are being used in the online and JULIA corrections to the ECAL data.

5.7. Cosmic Ray Testing

Each petal (and barrel) module underwent cosmic ray testing after construction. The response of each of the petals to the cosmic ray muon flux was recorded, in order to check the successful operation of all modules, to find and map faults and also to measure the uniformity of response of each module. Cosmic ray test stands were constructed at Rutherford Appleton Laboratory for testing the end–cap petal modules, and at the Saclay laboratory near Paris for the testing of the barrel modules. The Saclay set–up had a substantially different construction and is not discussed here.

5.7.1 The Cosmic Ray Petal Testing Rig

In the cosmic ray test rig at RAL, Fig. 5.7.1, the petal was mounted horizontally on a large iron frame. A trigger formed by ten plastic scintillators detects the passage of a cosmic ray and initiates readout of the petal and multi–wire chambers. Two small 25 x 25cm scintillators are situated above the petal on the gallery, and eight large scintillators are on the floor below the petal. The scintillators are arranged to define a beam of particles which roughly mimics the incoming paths in the completed detector. Each of the bottom scintillators is also read out by a CAMAC pattern unit. The trigger rate is around 0.5 Hz. To measure the cosmic ray tracks there are two varieties of multiwire proportional chambers in the system : large chambers from experiment NA4 [143] and small 30 x 30cm chambers from NA1. There are six small chambers on the gallery above the petal which serve to define the incoming track. There are ten large multi–wire chambers in the system - three above the petal and seven below. When a trigger occurs a region of 5 x 5 pads around the reconstructed track is read out to tape along with the 45 wire plane signals. Following each event a pedestal readout of the same region is taken. Petal readout is by ADC modules

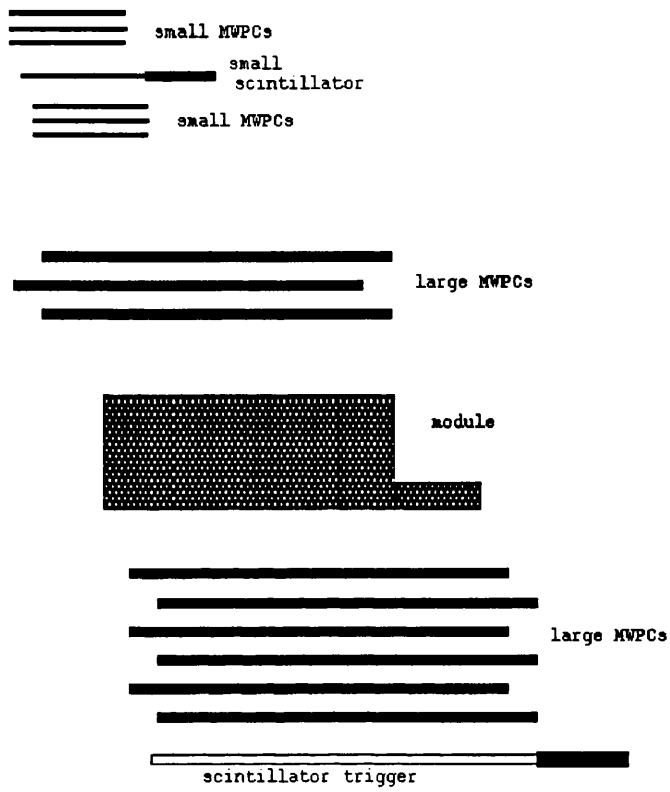

Fig. 5.7.1: Cosmic ray test rig at RAL

in the FASTBUS crate. The ADCs are controlled by the sequencer module, which holds several readout configuration programs. The anode readout is controlled by the MUX45 module. The petals were filled with an 80% Argon / 20% CO_2 mixture at around 1020 mbar and run at a voltage of 1375 volts. Each petal was on the test stand for around 3 weeks, and over 100 000 events were taken. The number of cosmic triggers recorded for each petal is given in Table 5.7.1.

5.7.2 Results of Cosmic Ray Testing

Data were taken for both the pads and wires of each stack. The following histograms of data are available for each petal :

- 45 individual wire planes energy deposition spectra
- pad energy deposition spectra for all three stacks
- wire energy deposition spectra for all three stacks
- pad/wire ratios for all three stacks
- pad data for each of 68 regions in 3 stacks (as described in the next section)
- wire data for each of 68 regions in 3 stacks (as described in the next section)

Petal Number	Number of Events	Petal Number	Number of Events
A1	145245	B1	203367
A2	123676	B2	201117
A3	302635	B3	35677
A4	229474	B4	66866
A5	243985	B5	93831
A6	192045	B6	89974
A7	226178	B7	149348
A8	197390	B8	188874
A9	216377	B9	142050
A10	175483	B10	187616
A11	301381	B11	206458
A12	243279	B12	180654
	mean	180957	

Table 5.7.1: Number of Cosmics Events

In each of the three stacks, a pad cluster is formed by taking the four highest energy storeys (any storeys with less than five counts are excluded) and summing the deposited energy. For each of the three stacks, the ratio of energy deposition on the pads and wires is calculated, and a cut is made on this quantity. This cut helps to reduce any effects caused by missing storeys. For each cluster, the tower with the largest energy is found and is used to define the 4×4 region in which the event has occurred (these regions are described in the next section on uniformity.)

Several corrections are applied to the data when the offline data analysis job is run at RAL. In the case of the pads a $1/\cos(\theta)$ correction is applied (this is because an oblique track will traverse a greater effective thickness of the gas layers and deposit more energy.) Detailed studies by S. Snow and T. Sloan [144-145] of the uniformity data from the first few petals to be tested exposed several effects which must be corrected for if a more accurate measurement of the uniformity is to be made.

As has already been discussed in 5.6 in the case of the end-caps the PC board track length has a significant contribution to the capacitance of some channels. There was found to be a correlation between the deviation in response of storeys in the petal and their capacitance to ground. The charge collected by a front end channel after time t is given by :

$$q(t) = q_0\left(1 - e^{t/\tau}\right) \tag{5.7.1}$$

where $\tau = C_d R_{eff}$ and C_d is the capacitance of the storey. The front-end electronics have $R_{eff} = 440\Omega$. In the case of the barrel modules $C_d \lesssim 3nF$ and virtually all the charge is

collected within 6 μs. A longer integration time, of up to 10 μs, would be needed to collect all the charge from the channels in the petal which have a high capacitance. A Monte Carlo study [144] also showed that there are variations in the ionisation energy deposited by cosmic ray muons over the face of the petal due to:

- a rise in the mean muon momentum with azimuthal angle
- an enhancement of signal at the edges of the petal from the loss of lower energy muons via multiple scattering

Position dependent correction factors are applied to the pads to correct for these effects.

In the case of the anode wires, a $1/\cos(\theta)$ correction is applied, the correction for the muon momentum spectrum and multiple scattering is made then sums of the energy deposition of the layers in each stack are taken. The stack 1 data is divided by 10, the stack 2 by 23 and the stack 3 by 12 to correct for the number of layers traversed. No corrections are applied for missing pads/wires or for gain variations with time. Finally, if the stack has a cluster pad energy greater than five counts the pad energy, wire energy and pad/wire ratio are entered into histograms. As an example, Fig. 5.7.2 shows the signals from all pads from stacks 1, 2 and 3 of petal A6, and from the grouped wire planes of stacks 1,2 and 3. The mean for the stack 2 pads is greater as there are 23 sampling layers traversed by the muons here, as opposed to 10 in stack 1.

The procedure used to get a number proportional to the gain for each stack is simply to take the HBOOK mean. Studies were made of the possibility of fitting the spectra with Landau distributions or with bifurcated Gaussian functions (for a thin gas layer, the distribution of energy loss approaches a Gaussian). Such a fit is shown in Fig. 5.7.3 for the stack 1 pads spectrum of petal A6. It may be seen that the distribution is not exactly given by a Landau. The shape of the distribution is altered at different track angles in the module, and also when there is a variation in the number of summed layers, making such fits less reliable. The attempts to find a suitable fit function proved to be no more useful than the procedure of taking the truncated mean already adopted.

The mean values of the pads distribution for stacks 1, 2 and 3 of each of the petals is given in Table 5.7.2 and those for the wires in Table 5.7.3. The 'overall' figure given for the pads is found by weighting stacks 1 2 and 3 by factors of 1, 10/23 and 10/12. The figure for the wires is a simple average. The pad-to-wire ratio figures in Table 5.7.4 are obtained from Gaussian fits to the pad-to-wire ratio histograms for each stack (the stack 2 value has been multiplied by a factor of 10/23 and stack 3 by 10/12 to again account for

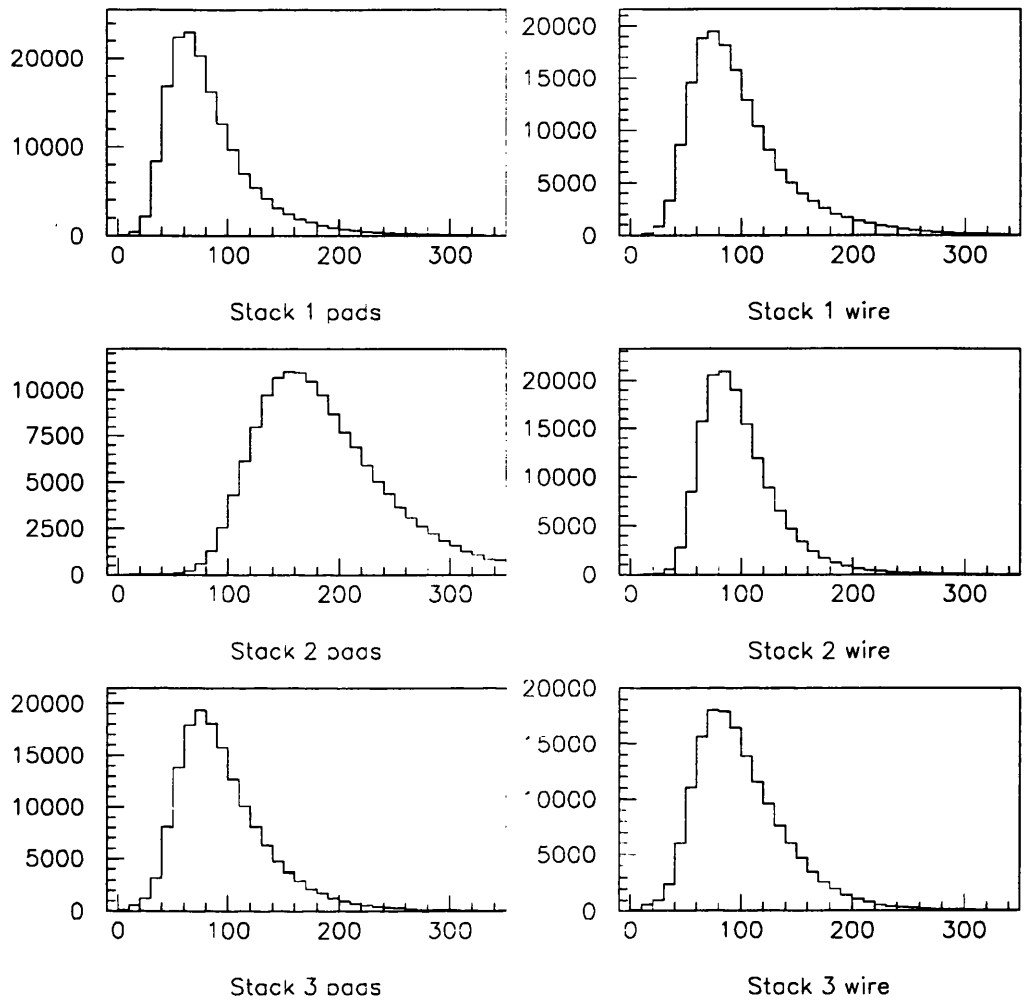

Fig. 5.7.2: Petal A6 Cosmics

the number of layers traversed). It must be pointed out that an inter-calibration among the petals is not possible using these data, as the data were obtained over a period of many months, the platine information is not used to correct for changes in gain and the running conditions (e.g. the front-end electronics) between the running periods for each petal may have changed.

5.7.3 Uniformity from Cosmic Ray Results

The data from the pad towers is grouped into 68 regions each of 4 × 4 pads, as shown in Fig. 5.7.4. The region numbering scheme chosen starts at the lower left corner, increases up the left hand side, returns to the bottom of the right hand side and finishes with the 68th region in the upper right hand corner. It would perhaps have been possible to analyse the petal data on the basis of individual towers, but to get a reliable calibration for each of the 1024 towers would have required much larger statistics, and hence much longer running

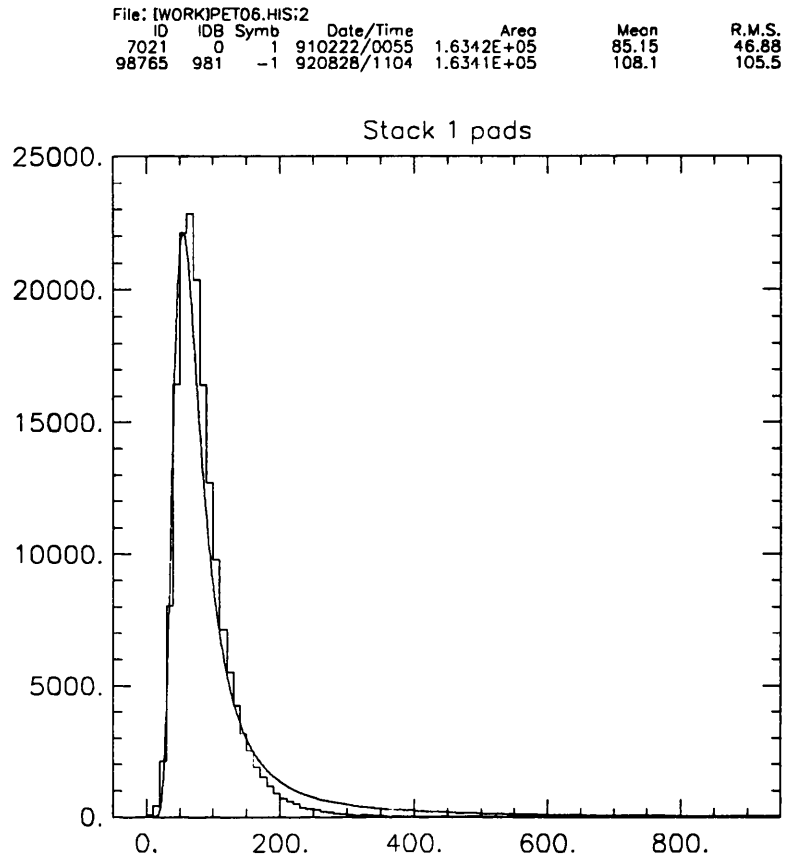

Fig. 5.7.3: Landau Fit to Cosmic Ray Energy Deposition Spectrum

time, which was not possible as the petals had to be shipped to CERN and installed in the detector.

For each individual region, a similar scheme of cluster formation, correction and histogramming to the one described in the previous section for the overall stack signals is applied. Again, the HBOOK mean of each distribution is taken.

A typical petal, viz. petal 6 of end-cap A (which was allocated 'build number' 6 at RAL) is selected as an example. For each of the 3 stacks, the petal is split up into 68 regions as described above. Fig. 5.7.5 shows the values for the pad regions in each of the three stacks. Fig. 5.7.6 shows a similar plot for the anode wire regions of petal A6. The values are plotted as a colour code, with red shades indicating a higher value and blue lower. The black areas are those areas with too few events: any region with less than 200 events is excluded from the analysis since taking a mean from such a small number of events is unreliable. If the uniformity maps for stack 3 are inspected, the row of regions at the broad end is seen to display low values. This is also seen in the other petals. If the distributions

Petal Number	Stack 1 Mean	Stack 2 Mean	Stack 3 Mean	Overall
A1	69.7	152.7	80.3	67.7
A2	65.3	151.7	79.0	65.7
A12	83.9	191.6	95.9	82.4
A10	65.8	155.8	77.6	66.1
A11	62.1	140.0	72.7	61.2
A6	84.5	192.1	96.7	82.9
A9	85.5	193.8	97.2	83.6
A8	71.9	167.8	84.4	71.7
A7	78.0	180.5	90.8	77.4
A5	60.4	137.0	66.0	58.3
B11	59.8	161.5	81.4	66.0
B12	71.8	163.6	83.4	70.8
A3	87.2	199.7	103.5	86.8
A4	65.1	144.1	72.7	62.8
B7	61.0	140.2	72.6	60.8
B6	80.8	187.3	95.8	80.7
B1	71.1	162.6	83.3	70.4
B4	62.8	142.3	74.3	62.2
B9	57.3	141.1	67.0	58.2
B8	70.6	160.4	83.2	69.9
B5	73.6	169.4	87.4	73.4
B10	69.2	155.6	80.7	68.0
B3	58.0	132.1	68.5	57.5
B2	76.7	175.9	88.7	75.7

Table 5.7.2: Cosmics Pads

for these regions are inspected a change of shape is seen. It is assumed that effect is due to the fact that the projective geometry projects some of the towers in this region of stack 3 out of the boundaries of the petal. The cosmic rays will therefore traverse fewer layers in these towers. For stack 3 only, this row of regions at the broad end is excluded from the calculation of the uniformity, ie. only 11 regions are used for this stack.

For each stack, a mean value and rms is calculated for pads and wires. The rms values for each petal are given in Table 5.7.5. The 'overall' figure is found from a weighted average of stacks 1, 2 and 3 in the proportion 0.42 : 0.47 : 0.11 . These weights are derived from the relative energy depositions in each stack from an average shower profile. The average rms. of the pad uniformity is 1.71%. The average rms. of the anode wire uniformity is 3.05%. The rms value for the wires is significantly larger than that for the pads due to

Petal Number	Stack 1 Mean	Stack 2 Mean	Stack 3 Mean	Overall
A1	87.3	84.9	81.8	84.7
A2	77.5	83.6	80.3	80.5
A12	93.1	96.1	89.1	92.8
A10	72.3	78.7	72.8	74.6
A11	75.9	76.0	71.4	74.4
A6	101.0	100.5	101.3	100.9
A9	101.8	105.1	97.8	101.6
A8	89.5	82.8	79.8	84.0
A7	94.8	92.7	92.8	93.4
A5	73.5	73.4	67.0	71.3
B11	74.6	85.1	84.0	81.2
B12	91.6	87.4	87.9	89.0
A3	100.8	114.5	102.0	105.8
A4	79.4	79.0	75.0	77.8
B7	69.9	79.2	71.2	73.4
B6	93.9	108.7	94.0	98.9
B1	82.5	92.7	80.4	85.2
B4	73.1	80.2	71.9	75.1
B9	64.4	79.0	65.0	69.5
B8	82.1	91.5	81.0	84.9
B5	79.9	89.3	81.2	83.5
B10	80.4	87.6	77.2	81.7
B3	64.4	70.5	64.2	66.4
B2	86.0	99.3	84.5	89.9

Table 5.7.3: Cosmics Wires

the so-called *anode step effect* seen in the analysis of S. Snow. The results from uniformity maps of the wire data were seen to display a step of a few percent downwards in the wire response when crossing over into the third high voltage region at the right hand side of the petals. If the uniformity plots in Fig. 5.7.6 are inspected closely, the effects of anode step effect may be seen as low areas at the right-hand sides of the plots. As has already been described in section 5.2 and Fig. 5.2.3 the high voltage supply to each multi-wire layer is split into three sections. These sections have equal area, and it was therefore assumed that they will have equal capacitance. It may be surmised that the anode step effect arises from a different capacitance of the third section. The last column of Table 5.7.5 gives the results from a calculation of the uniformity in which any wire regions in the affected third of the module have been excluded. The average rms. of the anode wire uniformity is now 2.53% .

5.7.4 Correlation between Pads and Wires

Petal Number	Stack 1 Ratio	Stack 2 Ratio	Stack 3 Ratio	Overall
A1	0.81	0.79	0.83	0.81
A2	0.86	0.79	0.83	0.83
A12	0.92	0.90	0.93	0.92
A10	0.93	0.89	0.94	0.92
A11	0.83	0.81	0.91	0.85
A6	0.85	0.84	0.80	0.83
A9	0.85	0.81	0.84	0.83
A8	0.81	0.92	0.91	0.88
A7	0.83	0.87	0.83	0.84
A5	0.83	0.83	0.84	0.83
B11	0.81	0.84	0.82	0.82
B12	0.79	0.82	0.80	0.80
A3	0.88	0.76	0.85	0.83
A4	0.83	0.80	0.82	0.82
B7	0.89	0.77	0.87	0.84
B6	0.88	0.75	0.87	0.83
B1	0.87	0.76	0.87	0.83
B4	0.87	0.77	0.87	0.84
B9	0.91	0.78	0.88	0.86
B8	0.88	0.76	0.86	0.83
B5	0.95	0.83	0.91	0.90
B10	0.88	0.77	0.88	0.84
B3	0.92	0.82	0.92	0.89
B2	0.91	0.77	0.88	0.85

Table 5.7.4: Cosmics Pad to Wire Ratios

It was decided to investigate whether or not the uniformity features of a particular stack were correlated with the highs and lows of the two other stacks, and whether or not any correspondence between the pad regions and wire regions of a particular stack can be seen. Fig. 5.7.7 shows the pads data for petal A6 as an HBOOK histogram, with regions numbered 1–68. Overlaid on the plot are the signals from the same regions in stacks 2 and 3. The data from stack 2 has been scaled by a factor 10/23 and that from stack 3 by 10/12 to correct for the different numbers of layers in each stack. There is little correlation of values in each region between the three stacks. Fig. 5.7.8 shows the wires data for petal A6. Data from stacks 1, 2 and 3 are overlaid. There seems to be a better correlation between the 3 stacks. This plot clearly illustrates the anode step effect. The regions from about number 48 onwards have values clearly lower than the mean.

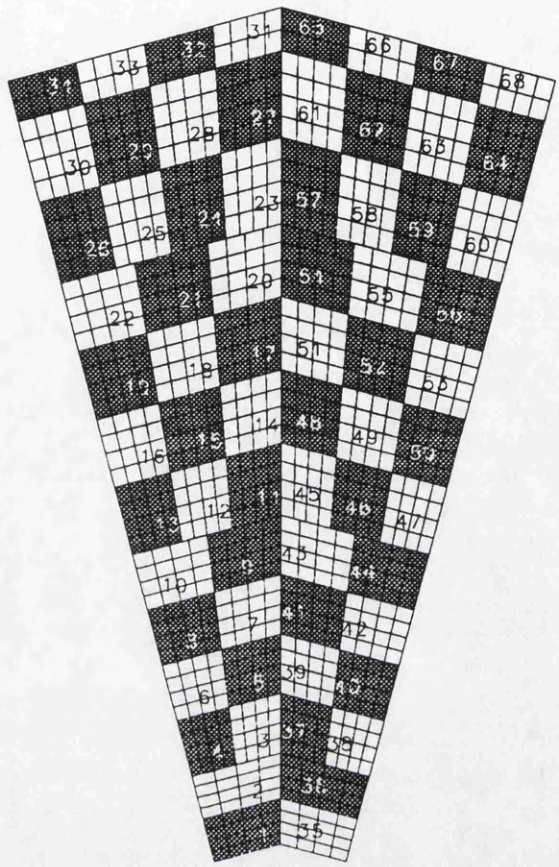

Fig. 5.7.4: Cosmic Ray Pad Regions

Fig. 5.7.9 is a comparison of the anode wire signals and the pad region signals for stack 1. The histograms have been normalized to the arbitrary value of 6000 to enable a comparison to be made. The y–values are therefore arbitrary. There is no correlation between the values. Similar plots for stacks 2 and 3 show no correlation.

5.7.5 Comparison with Uniformity from Radioactive Gas Measurements

Comparisons of the results obtained from the radioactive gas calibration procedures and the results from the cosmic ray testing have been made. The method of radioactive gas calibration and the results obtained in the radioactive gas calibration runs in the summer of 1989 are discussed in section 5.9. The overall pad, wire and pad/wire ratio figures for each of 24 petals were compared with the radioactive gas calibration factors. No correlation was found.

It was decided to investigate whether or not there is any correlation between the uniformity values obtained from the cosmic ray tests and the radioactive gas tests.

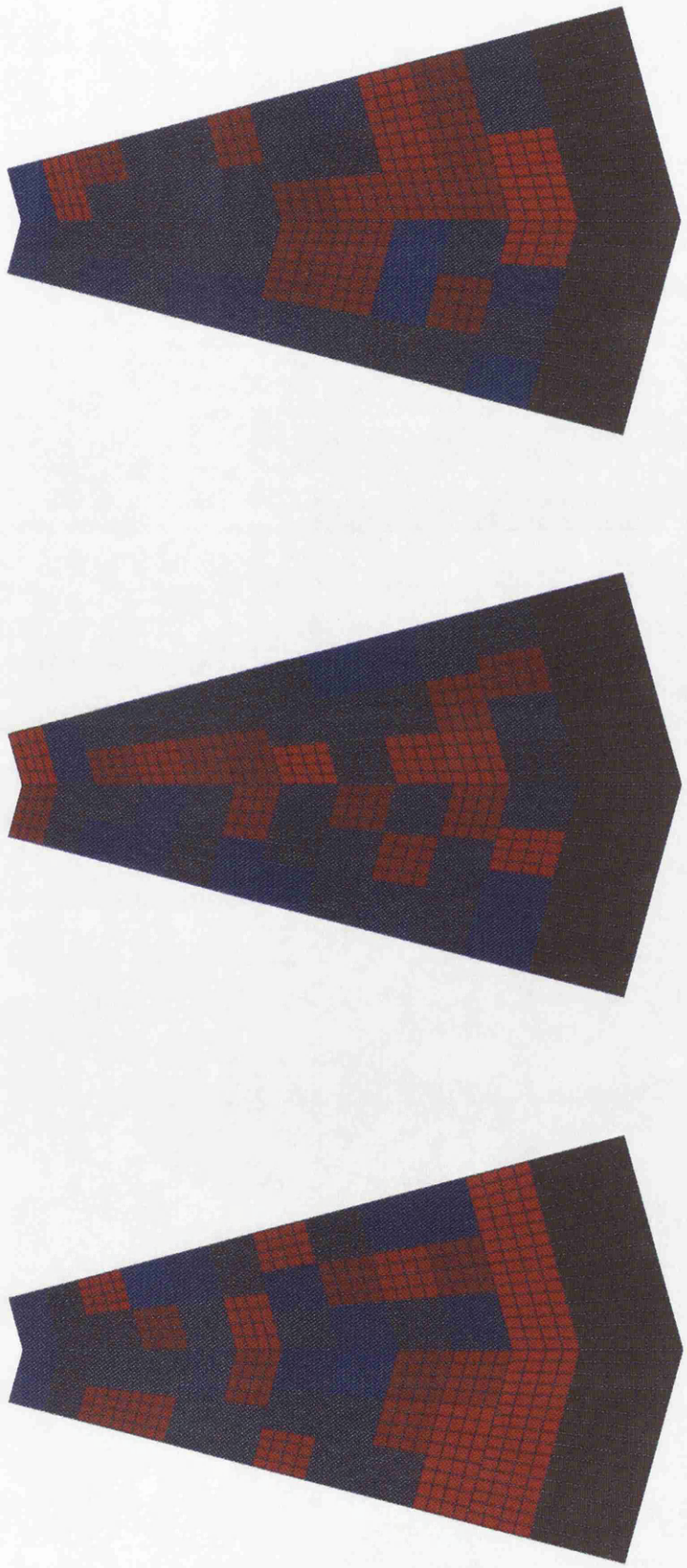

Fig. 5.7.5: Pads Uniformity Results from Stacks 1,2 and 3 of Petal A6

In Fig. 5.7.10 a comparison of the anode wire uniformity regions and the data from radioactive gas uniformity regions is made. From a visual inspection it may be seen that there is a good correlation between the radioactive gas data points and the cosmic ray data for the anode wire regions, except in the regions corresponding to the broad end of the petal. The low values in the cosmic ray data for these regions have already been explained above. This correlation is perhaps not surprising as the cosmic ray anode data and the radioactive gas data are obtained in a similar fashion: the pad data are used to localize the region in which the 'event' took place, and a value is read out from the complete anode plane. Perhaps if it was possible to use the pad signals directly in the radioactive gas calibration, a correspondence between the cosmics pad data and the radioactive gas pad data could be found.

5.7.6 Plane Profiles

As will be introduced later, in section 5.9, a variation in the plane calibration factor from radioactive gas measurements was noted. This effect was also investigated in the cosmic ray data. For each of the 45 wire layer spectra of each petal the HBOOK mean of the distribution is taken as the characteristic point. The wire plane profile resulting from the addition of all petals is shown in Fig. 5.7.11. There is no evidence for any structure in the front–to–back profile. However, it may be conjectured that the values for stack 3, i.e. planes 34 to 45, are slightly lower than the rest. This figure should be compared with the average wire plane profile from the radioactive gas measurements, Fig. 5.9.6.

5.8. Beamline Tests of ECAL Modules

In the beamline tests the ECAL modules were exposed to beams of different types of particles whose energies and trajectories are well measured. Readouts were performed with equipment as similar as possible to the final configuration in ALEPH. The aims of the beam tests were to :

- measure resolution
- measure linearity
- measure uniformity
- compare the different responses to electrons, photons, muons and pions
- measure the coefficients of response with pressure, temperature and voltage
- look at pedestal stability with time

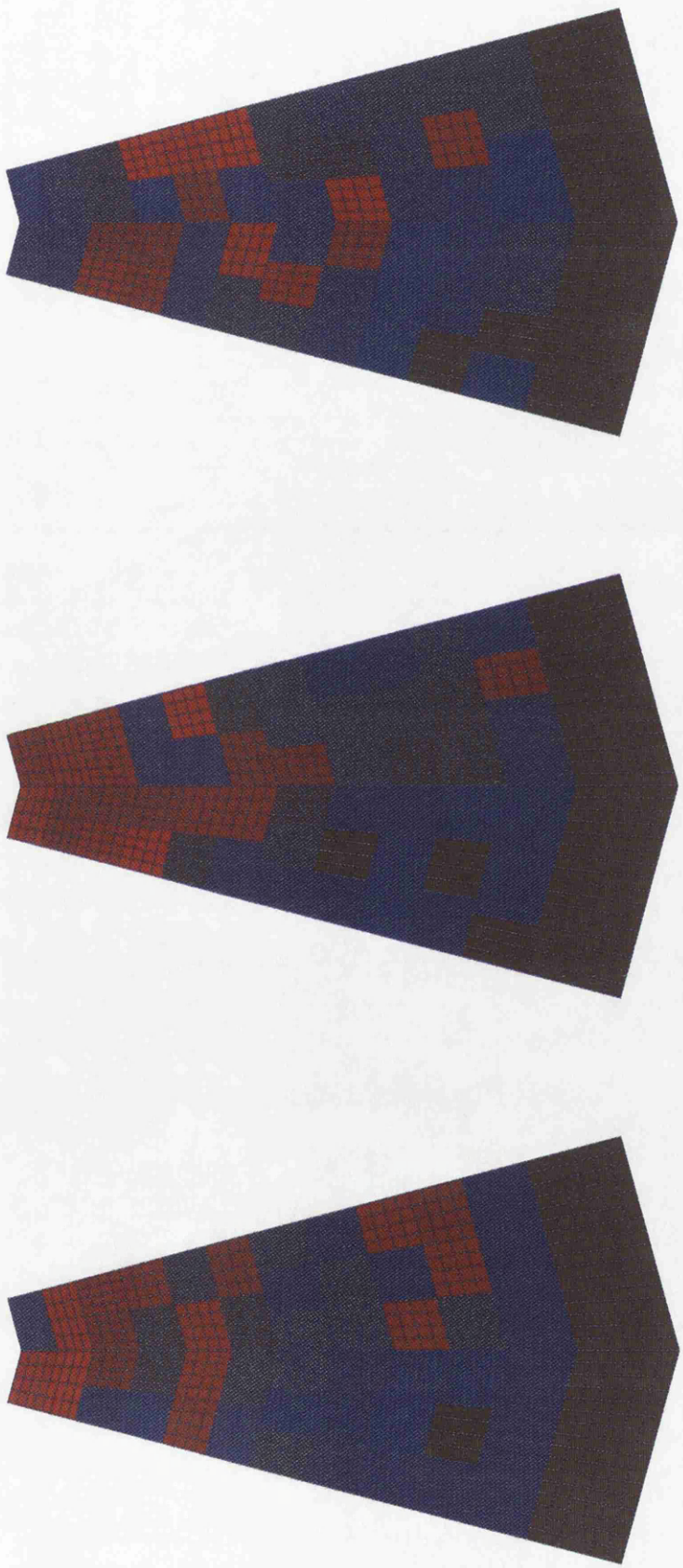

Fig. 5.7.6: Wires Uniformity Results from Stacks 1,2 and 3 of Petal A6

Petal Number	Pads Stack 1 σ_{rms} (%)	Pads Stack 2 σ_{rms} (%)	Pads Stack 3 σ_{rms} (%)	Pads Overall σ_{rms} (%)	Wires Stack 1 σ_{rms} (%)	Wires Stack 2 σ_{rms} (%)	Wires Stack 3 σ_{rms} (%)	Wires Overall σ_{rms} (%)	Wires w/o third region σ_{rms} (%)
A1	2.02	2.10	1.51	2.00	4.23	4.00	2.48	3.93	3.04
A2	1.82	1.47	1.21	1.59	4.16	2.95	2.81	3.44	2.81
A12	2.28	1.60	1.22	1.84	3.81	2.39	1.82	2.92	2.32
A10	1.93	1.39	1.45	1.62	3.08	2.44	2.61	2.73	1.72
A11	1.74	1.55	1.24	1.59	2.70	2.03	2.07	2.31	1.90
A6	1.75	1.05	1.05	1.34	3.02	2.99	2.85	2.98	2.22
A9	1.77	1.43	1.42	1.57	2.98	2.51	2.53	2.71	2.11
A8	1.58	1.62	1.19	1.55	3.51	2.61	2.64	2.99	2.10
A7	1.72	1.35	1.29	1.50	3.28	2.60	2.31	2.85	2.06
A5	3.09	1.90	1.69	2.37	3.32	1.91	1.97	2.51	2.43
B11	1.69	1.03	1.06	1.31	2.54	2.11	2.32	2.31	2.01
B12	1.75	1.23	1.48	1.47	3.40	2.21	1.80	2.66	2.30
A3	1.91	1.11	1.45	1.48	3.03	2.67	2.40	2.79	2.42
A4	2.00	1.59	2.63	1.88	3.30	3.16	2.36	3.13	2.87
B7	2.37	1.44	1.14	1.80	2.98	2.58	2.11	2.69	2.30
B6	2.42	1.09	1.19	1.66	2.87	2.93	2.22	2.82	2.38
B1	1.93	1.34	1.22	1.57	2.88	2.82	2.01	2.75	2.36
B4	1.96	1.55	1.69	1.74	3.47	3.20	2.56	3.24	2.74
B9	2.04	1.46	1.91	1.75	4.30	3.03	2.84	3.54	2.63
B8	1.56	1.21	1.23	1.36	5.04	3.43	2.38	3.99	3.76
B5	1.92	1.54	1.77	1.72	3.59	3.49	2.60	3.43	2.87
B10	2.40	1.56	1.35	1.89	4.00	3.68	2.55	3.69	3.43
B3	3.55	2.21	2.86	2.84	3.75	3.31	3.39	3.50	2.96
B2	1.83	1.20	1.29	1.47	3.89	3.26	2.02	3.38	3.00
mean	2.04	1.46	1.48	1.71	3.46	2.85	2.40	3.05	2.53

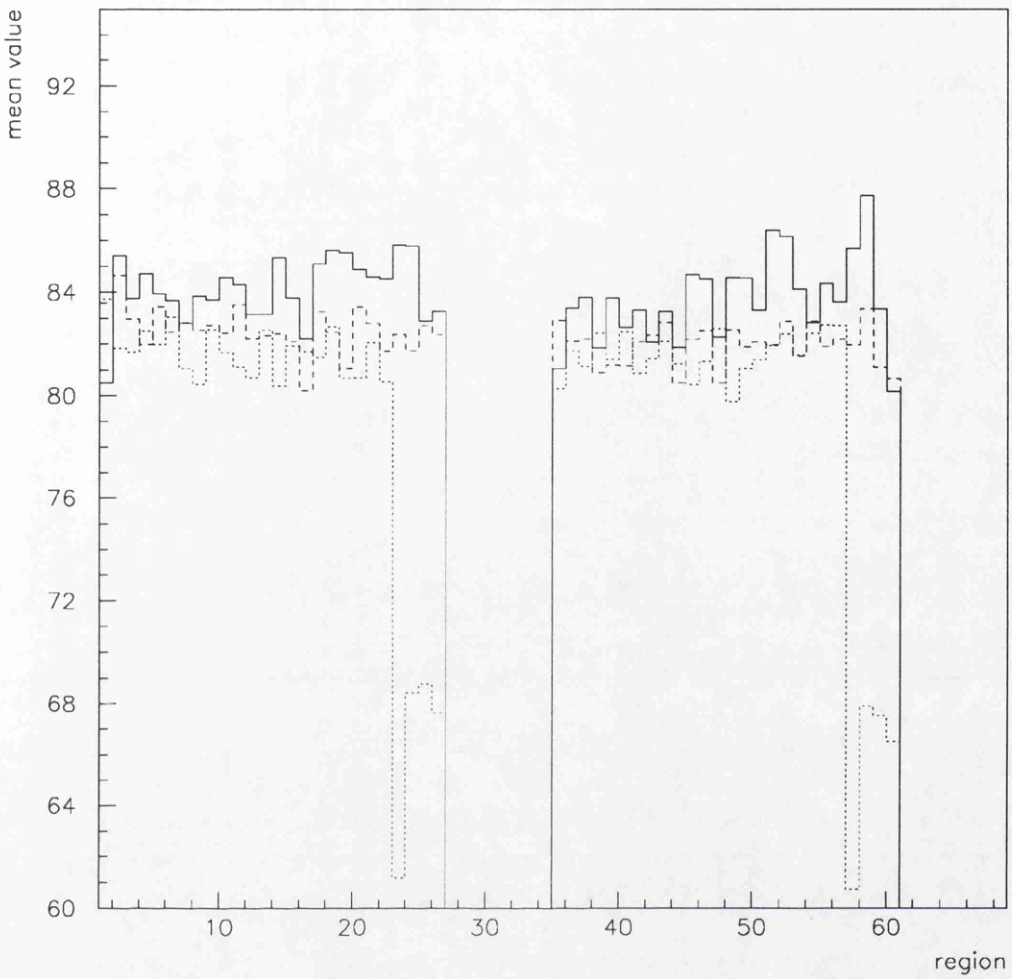

Fig. 5.7.7: Petal A6 pad regions: 3 stacks overlaid

- look at the joint ECAL /HCAL response to pions and muons
- look at the behaviour in the overlap region between barrel and petal
- test the DAQ system in a realistic situation
- test and develop the offline reconstruction program

At the same time as providing test data on the modules themselves, the test beam work also provided a test–bed for the front–end electronics, the FASTBUS modules and the ALEPH data–acquisition software.

The ALEPH collaboration was given the use of test beam facilities in the CERN West Experimental Area. In 1982 and 1983 a series of tests were conducted on three small prototype ECAL modules [146]. The wire energy resolution was measured to be around $0.5\% + 18\%/\sqrt{E}$. The prototype tests confirmed that the design of the calorimeter would work before full–scale production was started. In 1986 the first complete barrel module was

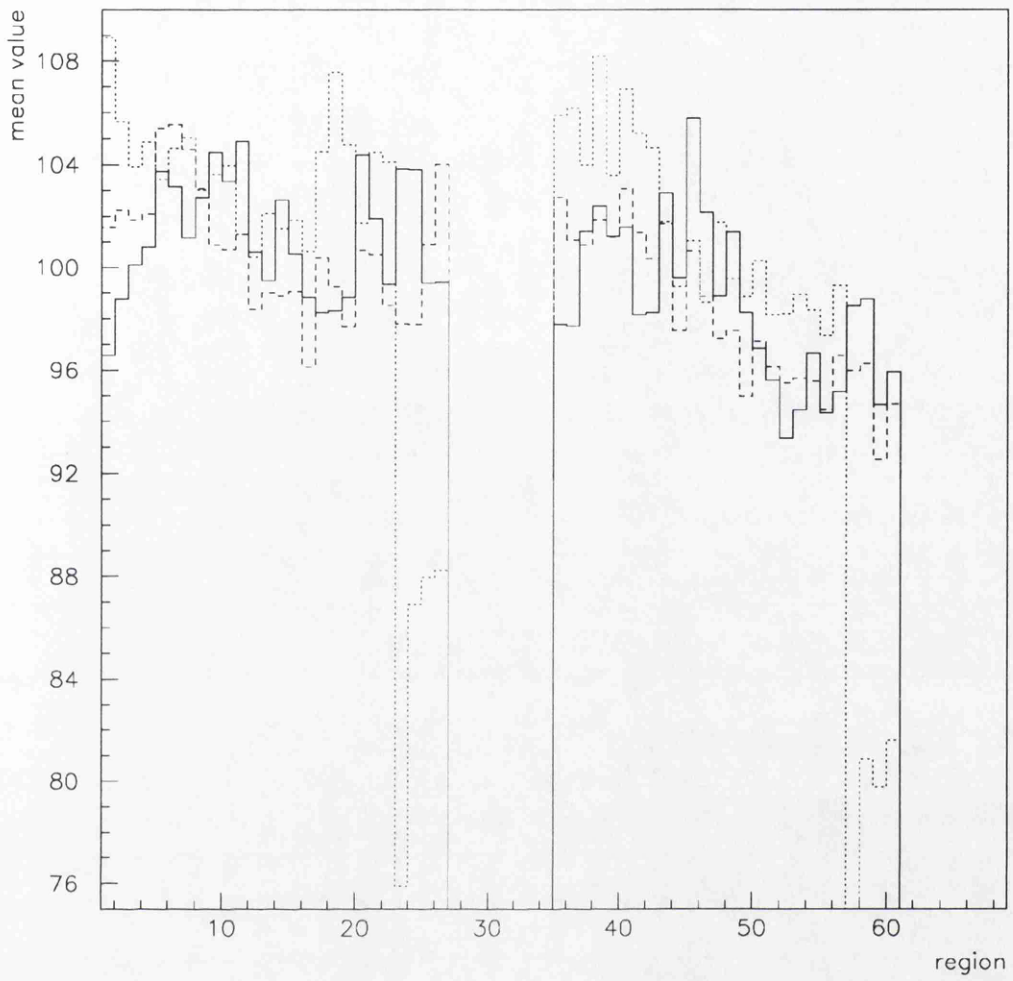

Fig. 5.7.8: Petal A6 wire regions: 3 stacks overlaid

tested. In 1987 barrel and petal modules from the ECAL were tested in beams of electrons, pions and muons (the end–cap module tested was number 4). Tests in the overlap region of an end–cap and barrel module together were conducted. Tests of the response to pions of an end–cap module together with a prototype HCAL module [147] were also conducted. The 1988 running consisted of individual petal and barrel modules being cross-calibrated, plus combined petal/barrel ECAL runs and combined petal/HCAL runs. Four end–cap modules were tested with electron and muon beams. (The modules tested were those with 'build numbers' 2, 3, 4 and 9. These numbers were allocated in chronological order at the time of construction. In some other sections of this chapter, the petals are referred to by the more usual numbering scheme as a certain petal number, 1–12, in end–cap A or B). The barrel modules tested were numbers 4 and 8. The author participated in the beam line tests in 1987 and 1988.

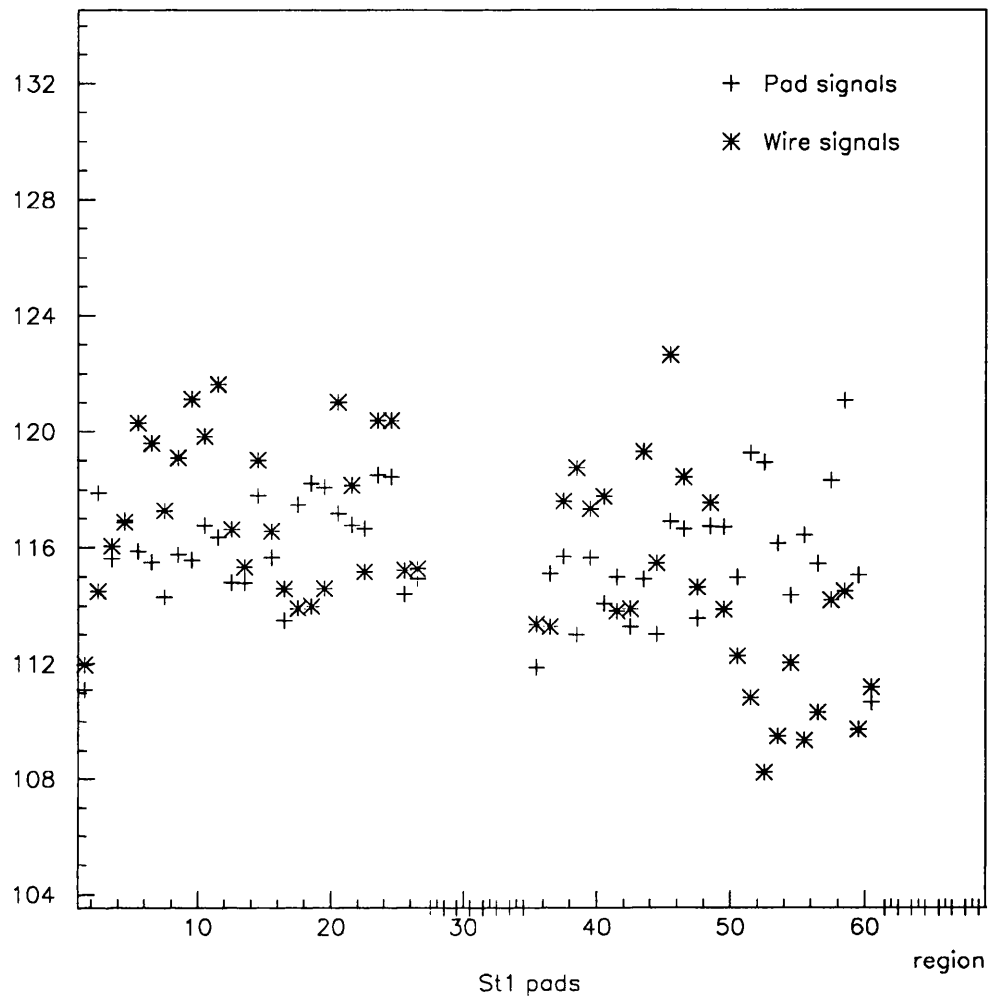

Fig. 5.7.9: Pad and wire region comparison

5.8.1 Test Beam Setup

The test beam used was the X7 beam line from the CERN SPS accelerator. Protons at an energy of 450GeV/c^2 are taken from the SPS by an electrostatic septum and strike a primary beryllium target. The primary beam is split into three secondary test beams which are directed onto a user–selectable secondary target. A series of collimators, stripping foils and sweeping magnets serve to select out the desired type and momentum of secondary particles which are delivered to the experimental area at the end of the beam line. The particles used were gammas, positrons, muons and pions at energies up to 70GeV/c^2. (Gammas were produced in a tagged photon beam: an electron beam passed through a thin foil. Electrons which lost energy by bremsstrahlung were deflected by a magnet and their presence triggered by scintillators). During the 1988 running the beam line was specially configured to allow low energy running, with pion energy down to around 2GeV/c^2.

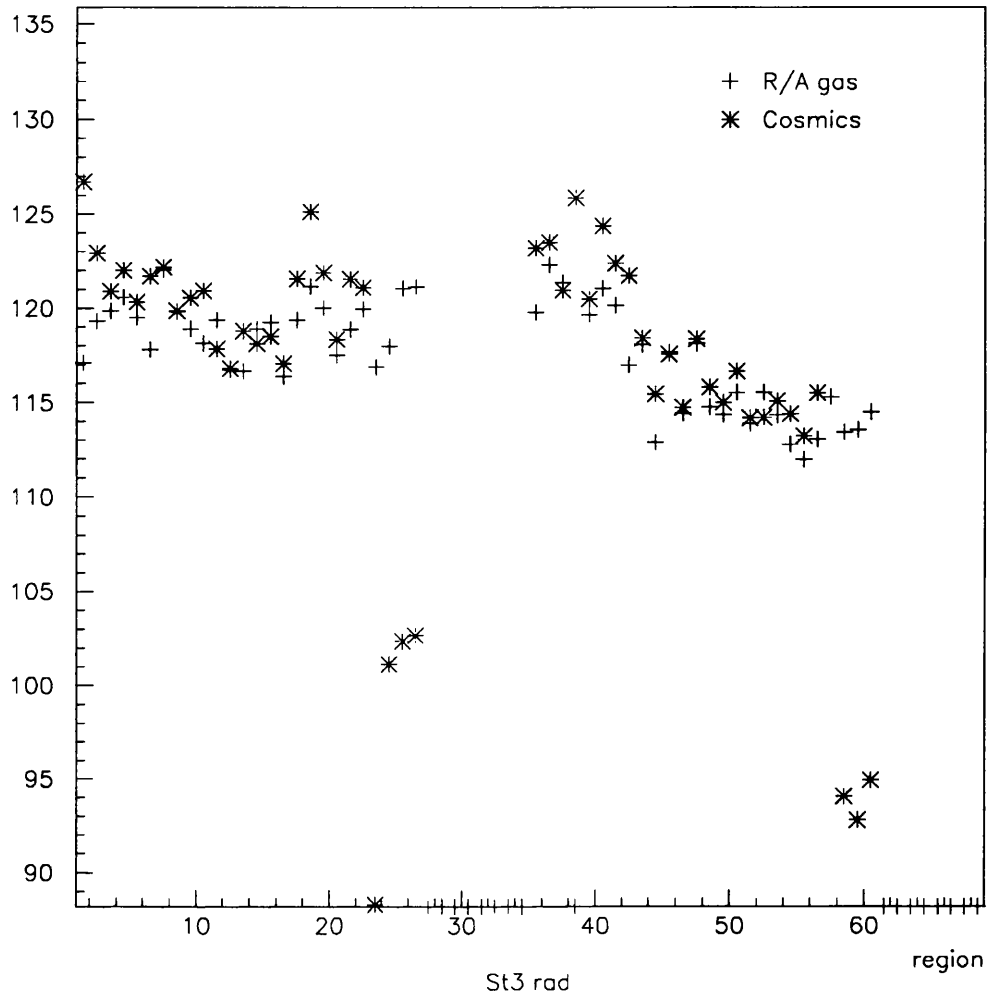

Fig. 5.7.10: Comparison of Cosmics and Radioactive Gas Data

A telescope of plastic scintillators with an acceptance of approximately 2×2cm provided a trigger for the module readout. A large scintillator with a hole for the beam was used to veto those events with beam halo muons. During the pion running, plastic scintillators placed behind a 40cm iron block after the calorimeters were used to identify muons passing through the calorimeters. Two threshold Cherenkov counters in the beam line provided particle identification. The particle momenta were measured by a magnetic spectrometer setup in the beamline consisting of a bending magnet plus four multi–wire chambers. This has an accuracy of better than 1%. The impact point on the face of the calorimeter of each incoming beam particle was measured to ±2mm by two multi–wire chambers, known as the Saclay chambers, in the experimental area. The information from the beam momentum spectrometer and the Saclay chambers was used to reject events with off–axis particles and beam halo muons. When tests were being conducted on ECAL modules only, the modules

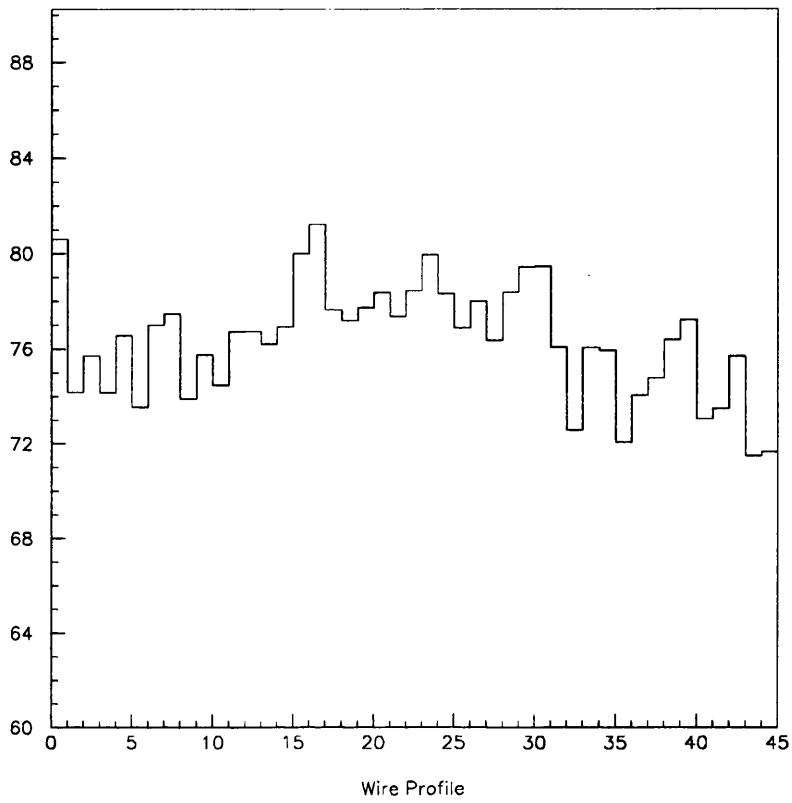

Fig. 5.7.11: Overall Wire Plane Profile (Cosmics)

were mounted on a large movement rig with movements possible on three axes which enabled the beam to be scanned across different towers. The modules were mounted in such a way that the beam appears to originate at the nominal ALEPH interaction point.

For each event a region of 10 × 10 towers around the interaction point was read out using a $6\mu s$ integration time. The 45 wire plane signals were also read out. Pedestal events were taken interspersed with the real events. Platine temperature, pressure and Fe^{55} peaks, beam spectrometer, Saclay wire chamber and Cherenkov counter data were also read for each event. During each running period, the high voltage setting was normally adjusted such that there was 4 MeV of energy deposited per ADC count.

5.8.2 Energy Resolution

To measure the petal energy resolution data were taken with a range of electron energies between 2.5 and 70 GeV. A factor of 1.93 was applied to the stack 3 data to compensate for the different sampling ratio (this is the ratio of radiation lengths of the stacks). The off–line clustering applied was from the JULIA program, with an upper threshold of 500 MeV and

a lower threshold of 30 MeV. No corrections were made for dead wires or missing pads. For each energy the width was measured by fitting to a Gaussian, cutting at 2σ and re–fitting. The data from the 1988 running from petal 2, Fig. 5.8.1, give the energy resolution for the wires as:

$$\frac{\Delta E}{E} = \frac{(16.98 \pm 0.44)\,\%}{\sqrt{E}} + 0.45\% \tag{5.8.1}$$

and that for the pads as:

$$\frac{\Delta E}{E} = \frac{(19.23 \pm 0.49)\,\%}{\sqrt{E}} + 0.33\% \tag{5.8.2}$$

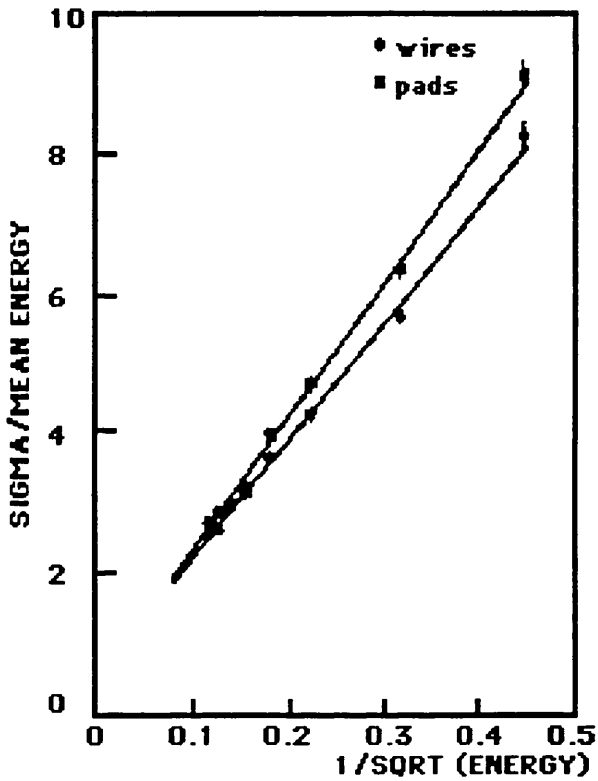

Fig. 5.8.1: Energy Resolution. From [111].

5.8.3 Linearity

At high energies the response of the calorimeter shows a small deviation from linearity. Electron test beam data up to 70 GeV give the non–linearity as:

$$E_{meas}/E_{true} = 1 - \alpha E \tag{5.8.3}$$

where: $\alpha = (9.0 \pm 0.7) \times 10^{-4}$GeV. The non–linearity arises from two effects: saturation, i.e. at the core of high energy showers space charge builds up round the wires and the

avalanches do not grow any bigger: and leakage of energy from the modules. Assuming that saturation is proportional to the gas gain data taken at different high voltage settings gives the saturation coefficient (which is the dominant effect) as $(7.8 \pm 0.6) \times 10^{-4}$GeV.

5.8.4 Dependence of Gain on HT, Pressure and Temperature

If the gas volume and composition are constant, the gain of the module is dependent on the high voltage and on the density. During the 1988 running, the variation of the petal module response to electrons with these quantities was measured by changing the voltage or pressure in small steps. The platine Fe^{55} peak response was also simultaneously recorded. As has already been mentioned the platine Fe^{55} peak has a different dependence on the gas density as compared to the electron response. This effect must be taken into account if the platines are used to correct the calibrations of the modules during ALEPH running. The dependence of gas gain on density is an inverse power law, given by $(P/T)^{\alpha}$. The indices α were measured to be:

$$\begin{aligned} \alpha\,(P/T)_{electron} &= -5.30 \pm 0.05 \\ \alpha\,(P/T)_{platine} &= -6.84 \pm 0.06 \\ \alpha_e/\alpha_{platine} &= 0.77 \end{aligned} \tag{5.8.4}$$

Similarly, there is a power law dependence of the gas gain on the high voltage applied to the platine and the anode layers :

$$\begin{aligned} \beta\,(HV)_{electron} &= 16.2 \pm 0.05 \\ \beta\,(HV)_{platine} &= 17.6 \pm 0.01 \\ \beta_e/\beta_{platine} &= 0.92 \end{aligned} \tag{5.8.5}$$

5.8.5 Uniformity Scans

The uniformity of response to electrons across the face of the modules was measured using an electron energy of 20 GeV (which gives a reasonable signal in stack 3). The end-cap modules were scanned on a grid of 40 points. A 'standard point' was chosen near the broad end of the petal under test. Repeat runs were taken at frequent intervals at this standard point to track gain changes with time and to enable cross-comparisons to be made with the platine data. No corrections were made for dead wires or missing pads, although any scan points near known missing channels were excluded from the analysis.

The results of uniformity scans in the petals were seen to display the anode step effect, i.e. there is a step of about 5% in the wire response when crossing over into the third high

Petal Number	'Build' Number	σ_{rms} Pads	σ_{rms} Wires
A2	2	1.0%	1.9%
A12	3	1.7%	1.6%
A10	4	1.0%	1.6%
A7	9	1.0%	1.7%

Table 5.8.1: Results of Uniformity Scans

voltage region. This effect has already been described in section 5.7.3 which deals with the results of the cosmic ray tests. After corrections to the wire data have been made for this effect, the rms. deviations of the mean responses for the petal scans are as given in Table 5.8.1. These figures should be compared with the values obtained from analysis of the cosmic ray data, section 5.7.3. The values of the wire uniformity from the beamline tests are similar to the values of the pad uniformity from the cosmic ray tests.

5.8.6 Muon and Pion Results

The response of the ECAL to minimum ionising particles was studied using muons and (non–interacting) pions. The ratio of signal per unit energy deposited by electron showers compared to mips was found to be 0.62 [133]. The ratio $e/mip < 1$ is as seen in other sampling calorimeters.

The response of the combination of an ECAL petal and an HCAL prototype module to pions was also studied [148–149]. Data were taken with pions at a range of energies between 2 and 30 GeV. A weighting scheme was used to minimize the resolution as a function of energy. The energy resolution of the combined device is $62\%/\sqrt{E}$ at low energy and rises to $82\%/\sqrt{E}$ at over 10 GeV, which is consistent with the energy resolution of the hadron calorimeter alone. The e/π ratio for the electromagnetic calorimeter is greater than 1 and depends on the pion energy: it was measured to be 1.7 at 2 GeV , and about 1.3 in the region 20 to 30 GeV.

The electron/pion discrimination of a barrel module was examined at 10 GeV and 5 GeV. If only the ratio of energy deposited to particle momentum is considered, then at 10 GeV the pion contamination is 1.5% for an electron efficiency of 99%. The discrimination between charged pions and electrons is very much improved by using the information available from the segmentation of the calorimeter. As described in 4.5.6 'estimators' are constructed based on the shower shape which enable very good electron identification. Using cuts on the transverse compactness and longitudinal shape of the shower, and comparison between the barycentre of the shower and the impact point from the TPC the fraction of

pions at 10 GeV faking an electron signal is $(1.1 \pm 0.5) \times 10^{-3}$ and at 5 GeV is $< 3 \times 10^{-3}$ for an electron efficiency of 95%. It can be seen that the granularity of the ECAL when combined with the tracking properties of the TPC gives excellent particle identification, even within jets.

5.9. Radioactive Gas Calibration

The calorimeter modules are also calibrated by the temporary injection of a gaseous radioactive isotope into the gas circulation system. This provides an intercalibration among modules, and when compared with the 1988 test beam electron data, an absolute calibration with respect to known electron calibrations. In the summer of 1988 two petals were tested with radioactive gas in the same period as beamline tests were being run on these modules. Prior to LEP startup in 1989 radioactive gas calibration was performed with all modules. This was the primary method of intercalibration of modules before data from Bhabha scatter events was available. The technique allows the anode wire output of a module to be calibrated directly, and may also be used to measure the uniformity of response of a module's towers if the pad signal is used to locate the coordinates of the decay event.

5.9.1 Method

The radioactive source used is a mylar foil impregnated with ^{83}Rb (lifetime 80 days) which is made at the NBI cyclotron, Copenhagen. The rubidium decays to ^{83m}Kr gas, which has a lifetime of 1.86 hours. The ^{83m}Kr decays to ^{83}Kr by emission of 9.4 keV and 32 keV X-rays which by isomeric transition yield electrons of predominantly 1.8, 7.6 and 32 keV. The quantities involved are of the order of $1\mu Ci$ of activity per module. The source is contained in a section of pipe and incorporated into the gas circulation system via a branch circuit. As the petal modules are coupled in pairs to the gas supply, it is usual to have radioactive gas in two petals at once. However, it is also possible to arrange a global circulation mode where the same gas flows through all the modules.

The wire spectrum from each layer (at a time before a trigger threshold has been applied) is shown in Fig. 5.9.1. It shows a peak at 9.4 keV and a higher energy plateau extending to 40 keV produced by internal conversion electrons in the gas. The trigger threshold chosen is indicated on this diagram. Since the background from residual radioactivity is negligible above 20 keV a trigger threshold is set which is above the 9.4 keV peak, at around 20 keV. The trigger is an OR of the wire plane signals. Typical trigger rates are

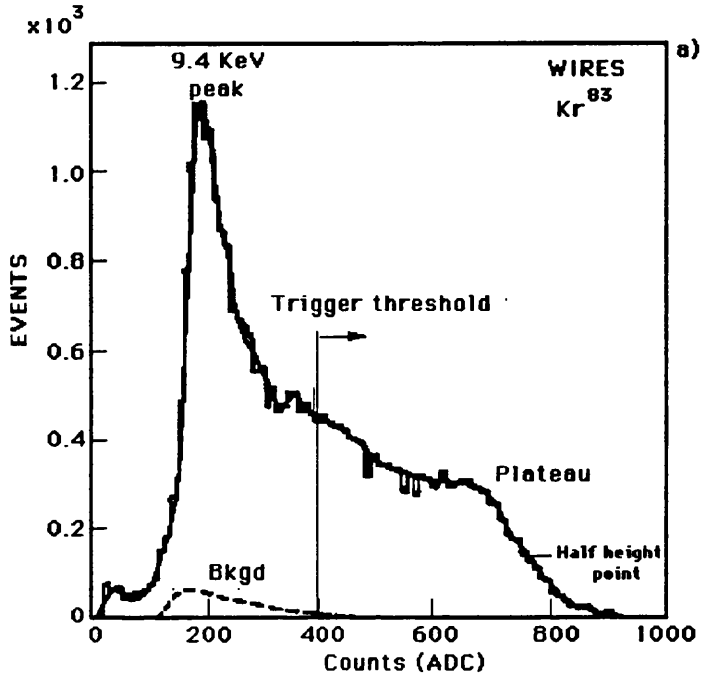

Fig. 5.9.1: Radioactive gas – wire spectrum

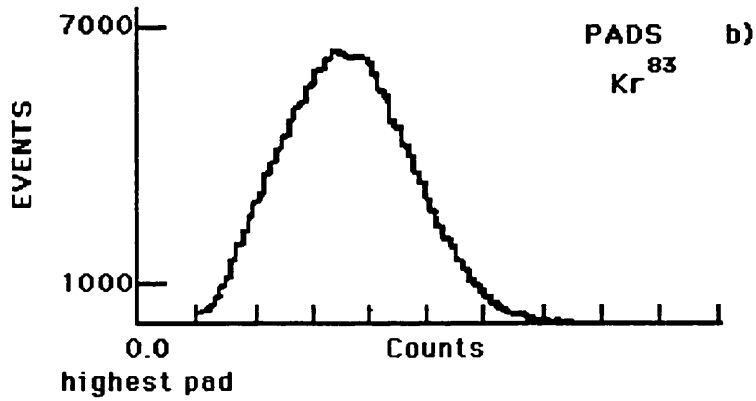

Fig. 5.9.2: Radioactive gas – pads spectrum

$\approx$ 100 Hz. The maximum rate of data-taking is limited by pile-up effects and by those events with a multiplicity of separated pads above threshold, which cannot be used for uniformity mapping.

The pulse height spectrum obtained from the pad readout channels, Fig. 5.9.2, shows a broad peak as the energy deposit depends on where the decay occurred in the gas volume relative to the anode wire. Therefore a direct measurement of pad uniformity is not possible.

The procedure adopted was to use the pad signal to localize the decay and then to read out the wire signal for that particular region.

The anode wire spectra are recorded for the whole of each wire layer (45 spectra in all), the combined layers 1-10, 11-33, 34–45 , i.e. stacks 1,2 and 3, and an overall spectrum from the sum of all 45 planes is also recorded. A typical spectrum of pulse heights from a plane is shown in Fig. 5.9.3. Each module will have a slightly different energy response, resulting in a shift of this calibration spectrum.

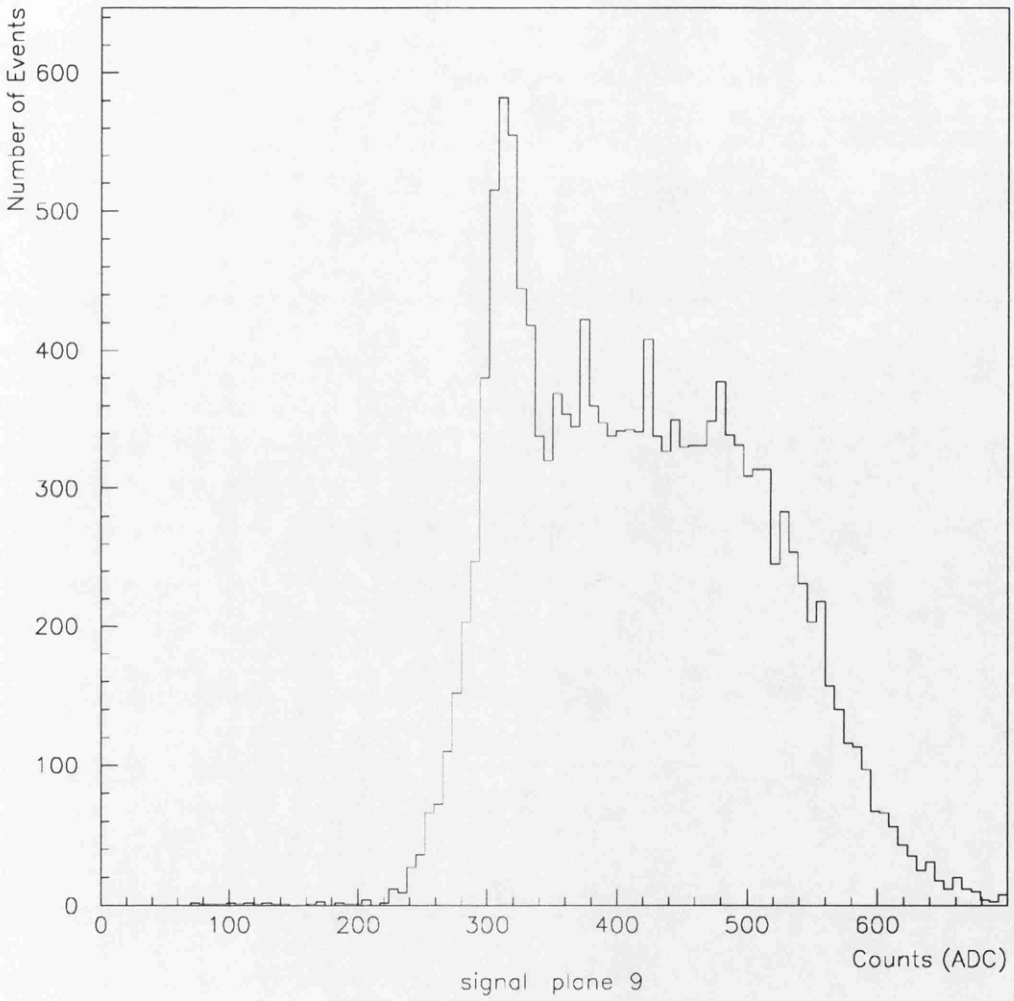

Fig. 5.9.3: A typical radioactive gas calibration spectrum

Attempts were made to fit complicated functions, such as double gaussians, to the calibration spectra using the PAW package, but no satisfactory function was found. Rather than perform a fit to a function over the spectrum, the calibration algorithm devised by M. G. de Bouard looks for a unique point on each spectrum. The algorithm is given a starting point roughly on the plateau in the middle. From there it searches for the

downward slope. The half-height point on the falling edge is chosen as the calibration point. Investigations using different starting points for the calibration algorithm have shown that this point is not sensitive to the choice of calibration start point.

5.9.2 1988 Radioactive Gas Data at Test Beam

During June 1988 when test-beam work was being conducted in the CERN West Area, petals 3 and 9 (these are numbered as end-cap A petals 12 and 7 when installed in ALEPH) were calibrated with radioactive gas during the same period in which beamline tests were being run on these modules. These measurements enable the radioactive gas response to be related to the absolute calibration in an electron beam. For petal module 3, a scan with 20 GeV electrons was performed. The running conditions were: high voltage = 1365 V, pressure = 982 mbar, temperature = 22°C. We take the calibration constant of the module as C_M (pC/GeV) and the electronic gain $\langle F \rangle$ (in fC/count) as defined in Eq. (5.5.1). The electron data taken for the wire readout gave $C_M/\langle F \rangle$ = 4260 counts/GeV. The ^{83}Kr parameter for this module, taken as the shower-weighted mean of 45 planes, was 506.8 ± 3 counts, equivalent to an energy deposition of 119 MeV. The electronic gain was measured to be $\langle F \rangle = 4.48 fC$/count. Therefore the ^{83}Kr figure has an 'equivalent' of 2.27 pC. If a 1.5% correction is made for the 'anode step' effect this is 2.30 pC. For the pad readout $C_M/\langle F \rangle$ = 256counts/GeV. The electronic gain for the pads was measured to be $\langle F \rangle = 25.2 fC$/count. The pad/wire ratio for this module is therefore $C_{M(pads)}/C_{M(wires)} = 0.338$.

The radioactive gas technique was also used to check the uniformity of response over the surface of a barrel module. Using the wire spectra subdivided into 4x4 tower regions, an excellent correlation was seen with the barrel electron scan data taken during the test beam running.

The radioactive gas data taken during the beam line tests in 1988 were used to determine the dependence of the radioactive gas calibration as a function of high voltage and P/T. These are power law dependences, similar to those found for the electron beam calibration, section 5.8. Data taken at a series of pressures gives the dependence of calibration point on P/T as $\alpha_{Kr} = -5.5 \pm 0.2$. The dependence of calibration point on voltage is $\beta_{Kr} = 12.5 \pm 0.2$. In June 1989 a short series of runs at three voltages on petal A1 confirmed this result.

5.9.3 Radioactive Gas Data Prior to LEP Startup

During the period between the middle of June and the end of July 1989 the ECAL end-caps had been mounted in the ALEPH detector and the detector was open, prior to the first LEP collisions. This section concerns the analysis of the radioactive gas data taken for the end-cap petals during this period. The radioactive gas technique was used to set the operating conditions required to equalize the energy response from the wires of each module. The absolute energy scale was determined from the data taken with two modules during the beam line tests described above. In the case of end-cap A, petal number twelve in end-cap A (one of the petals used in the beam line tests) was chosen as the 'reference' petal. After the calibration of each of the other petals was done, a short run on petal 12 was carried out, so the short petal 12 runs track any gas gain fluctuations and enable a comparison of all petals with petal 12 to be made. It would have been more natural to use the platines to track any gain changes whilst the radioactive gas data were being taken, however at this time reliable platine readouts were not available for all modules. In the case of end-cap B, a 'global' circulation mode was arranged, so that the same gas mixture was flowing in all petals. This should ensure that all petals in this end-cap were being calibrated under the same conditions.

The petals were operated with a high voltage setting of 1350V; a trigger threshold of $\approx$ 230mV; a pad cut of 8 ADC counts and an anode wire cut of 50 counts. Of the events which are above the trigger threshold, around 70% are acceptable events, i.e. only one pad tower and one wire plane are above threshold. Around 500 000 events were taken for each petal. An overall calibration figure for each module is taken by calculating the calibration point for each of the 45 individual plane spectra, then averaging these 45 values.

In order to make an accurate comparison between the calibration values from each of the petals, the raw data points must be adjusted for the following factors:

P/T the values of P/T of the modules changed during the course of the several weeks of data taking. For end-cap A, a comparison with the frequent petal 12 runs provides a normalization. For end-cap B, there was global circulation of the gas to all modules.

high voltage The slow control system was used to select a high voltage setting of 1350V for each petal. However, the true voltage delivered to the wire planes of a petal may differ slightly from this set value.

Petal Number	Calibration Point (Raw Data)	Normalized (P/T) Petal 12	Normalized for ΔV	Normalized electronic gain
1A	558	557	557	–
2A	561	556	543	542
3A	574	566	552	544
4A	530	568	563	559
5A	532	566	561	549
6A	525	541	543	544
7A	557	573	575	562
8A	510	504	509	514
9A	564	554	559	–
10A	542	531	536	540
11A	537	525	530	534
12A	541	541	541	541

Table 5.9.1: Radioactive Gas Calibration Points End-cap A 1989

Petal Number	Calibration Point (Raw Data)	Normalized (P/T) Petal 2	Normalized for ΔV	Normalized electronic gain
1B	590	586	580	550
2B	561	561	559	538
3B	563	542	547	525
4B	569	555	570	529
5B	557	519	534	–
6B	582	564	572	544
7B	577	559	568	549
8B	575	539	557	539
9B	553	534	551	537
10B	571	548	555	537
11B	565	559	564	545
12B	611	574	576	548

Table 5.9.2: Radioactive Gas Calibration Points End-cap B 1989

The actual voltage at the output of each power supply* was measured manually, and the voltage drop over the supply cable due to the measured current drawn by each module was calculated and subtracted from this reading. This gives an actual

* The petals are connected in pairs to the high voltage supplies, there are therefore six supplies for each end-cap.

voltage differing by up to as much as four volts in the worst case.

electronic gain The wire readout electronics for most modules was calibrated at the time of data taking, and the gains are then normalized using these factors. There are three runs for which these calibration factors are not available, and thus this correction cannot be applied.

The results for each end-cap are shown in Table 5.9.1 and Table 5.9.2. There is no reliable way of directly relating the end-cap A values to the end-cap B values. End-cap B has been normalized to P = 991 mbar and T = 295 K, the same values as end-cap A. The average calibration points for both end-caps are then within 0.6% of each other.

	Raw Data	Normalized (P/T)	Normalized for ΔV and electronics
End-cap A	12%	13%	9%
End-cap A w/out petal 8	9%	8%	5%
End-cap B	10%	12%	4.6%

Table 5.9.3: Spread in Radioactive Gas Data

Table 5.9.3 shows the spread in the calibration points for each end-cap. The second row is the data for End-cap A omitting petal 8, which was not considered to be in a good state at the time of calibration*. The spread of values in the raw data is reduced when

* The log-book entries at the time of data taking indicate that there were large variations in the pad amplifier pedestals from three of the front end cards of this petal. The σ of the pedestals was $\approx$ 4–5 counts, and as there is a σ cut of 3.8 applied this meant that data taking for this petal was only $\approx$ 60% efficient. As can be seen from inspection of the first column of Table 5.9.1, petal 8A has a calibration point of 510. This is significantly lower than the average value of 547 obtained from the other eleven petals. Inspection of the data taken for petal 8A shows that there were two planes disconnected from the readout. It is also seen that the values from the individual planes lie at two levels: twelve planes having a much higher calibration point (of around 580) than the others (which lie around 500). The spread in the calibration points from the planes of petal 8A is $\approx$ 5%, compared with $\approx$ 1–3 % for the other petals. The problems responsible for this behaviour were dealt with before the start of LEP running.

the corrections are applied. There appears to remain differences associated with the power supplies. The maximum spreads between pairs of petals on the same power supply are 4.0% (end-cap A) and 2.4% (end-cap B) compared with 5.2% and 4.6% overall.

5.9.4 Setting of Running Conditions

The high voltage settings of the end-cap modules for the LEP pilot run in September 1989 were based on the radioactive gas calibration described in the previous section. The pad/wire ratio found in the beamline tests for petal A12 was used for all petals. (This is justified as the pad/wire ratios found for all modules in the beamline tests were similar.) It was decided to set the module gains to be $C_M = 6.30pC$/GeV for the pads (similar to the 20 GeV electron running of the year before), therefore giving $C_M = 18.6pC$/GeV for the wires. The ^{83}Kr values above were then used to adjust the original high voltage setting of 1350 volts by the following procedure:

1. the average ^{83}Kr for the two petals on an HT supply was taken
2. use the electronic gain $\langle F \rangle$ of the wire electronics to get the ^{83}Kr value in equivalent pC.
3. adjust the voltage, using the dependence to the power 12.5 measured above, to get a calibration factor equal to petal A12
4. correct for (p/T) by adjusting voltage (using the power law dependencies found in 5.8). This gives a calibration of 256 counts/GeV.
5. make a final adjustment to 250 counts/GeV

In the case of endcap B, all petals were normalized to petal B2. Petal B2 has a ^{83}Kr parameter of 538 counts when adjusted to the same (p/T) as A12, which has 541 counts. As the ^{83}Kr parameters have an error of ≈ 3 when the mean of 45 planes is taken, the two petals are taken as equivalent.

5.9.5 Uniformity from Radioactive Gas Measurements

As has been explained above, the pad data were used to localize the place where the decay has occurred, and the wire data were read out. Each stack is split into 4 × 4 tower regions, as already used in the cosmic ray analysis, see Fig. 5.7.4. This gives 68 regions per stack. A spectrum is accumulated for each of these regions.

The data were taken with the primary purpose of performing an intercalibration among modules, and were also taken when there was some pressure on the amount of time available.

The use of the data for uniformity mapping was a secondary goal. Consequently, in several cases there is either no uniformity data available on tape for a petal, or not enough data to calibrate many of the individual regions. There are no uniformity data available on tape for end-cap B petals 5, 8, 9 and 12. In the case of end-cap B petal 3, insufficient data exists to perform a uniformity measurement of stack 1 of this module.

The same method of calculating the uniformity as in the case of the cosmic ray analysis was applied, i.e. the mean and rms. of each of the three stacks was taken. However, all of the 68 regions of each stack are considered as candidates for the uniformity calculation (i.e. the broad end regions in stack 3 are not excluded, as was the case in the cosmic ray data analysis). Any region for which there are too few entries for calibration (below 800 events), or in which the calibration algorithm abnormally terminates (is unable to find a reliable calibration point) is discarded from the analysis. The rms values for each petal are given in Table 5.9.4. The 'overall' figure is found from a weighted average of stacks 1, 2 and 3 in the proportion 0.42 : 0.47 : 0.11 . These weights are again derived from an average shower profile. The average rms. of the uniformity is 2.54%. In the calculation of the rms. value in the last column of the table, the regions which lie in the third high voltage region, i.e. those likely to be affected by the 'anode step' effect, have been excluded from the calculation. This improves the overall rms., which is now 1.78%. This is similar to the average rms. value of 1.71% found for the pad uniformity in the cosmic ray tests.

5.9.6 Wire Plane Profiles

Fig. 5.9.4 shows the calibration points for the individual planes 1–45 of petal 1 of end-cap A. It may be seen that there the planes have deviations of the order of a few percent from the mean value. There may be several explanations for these variations:

- the calibration algorithm not working correctly
- variations in the gain of the signal amplifiers for each wire plane
- differences in the high voltage decoupling capacitor for each plane
- genuine differences in the gas gain for each plane

The first explanation may be ruled out if a comparison of wire planes profiles from data taken a few months apart is made. Fig. 5.9.5 shows the wire plane profile of petal 9 of end-cap A with data taken in June 1989 and September 1989. The upper plot shows the June data as crosses and the September data as circles. This plot shows that there has been a global shift of 4% downwards in the calibration. In the lower plot, this factor has been

Petal Number	Stack 1 σ_{rms} (%)	Stack 2 σ_{rms} (%)	Stack 3 σ_{rms} (%)	Overall σ_{rms} (%)	third region σ_{rms} (%)
A1	3.72	3.43	2.56	3.45	2.21
A2	3.03	2.78	2.61	2.86	2.02
A3	2.70	2.05	2.02	2.32	1.54
A4	2.53	2.52	2.11	2.48	1.93
A5	1.89	1.85	1.83	1.86	1.21
A6	2.53	2.71	2.33	2.59	1.58
A7	2.68	2.77	2.35	2.68	1.58
A8	2.70	2.96	2.67	2.82	1.81
A9	2.40	2.34	2.43	2.37	1.39
A10	2.46	2.79	2.40	2.61	1.68
A11	2.13	2.39	2.32	2.27	1.25
A12	3.06	2.55	1.82	2.68	1.65
B1	2.50	2.32	2.34	2.40	2.67
B2	2.91	2.35	2.16	2.56	2.74
B3	-	3.28	2.35	3.10	1.56
B4	2.27	2.31	2.18	2.28	1.55
B6	2.22	2.41	2.39	2.33	1.47
B7	2.88	2.28	2.06	2.51	1.58
B10	2.88	2.80	2.14	2.76	2.28
B11	1.83	2.14	1.74	1.96	2.24
mean	2.60	2.55	2.24	2.54	1.78

Table 5.9.4: Uniformity Results from Radioactive Gas Tests

corrected for in the September data and the plots again overlaid. The plane calibration points may be seen to coincide within errors (except for planes 15 and 32). It may therefore be concluded that the variations are a characteristic of the module and/or its wire readout electronics.

For each module, the wire profile is plotted and the HBOOK package used to take the mean and RMS. These RMS values range from 0.94% to 3.5% of the mean. On average, there is a 2% spread in the plane calibration factors within a petal. When examining the plots of wire plane calibration factors, it was seen that there was a tendency for the value to increase with higher plane number, i.e. front-to-back. The average over all available petals was taken for each plane, and is plotted in Fig. 5.9.6. The fit shown is to a straight line (the χ^2 of the fit is 0.4633). It may be seen that there is a clear increase of 1.7% from front to back. The explanation for this effect is unclear, but it may be noted that pad size also increases from front to back.

5.10. ECAL Calibration using 'Bhabha' Events

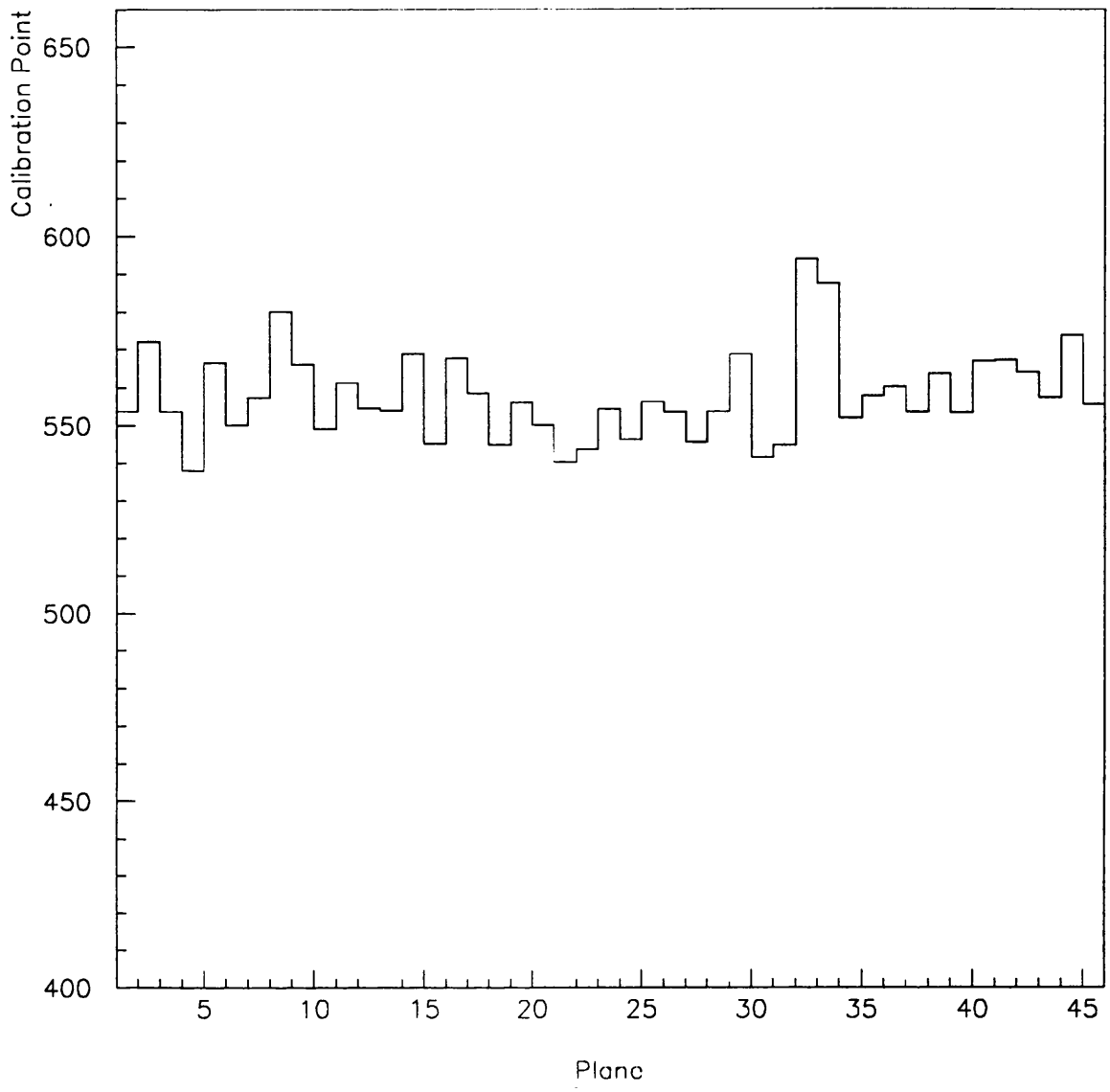

Fig. 5.9.4: Wire Plane Profile for Petal A1

The interaction $e^+e^- \rightarrow e^+e^-$ provides events which are very useful in calibrating the calorimeter. This is because the events have a very well known energy distribution, as predicted by QED, up to a maximum energy for each electron equal to the beam energy. Also, if enough events are taken, energy deposits are recorded over the whole calorimeter with equal energies. A preliminary study by G. D'Agostini [150] using simulated Bhabha events showed that these events can be used to calibrate the modules. Bhabha events at LEP are also used for luminosity monitoring, line shape measurements and forward-backward asymmetry measurements. The energy spectrum and angular distribution for these events is derived in [151] which also includes discussion of the radiative effects. The

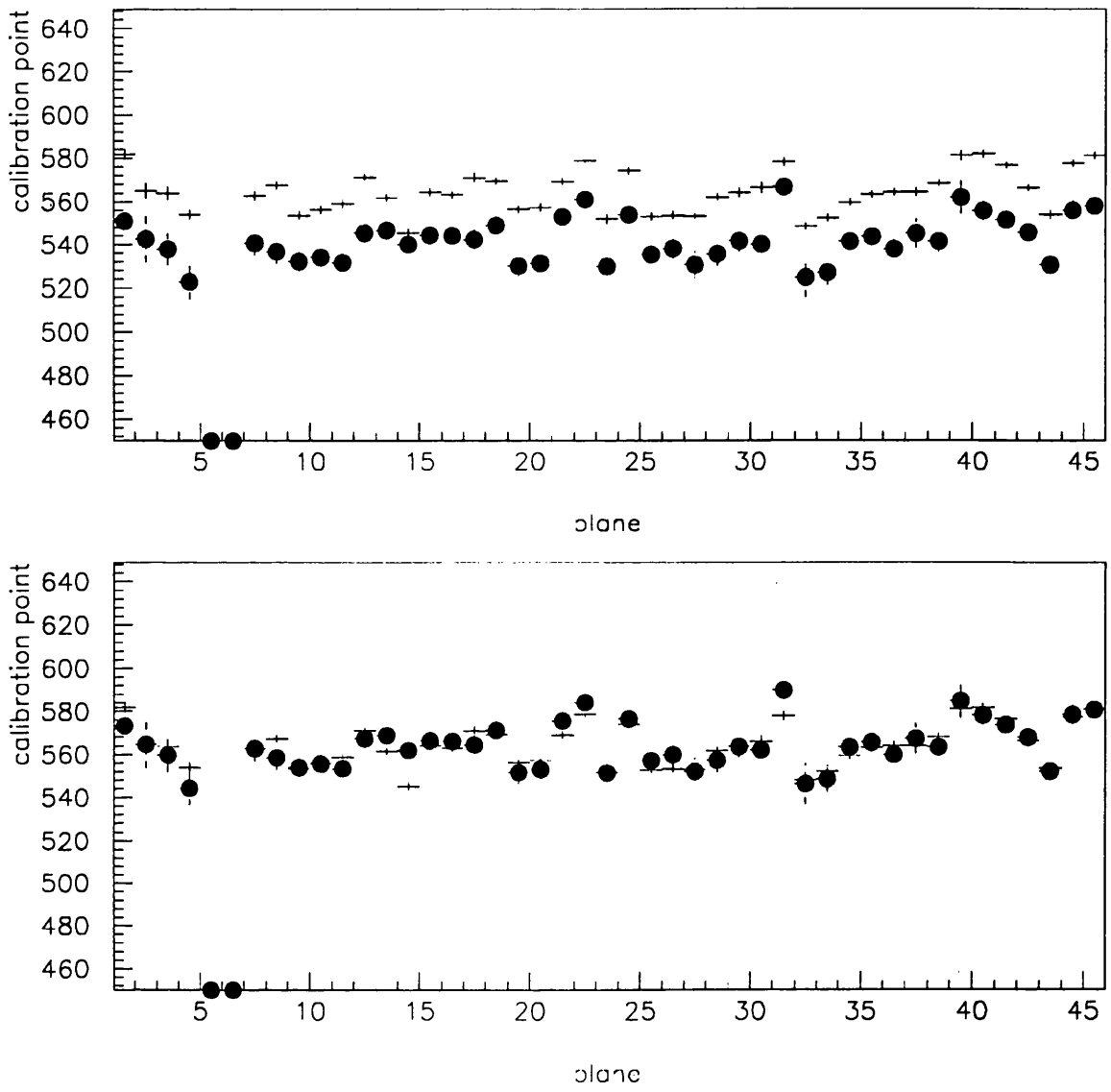

Fig. 5.9.5: Comparison of June and September 1989 Calibrations

reaction $e^+e^- \rightarrow e^+e^-$ can take place by virtual photon exchange in the t-channel and by space-like photon or Z^0 exchange in the s-channel. It is possible to have both elastic Bhabha scattering: $e^+e^- \rightarrow e^+e^-$ and radiative Bhabha scattering, with the emission of a photon: $e^+e^- \rightarrow e^+e^-\gamma$. This section presents the results of a short study of the wide-angle Bhabha events in the electromagnetic calorimeter for the events taken in the first ALEPH running period from September to December 1989. This study was performed as a check on the preliminary calibration made with the radioactive gas technique and to demonstrate the applicability of small-angle Bhabha events for calibration. The results from similar, more

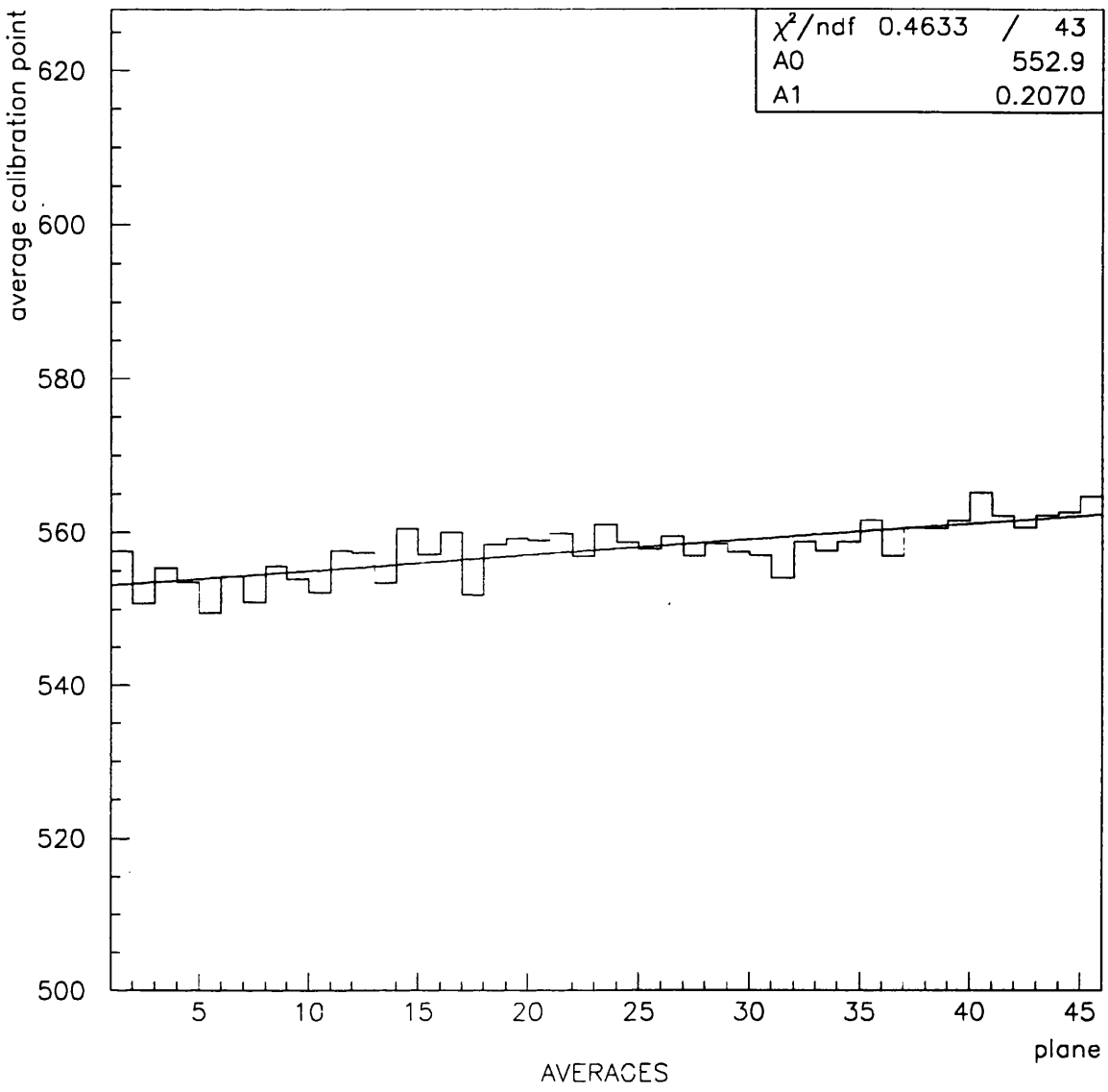

Fig. 5.9.6: Average Values of Wire Planes – All Petals

comprehensive studies are used to determine the calibration constants for the reconstruction of the calorimeter data in JULIA.

5.10.1 Bhabha Selection

The selection program made use of the EDIRs created for each ALEPH run, described in section 4.7. The Bhabha selection program was run on classes 1 and 3, which are those events with more than two ECAL modules with wire energy over 2.5 GeV in each, those events with ECAL barrel energy over 6 GeV and those events with ECAL End-cap A and End-cap B both over 2 GeV. The Bhabha selection program selected all those events with

two or more ECAL modules with wire energy over 30 GeV. To reject energetic $q\bar{q}$ events, those events with more than 5 charged tracks were rejected. Fig. 5.10.1 shows a typical selected event which deposits energy in the end-caps. The calorimeter is shown in the $\theta - \phi$ projection.

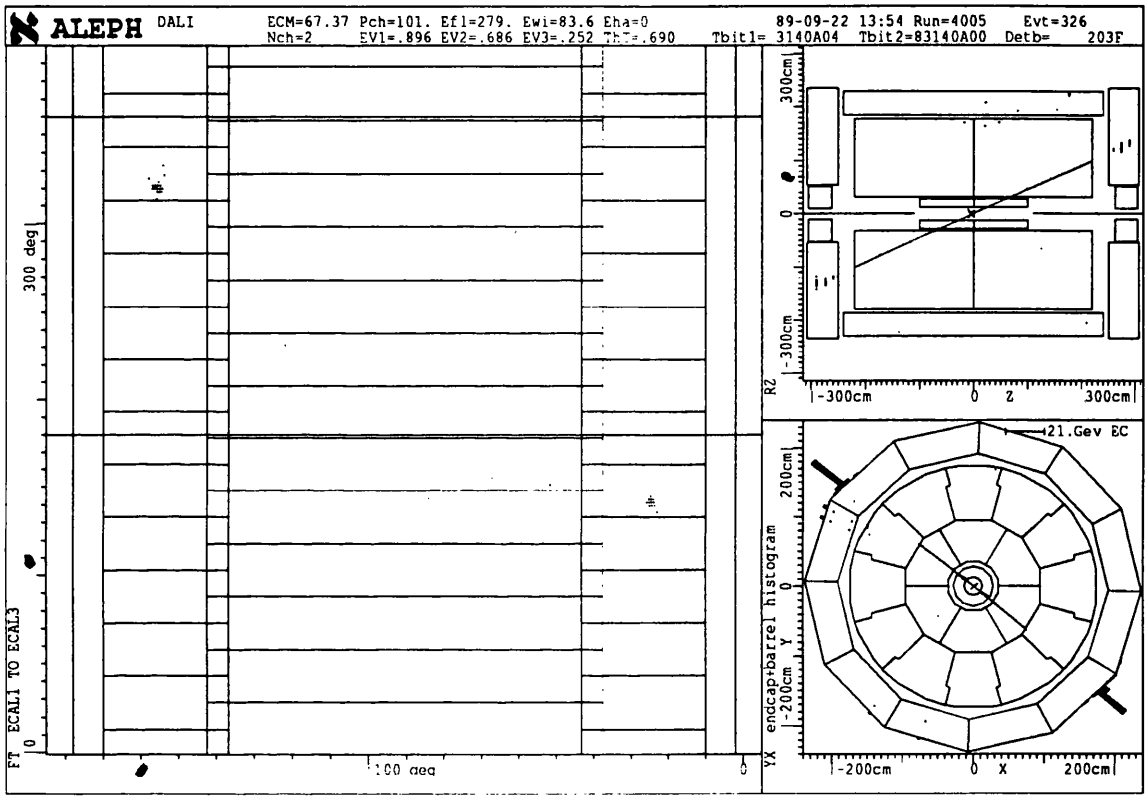

Fig. 5.10.1: A Typical Wide-Angle Bhabha Event

In the September to December runs of LEP, ALEPH recorded an overall luminosity of $1182 \pm 7nb^{-1}$. From runs 4001 to 5090 there were 63240 events in EDIR classes 1 and 3. The selection procedure identified 5798 Bhabha candidates from these.

5.10.2 Module Calibrations with Bhabhas

If the Bhabha events taken when LEP was running only on the Z^0 peak during the 1989 running are split up on a module-by-module basis, then there are too few events per module (≈ 50) to do a meaningful calibration. In order to make use of events from all the 1989 running in the same calculation, the ratio of module energy to beam energy was used. This means that there are approximately 100 useful events per module. The LEP beam

energies in question lie between 44 and 48 GeV. Only wire and pad energies between 30 and 60 GeV were included in the analysis.

A typical plot of the ratio of pad to beam energy (in this case for module 1 of end-cap A) is shown in Fig. 5.10.2. The fit is to a Gaussian function. The same analysis was carried out for the wire energy in each module.

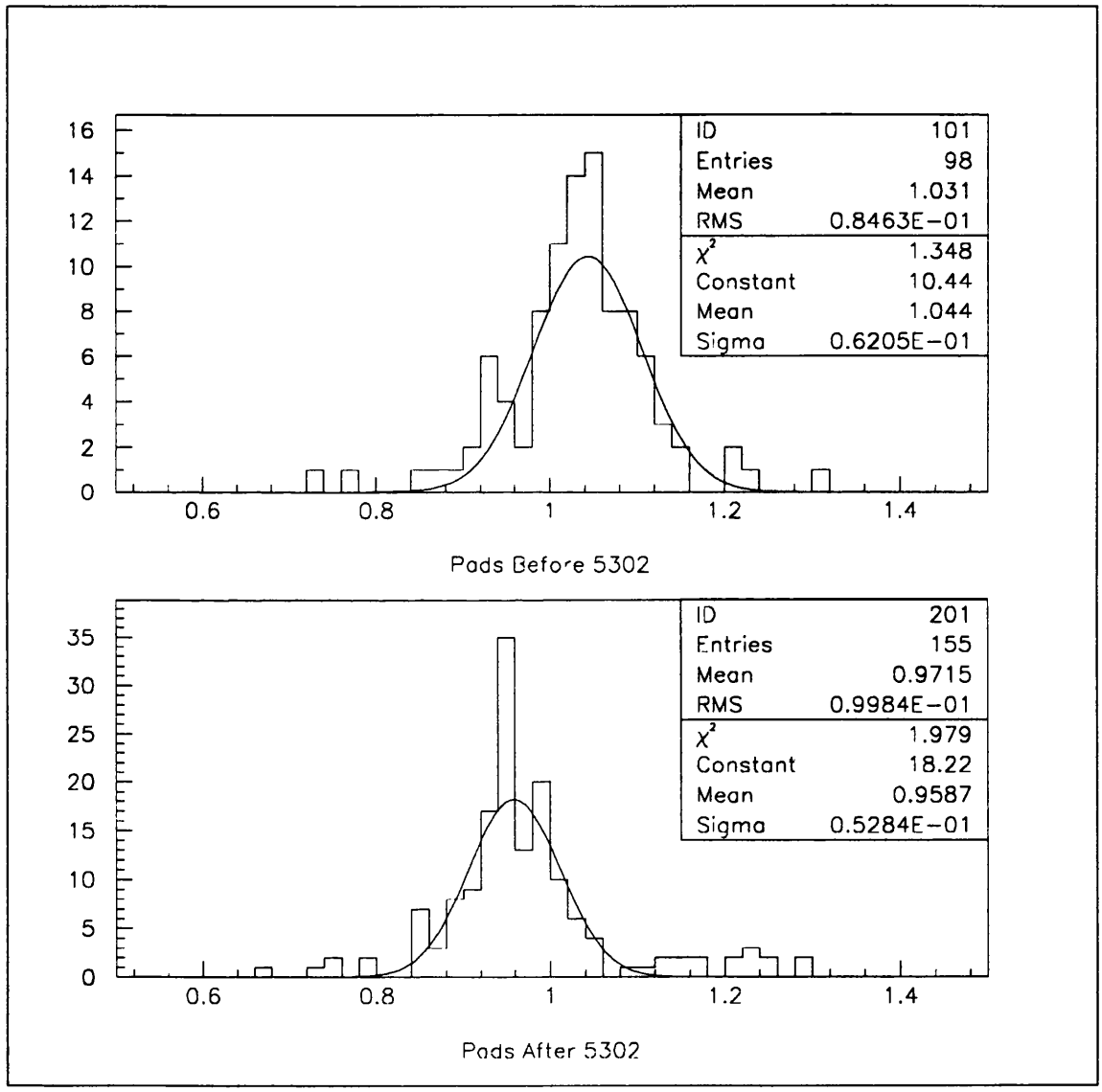

Fig. 5.10.2: Ratio of Pad to Beam Energy for Module 1

On 14/11/89, between runs 5301 and 5302, an adjustment of the high voltage settings of the modules was carried out, in order to bring the calibration points of the modules closer together. The analysis of the results is therefore split into two parts viz. those events before run 5302 and those after. An attempt was made to measure the effect of re-tuning the high voltages after run 5302. The results of the Gaussian fits to the pad energy distributions are

Module Number	Mean before 5302	Sigma	Mean after 5302	Sigma
A1	1.04	0.06	0.96	0.05
A2	1.01	0.04	0.93	0.04
A3	1.00	0.05	0.93	0.05
A4	1.01	0.06	0.94	0.04
A5	1.02	0.05	0.94	0.04
A6	1.06	0.05	0.94	0.04
A7	1.11	0.04	0.98	0.04
A8	1.11	0.05	0.97	0.04
A9	1.11	0.09	0.94	0.05
A10	1.10	0.10	0.92	0.05
A11	1.12	0.06	0.96	0.06
A12	1.05	0.06	0.94	0.06
B1	0.94	0.04	0.93	0.06
B2	1.03	0.04	0.89	0.04
B3	1.07	0.05	0.93	0.04
B4	1.05	0.05	0.95	0.05
B5	1.01	0.10	0.92	0.04
B6	0.99	0.06	0.92	0.05
B7	1.00	0.05	0.92	0.05
B8	1.07	0.04	0.89	0.04
B9	1.06	0.06	0.93	0.07
B10	1.00	0.06	0.91	0.08
B11	1.03	0.06	0.91	0.06
B12	0.94	0.04	0.90	0.06
mean	1.04	0.06	0.93	0.05

Table 5.10.1: Pad Energy / Beam Energy in Bhabha Events

given in Table 5.10.1 and to the wire energy distributions in Table 5.10.2. The spread in the pad calibration points is reduced from 17% to 10% after the high voltage adjustments have been carried out; the spread for the wires is reduced from 15% to 6%.

The 'sigma' value given is the width of the Gaussian fit. For both pads and wires, this gives an energy resolution of $\simeq$ 5.5%. From the electron energy resolution measured at the beamline, Eqs. (5.8.1)and (5.8.2), the expected $\Delta E/E$ = 3.2% at 45 GeV for the pads, and 3% for the wires. It must be stressed that the data here is of a low statistics sample, from the very start of the ALEPH running. Later studies with more statistics [111], and more up–to–date calibration constants for the modules have found energy resolutions of $17\%/\sqrt{E}$ + 1.6% for the wires and $19\%/\sqrt{E}$ + 1.7% for the pads.

Module Number	Mean before 5302	Sigma	Mean after 5302	Sigma
A1	0.91	0.07	0.93	0.06
A2	0.99	0.06	0.94	0.05
A3	0.90	0.05	0.95	0.04
A4	0.88	0.05	0.92	0.05
A5	0.88	0.06	0.94	0.04
A6	0.92	0.04	0.96	0.04
A7	0.96	0.07	0.96	0.05
A8	0.89	0.03	0.94	0.04
A9	0.95	0.08	0.97	0.04
A10	0.90	0.06	0.92	0.06
A11	0.93	0.06	0.94	0.04
A12	0.91	0.04	0.95	0.05
B1	0.85	0.03	0.95	0.07
B2	0.92	0.04	0.93	0.03
B3	0.88	0.04	0.91	0.04
B4	0.94	0.04	0.94	0.06
B5	0.89	0.07	0.95	0.05
B6	0.87	0.04	0.93	0.05
B7	0.89	0.04	0.91	0.06
B8	0.96	0.04	0.92	0.04
B9	0.93	0.01	0.95	0.06
B10	0.91	0.05	0.95	0.04
B11	0.90	0.05	0.95	0.05
B12	0.86	0.04	0.94	0.04
mean	0.91	0.05	0.94	0.05

Table 5.10.2: Wire Energy / Beam Energy in Bhabha Events

Chapter 6.
Inclusive π^0 Cross–Section in Z^0 Decays

6.1. Introduction

An important function of electromagnetic calorimeters is their ability to identify π^0s. This chapter is concerned with a measurement of the inclusive cross–section for the production of neutral pions in hadronic events. The pions are reconstructed from combinations of pairs of photons measured in the electromagnetic calorimeter. Their distribution as a function of the Feynman variable x_p is measured. where x_p is defined as the ratio of the particle momentum to the beam energy $\sqrt{s}/2$. This distribution is compared to the distribution from Monte Carlo events. and is compared to measurements made by the L3 collaboration [152]. As discussed in 1.5.7 the measurement of inclusive particle distributions are an important part of studying the hadronisation process and testing the validity of Monte Carlo models.

6.2. Event Sample

Using samples of Monte Carlo generated data, the ALEPH QCD group has agreed upon a standard set of cuts to select $q\bar{q}$ events. There are two selection procedures: one based on the ECAL information and one on TPC information. The former, which selects both hadronic and τ events, requires more than 20 GeV to be deposited in the calorimeters, with $\geq$ 20GeV in the ECAL barrel or at least 1.5 GeV in each end–cap. Large angle Bhabhas are rejected on the basis of their tight energy clusters. For events with no tracks, the PASTIS timing information is used to reject out of time events, and also more than 2 clusters above 3 GeV are demanded in ECAL. This selection has an efficiency of 0.974 ± 0.006 for hadronic and τ events.

The charged track selection requires at least five charged TPC tracks in the event. Each track must have a polar angle of more than 18.2°, at least 4 TPC hits, and an origin less than 2cm in radius and less than 10cm in z from the vertex. In addition the total energy of all TPC tracks satisfying the above cuts should be more than 10% of the centre–of–mass energy. Comparison with Monte Carlo data shows that this method has an efficiency for selection of $q\bar{q}$ events of 97.4%. The background from $\tau\tau$ events is 0.26 ± 0.03%. The

background from two–photon events* is $0.39 \pm 0.07\%$. The EDIR facility introduced in section 4.7 was used to select $q\bar{q}$ events for the analysis described in this chapter. The events used are EDIR 'class 16' events which are the ALEPH $q\bar{q}$ events selected on the basis of TPC track information. For this study, events were selected at the Z^0 peak only, i.e. at LEP energies of 91.250 ± 0.1GeV.

The selected data sample consists of all the $q\bar{q}$ events at the Z^0 peak taken by ALEPH in 1991. The sample contains 225951 hadronic events, equivalent to 231744 events when an efficiency correction is applied. The corresponding integrated luminosity was $7556 \pm 17 nb^{-1}$, where again only the statistical error is quoted.

The Monte Carlo data sample used was a sample of 337638 events, produced by JETSET 7.3 and the HVFL02 event generator, described in section 4.2.1. The detector simulation was performed on these events by GALEPH version 242 (and GALEPH version 250 for a small proportion of the events), using the 1991 detector geometry. The events were reconstructed by JULIA version 258.

It should be noted that there are some differences in the treatment of Monte Carlo data and real data at the reconstruction stage. Within the detector simulation GALEPH, the readout thresholds on all storeys are set to 30 MeV. In the reconstruction program JULIA, a clustering correction is applied to all clusters which takes into account energy losses due to the online threshold values. The online thresholds are held in the database bank EZTH and are 20, 28 and 42 MeV for stacks 1,2 and 3 respectively for the runs dealt with in this analysis. Also, all storeys are considered to be perfect in GALEPH: that is to say, there are no 'dead' or 'killed' storeys in the Monte Carlo. See section 4.4 for a description of the dead storeys in the real data.

6.3. The GAMPEK package

The GAMPEK package is used to reconstruct photons in the electromagnetic calorimeter at the JULIA reconstruction stage, for both real and Monte Carlo data. During reconstruction, the GAMPEK package is called for each Ecal calorimeter cluster (PECO). The input is the cluster number of the PECO and a minimum energy – each reconstructed photon will have an energy greater than this number. The package returns the number

* These are events in which two virtual photons, radiating from the incident electron and positron, scatter from each other.

of photons found in the cluster and a list of the photons. For each photon the following information is returned and stored in the bank EGPC :

- the three–vector of the photon
- the proportion of energy in stack 1 and in stack 2
- the F4 estimator: the energy fraction in the 4 central towers
- number of storeys in stacks 1, 2 and 3
- distance to the nearest charged track
- flag if photon is in ECAL crack region
- number of dead storeys in each stack
- number of the PECO cluster containing the gamma

The parameters used by GAMPEK are stored in the database in the bank EGRP. The parameters used when these data were processed are:

- minimum distance of charged track to stack 1 energy deposit > 2 cm
- minimum gamma energy = 250MeV
- minimum storey energy = 30MeV
- threshold in stack 1 to start forming cluster = 75MeV
- threshold in stack 2 to start forming cluster = 150MeV
- threshold in stack 3 to start forming cluster = 200MeV
- minimum energy in stacks 1 and 2 for a gamma = 150MeV
- a cluster with energy deposits only in stacks 1 and 2 may be accepted as a photon
- a cluster with energy deposits only in stacks 2 and 3 may be accepted as a photon

The default values of the GAMPEK parameters, chosen following studies of Monte Carlo data and data from well–defined final states, were used in this analysis.

6.4. π^0 Reconstruction

The selection criteria for the gamma pairs used to reconstruct π^0 are discussed below. The cuts were decided on the basis of studies of small Monte Carlo data samples.

6.4.1 Cut on Angle Between γs

A sample of 2000 Monte Carlo events was used to study the effect of cutting on the angle θ between the decay gammas of the π^0. The study was done solely at the Monte Carlo truth level, before reconstruction. No cuts, other than the decay angle cut, were made on the data. At the truth level, there are 19845 pairs of gammas which are the daughters of π^0, and 606826 combinations of gamma pairs overall (this 'background' figure includes all pairs from π^0). Fig. 6.4.1 shows the distribution of $\cos(\theta)$ for the background pairs as a solid line, and the real pairs as a dashed line.

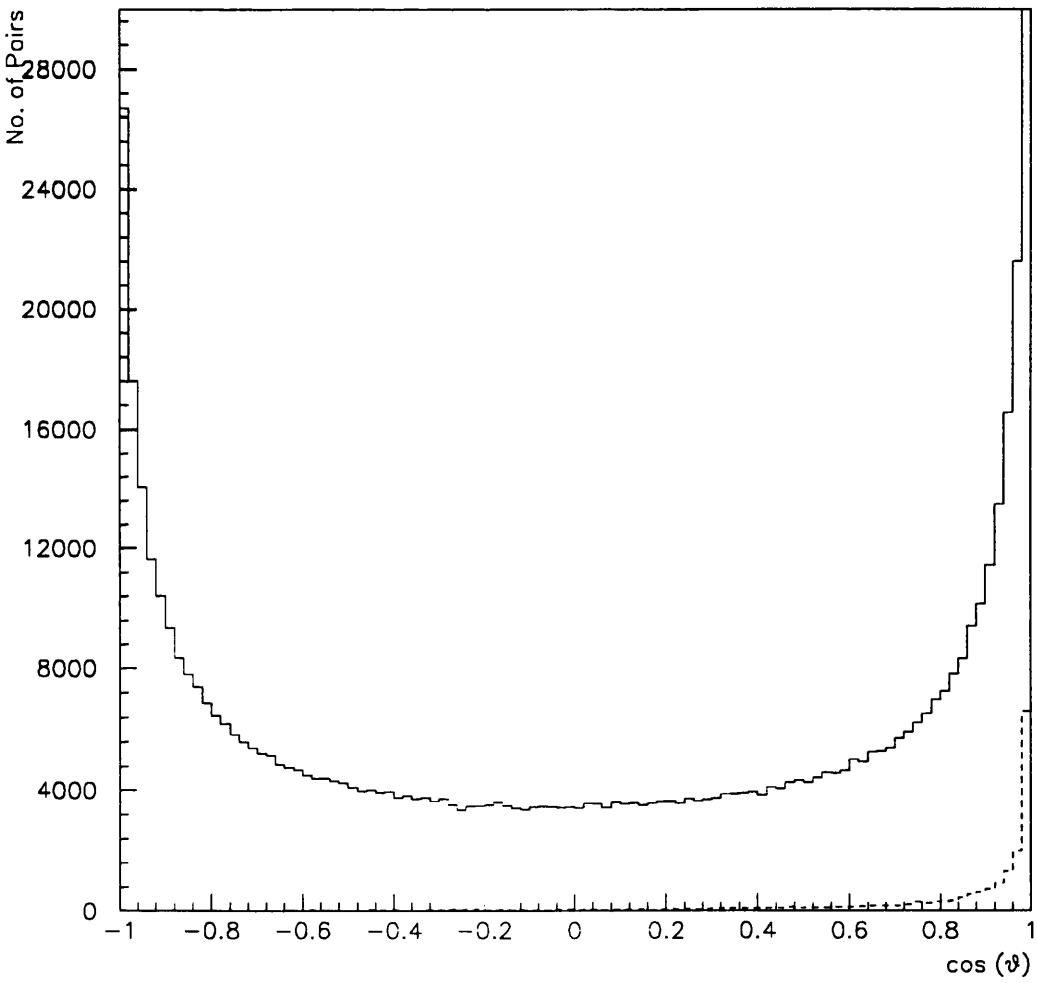

Fig. 6.4.1: Angle between decay gammas - background and real

Table 6.4.1 gives the percentage of pairs remaining as a function of the cut on $\cos(\theta)$, and gives a 'theoretical' signal/background ratio, which is simply the ratio of the π^0 pairs remaining to the background pairs. It was decided to make a cut of 0.5 on $\cos(\theta)$. This

cut on $\cos(\theta)$	π^0 remaining (%)	background remaining (%)	signal/background ratio (%)
-0.75	98.9	77.6	4.2
-0.50	98.8	67.7	4.8
-0.25	95.3	59.8	5.2
0.00	92.8	52.7	5.8
0.10	91.6	50.0	6.0
0.20	90.3	46.8	6.3
0.30	88.7	43.8	6.6
0.40	86.4	40.6	7.0
0.50	83.8	37.3	7.4
0.60	80.7	33.6	7.9
0.70	76.5	29.3	8.5
0.80	70.0	24.1	9.5
0.90	58.2	17.1	11.2
0.95	46.9	11.7	13.1

Table 6.4.1: Effect of decay angle cut

is a very loose cut. A tighter cut would improve the 'signal/background' ratio, but would reduce the statistics of the π^0 signal.

6.4.2 Gamma Energy Cut

Two samples of 20000 real and 20000 Monte Carlo events were compared. The effect on the invariant mass spectrum of changing the minimum gamma energy was studied. Fig. 6.4.2 shows the invariant mass spectrum as the minimum gamma energy is varied. The real data is shown as a solid line, and the Monte Carlo as dashed. On the basis of this comparison it was decided to make a cut of 500 MeV on the minimum gamma energy.

This cut may also be justified on the basis of the low energy Monte Carlo simulation of the calorimeter at low energies, as discussed in 6.6. It could be argued that a higher energy gamma cut, perhaps around 1 GeV, would give a better agreement between data and Monte Carlo. However, it was desired to extend the range of x_p studied to the lowest values possible. Therefore, the lowest acceptable gamma energy cut was chosen.

6.4.3 Quality Cut

It was decided to remove all those gammas which are flagged as having had corrections made to them for missing storeys in the cluster etc. and to remove all those gammas which are near to cracks in the calorimeter. (In technical terms, only those GAMPEK gammas with a 'correction code' of zero are accepted). This cuts the average number of GAMPEK gammas per event from 10.9 to 9.3, i.e. by 15%.

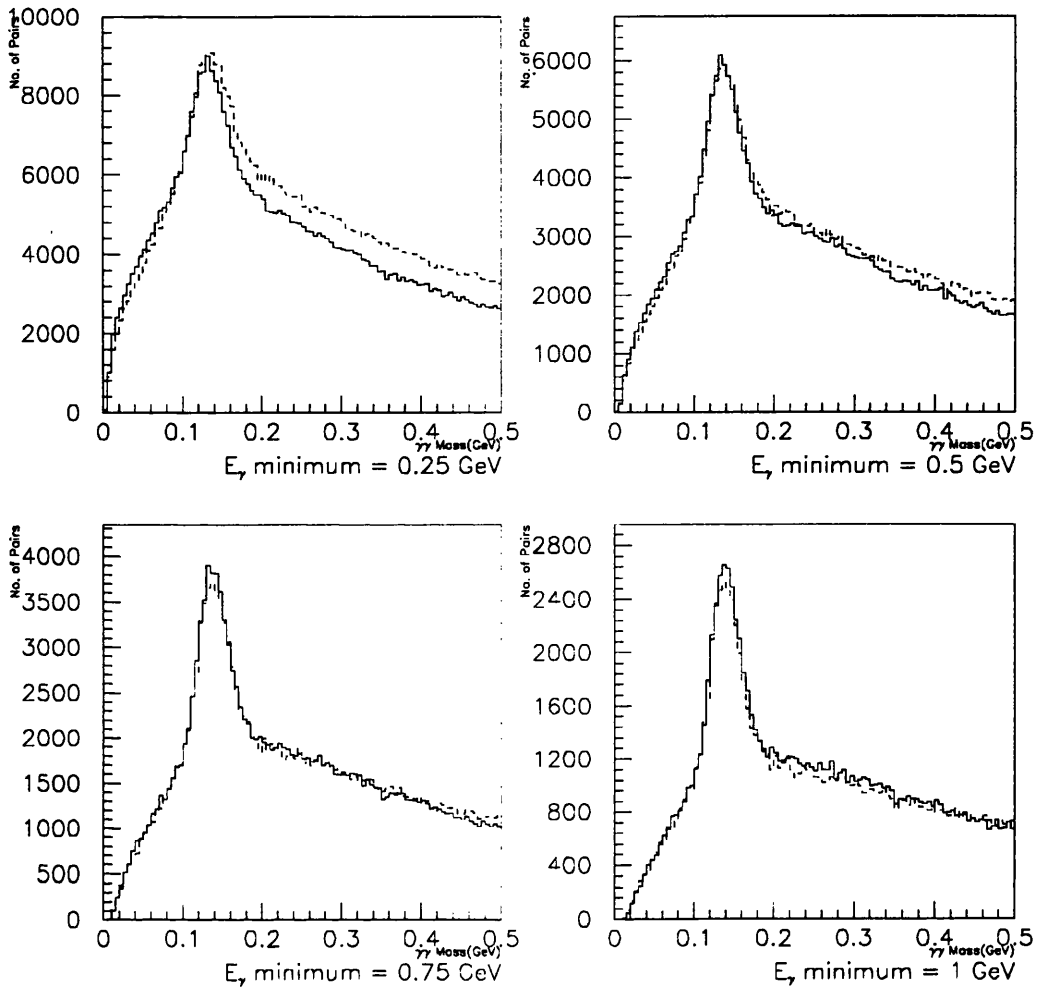

Fig. 6.4.2: Effect of changing minimum γ energy on $\gamma\gamma$ mass distribution

6.4.4 Angular Cut

It was decided to perform the analysis with data from the barrel section only, i.e. to cut out the angular range with $\theta < 40°$ and $\theta > 140°$, which effectively removes the end-caps. The barrel modules have a more uniform cell size and a simpler geometry. The clustering of calorimeter energy is therefore more complicated in the end-caps. Any background from synchrotron radiation and off-axis particles will also be concentrated in the end-caps.

6.4.5 Restriction on gammas to be members of same cluster

The effect of restricting the two gammas combined to make a π^0 candidate to be members of the same PECO cluster was studied. A sample of 10000 $q\bar{q}$ events from the 1991 data in DST format was used. The lower plot in Fig. 6.4.3 shows the invariant mass of all GAMPEK gamma pairs, where the restriction is made that the gammas are members of

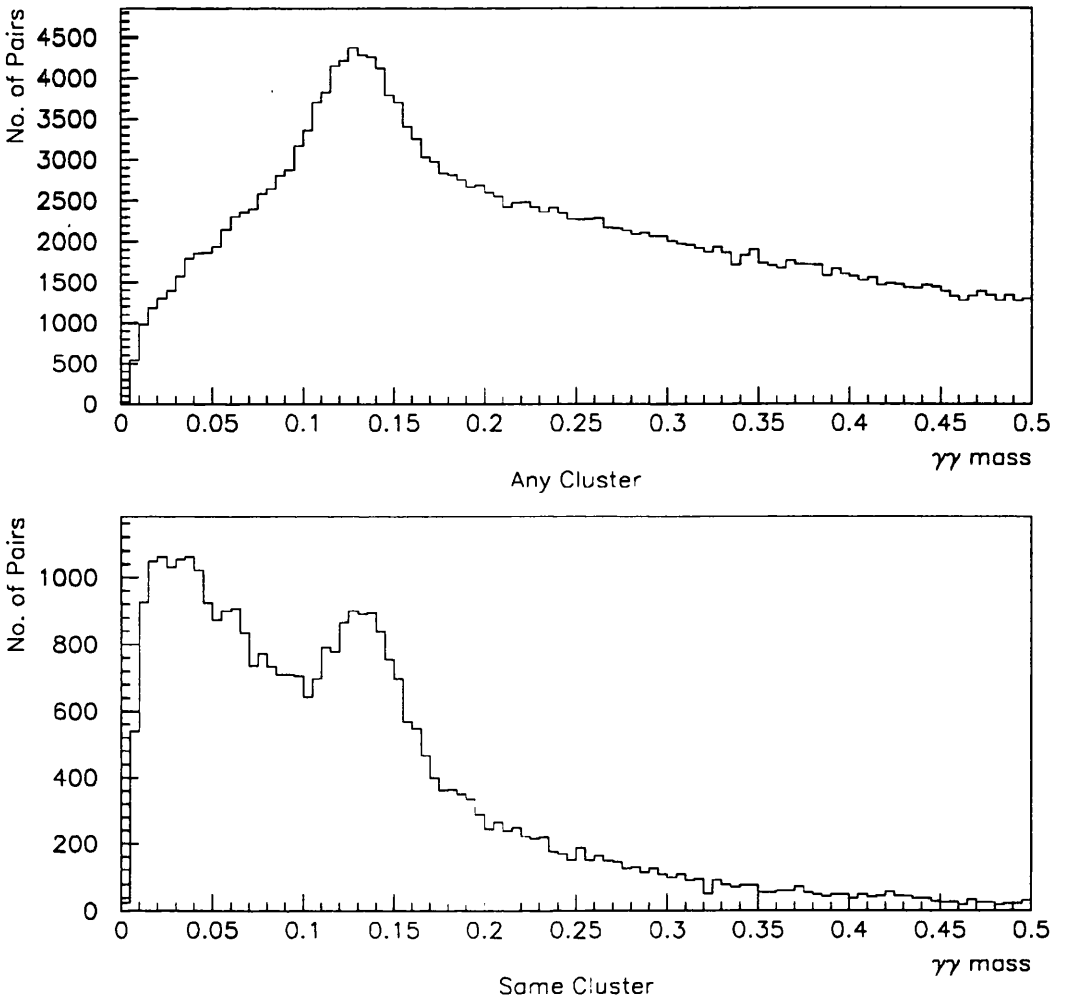

Fig. 6.4.3: Effect of having both gammas in same cluster

the same PECO cluster. The upper plot has no restriction. No other cuts (i.e. no angular cut, no energy or quality cuts) have been made on these data.

The total number of combinations in the case where the gammas are unrestricted is 218132 and in the case where they are restricted to be members of the same cluster is 34592, thus substantially cutting down the combinatorial background. While this restriction cuts down the number of combinations considered, the number of π^0 in the peak of the $\gamma\gamma$ mass distribution is also reduced. It may be seen that there is a significant number of low invariant mass combinations in the case where the restriction is made that the gammas are members of the same cluster. Fig. 6.4.4 shows the effect of raising the gamma energy cut on the invariant mass peak in this sample.

It is clearly seen that the low energy shoulder in the $\gamma\gamma$ mass plot of Fig. 6.4.4 is associated with low energy gamma pairs, such that when a gamma energy cut of 1 GeV is

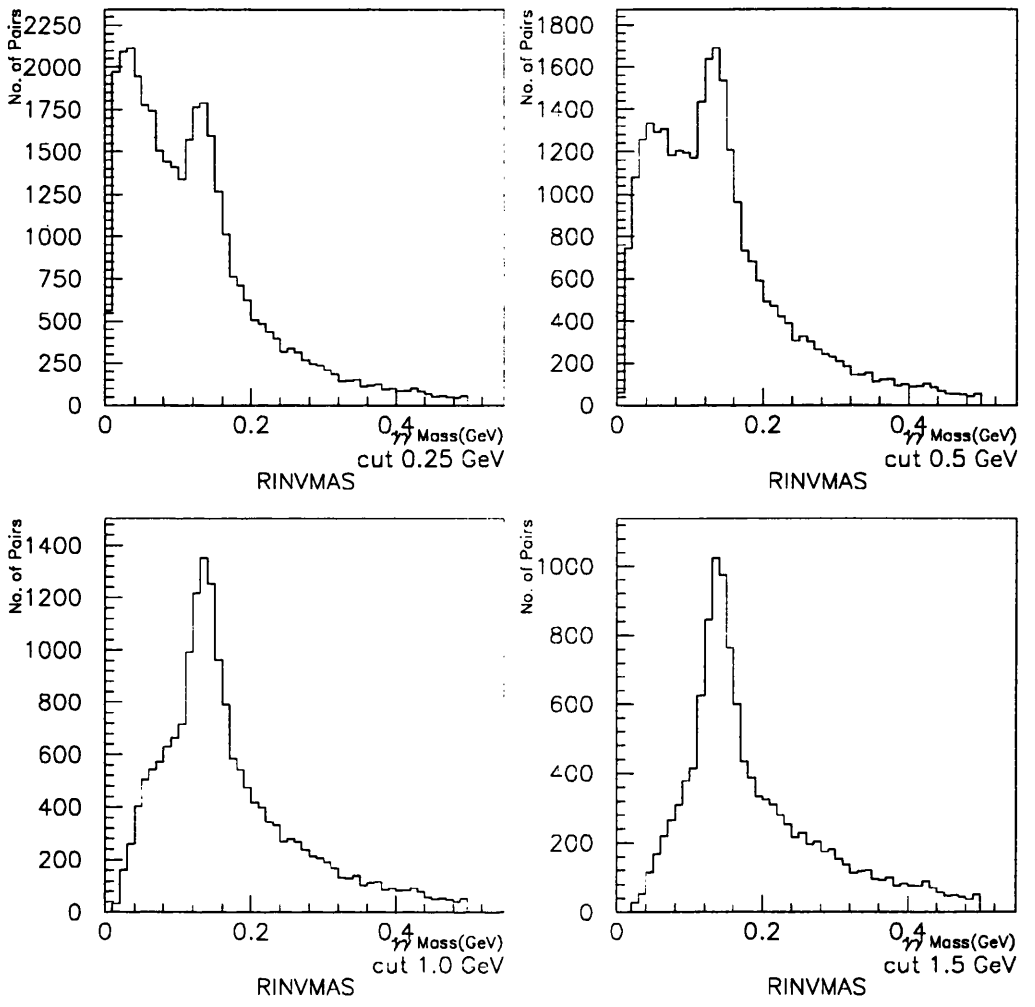

Fig. 6.4.4: Gammas in same cluster – effect of energy cut

reached it has been eliminated. It was decided not to use the restriction on the gammas being members of the same cluster as a cut in this analysis. in the light of the low gamma energy cut of 0.5 GeV which is being used.

6.5. Results

Fits are made using the PAW program to the histograms of each x_p interval. The functions used are a gaussian for the peak. plus a fifth degree polynomial for the background. The errors on the fit parameters are those given by the MINUIT package.

6.5.1 Overall peak

Fig. 6.5.1 shows the invariant mass spectrum resulting from the 1991 data. All pairs of gammas. subject to the cuts defined in 6.4 are included. The data are well fitted by a

gaussian plus polynomial background. The parameters P1 to P9 given in the diagram are the fit parameters reported by PAW: there are nine parameters as the fit is to a gaussian plus a fifth–degree polynomial. The peak is at 134 MeV and has a width of 18 MeV. The peak contains 179200 ± 1200 π^0.

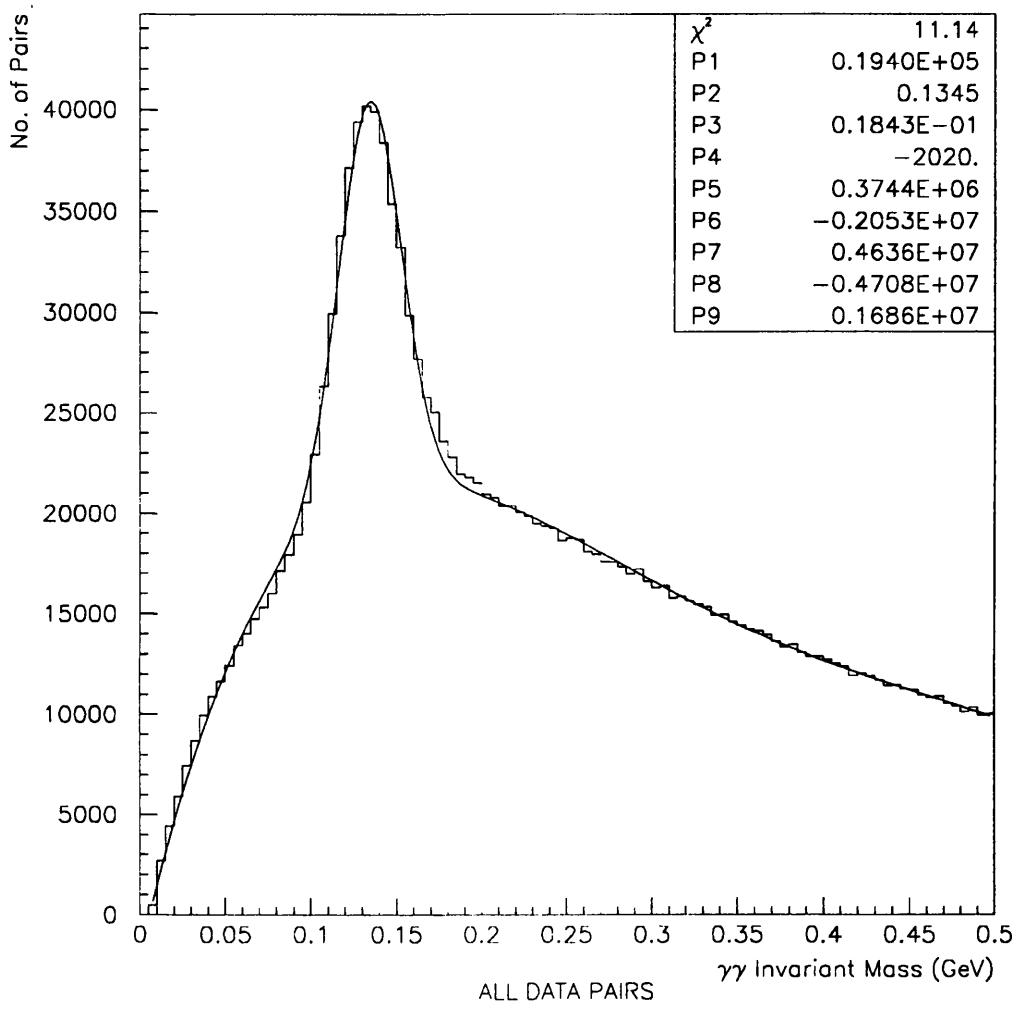

Fig. 6.5.1: $\gamma\gamma$ Invariant Mass Spectrum

The average number of π^0s per event in the x_p range from 0.02 to 0.4 is then $\langle\, n_{pi^0} \rangle = 6.68 \pm 0.06$. The number of π^0s generated by JETSET 7.3 in the corresponding range is $\langle\, n_{pi^0} \rangle = 5.4$.

6.5.2 x_p Distribution

For each $\gamma\gamma$ pair, the x_p value of the supposed π^0 which is their parent is calculated as

$$x_p = \left((E_{\gamma 1} + E_{\gamma 2})^2 - m_{\pi^0}^2 \right)^{\frac{1}{2}} \times 2/E_{LEP} \qquad (6.5.1)$$

Larger bin widths were chosen at higher x_p due to the lower statistics at these values. Fig. 6.5.2 shows the $\gamma\gamma$ invariant mass distributions for four of the x_p bins selected, and shows that the data are well fitted by a gaussian plus polynomial background over the whole x_p range.

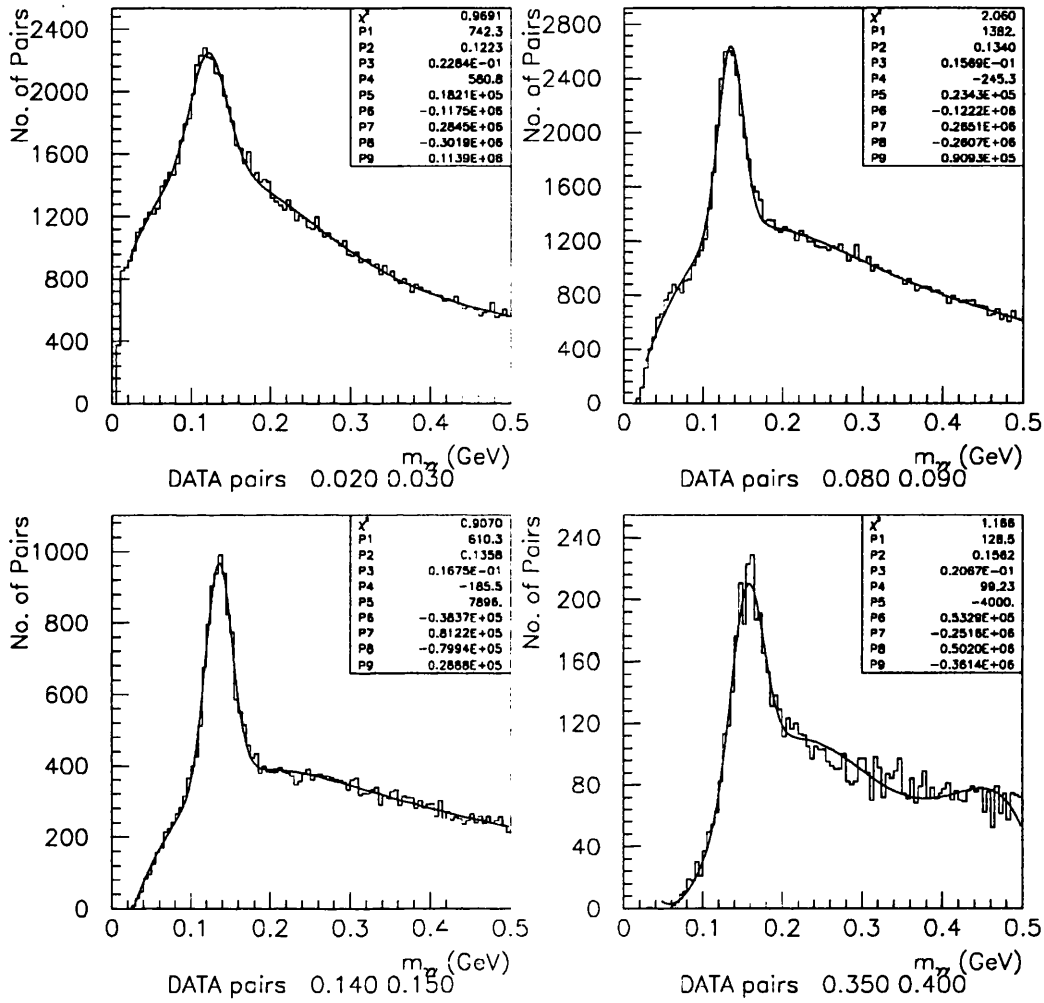

Fig. 6.5.2: Invariant mass for different ranges of x_p

Table 6.5.1 gives the results for the cross-sections for the various x_p bins. The results are normalized as $1/\sigma_h d\sigma/dx_p$.

6.5.3 Comparison of Data and Monte Carlo

Fig. 6.5.3 shows a comparison of the 1991 data and the Monte Carlo sample. The Monte Carlo is the solid lines, and the data points are shown as diamonds. The lower plot is the same comparison, with a logarithmic scale on the y-axis. It may be seen that there is good agreement above $x_p \approx 0.04$ i.e. above a π^0 momentum of 1.8 GeV.

x_p interval	$1/\sigma_h d\sigma/dx_p$ 91 data
0.02–0.03	67.7 ± 3.5
0.03–0.04	38.5 ± 1.2
0.04–0.05	34.2 ± 1.1
0.05–0.06	26.0 ± 0.9
0.06–0.07	20.1 ± 0.65
0.07–0.08	17.2 ± 0.6
0.08–0.09	12.3 ± 0.4
0.09–0.10	10.2 ± 0.35
0.10–0.11	8.7 ± 0.3
0.11–0.12	7.3 ± 0.3
0.12–0.13	6.3 ± 0.3
0.13–0.14	6.0 ± 0.25
0.14–0.15	4.7 ± 0.2
0.15–0.20	3.09 ± 0.07
0.20–0.25	1.67 ± 0.05
0.25–0.30	1.07 ± 0.04
0.30–0.35	0.48 ± 0.03
0.35–0.40	0.33 ± 0.025

Table 6.5.1: Differential Cross-Section

No comparison of the 1990 data sample with Monte Carlo is presented in this analysis. At the time when the analysis was being performed, no suitable large sample of Monte Carlo data with the 1990 geometry was available. Such a sample has recently been made available, and it would be of obvious interest to perform a similar comparison with the 1990 data.

6.5.4 Comparison with the L3 Experiment

Table 6.5.2 gives the inclusive π^0 cross-section as measured by L3 [152]. This table gives both systematic and statistical errors. It may be noted that the ALEPH data analysed above covers a somewhat different energy range. The L3 data is compared with the 1991 ALEPH data in Fig. 6.5.4: the solid crosses are the L3 results and the dashed crosses are ALEPH results. The error bars in this plot are a quadratic combination of the statistical and systematic errors given by L3. In the L3 analysis, the systematic uncertainties were estimated by using sets of Monte Carlo data with different detector calibration constants and JETSET fragmentation parameters. Unfortunately, a large sample of similar Monte Carlo data relevant to the ALEPH detector was not available to the author at the time the analysis was conducted. Therefore, in the case of the ALEPH data, as indicated above, only

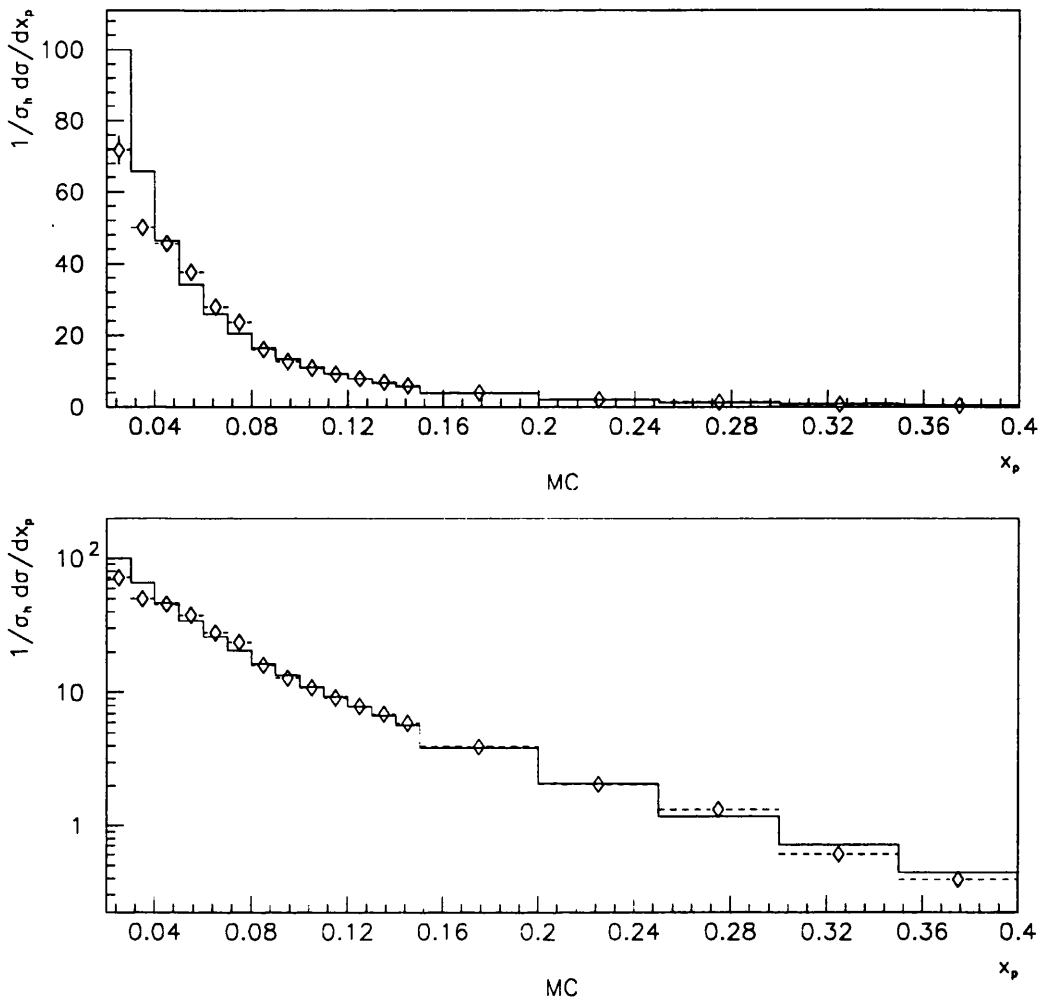

Fig. 6.5.3: Comparison of 1991 data with Monte Carlo

the statistical errors are shown, resulting in error bars which should not be directly compared to the L3 data. It would be desirable in any future analysis to study the systematic effects with ALEPH data. The data are seen to agree above $x_p = 0.04$.

6.6. Gamma Energy in the Monte Carlo

If the x_p distribution of π^0s. Fig. 6.5.3 is inspected, there is clearly a discrepancy between data and Monte Carlo at low energies. As the π^0 candidates for this study are found by combining gamma pairs, and the final cross–sections obtained depend on a Monte Carlo calculation of the detector efficiency, it is obviously of interest to compare the gammas in real data with the gammas in a Monte Carlo sample. The low energy behaviour of the gammas in the Monte Carlo was studied using a sample of 100000 class 16 events in DST

x_p interval	$1/\sigma_h d\sigma/dx_p$
0.0075–0.010	$304 \pm 35 \pm 20$
0.010–0.015	$283 \pm 16 \pm 30$
0.015–0.020	$207 \pm 10 \pm 20$
0.020–0.025	$153 \pm 7 \pm 15$
0.025–0.030	$121 \pm 6 \pm 10$
0.030–0.035	$94 \pm 5 \pm 10$
0.035–0.040	$74 \pm 4 \pm 10$
0.040–0.045	$54 \pm 3 \pm 10$
0.045–0.050	$46 \pm 3 \pm 10$
0.050–0.055	$39 \pm 3 \pm 10$
0.055–0.060	$31 \pm 3 \pm 9$
0.060–0.065	$24 \pm 4 \pm 7$

Table 6.5.2: π^0 Cross-Section from L3

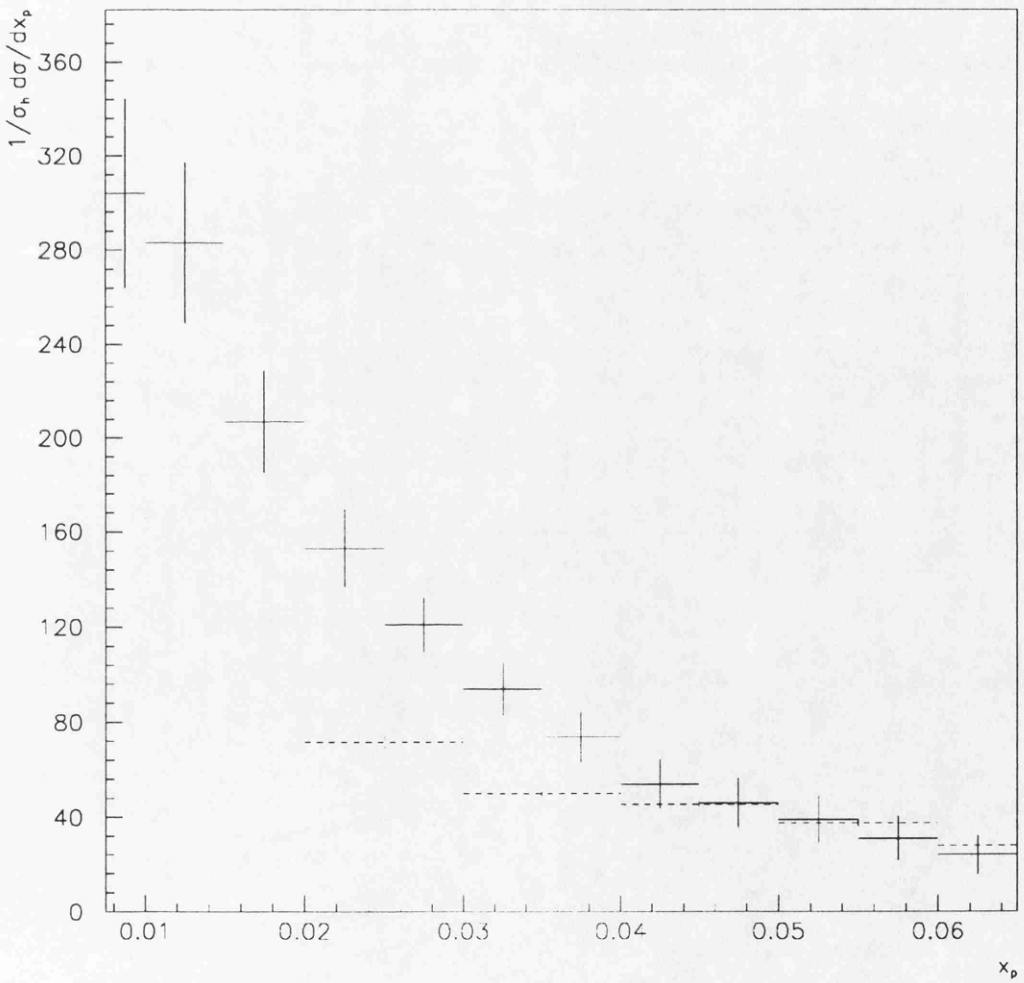

Fig. 6.5.4: Comparison of ALEPH Data with L3 Results

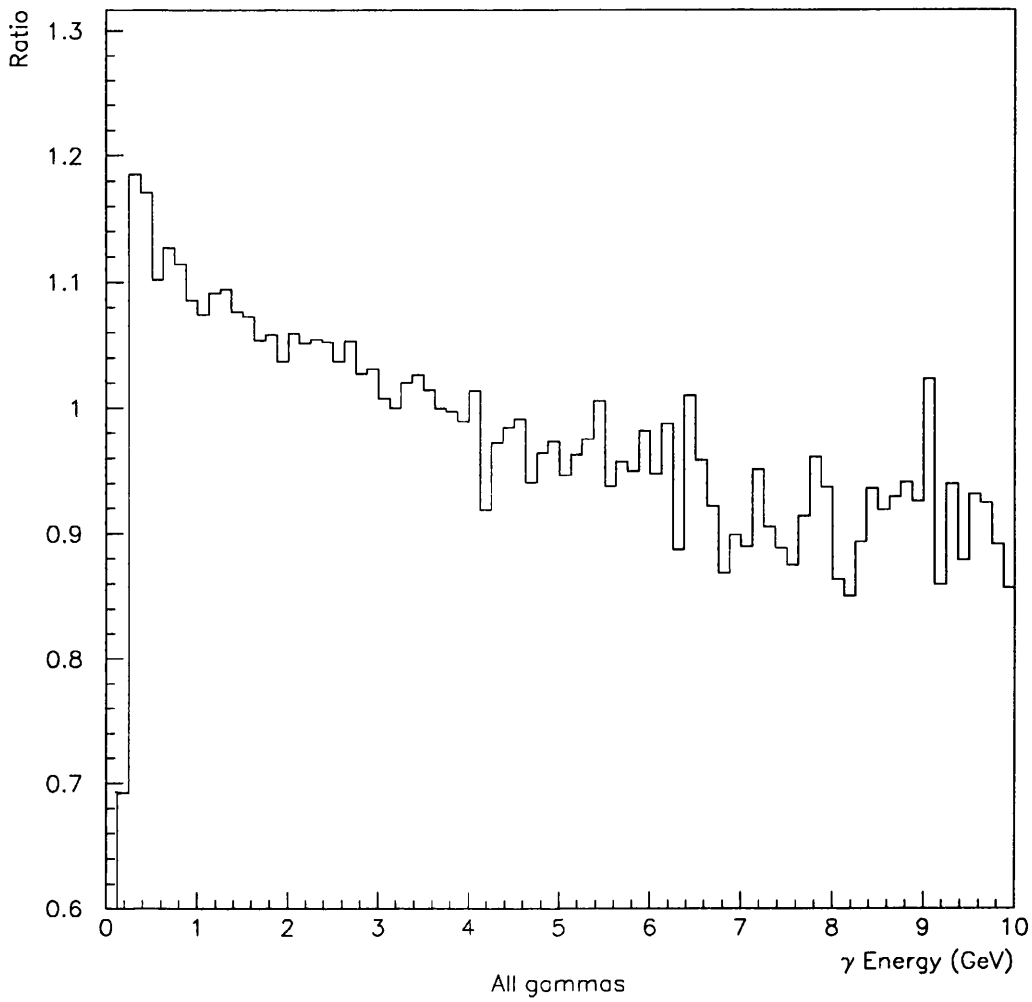

Fig. 6.6.1: Ratio of gammas in data and Monte Carlo

format from the 1991 data sample. The Monte Carlo sample used for comparison was 100000 events in POT format, generated using JETSET and the HVFL02 generator.

Fig. 6.6.1 is a comparison of the energy distribution of gammas in the data and Monte Carlo. There is an obvious excess of gammas found by GAMPEK at low energy in the real data. This discrepancy at low energy then reflects the lack of knowledge of ECAL behaviour at extremely low energies. For the analysis of inclusive π^0 production detailed above, a cut on the gamma energy was therefore applied at 0.5 GeV, as already discussed above.

The discrepancy between the number of photon clusters produced in the Monte Carlo and in the data has already been noted in the early 1989 data sample by other researchers in ALEPH [153]. As the GAMPEK package was not in use at this time, their study used neutral calorimeter clusters which were identified as photons using the cluster estimators.

These authors conclude that the excess of electromagnetic clusters in the Monte Carlo cannot be explained by the detector effects discussed above (the thresholds applied in GALEPH and the lack of dead storeys). The excess can be attributed to a failure of the Monte Carlo simulation to reproduce exactly the fluctuations and shapes of electromagnetic showers in the calorimeter, or possibly to an inadequacy in the clustering algorithms used for neutral calorimeter clusters.

6.7. Conclusion

Above a π^0 energy of around 2GeV, the JETSET Monte Carlo cross-section for inclusive π^0 production is in good agreement with the ALEPH data. It may be concluded that the measured data are well described by LUND string model.

At low energy, in the case of the charged particle distributions [33], a systematic discrepancy of around 5 % between the JETSET parton shower prediction and the data at values of x_p between 0.1 and 0.2 has already been reported by ALEPH. As described above, this study has also found a similar disagreement at low energies.

The reason for the disagreement are thought to lie in the Monte Carlo simulation of the low-energy behaviour of the calorimeter. There are slightly different thresholds applied in the Monte Carlo compared to the real online system; the material used in the GEANT simulation is a homogeneous composite, rather than a series of layers; there may be shortcomings in the parameterization used in GALEPH,which is based on testbeam data which did not extend to very low energies. It is recommended that the low energy behaviour of the calorimeter is examined in detail in the future, perhaps by using isolated, low-energy charged tracks which are well measured in the TPC, or possibly in further test beam work if this is ever possible. It may well prove worthwhile to investigate the possibility of implementing a more detailed Monte Carlo simulation.

It would also be desirable to repeat the above analysis with the 1990 ALEPH data sample, and also with the end-cap γ clusters accepted in the analysis.

Conclusions

The careful attention paid to the design, construction and testing of a complex device has enabled the collaboration to have a highly granular calorimeter with an energy resolution of $17\%/\sqrt{E}$. The device has been successfully operated at LEP for three years.

The wire pulsing technique is used for finding and mapping faults in the modules and for confirming the correct operation of the electronics readout chain prior to data taking. Wire pulsing values are used in addition to other information to provide uniformity maps of the barrel ECAL modules. Due to the effects discussed, and despite attempts to correct the data by several methods, the wire pulsing data are not as yet used to map petal uniformity.

Data were taken on the response of each module to many thousands of cosmic ray muons. After careful corrections have been applied to the uniformity data collected at the cosmic ray testing stand, the average rms. of the pad uniformity is 1.7%. The uniformity values obtained by this method are in agreement with the values obtained from electron test beam running.

Beam–line tests have been used to obtain an absolute calibration for three of the modules. The energy resolution, linearity and uniformity of response to electron beams has also been measured. The uniformity of response for the anode wires readout is similar to that measured by the cosmic ray technique.

The method of inter–calibration of modules with radioactive ^{83}Kr gas has been presented. This method gives a mean uniformity of 1.8% (if the regions affected by the 'anode step' effect are excluded), which is similar to the value for the pad uniformity measured with cosmic rays. The uniformity distributions obtained from radioactive gas testing agree closely with the data obtained from the anode wire uniformity distributions in cosmic ray tests.

Further studies of the operation of the calorimeter were made using the ALEPH data sample of hadronic events at the Z^0 peak. The calorimeter was found to resolve easily the π^0 mass peak. When the x_p distribution of π^0 was examined, it was found to agree with the Lund Monte Carlo prediction, and the data from the L3 experiment, at high x_p values. However, at low energy there is a disagreement. This is due to a lack of detailed knowledge of the calorimeter at very low energies, to the simulation methods used in the Monte Carlo and to the slightly different clustering thresholds used in the Monte Carlo. It must be stressed that the electron beam line test data upon which the parameterizations

used in the Monte Carlo are based had a lowest energy of 2.5 GeV, and also that studies are under way in the collaboration into π^0 identification using more sophisticated methods.

References

1. S. Weinberg: Rev. Mod. Phys. 46 (1974) 255 *Recent Progress in Gauge Theories of the Weak, Electromagnetic and Strong Interactions.*
2. F.J. Hasert et.al.: Phys. Lett. 46B (1973) 138 *Observation of Neutrino Like Interactions without Muon or Electron in the Gargamelle Neutrino Experiment.*
3. G. Arnison et.al. (UA1 Collaboration): Phys. Lett. 122B (1983) 103 *Experimental Observation of Isolated Large Transverse Energy Electrons with Associated Missing Energy at* $\sqrt{s} = 540\text{GeV}$.
4. M. Banner et.al. (UA2 Collaboration): Phys. Lett. 122B (1983) 476 *Observation of Single Isolated Electrons of High Transverse Momentum in Events with Missing Transverse Energy at the CERN* $p\bar{p}$ *Collider.*
5. C.D. Anderson: Phys. Rev. 43 (1933) 491 *The Positive Electron.*
6. J.C. Street and E.C. Stevenson: Phys. Rev. 52 (1937) 1003 *New Evidence for the Existence of a Particle of Mass Intermediate Between the Proton and Electron.*
7. C.M.G. Lattes et.al.: Nature 159 (1947) 694 *Processes Involving Charged Mesons.*
8. A.G. Carlson, J.E. Hooper and D.T. King: Phil. Mag. 41 (1950) 701 *Nuclear Transmutations Produced by Cosmic Ray Particles of Great Energy – Part V. The Neutral Mesons.*
9. R. Bjorklund, W.E. Crandall, B.J. Moyer, H.F. York: Phys. Rev. 77 (1950) 213 *High Energy Photons from Proton Nucleus Collisions.*
10. G.D. Rochester and C.C. Butler: Nature 160 (1947) 855 *Evidence for the Existence of New Unstable Elementary Particles.*
11. Richard Rhodes: *The Making of the Atomic Bomb*, pub. Simon & Schuster, New York 1986.
12. O. Chamberlain, E.Segre, C.Wiegand and T.Ypsilantis: Phys.Rev. 100 (1955) 947 *Observation of Antiprotons.*
13. G.K. O'Neill and E.J. Woods: Bull.Am.Phys.Soc. 3 (1958) 158 *Concentric Storage Rings.*
14. W. Barber et.al.: Phys.Rev.Lett. 16 (1966) 1127 *Test of Quantum Electrodynamics by Electron–Electron Scattering.*
15. J.E. Augustin et.al.: Phys. Rev. Lett. 33 (1974) 1406 *Discovery of a Narrow Resonance in* e^+e^- *Annihilation.*

16. J.J. Aubert et.al.: Phys.Rev.Lett. 33 (1974) 1404 *Experimental Observation of a Heavy Particle J.*

17. M.Perl et.al.: Phys.Rev.Lett. 35 (1975) 1489 *Evidence for Anomalous Lepton Production in e^+e^- Annihilation.*

18. S.W. Herb et.al.: Phys. Rev. Lett. 39 (1977) 252 *Observation of a Dimuon Resonance at 9.5* GeV *in 400* GeV *Proton–Nucleus Collisions.*

19. G. Hanson et.al.: Phys. Rev. Lett. 35 (1975) 1609 *Evidence for Jet Structure in Hadron Production by e^+e^- Annihilation.*

20. R. Brandelik et.al.: Phys. Lett. B83 (1979) 261 *Properties of Hadron Final States in e^+e^- Annihilation at 13* GeV *and 17* GeV *Center–of–mass energies.*

21. D.P. Barber et al.: Phys.Rev.Lett. 43(1979) 830 *Discovery of Three Jet Events and a Test of Quantum Chromodynamics at Petra Energies.*

22. F.Dydak: CERN–PPE/91–14 *Results from LEP and the SLC*
Rapporteur's talk at the 25th Int. Conf. on High Energy Physics. Singapore 1990.

23. The ALEPH EW Group: ALEPH 92–124 *Electroweak Parameters from Z Decays.*
Paper contributed to the 26th Int. Conf. on High Energy Physics, Dallas 1990.

24. The Working Group on LEP Energy: CERN–PPE/92–125 *The Energy Calibration of LEP in 1991.*

25. The Particle Data Group: Phys. Rev. D45 (1992) No.11 *Review of Particle Properties.*

26. D. Decamp et.al.: Phys. Lett. B259 (1991) 377–388 *Measurement of Charge Asymmetry in Hadronic Z Decays.*

27. D. Decamp et.al.: Phys.Lett. B244 (1990) 551 *Heavy Flavor Production in Z Decays.*

28. The LEP Collaborations: CERN–PPE/91–232 *Electroweak Parameters of the Z^0 Resonance and the Standard Model.*

29. D. Decamp et.al.: Phys.Lett. B234 (1990)219 *Properties of hadronic events in e^+e^- annihilation at $\sqrt{s}$ = 91* GeV.

30. R.P. Feynman et.al.: Nucl. Phys. B136 (1977) 1 *Correlations among Particles and Jets Produced with Large Transverse Momenta.*

31. G.Marchesini and B.R.Webber: Nucl. Phys. B310 (1988) 461 *Monte Carlo Simulation of General Hard Processes with Coherent QCD Radaition.*

32. C. Peterson et.al.: Phys. Rev. D27 (1983) 105 *Scaling Violations in Inclusive e^+e^- Annihilation Spectra.*

33. D.Buskulic et.al.: CERN–PPE–92–062 *Properties of hadronic Z decays and test of QCD generators.*

34. U. Pettersson: Lund Preprint LU TP 88–5 (1988) *ARIADNE - A Monte Carlo for QCD Cascades in the Colour Dipole Formulation.*

35. D. Decamp et.al.: Physics Reports 216 (1992)253–340 *Searches for New Particles in Z Decays using the ALEPH Detector.*

36. D. Decamp et.al.: Physics Letters B 236 (1990)511 *A Search for New Quarks and Leptons from Z^0 Decay at LEP.*

37. K. Sliwa: *A new limit on the mass of the top quark* in Proceedings of the XXVth Rencontres de Moriond 1990. pub. Editions Frontieres.

38. D. Schaile: CERN–PPE/91–187 *Experimental Limits on M_t and M_H – Present and Future.*

39. D.A. Glaser: Phys. Rev. 87 (1952) 665 *Some Effects of Ionizing Radiation on the Formation of Bubbles in Liquids.*

40. G. Charpak and F. Sauli: Ann. Rev. Nucl. Sci. 34 (1984) *High Resolution Electronic Particle Detectors.*

41. C.W. Fabjan : CERN-EP/85-54 *Calorimetry in High Energy Physics*
and in: *Concepts and Techniques in High Energy Physics III* ed. T. Ferbel, pub. Addison Wesley 1987.

42. C.W. Fabjan : Nucl. Instr. and Meth. A252 (1986) 145–157 *Calorimeters: Gaseous Readouts Compared to Alternatives.*

43. G. Barbiellini : CERN EP/86-203 *Calorimetry in Particle Physics.*

44. C.W. Fabjan and R. Wigmans : CERN EP/89-64 *Energy Measurement of Elementary Particles.*

45. P.B. Cushman : YCTP–P47–91 *Electromagnetic and Hadronic Calorimeters.*

46. A.N. Diddens et.al. (CHARM Collaboration): Nucl. Instr. and Meth. 27 (1980)178 *A Detector for Neutral–Current Interactions of High-Energy Neutrinos.*

47. Ch. Berger et.al.: Nucl. Instr. and Meth. A262 (1987) 463 *The Frejus Nucleon Decay Detector.*

48. D.S. Ayres et.al.: ANL–HEP–CP–85–57 : *Construction of the Soudan-2 Detector.*

49. E. Beier UPR-0138E : *The Kamiokande II Detector.* Presented at 7th Workshop on Grand Unification: ICOBAN 86.

50. R. Becker–Szendy et.al.: BU–HEP–92–6 *The IMB–3 detector.*

51. V.S.Murzin: *Progress in Elementary Particle and Cosmic Ray Physics* Vol 9 North Holland (1967).

52. R.M. Baltrusaitis et.al.: Nucl. Instr. and Meth. A264 (1988) 87–92 *The Fly's Eye Detector: Present and Future.*

53. G. Gerbier : *Dark Matter, an Overview* in Proceedings Conf. Physics in Collision – Colmar 20–22/6/91.

54. Smithsonian Astrophysical Observatory SO5-06510 *Feasibility Investigation of a Superheated Superconducting Colloid (S.S.C.)Calorimeter.*

55. M. Spiro : DPhPE 91–17 *Calorimeters for Astroparticle Physics*
Talk given at the 2nd Int. Conf. on Calorimetry in High Energy Physics, Capri 1991.

56. B.Rossi : *High Energy Particles*, pub. Prentice Hall, New York 1964.

57. H. A. Bethe : Annalen der Physik 5 (1930) 325 *Zur Theorie des Durchgangs schneller Korpus–kularstrahlen durch Materie.*

58. Bathow et.al.: Nuclear Physics B20 (1970) 592-602 *Measurements of the Longitudinal and Transverse Development of Electromagnetic Cascades in Lead, Copper and Aluminium at 6* GeV.

59. T. Yuda : Nucl. Instr. and Meth. 73 (1968) 310 *Electron–Induced Cascade Showers in Inhomogeneous Media.*

60. E.Longo and I.Sestili : Nucl. Instr. and Meth. 128 (1975) 283 *Monte Carlo Calculation of Photon Initiated Electromagnetic Showers in Lead Glass.*

61. R. Wigmans : Ann. Rev. Nucl. Part. Sci. 41 (1991) 133 *Advances in Hadron Calorimetry.*

62. C.W. Fabjan et.al.: Nucl. Instr. and Meth. 141 (1977) 61 *Iron Liquid–Argon and Uranium Calorimeters for Hadron Energy Measurement.*

63. T. Akesson : Nucl. Instr. and Meth. A241 (1985) 17 *Properties of a Fine–Sampling Uranium–Copper Scintillator Hadron Calorimeter.*

64. R. Wigmans : Nucl. Instr. and Meth. A259 (1987) 389 *On the Energy Resolution of Uranium and Other Hadron Calorimeters.*

65. H1 Calorimeter Group: DESY 88–073 (1988) *Performance of a Pb Cu Liquid Argon Calorimeter with an Iron Streamer Tube Tail Catcher.*

66. R. Wigmans: CERN-PPE/91-205 *Performance and Limitations of Hadron Calorimeters.* Talk given at the 2nd Int. Conf. on Calorimetry in High Energy Physics, Capri 1991.

67. M. Oreglia et.al.: Phys. Rev. D 25 (1982) 2259 *Study of the Reaction* $\Psi' \rightarrow \gamma\gamma J/\Psi$.

68. H. Grassmann et.al.: Nucl. Instr. and Meth. A235 (1985) 319 *Results from a Cs(I)Test Calorimeter with Photodiode Readout Between 1 and 20* GeV.

69. G. von Dardel et.al.: CERN/LEPC/83-5 (1983) *L3 Technical Proposal.*

70. E.Lorenz : Nucl. Instr. and Meth. A225 (1984) 500 *Status of BGO Development and Perspectives of BGO Calorimeters in High Energy Physics.*

71. L.Bachman : Nucl. Instr. and Meth. 206 (1983) 85 *A Fine-Grained Electromagnetic Lead-Liquid Scintillator Calorimeter.*

72. B.Loehr : DESY 86-072 *An Electromagnetic Calorimeter with Wavelength Shifting Fibre Readout.*

73. D. Acosta et.al.: Nucl. Instr. and Meth. A294 (1990) 193 *Results of Prototype Studies for a Spaghetti Calorimeter.*

74. W.J. Willis and V. Radeka : Nucl. Instr. and Meth. 120 (1974) 221 *Liquid-Argon Ionisation Chambers as Total Absorption Detectors.*

75. A. Baranov et.al.: CERN-EP/90-03 *Liquid Xenon Calorimeter for the Detection of Electromagnetic Showers.*

76. M.Albrow et.al. (UA1 Collaboration): CERN EP/87-55 *Performance of a Uranium / Tetramethylpentane Electromagnetic Calorimeter.*

77. G. Battistoni et.al.: Nucl. Instr. and Meth. 152 (1978) 423 *Detection of Induced Pulses in Proportional Wire Devices with Resistive Cathodes.*

78. H. Videau : Nucl. Instr. and Meth. 225 (1984) 481 *The Aleph Electromagnetic Calorimeter.*

79. M. Edwards : RAL 86 007 *The Aleph Electromagnetic Calorimeter.*

80. M. Bergrenn : Nucl. Instr. and Meth. A225 (1984) 447 *Performance of a High Density Projection Chamber.*

81. H.G.Fischer and O.Ullaland: IEEE Transactions on Nuclear Science 27 (1980) 38 *A High Density Projection Chamber.*

82. J. Appel: FERMILAB FN-380 *Summary Session of the Gas Sampling Calorimetry Workshop October 29, 1982 .*

83. M. Atac: *Proceedings of the Gas Sampling Calorimetry Workshop, Fermilab (1982).*

84. M. Atac: *Proceedings of the 2nd Gas Sampling Calorimetry Workshop, Fermilab (1985).*

85. M. Atac: FERMILAB FN-332 (1980) *Gas Ionisation Sampling Calorimeters.*

86. J. Engler : Nucl. Instr. and Meth. A217 (1983) 9–18 *Electromagnetic Calorimeters Using Wire Chambers.*

87. H.G. Fischer : Nucl. Instr. and Meth. 156 (1978) 81–85 *Multiwire Proportional Quantameters.*

88. T. Ludlam et.al.: Nucl. Instr. and Meth. A198 (1982) 233–241 *A High Density Proportional Wire Calorimeter.*

89. U. Amaldi : Physica Scripta 23:409 (1981) *Fluctuations in Calorimetric Measurements.*

90. R.L. Ford and W.P. Nelson : SLAC-210 *EGS. Version IV.*

91. R. Brun et.al.: CERN DD/EE/84-1 *GEANT3.*

92. J. Del Peso and E. Ros : Nucl. Instr. and Meth. A276 (1989) 456–467 *On the Energy Resolution of Electromagnetic Sampling Calorimeters .*

93. Proceedings of the Workshop on Shower Simulation for LEP Experiments, 21–31 January 1985, CERN, Geneva, Switzerland.

94. Ren-yuan Zhu : Nucl. Instr. and Meth. A306 (1991) 145-149 *Precision Calibration of Electromagnetic Calorimeters with a Radio-Frequency Quadrupole Accelerator.*

95. Cochet et.al.: Nucl. Instr. and Meth. A243 (1986) 45 *The Central Electromagnetic Calorimeter of UA1.*

96. Drescher et.al.: Nucl. Instr. and Meth. A249 (1986) 277 *Calibration and Monitoring of the ARGUS Shower Counters.*

97. Dorenbosh et.al.: Nucl. Instr. and Meth. A276 (1987) 253 *Calibration of the CHARM Fine-grained Calorimeter.*

98. J.P.De Wulf et.al.: Nucl. Instr. and Meth. A278 (1989) 670 *A Detector for the Study of Neutrino and Anti-neutrino Scattering off Electrons* CHARM II Collaboration.

99. M. Franklin : *Performance of the Gas Calorimetry at CDF* presented at the Topical Workshop on Proton-Antiproton Physics Fermilab 1988.

100. T.Camporesi et.al.: IEEE Trans. Nucl. Sci. NS-36 (1989) 344 *Characteristics of a Large System of Pad Readout Wire Proportional Chambers for the HPC Calorimeter.*

101.The LEP Study Group: CERN-LEP/TH/83-29 and CERN-LEP/84-01 *The LEP Design Report.*

102.G. Bachy, A. Hofmann, S. Myers, E. Picasso, G. Plass : CERN/LEP-DI-IM-RF/89-41 *The LEP Collider – Construction, Project Status and Outlook.*

103.L. Camilleri et.al.: CERN 76-18 (1976) *Physics with Very High-Energy e^+e^- Colliding Beams.*

104.J.R.J. Bennett et.al.: CERN 77-14 (1977) *Design Concept for a 100* GeV *e^+e^- Storage Ring (LEP).*

105.The LEP Study Group: CERN/ISR-LEP/78-17 *The LEP Design Report.*

106.The LEP Study Group: CERN/ISR-LEP/79-33 *Design Study of a 22 to 130* GeV*e^+e^- Colliding Beam Machine (LEP).*

107.S. Myers : CERN 91-08 *The LEP Collider. From Design to Approval and Commissioning.*

108.Brown and Redlinger : ALEPH NOTE 92-008 *1991 Beam Spot and Beam Envelope Measurements.*

109.D. Decamp et.al.: CERN/LEPC/83-2 and CERN/LEPC/84-15 *ALEPH: Technical Report.*

110.D. Decamp et.al.: ALEPH NOTE 89-03 *The ALEPH Handbook.*

111.D. Decamp et.al.: Nucl. Instr. and Meth. A294 (1990) 121-178 *ALEPH : a Detector for Electron-Positron Annihilations at LEP.*

112.G. Batignani : ALEPH NOTE 91-158 *Recent Results and Running Experience of the New ALEPH Vertex Detector.*

113.G.J. Barber et.al.: Nucl. Instr. and Meth. A279 (1989) 212 *Performance of the Three-Dimensional Readout of the ALEPH ITC.*

114.D. R. Nygren: PEP-0198 (1975) *A Time Projection Chamber.*

115.Atwood et.al.: CERN-PPE/91-21 *The Performance of the ALEPH Time Projection Chamber.*

116.D. Decamp et.al.: Z.Phys. C53 (1992) 375-390 *Measurement of the Absolute Luminosity with the ALEPH Detector.*

117.E. Barsotti et.al.: FERMILAB-PUB-87/190-E *Fastbus Data Acquisition for CDF.*

118.G. Kellner: Computer Physics Communications 45 (1987) 229 *Development of Software for ALEPH using Structured Techniques.*

119.Z. Quian et.al.: Computer Physics Communications 45 (1987) 283 *Use of the ADAMO Data Management System in ALEPH.*

120.M.G. Green: ALEPH 89-47 *The ADAMO Data System – An Introduction for Particle Physicists.*

121.A. Putzer : *Data Base Systems in HEP* in Proceedings of CERN School of Computing Troia, Portugal 1987.

122.Opcode Inc. : CERN/DD/US/101 (1987) *Historian Plus Users Manual.*

123.V. Blobel: DESY RI-88-01 *The BOS System – Dynamic Memory Management.*

124.A.Falvard and B. Bloch-Devaux : ALEPH NOTE 88-197 *Simulation of $B\bar{B}$ Mixing within Lund.*

125.S. Dugeay and P. Henrard : ALEPH NOTE 88-82 *Heavy Quark Production with the LUND Generator: Comparison with e^+e^- Data.*

126.P.Henrard : ALEPH NOTE 89-25 *A Study of the Exclusive and Inclusive Branching Ratios of Heavy Mesons Obtained with the LUND Generator: Comparison with Data.*

127.T. Sjostrand : LU TP 85-10 *The Lund Monte Carlo for Jet Fragmentation and e+e- Physics.*

128.B.W. Lynn & D. Kennedy : SLAC-Pub 4039 *Effective Lagrangian for Electroweak Radiative Corrections in Four Fermion Processes.*

129.J. E. Campagne and R. Zitoun: LPNHE 88-06 *An expression of the electron structure function in QED.*

130.A.M. Lutz: NA31-5 *EM and Hadronic Shower Simulation.*

131.J. Badier and M. Bardadin-Otwinowska : ALEPH NOTE 87-09 (1987) *Longitudinal Distribution of Electromagnetic Showers in the ALEPH Electromagnetic Calorimeter.*

132.J. Badier et.al.: ALEPH NOTE 87-73 (1987) *Transverse Distribution of Electromagnetic Showers in the ALEPH Electromagnetic Calorimeter.*

133.M. Bardadin-Otwinowska et.al.: ALEPH NOTE 89-2/EMCAL 89-1 (1989) *Electromagnetic Calorimeter Response to Muons and Non-Interacting Pions .*

134.G. de Bouard: ALEPH NOTE 89-171 *ECAL Barrel Modules Intercalibration.*

135.J.P. Albanese et.al.: Nucl. Instr. and Meth. A253 (1986) 73–76 *A Fast Clustering Algorithm for the e/γ ALEPH Calorimeter.*

136.R. Brun et.al.: CERN–DD/89/17 *PAW: A General Purpose Portable Software Tool for Data Analysis and Presentation.*

137.C. Grab: ALEPH NOTE 89–12 *DALI — Event Display User's Guide.*

138.A. Bonissent and F. Etienne: ALEPH NOTE 88–106 *Pigal User's Guide.*

139.The ALEPH Collaboration : CERN/LEPC/82–18 *Electron–Photon Calorimeter (Addendum to Letter of Intent).*

140.P. Mine and D. Smith : ALEPH NOTE 103. May 1983 *Progress on EGS Simulation of ALEPH EM Calorimeter.*

141.J. Pascual, A. Joudon. J.F. Renardy : Orsay (1986) *The MUX ADC 512 towers F6845 – Specifications of Prototype.*

142.J. Le Francois and J. Rander: ALEPH NOTE 102 *Uniformity and Stability of the ALEPH e/γ Calorimeter.*

143.D. Bollini et.al.: Nucl. Instr. and Meth. 204 (1983) 333–349 *A High Luminosity Spectrometer for Deep Inelastic Muon Scattering Experiments.*

144.T. Sloan and S. Snow: ALEPH NOTE 88–23 *dE/dx of Cosmic Muons in ECAL.*

145.J. C. Thompson: ALEPH NOTE 89–23 *ECAL Production Modules – Calibration and Uniformity of Response.*

146.B. Michel: Nucl. Instr. and Meth. A263 (1988) 43–50 *Electron–Pion Separation in a Highly Segmented Electromagnetic Calorimeter Designed for the ALEPH Experiment.*

147.M.G. Catanesi et.al.: Nucl. Instr. and Meth. A247 (1986) 438 *Performance of a Limited Streamer Tube Hadron Calorimeter.*

148.M. de Palma et.al.: Nucl. Instr. and Meth. A277 (1989) 68 *Hadronic Energy Measurement in the ALEPH Calorimeter Prototype.*

149.Bagliesi et.al.: Nucl. Instr. and Meth. A286 (1990) 61–68 *The Combined Response of the ALEPH Electromagnetic and Hadronic Calorimeter to Pions.*

150.G. D'Agostini: ALEPH NOTE 87–90 *Studies on the ALEPH electromagnetic calibration with the Bhabha events.*

151.M. Caffo and E. Remiddi: *Bhabha Scattering* in CERN 89–08 *Z Physics at LEP Vol. 1* 171.

152.B. Adeva et.al. (L3 Collaboration): Physics Letters B 259 (1991)199 *Measurement of the inclusive production of neutral pions and charged particles on the Z^0 resonance.*

153.E. Lancon, P. Perez, F. Perrier: ALEPH NOTE 90-66 *Photons in Hadronic Events.*